

SYNTHESIS, CHARACTERIZATION AND SINGLE PARTICLE SPECTROSCOPY OF SEMICONDUCTOR QUANTUM DOTS AND QUANTUM DOT OLIGOMERS

Dissertation

zur Erlangung des Grades
„Doktor der Naturwissenschaften“
im Promotionsfach Chemie

am Fachbereich Chemie, Pharmazie und Geowissenschaften
der Johannes Gutenberg–Universität in Mainz

NAN HU

geb. in Shenyang, Liaoning Province, P. R. China

Mainz, 2015

Dekan:

1. Berichterstatter:

2. Berichterstatter:

Tag der mündlichen Prüfung: 16.12.2015

Dedicated to my loving parents and wife

Contents

1	Introduction	1
2	Theoretical background	5
2.1	Semiconductor nanocrystal quantum dots (QDs)	5
2.1.1	Electronic states and optical properties	5
2.1.2	Synthesis, growth and crystal structures	13
2.1.3	Core/shell structure	19
2.1.4	InP based quantum dots	21
2.2	Preparation of quantum dot oligomers	23
2.2.1	Self-assembly and separation of nanoparticles	23
2.2.2	Density gradient ultracentrifugation (DGU)	28
2.3	Single particle spectroscopy of quantum dots	32
2.3.1	Confocal fluorescence microscopy	32
2.3.2	Detection of a single particle (QD)	35
2.3.3	Fluorescence blinking	36
2.3.4	Spectral diffusion	43
2.3.5	Single particle spectroscopy at cryogenic temperature	44
3	Experimental materials and methods	51
3.1	Materials	51
3.2	Synthetic methods	53
3.2.1	Synthesis of CdSe/CdS/ZnS quantum dots	53
3.2.2	Assembly and enrichment of quantum dot oligomers	57
3.2.3	Synthesis of InP/ZnSeS quantum dots	57
3.3	Characterization techniques	58
3.3.1	Ensemble absorption and fluorescence spectroscopy	58
3.3.2	Transmission electron microscopy (TEM)	60

3.3.3	Energy dispersive X-ray spectroscopy (EDS)	60
3.3.4	X-ray diffraction (XRD)	60
3.3.5	Fluorescence lifetime measurements	61
3.4	Experimental setups for single particle investigations	61
3.4.1	Sample preparation	61
3.4.2	Excitation light sources	61
3.4.3	Confocal microscope for cryogenic temperature measurement	62
3.4.4	Confocal microscope for room temperature measurement	66
3.4.5	Experimental conditions for single particle measurements	67
4	Monomers, homo- and hetero- dimers of CdSe/CdS/ZnS QDs	69
4.1	Motivation and approaches	69
4.2	CdSe/CdS/ZnS QD monomers and homo-dimers	71
4.2.1	CdSe cores and CdSe/CdS/ZnS QDs	71
4.2.2	Assembly of CdSe/CdS/ZnS QDs	73
4.2.3	Enrichment and separation of QD oligomers	76
4.2.4	Fluorescence imaging of single QDs	83
4.2.5	Single particle spectroscopy of QD monomer and dimer samples at room temperature (T = 295 K)	85
4.2.6	Single particle spectroscopy of CdSe/CdS/ZnS QD monomers at cryogenic temperature (T = 4.5 K)	86
4.2.7	Single particle spectroscopy of QD dimer sample at cryogenic temperature (T = 4.5 K)	92
4.3	CdSe/CdS/ZnS QD hetero-dimers	96
4.3.1	Size dependent fluorescence of CdSe core particles	96
4.3.2	QD hetero-dimers whose QD components have different sizes	96
4.3.3	QD hetero-dimers whose QD components have similar sizes	103
4.3.4	Structure <i>Ila</i> : QD components with the same CdSe core	104
4.3.5	Structure <i>Ilb</i> : QD components with different CdSe cores	105
4.4	Summary	111
5	Investigations of InP/ZnSeS QDs	113
5.1	Introduction and motivation	113
5.2	Sample description	115
5.3	Ensemble characterizations	115
5.3.1	<i>HLim</i> series	115
5.3.2	<i>H</i> series	116

5.3.3	<i>L</i> series	118
5.4	Single particle measurements at room temperature ($T = 295$ K)	127
5.4.1	<i>HLim</i> series	127
5.4.2	<i>H</i> and <i>L</i> series	134
5.5	Single particle measurements at cryogenic temperature ($T = 4.5$ K)	141
5.5.1	Typical emission spectrum of InP/ZnSeS QDs at 4.5 K	142
5.5.2	Phonons contributions	142
5.5.3	Categories of single particle spectra	146
5.5.4	Average optical phonon energies	148
5.5.5	Fluorescence blinking at 4.5 K	148
5.6	Comparison of the different samples	151
5.7	Possible mechanisms of the strong blinking suppression	153
5.8	Summary	156
6	Summary and outlook	159
	References	163

1

Introduction

Along with the rapid development of nanotechnology, fluorescent colloidal quantum dots (QDs), which are semiconductor crystals with several nanometers in size, have attracted remarkable scientific and technological interest and been extensively studied since the 1980s [1]. In QDs, the quantum confinement of the charge carriers (electrons and holes) results in a discretization of the electronic energy levels at the energy band edges and leads to a size dependent energy band gap, which allows the absorption and the fluorescence energies to be tuned easily. Due to their broad absorption and narrow emission spectra, high photostability as well as other “tailor-made” optical properties, QDs have been widely applied in fields ranging from solid-state lighting [2–8], displays [9], photovoltaic devices [10, 11] to fluorescence imaging [12–14].

Since the pioneering breakthrough of QD synthesis by Murray et al. in 1993 [15], an enormous amount of research has been reported on the further improvement of the properties of QDs, such as narrow size distribution, high photoluminescence quantum yield, high photostability and narrow emission spectral profile [16–23]. From another perspective, the individual particles within an ensemble may behave quite differently due to variations in size, lattice stoichiometry, crystallinity, morphology, surface ligand state and local environment [24]. Moreover, applications of QDs such as biological fluorescent labelling [12, 14, 25], single particle tracking [26], quantum cryptography [27] and single-photon sources [28] can only be realized at the single particle level. Therefore, in order to have a comprehensive understanding of the photophysical properties of QDs, single particle investigations are indispensable. Owing to a good signal to noise ratio, laser scanning confocal microscopy is one of the essential tools for single particle fluorescence measurements [29].

Furthermore, as the applications of nano-materials continue to expand, nanoscale architectures with increasing complexity are evoking broad interest [30]. Like other nanoparticles, QDs can be considered as chemical building blocks and used to construct extended and more complex architectures [31, 32]. The properties of the assembled structures have been found to be different from those of the isolated components [33–39], and e.g., the emission energy can be controlled by electronic coupling among nanoparticles in three dimensional superlattices [40–43]. Obviously, the study of simple nanostructures, meaning dimers composed of two single particles, is an promising starting point of investigations on the fundamental mechanism of the interactions (e.g., electronic coupling) among nanoparticles. To date, although various nanoparticles have been connected by organic molecules or DNAs to form oligomers [32, 34, 35, 44], the reports on direct assembly of particles without linkers are rather rare and mainly limited to metal nanoparticles [45, 46]. In 2011, Xu et al. successfully assembled and enriched CdSe/CdS/ZnS QD dimers and trimers in an organic solvent [47]. However, a detailed investigation of the electronic interactions of the components in QD dimers at the single particle level is still lacking. Along these lines, a hetero-dimer system in which the two QDs have either different sizes or different compositions is a promising option. In this thesis, both CdSe/CdS/ZnS QD homo- and hetero-dimers were prepared, enriched and characterized. The fluorescence emission from the two QDs within a homo-dimer could be resolved by single particle spectroscopy at 4.5 K due to the narrowing of the spectral linewidths at cryogenic temperature. For hetero-dimers, two kinds of QDs with a large separation in emission wavelength were prepared and assembled. The obtained hetero-dimers were characterized by a combination of atomic force and confocal fluorescence microscopy at room temperature.

Previous studies of QDs have been mainly limited to group II-VI materials such as CdSe, CdS and CdTe. A big disadvantage is that the commonly used heavy metal element Cd is very toxic which can severely damage kidneys, bones and lungs of human beings and increase cancer risks [48]. Therefore, concerning practical applications, more environmentally benign or so-called “greener” QDs are urgently needed [49, 50]. Among the possible materials, InP-based QDs have been studied and considered to be promising alternatives due to their low toxicity and wide emission spectral tunability ranging from the visible region to the near-infrared region [4, 6, 51–53]. Therefore, the second part of this thesis focused on InP based (InP/ZnSeS) QDs.

At the single particle level, even under continuous illumination, QDs exhibit fluorescence intermittency (or blinking) on a broad time scale from microseconds to hours. The fluorescence intensity randomly switches between bright (*on*) and dark (*off*) states

with the *on* and *off* periods following inverse power-law distributions without any characteristic time scale. This becomes an intrinsic drawback for applications of QDs based on single particle emission as mentioned above. Since the first observation of blinking by Nirmal et al. in 1996 [54], numerous studies have focused on this mysterious phenomenon [55–63]. Although the mechanism of fluorescence blinking is still not completely understood, various approaches for blinking suppression have been developed, including changing the temperature and excitation energy [57, 64, 65], coupling QDs to a metal plasmon resonance [66–68], surface modification [69–75], overcoating QDs with thick shells (“giant” QDs) [76–78], changing the confinement potential [79–81] and improving the crystallinity [82–84].

Most of the studies on the suppression of fluorescence blinking have focused on group II-VI QDs (e.g. CdSe). In contrast, there are very few reports on the fluorescence blinking of InP based QDs [85–87], and no InP based QDs without blinking have ever been observed so far. Zan et al. discussed the influence of synthetic conditions on the blinking of InP/ZnS QDs [86], and Dennis et al. observed effective blinking suppression even when only a thin shell of CdS was overcoated onto InP core [87]. Besides the findings from other non-blinking QD systems of CdZnSe/ZnSe [80], zinc-blende CdSe/CdS [83] and (Zn)CuInS/ZnS [84], these two studies on InP based QDs also emphasized the significant impact of the internal structure on blinking suppression. Recently, an alloy ZnSeS shell was overgrown on InP cores by Lim et al. to prepare InP/ZnSeS QDs [7, 52], by which the large lattice mismatch between InP and ZnS was alleviated and therefore a high quantum yield was obtained [7, 52]. Based on this work, different series of InP/ZnSeS QDs were prepared under various experimental conditions and systemically investigated at 295 K and 4.5 K in this thesis. Particularly, it was found that InP/ZnSeS QDs with 0.2 mmol Se exhibited high quantum yield, good crystallinity and strong blinking suppression. Possible mechanisms of the blinking suppression were suggested and discussed.

The organization of this thesis is as follows: Chapter 2 introduces the theoretical background on the structure and synthesis of QDs, the assembly and separation of QD oligomers and single particle spectroscopy at room temperature and cryogenic temperatures. Chapter 3 focuses on the synthetic methods, characterization techniques, sample preparation and experimental setups. The experimental results are given in the subsequent two chapters: Chapter 4 addresses the strategies of preparations and characterizations of monomers, homo- and hetero-dimers of CdSe/CdS/ZnS QDs. Chapter 5 presents the investigations on InP/ZnSeS QD system, including synthesis, ensemble characterizations, single particle measurements at 295 K and 4.5 K as well as the results and discussions of the blinking suppression of samples under various synthetic

conditions. At last, Chapter 6 summarizes the findings of this thesis and presents an outlook.

2

Theoretical background

2.1 Semiconductor nanocrystal quantum dots (QDs)

2.1.1 Electronic states and optical properties

2.1.1.1 Bulk semiconductor

Semiconductors are materials with electronic structures between those of conductors and insulators.

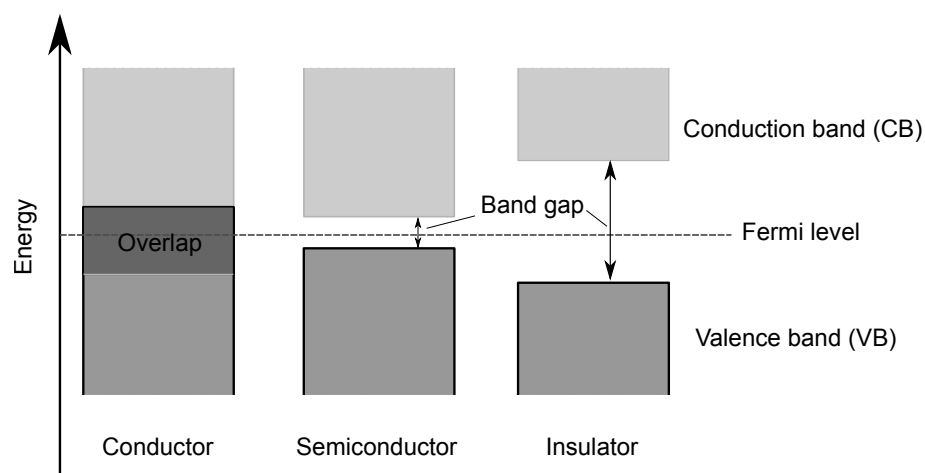


Figure 2.1: Schematic diagram of energy structures of conductors, semiconductors and insulators.

In a single free atom, electrons occupy atomic orbitals to form a structure of discrete energy levels. If two atoms are brought close together, the wavefunctions of them overlap spatially, which will induce a splitting of the energy eigenstates. As more and more atoms are introduced, the density of the energy states increases due to the increasing number of the split levels. Eventually, as a solid containing numerous atoms, the energy levels are so close and can be considered to form a continuum. Continua of allowed states are called energy bands. The band with the highest energy which is occupied in the ground state is the valence band (VB) while the band with the lowest energy which is unoccupied in the ground state is the conduction band (CB). As shown in Figure 2.1, in metals or other conductors the valence band overlaps the conduction band whereas in insulators the electrons in the valence band are separated by a large gap from the conduction band. Differently from both, in semiconductors the energy barrier to excite electrons from the valence to the conduction band is relatively small (usually between 0.3 and 3.8 eV) and can be overcome if an external energy is applied. Figure 2.2 reveals an overview of the band alignment of III-V and II-VI bulk semiconductors. An excited electron in the conduction

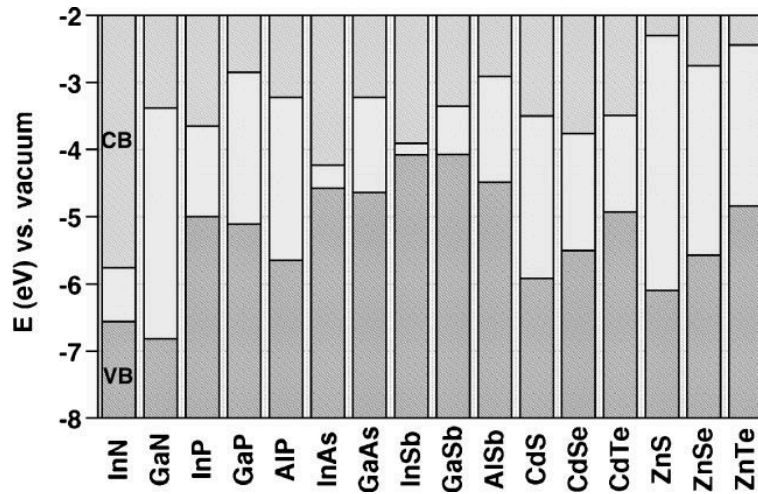


Figure 2.2: Electronic energy bands of some III-V and II-VI semiconductors. CB: conduction band; VB: valence band. From Ref. [88].

band is attracted to the resulting hole in the valence band by the electrostatic Coulomb force. When they approach each other in space, the “electron-hole pair” forms a bound state, which is considered as an electrically neutral quasi-particle, called exciton. The Bohr radius of the exciton is given by [89]:

$$a_{\text{exc}}^{\text{B}} = \frac{\hbar^2 \epsilon}{e^2} \left(\frac{1}{m_e^*} + \frac{1}{m_h^*} \right) \quad (2.1)$$

where ϵ denotes the bulk optical dielectric coefficient, e is the elementary charge, m_e^* and m_h^* are the effective mass of the electron and hole, respectively. The Bohr radii of excitons in bulk CdSe and bulk InP crystals are about 5.6 nm [90, 91] and 10.0 nm [92], respectively.

2.1.1.2 Nanocrystalline semiconductors: quantum dots

In the past decades, more and more research focused on crystals with very small dimensions. Fluorescent colloidal quantum dots (QDs), or also known as semiconductor nanocrystals (NCs), are small crystalline semiconductor particles whose sizes are about a few nanometers. As described below, Figure 2.3 shows schematically the development of the electronic structure from atoms to bulk crystals. Since the number of atoms in QDs is between the one of atoms or molecules and the one of bulk crystals, QDs represent an intermediate state between single atoms and macroscopic solids, composed of both continuous energy bands and discrete energy levels at the band edge. Compared to the bulk semiconductors, the excitonic wavefunctions of QDs are confined in all three spatial dimensions. When the size of a QD is smaller than the bulk exciton Bohr radius of the corresponding semiconductor defined by Equation 2.1, the band gap energy of the QD increases by an additional amount of confinement energy, which can be fine-tuned by the size of the particle. As a result of this quantum size effect [93, 94], QDs are featuring size dependent optical properties [95–97] such as “tailor-made” absorption and fluorescence spectra, which can be applied in wide range of fields such as LEDs [2–7, 98], lasers [99, 100], photovoltaic devices [10, 11], fluorescent labels [12–14]. Figure 2.4 shows solutions of some fluorescent CdSe QDs by own synthesis with sizes ranging from 1.5 to 5 nm.

For a theoretical description or calculation of the electronic structure of QDs, different approaches were proposed, such as: (1) *Tight-binding-model*, which uses linear superposition of atom orbitals (LCAO) of known orbital basic sets from isolated atoms to define a polyatomic wavefunction; (2) *Pseudopotential*, which replaces the true potential of the ion core (the nucleus and non-valence core electrons) with an effective potential; (3) *Effective mass approximation*, which is highlighted below with a more detailed description.

Effective mass approximation (EMA), based on the approach that the state continuum of the free electrons is split into separate bands by the periodic potential of the crystal lattice (a top-down approximation), is widely applied to calculate the electronic states of QDs. The transition from the bulk to the nanocrystal crystal passes through a three-dimensional spatial confinement of the charge carriers. By a definition of effective mass, the electrons in QDs exhibit a weak binding to the atomic cores and are considered to

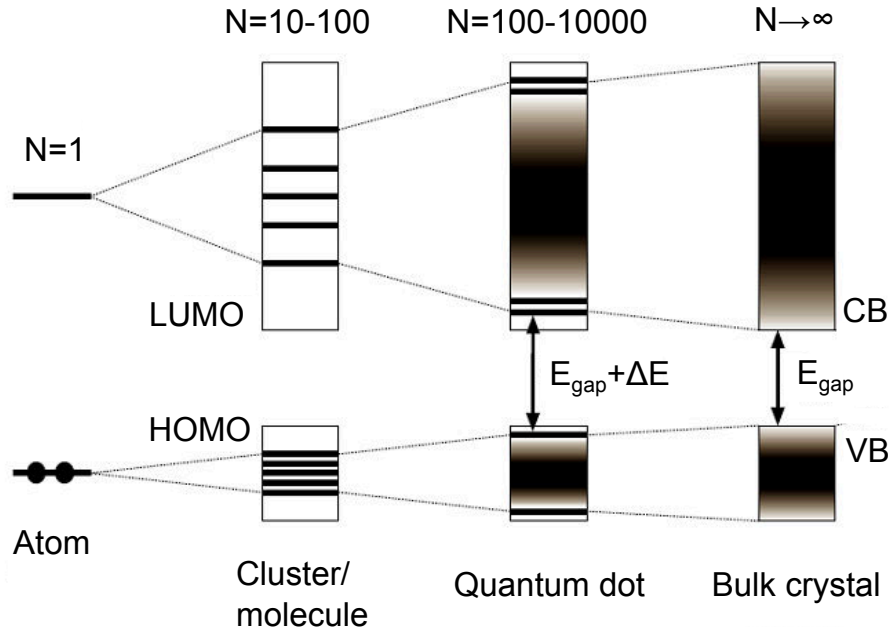


Figure 2.3: Schematic diagram of the energy structures from a single atom, cluster/molecule, quantum dot to bulk crystalline semiconductor. Adapted from Ref. [101].

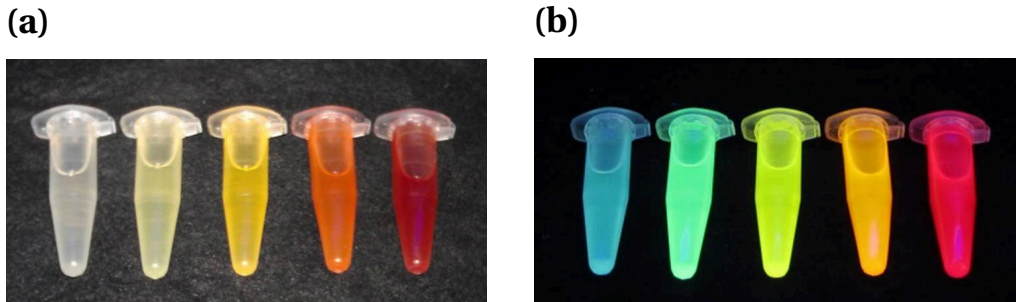


Figure 2.4: Photographs of solutions of CdSe quantum dots by own synthesis with different sizes (either photo from left to right: about 1.5 nm, 2.5 nm, 3.5 nm, 4 nm and 5 nm) under (a) room light and (b) the excitation of 366 nm from a UV-lamp.

be nearly free. Specifically, the electron is a particle described in a potential well. The time-independent Schrödinger equation is expressed as:

$$\hat{H}\Psi(\mathbf{r}) = \left[-\frac{\hbar^2}{2m^*}\nabla^2 + V_R(\mathbf{r}) \right] \Psi(\mathbf{r}) = E\Psi(\mathbf{r}) \quad (2.2)$$

with the position vector \mathbf{r} , the lattice vector \mathbf{R} and the lattice periodic potential $V_R(\mathbf{r}) = V_R(\mathbf{r} + \mathbf{R})$. As a solution in terms of Bloch waves with the form of

$$\Psi_{\nu,\mathbf{k}}(\mathbf{r}) = u_{\nu,\mathbf{k}}(\mathbf{r})e^{i\mathbf{k}\mathbf{r}} \quad (2.3)$$

where ν is the band index, the corresponding energy dispersion becomes:

$$E_\nu(\mathbf{k}) = \frac{\hbar^2}{2m_\nu^*(\mathbf{k})} \mathbf{k}^2 \quad (2.4)$$

With the assumption that there is no interaction between the electron and the hole, the wavefunction of an electron-hole pair can be separated:

$$\Psi_{\text{ehp}}(\mathbf{r}_e, \mathbf{r}_h) = \Psi_e(\mathbf{r}_e)\Psi_h(\mathbf{r}_h) = \prod_{i=e,h} \Psi_i(\mathbf{r}_i) \quad (2.5)$$

The QD is approximated as a hard sphere with the radius R and spatially confined by a spherical potential described as:

$$V_i(\mathbf{r}_i) = \begin{cases} 0 & \text{if } \mathbf{r}_i < R \quad (i = e, h) \\ \infty & \text{if } \mathbf{r}_i \geq R \quad (i = e, h) \end{cases} \quad (2.6)$$

Then a new wavefunction which can represent the boundary condition of the spatial confinement should be introduced, and eventually the quantization of the energy eigenvalues becomes [102]:

$$\Psi_i(\mathbf{r}_i) = u_k(\mathbf{r}_i)\phi_i(\mathbf{r}_i) \quad (2.7)$$

with the corresponding Hamiltonian operator

$$\hat{H}_i = -\frac{\hbar^2}{2m_i^*} \nabla^2 + V_i(\mathbf{r}_i) \quad (2.8)$$

Thus, the solutions of the stationary Schrödinger equation are obtained [102]:

$$\phi_{nlm}^i(\mathbf{r}_i) = \sqrt{\frac{2}{R^3}} Y_{lm} \frac{J_l(\chi_{nl} + \frac{r_i}{R})}{J_{l+1}(\chi_{nl})} \quad (2.9)$$

where Y_{lm} is spherical harmonics, J_l are Bessel functions and χ_{nl} are their n th roots. The quantum numbers n ($= 1, 2, \dots$), l ($= 0, 1, 2, \dots$) and m ($= -l, -l+1, \dots, l$) are similar to those of the hydrogen atoms. Hence, the designations S, P, D, \dots are used for $l = 0, 1, 2, \dots$. The energy eigenvalues are:

$$E_{nl}^i = \frac{\hbar^2}{2m_i^*} \frac{\chi_{nl}^2}{R^2} \quad (2.10)$$

and for the lowest state with $n = 1$ and $l = 0$,

$$E_{10}^i = \frac{\hbar^2 \pi^2}{2m_i^* R^2} \quad (2.11)$$

In optical spectra, size dependent transitions between energy levels of the electrons and holes can be observed. With the selection rule for optical transitions in this case $\Delta n = 0$ and $\Delta l = 0$ [101], as depicted in Figure 2.5, the resulting energy of the lowest excited state of a CdSe QD is:

$$E(1S_h - 1S_e) = E_{\text{gap}} + E_{10}^e + E_{10}^h = E_{\text{gap}} + \frac{\hbar^2 \pi^2}{2R^2} \left(\frac{1}{m_e^*} + \frac{1}{m_h^*} \right) \quad (2.12)$$

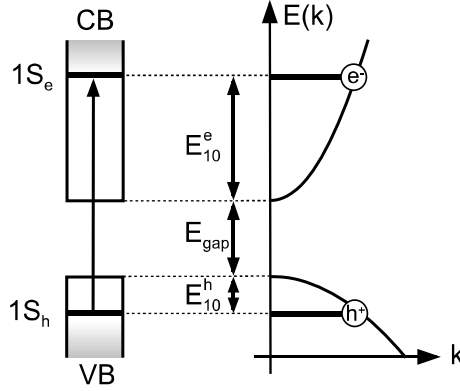


Figure 2.5: Energy structure of the lowest excited state ($1S_h - 1S_e$) in a CdSe QD corresponding to Equation 2.12. CB: conduction band; VB: valence band. E_{gap} is the band gap of the bulk crystal based on the periodic lattice potential. E_{10}^e and E_{10}^h are the energies resulting from the confinement of the electron and hole, respectively.

Furthermore, taking the Coulomb interaction between the electron and hole as a disturbance, one can extend the Hamiltonian by a Coulomb term. Thus [102],

$$\hat{H}_{\text{ehp}} = -\frac{\hbar^2}{2m_e^*} \nabla^2 - \frac{\hbar^2}{2m_h^*} \nabla^2 + V_e(\mathbf{r}_e) + V_h(\mathbf{r}_h) - \frac{e^2}{4\pi\epsilon_0\epsilon_r |\mathbf{r}_e - \mathbf{r}_h|} \quad (2.13)$$

where ϵ_0 is the permittivity of the vacuum and ϵ_r is the relative permittivity of the semiconductor. By means of a first order perturbation theory with the Coulomb term as a correction, the lowest excited energy of CdE ($E=S$ or Se) QDs can be expressed as [103–105]:

$$E(1S_h - 1S_e) = E_{\text{gap}} + E_{\text{conf}} + E_{\text{coul}} = E_{\text{gap}} + \frac{\hbar^2 \pi^2}{2R^2} \left(\frac{1}{m_e^*} + \frac{1}{m_h^*} \right) - \frac{1.8e^2}{4\pi\epsilon_0\epsilon_r R} \quad (2.14)$$

where E_{gap} denotes the bulk semiconductor energy gap, E_{conf} is the confinement energy, E_{coul} is the Coulomb interaction between the electron and hole and R is the radius of the QD. Equation 2.14 suggests that when the size of QD decreases, E_{conf} scales with $1/R^2$ whereas E_{coul} scales with $1/R$. Since the confinement energy varies in a more pronounced manner than the Coulomb energy, the transition will shift to higher energy with decreasing QD size. According to particle size, QDs can be divided into three types:

- $R > 3a_{\text{exc}}^{\text{B}}$ ($\approx 10\text{nm}$): weak confinement. Coulomb term dominates and the exciton can move quasi freely.
- $R \approx a_{\text{exc}}^{\text{B}}$ medium confinement.
- $R \ll a_{\text{exc}}^{\text{B}}$ strong confinement. In this case, the Coulomb term can be neglected, meaning the electron and hole are confined independently.

Figure 2.6 shows the electronic energy structure of the lowest excited state ($1S_{\text{h}} - 1S_{\text{e}}$ state) in a CdSe QD. Contributions of terms in Equation 2.14 can be compared.

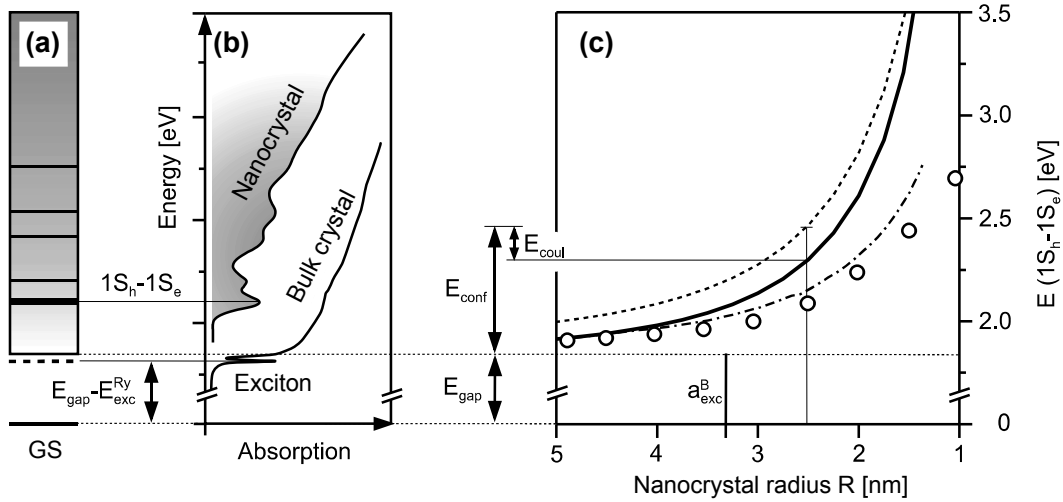


Figure 2.6: Energy structure of the lowest excited state ($1S_{\text{h}} - 1S_{\text{e}}$) in a CdSe QD: (a) An illustration of the continuum and the discrete states of the electron/hole near the band edge above the ground state (GS) for the bulk crystal and nanocrystal, respectively. $E_{\text{exc}}^{\text{Ry}}$ denotes the binding energy of the exciton in the bulk crystal. (b) Schematic optical absorption spectrum of bulk crystal with exciton band and real absorption spectrum of nanocrystal ($T = 10\text{K}$) with a mean radius of $R = 2.6\text{ nm}$ [106]. The lowest-transition corresponds to the transition of $1S_{\text{h}} - 1S_{\text{e}}$ state. (c) Dependence of the energy of the $1S_{\text{h}} - 1S_{\text{e}}$ state on the nanocrystal radius R : (o) Experimentally determined values ($T = 10\text{K}$) [101]; (---) EMA approach: $E_{\text{gap}} + E_{\text{conf}}$ calculated according to Equation 2.12 ($E_{\text{gap}}(T = 10\text{K}) = 1.84\text{ eV}$); (—) After considering the Coulomb interaction: $E_{\text{gap}} + E_{\text{conf}} + E_{\text{coul}}$ calculated according to Equation 2.14 (with $\epsilon_{\text{r}} = 6.23$); (- · - · -) Extended empirical EMA approach [107]. Adapted from Ref. [101].

The zero-order effective-mass approach above considers only single conduction and valence bands with a confinement of infinite spherical wells. This is sufficient for the conduction-band states. However, Efros et al. demonstrated that substantial mixing takes place among the energy levels in the valence-band [90, 108]. For the energy levels of the hole, the more proper description is the Luttinger Hamiltonian with spherical boundary conditions, which has been applied to group II-VI and other QDs [90, 107, 109]. With this treatment, the only good quantum numbers are the total hole angular momentum $F = L_h + J$ (where L_h is the orbital angular momentum of the lowest contributing hole level, J is the total angular momentum without mixing), and the parity [110]. Ekimov et al. [90] proposed a notation for the states of QDs: hole levels are denoted by nL_F , where n is the number of the level, L represents the orbital angular momentum of the lowest contributing hole sublevel, and F is the total hole angular momentum, whereas electron levels are denoted by nl_e where n is the number of the level and l_e is the orbital angular momentum. The selection rules in this case becomes $L_h - l_e = 0$. With this definition, in CdSe QDs, as a model QD system which has been widely investigated, lower energy transitions such as $1S_{3/2} - 1S_e$, $2S_{3/2} - 1S_e$, $1S_{1/2} - 1S_e$ and $1P_{3/2} - 1P_e$ are commonly observable in ensemble spectra [107, 111]. Figure 2.7 gives an example of an absorption spectrum with assigned lowest energy transitions [112].

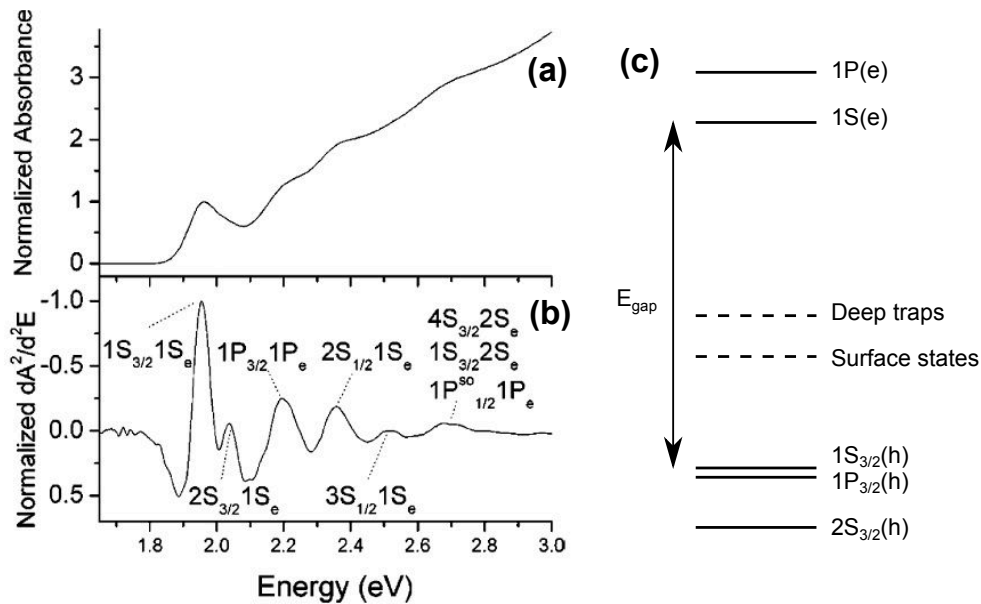


Figure 2.7: (a) Absorption spectrum of 6.4 nm CdSe quantum dots and (b) normalized second derivative of (a) (adapted from Ref. [113]). The energy transitions are assigned according to Ref. [107]. (c) The electron and hole energy levels of CdSe QDs in the strong confinement regime. The dashed lines stand for deep traps and surface states, respectively. Adapted from Ref. [112].

Based on the quantum size effect, empirical relationships between the size (obtained from methods as, e.g., transmission electron microscopy) and the first excitonic absorption wavelength can be established for various types of semiconductor QDs. Equation 2.15 [114] and Equation 2.16 [115] are the empirical formulas of the diameter d and the wavelength λ at the first excitonic absorption peak for CdSe QDs and InP QDs, respectively:

$$d = (1.6122 \cdot 10^{-9})\lambda^4 - (2.6575 \cdot 10^{-6})\lambda^3 + (1.6242 \cdot 10^{-3})\lambda^2 - 0.4277 \cdot \lambda + 41.57 \quad (2.15)$$

$$d = 0.1456 \cdot e^{0.0052 \cdot \lambda} \quad (2.16)$$

2.1.2 Synthesis, growth and crystal structures

2.1.2.1 Evolution of organometallic synthesis

The very first techniques of QD synthesis were developed based on aqueous ion chemistry in the 1980s by Brus and Henglein accompanied by a series of investigations on the quantum confinement effect [93, 103–105, 116–119]. In the beginning, the method was a one-phase synthesis involving a precipitation reaction in homogeneous aqueous solutions containing surfactant-type or polymer-type stabilizers. Then a two-phase route was invented to prevent the particles from aggregation and to stop further growth by taking advantage of the arrested precipitation of QDs within inverse micelles which were formed with an amphiphilic surfactant. However, these approaches resulted in relatively broad size distributions and poor fluorescence quantum yield, which was ascribed to many crystal defects due to the low growth temperature. Therefore, reactions taking place at high temperature were attempted. A remarkable report by Murray et al. with a breakthrough was published in 1993, in which crystalline, monodispersed, highly luminescent high-quality cadmium chalcogenide QDs (CdX; X = S, Se, Te) were prepared based on the pyrolysis of organometallic precursors with coordinating ligands in an organic solvent with high boiling point [15]. The high reaction temperatures in this procedure ($\sim 300^\circ\text{C}$), provided by a mixture of trioctylphosphine (TOP) and trioctylphosphine oxide (TOPO) which also served as the coordinating solvent, efficiently annealed out defects and improved crystallinity. The growth rate and the resulting size of the QDs were also controlled by the temperature. The key point to achieve monodispersity of the QDs is the injection of organometallic precursors into an organic solvent at high temperature, termed as “hot-injection” method. The efficient separation of the processes of nucleation and

growth has been considered to be responsible for the high quality of the QDs synthesized by “hot-injection”.

Although heat-up synthetic routes in organic solvents [120, 121] without precursor injections and syntheses in aqueous solution [122–124] have also been reported, the high temperature organometallic synthesis with hot injection remains a common technique. A few minor improvements of the procedure result in CdSe QDs with high quantum yield of 10–25% and size dispersion of 5–10% [16, 17]. Besides the original TOPO and TOP, Talapin et al. used hexadecylamine (HDA) as an additional coordinating component to achieve better quality [17]. Later in the year 2003, octadecylamine (ODA) was substituted for HDA and the non-coordinating, non-polar solvent 1-octadecene (ODE) with low volatility was introduced by the research group of Peng [20]. Murray et al. originally used dimethyl cadmium as the cadmium precursor [15]. However, insoluble precipitate was found in TOPO with dimethyl cadmium because of its instability at high temperature. As an alternative, cadmium oxide with tetradecylphosphonic acid (TDPA) as well as other cadmium based complexes were adopted [18, 125]. More recently, to further reduce the toxicity, besides using the less toxic ODE as a solvent, more environment friendly phosphine-free chemicals such as oleic acid (OA) were used as ligands in the synthesis [19, 23, 126].

2.1.2.2 Mechanism of crystallization

The route to colloidal particles with uniform size distribution is derived from the classical theory proposed in the work by La Mer et al. in the 1940s [127]. The growth of crystals in solution requires some kind of seed materials which are called nuclei, so that the crystallization is able to occur at the interface between the seeds and the solution. The nuclei can either be generated directly in the solution or introduced externally with foreign seeds. The former process consisting of a single liquid phase is termed “homogeneous nucleation” whereas the latter is termed “heterogeneous nucleation” [128, 129]. The heterogeneous nucleation method is not popular for the synthesis of QDs due to the difficulty in preparation of very small and uniform seeds for nanocrystal formation [130].

To trigger the homogeneous nucleation process in the solution, a high energy barrier has to be overcome and an extremely high supersaturation level has to be reached. La Mer’s theory is schematically depicted in Figure 2.8. In stage I, the concentration of the monomers (molecular species) increases gradually until a critical concentration at which self-nucleation occurs. Once stage II started, the rate of nucleation drops rapidly to almost zero because of the abrupt termination of supersaturation. Therefore, this process is called “burst nucleation”. Subsequently, the monomers will diffuse to the existing nuclei

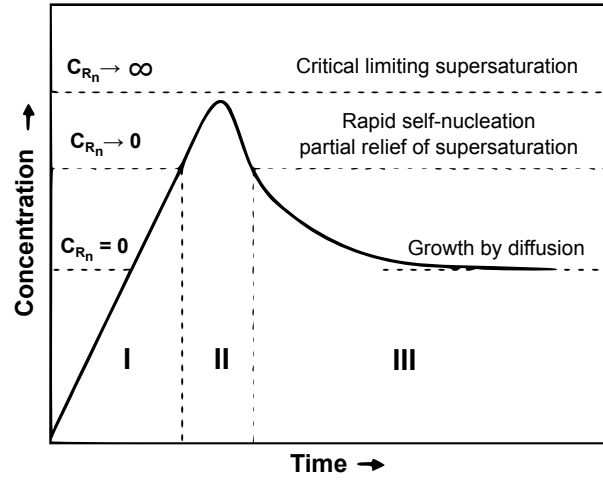


Figure 2.8: Schematic graph of the concentration of monomer before and after nucleation as a function of time based on La Mer's theory. Adapted from Ref. [127].

instead of forming new nuclei. Hence, stage III is diffusion controlled growth without additional nucleation, which facilitates the narrow size distribution. For the synthesis of QDs, the extremely quick formation of nuclei (stage II) can be realized by the hot-injection method as mentioned above. Due to the very rapid injection at high temperature, ideally the processes of nucleation and growth are efficiently separated and the size distribution can be well controlled [131]. However, in practice, there is also crystal growth during the nucleation process. As a result, the nuclei right after nucleation always have a size distribution. For a given monomer concentration in a diffusion controlled kinetic process, the size dependent growth rate can be obtained by considering the Gibbs-Thomson equation [132, 133]:

$$S_r = S_b \cdot e^{2\sigma V_m / rRT} \quad (2.17)$$

where S_r and S_b represent the solubility of the QD and the corresponding bulk crystal, respectively; σ is specific surface energy; r is the radius of the QD; V_m is the molar volume of the materials; R is the gas constant and T is the temperature.

In the case of $2\sigma V_m / rRT \ll 1$, the growth rate of a particle with the radius r is [133]:

$$\frac{dr}{dt} = K \left(\frac{1}{r} + \frac{1}{\delta} \right) \left(\frac{1}{r^*} - \frac{1}{r} \right) \quad (2.18)$$

where, K is a constant proportional to the diffusion constant of the monomer. δ is the thickness of the diffusion layer. For a given concentration, r^* is the critical radius for which the solubility of the QDs is exactly the concentration of the monomers in solution (zero growth rate). Under the assumption of a infinite diffusion radius, the rate as a function of

particle size is illustrated in Figure 2.9. This function suggests a growth equilibrium which is related to a critical size r^* . QDs smaller than r^* will dissolve or melt (corresponding to negative growth rate) while QDs larger than r^* will grow. Another important point is that there is a maximum rate corresponding to $2r^*$ within the positive growth rate regime. If every QD in the system has a radius larger than $2r^*$, the smaller QDs will grow faster while the larger ones grow slower. As a result, the size distribution becomes narrower and narrower over time, which is called *size focusing*. The value of r^* depends mainly on the overall concentration of free monomers. Therefore, as the reaction proceeds, the concentration of monomers decreases and the critical size shifts to higher values. When some QDs start to be smaller than $2r^*$, the bigger QDs grow faster than the smaller ones, the system enters the *size defocusing regime* or *broadening regime*. Furthermore, if some QDs start to become even smaller than r^* , then the smallest particles are dissolved to free monomers which are incorporated into larger QDs. This means that the system enters the *Ostwald ripening regime*, which results in not only a broadening of the size distribution, but also a decrease of the total number of QDs.

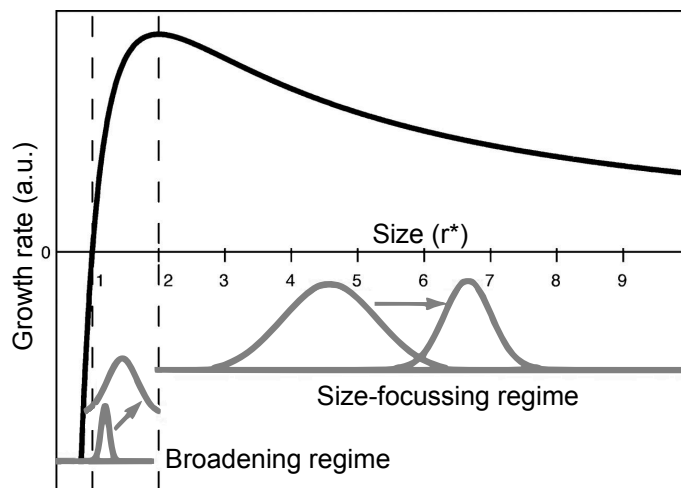


Figure 2.9: Schematic representation of the growth rate dr/dt of the QDs in units of the critical size r^* . Examples of size distributions in the *size focusing regime* and *broadening regime* and their development with time are displayed. From Ref. [134].

As a result of the analysis above, burst nucleation and separation of nucleation and crystal growth are the key factors for the uniformity of QDs which are facilitated by the hot-injection method. To achieve a narrow size distribution, the appropriate amount of concentration of monomers is crucial: if the concentration is too high, the nucleation and growth processes cannot be efficiently separated; if the concentration is too low, *size defocusing* and *Ostwald ripening* will take place. In both cases the size distribution is broadened. In addition, the concentration of the monomer as well as the reactivity of the

ligands was also proven to have a strong influence on the shape and morphology of the QDs [135–137].

2.1.2.3 Crystal structure

Most group II–VI and III–V semiconductor materials crystallize in either the hexagonal wurtzite (WZ) or cubic zinc blende (ZB) structure. Both structures are tetra-coordinated and vary in the layer stacking along (111), forming an ABCABC... or an ABAB... sequence, respectively (Figure 2.10).

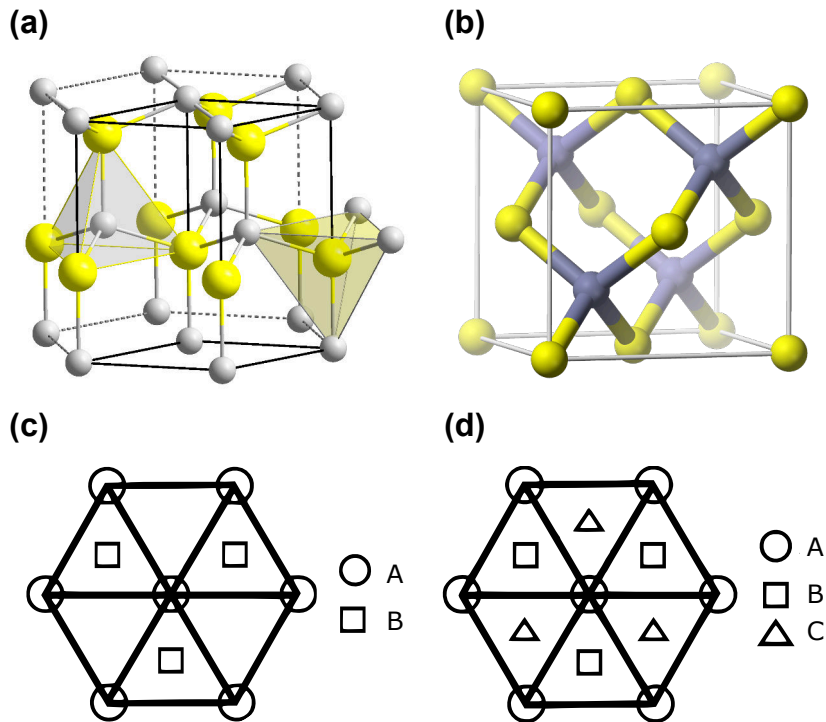
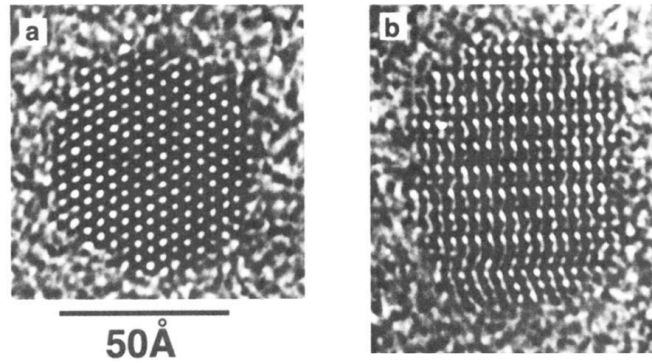


Figure 2.10: Crystal structures of (a) wurtzite and (b) zinc blende, respectively. The spheres in different colors represent different kinds of atoms. (c) The ABAB... arrangement viewed along [001] (c -axis of wurtzite lattice). (d) The ABCABC... arrangement viewed along [111] (body diagonal direction of the face-centered cubic of zinc blende lattice).

X-ray diffraction (XRD) and high resolution transmission electron microscopy (HRTEM) are widely used techniques for the crystallographic characterization of QDs. The stable structures (ground state) as well as other structural parameters of selected II–VI, III–V and IV–VI semiconductors at room temperature are given in Table 2.1. Some materials such as ZnSe and CdTe which have very little difference in total energy between the WZ and ZB structure exhibit the WZ-ZB polytypism [138]. Therefore, according to the specific experimental conditions, nucleation and growth can occur in either structure, and under certain circumstance, even both may coexist in the same single QD [134].

Table 2.1: Structural parameters of selected bulk semiconductors [134].

Material	Structure (300K)	Type	E_{gap} (eV)	Lattice parameter (Å)	Density (kg/m ³)
ZnS	Zinc blende	II-VI	3.61	5.41	4090
ZnSe	Zinc blende	II-VI	2.69	5.668	5266
ZnTe	Zinc blende	II-VI	2.39	6.104	5636
CdS	Wurtzite	II-VI	2.49	4.136/6.714	4820
CdSe	Wurtzite	II-VI	1.74	4.3/7.01	5810
CdTe	Zinc blende	II-VI	1.43	6.482	5870
GaN	Wurtzite	III-V	3.44	3.188/5.185	6095
GaP	Zinc blende	III-V	2.27	5.45	4138
GaAs	Zinc blende	III-V	1.42	5.653	5318
GaSb	Zinc blende	III-V	0.75	6.096	5614
InN	Wurtzite	III-V	0.8	3.545/5.703	6810
InP	Zinc blende	III-V	1.35	5.869	4787
InAs	Zinc blende	III-V	0.35	6.058	5667
InSb	Zinc blende	III-V	0.23	6.479	5774
PbS	Rocksalt	IV-VI	0.41	5.936	7597
PbSe	Rocksalt	IV-VI	0.28	6.117	8260
PbTe	Rocksalt	IV-VI	0.31	6.462	8219

**Figure 2.11:** High resolution electron transmission electron microscopy images of CdSe QDs viewed along the (a) [001] and (b) [010] zone axes. Reprinted from Ref. [139].

CdSe QDs synthesized by pyrolysis using conventional ligands, such as TOPO and HDA exhibit WZ structure with a three-fold rotation axis C_{3v} and are able to generate every high crystallinity with less than one fault per crystallite as shown in Figure 2.11 [15, 17, 136, 139, 140], while InP QDs from organometallic syntheses were frequently observed as ZB structure [4, 51, 141–144]. However, as shown in Table 2.1, lead chalcogenides crystallize in the rocksalt structure. Although it is reported that the CdSe

QDs whose diameters exceed 11 nm may also crystallize in the rocksalt structure, the ones with the diameters below 11 nm remain a four-coordinate arrangement [145].

2.1.3 Core/shell structure

Regarding the application requirements of QDs, besides the size distribution as above discussed, the fluorescence quantum yield (QY) and the stability against photo-oxidation are two other crucial factors, which are strongly dependent on the surface state of the QDs due to the very high surface-to-volume ratio of QDs compared with the bulk materials. As such, on the one hand, the organically passivated QD cores are vulnerable and easy to be photo-oxidized and bleached [146, 147]; on the other hand, they typically exhibit surface-related trap states from dangling bonds and surface defects serving as fast non-radiative de-excitation channels for photogenerated excitons, thereby decreasing the QY [148, 149].

In order to suppress such effects and improve the surface passivation of QDs, one of the most important strategies is to overcoat the QD cores with another inorganic semiconductor which has a wider energy band gap, forming a core/shell (CS) structure. The shell with a wide band gap efficiently confines the wavefunctions of the charge carriers in the core, thereby raising the quantum yield by decreasing the probability of non-radiative recombinations [150, 151]. For example, by capping CdSe QD cores with ZnS, Hines et al. in 1996 found that the QY can be increased from ~10% to ~50% [16]. After that, more and more effort has been devoted to core-shell systems, and the best prepared CdSe/CdS and ZnSe/CdSe core/shell QDs are able to exhibit QYs as high as 85% and 80–90%, respectively [152, 153]. The shell also serves as a physical barrier between the optically active core and the surrounding medium, decreasing the sensitivity of the QDs to environmental influences [1].

ZnS as a non-toxic material with wide band gap was initially and extensively used as the passivation shell of CdSe QDs [16, 151]. However, as the thickness of ZnS shell approaches two or more monolayers, the growth of the shell cannot follow the template of the core lattice due to the big lattice mismatch between them, inducing lattice strain and defects at the core/shell interface and inside the shell [151, 154]. The size distribution of QDs often broadens substantially after coating ZnS shells onto CdSe as well [151]. In contrast, since the lattice mismatch between CdS and CdSe is much smaller than the one between ZnS and CdSe (3.9% versus 12%, as shown in Figure 2.12), CdSe/CdS QDs have better crystallinity. Yet, the wavefunctions of the excitons in CdSe/CdS QDs will extend across the shell due to the relatively small band gap of CdS compared with ZnS, and hence the QY is also sensitive to surface states [150].

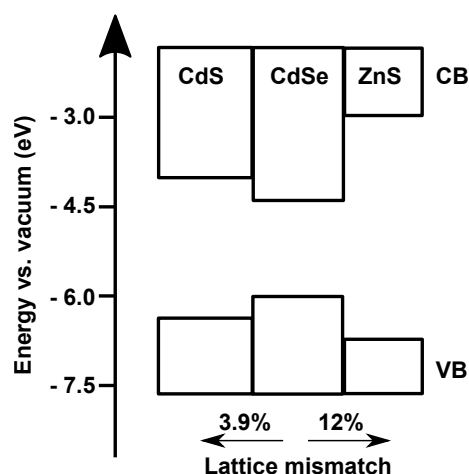


Figure 2.12: Energy band alignment and lattice mismatch of bulk semiconductor combinations. CB: conduction band; VB: valence band. From Ref. [21].

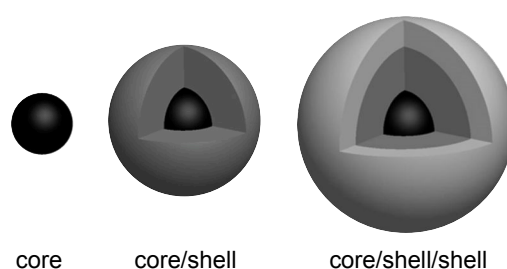


Figure 2.13: Schematic diagrams of the core, core/shell and core/shell/shell structures of quantum dots.

To combine the advantages of both the efficient confinement of ZnS and the lattice matching of CdS with respect to CdSe core, the CdSe/CdS/ZnS core/shell/shell structure has been proposed and prepared [155, 156]. Figure 2.13 displays the structures of the core, core/shell and core/shell/shell of QDs. With this idea, to have an even more stepwise change of the band gap and the lattice spacing, the alloyed precursor of $\text{Cd}_{0.5}\text{Zn}_{0.5}\text{S}$ was additionally introduced, resulting in CdSe/CdS/ $\text{Cd}_{0.5}\text{Zn}_{0.5}\text{S}$ /ZnS complex multishell system [21, 157]. In 2003, the research group of Peng introduced the successive ion layer adsorption and reaction (SILAR) technique, which was originally applied to the deposition of thin film onto solid substrates, into the shell growth of QDs. This SILAR method enables the formation of one monolayer at a time by alternative injections of cationic and anionic precursors, allowing a precise control over the shell thickness [20]. Upon the shell coating, the absorption and emission spectra shift to longer wavelengths. This red-shift has been observed for various core/shell materials as revealed in Figure 2.14(a). This is explained by a partial extension/tunneling of the wavefunctions of the excitons from the core into the

shell [150, 151]. Figure 2.14(b) represents the influence of the introduction of the “adapter shell” on the quantum yield.

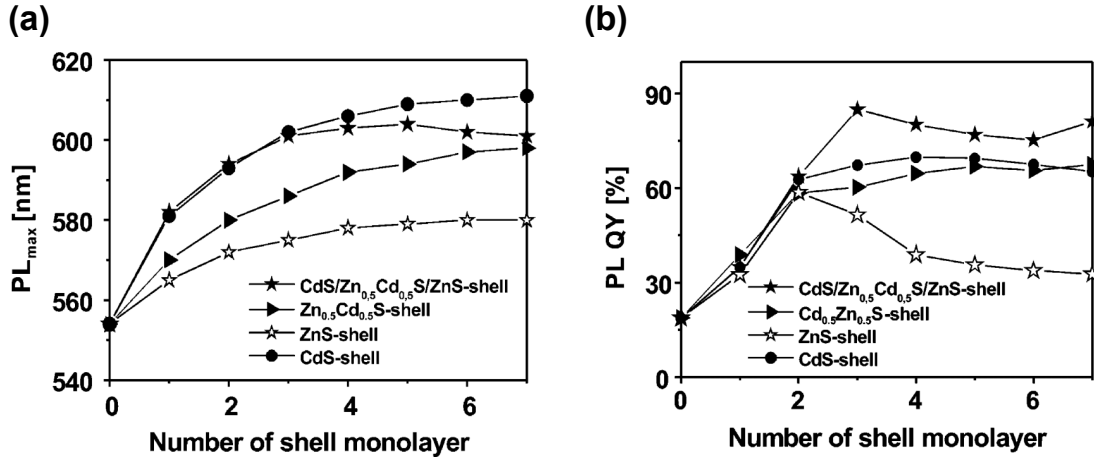


Figure 2.14: Evolution of the peak position in the fluorescence emission spectra for different core/shell quantum dots. The red-shift of the fluorescence emission spectra upon shell growth on the CdSe cores are due to the decrease of confinement. The slight blue-shift upon growth of the outer ZnS layers for the multishell particles is attributed to the formation of a Zn_xCd_{1-x}S alloy shell. (b) Evolution of the QY for different core/shell quantum dots. From Ref. [21].

Besides overcoating the QD core with wide band gap materials, the electronic structure can also be tuned by core/shell design according to the band gaps and the relative positions of electronic energy levels of the involved semiconductors as shown in Figure 2.2. Some common structures are illustrated in Figure 2.15. Unlike the type-I structure discussed above aiming at better QY, type-II includes an offset of the band gaps of the core and epitaxial shell and can be applied to efficient separation of the carriers, e.g. in the photovoltaic field [158, 159]. In reverse-type-I systems, as it is called, the core is overcoated by a material with a narrower band gap. In quasi-type-II structures, one carrier is confined in the core while the other is delocalized over the entire core shell structure [160]. This quasi-type-II was reported to suppress the fluorescence blinking of single QDs (see Section 5.7) [78, 161, 162]. Specific examples of various types of core/shell systems include: CdSe/ZnSe [163, 164], CdSe/ZnS [16, 165], CdSe/CdS [20, 82, 166], CdS/HgS/CdS [167, 168], InP/ZnS [4, 51, 86] and PbSe/PbS [169, 170].

2.1.4 InP based quantum dots

QDs from group II-VI (e.g., CdSe, CdTe or PbS) have been well developed and investigated. However, they contain very toxic elements (i.e., Cd, Pb and Hg), which are environment unfriendly and greatly limit the practical applications. Therefore, the “greener” colloidal

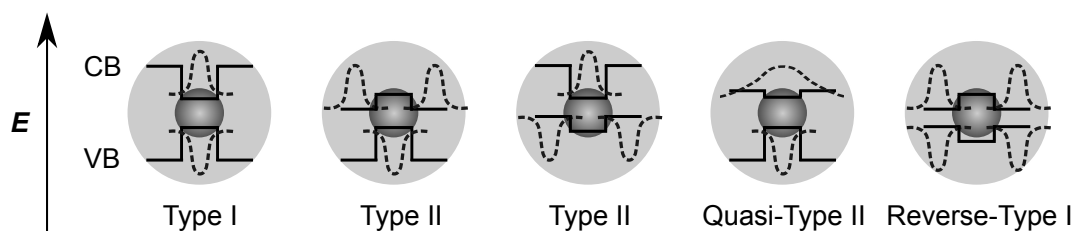


Figure 2.15: Schematic diagrams of the various types of core/shell structures of quantum dots. The dashed line indicates the wavefunctions of electrons and holes. CB: conduction band; VB: valence band.

QDs from group III-V, especially InP QDs whose emission covers the visible and near infrared spectral range, have aroused increasing interest in both fundamental and industrial fields in recent years [4, 7, 51–53, 171, 172]. Nevertheless, the investigations and applications of III-V QDs are rather sparse compared to the group II-VI QDs, mainly because of the difficulties in synthesis and the poorer optical properties. Specifically, due to the stronger covalent bonding of the precursor, a higher reaction temperature and longer reaction time are required to synthesize InP QDs. However, these conditions favor Ostwald ripening, resulting in an increase of size distribution. Therefore, highly reactive organometallic precursors such as the expensive and pyrophoric phosphorus precursor tris(trimethylsilyl)phosphine ($\text{P}(\text{TMS})_3$) are indispensable. Like the cadmium chalcogenide system [15], initial synthetic routes to InP QD have used TOPO/TOP as the solvent. Nevertheless, reaction times as long as 3–7 days were necessary to yield well crystalline InP QDs [173, 174]. In 2002, the research group of Peng developed a new procedure based on fatty acids as stabilizers combined with the non-coordinating solvent ODE [175]. Relatively high quality InP QDs were synthesized in this medium in a fast and controllable reaction. However, most properties of InP QDs are still inferior to those of group II-VI QDs. For example, the full width at half maximum (FWHM) of the fluorescence peak for InP is generally as large as ~50-100 nm and the QY is typically below 1%, frequently accompanied by emissions from defect states [51, 134, 141, 171, 176]. In addition, InP QDs also exhibit weak photo- and chemical stabilities due to facile oxidation [52, 171]. To overcome these surface related problems, besides the method of photo-assisted etching of their surface with HF (hydrogen fluoride) [177], using a ZnS shell for surface passivation is the most commonly used approach [51, 176]. Similar to the case of the CdSe/ZnS core/shell system, the large lattice mismatch between InP and ZnS (7.7%) induces strain at the interface, resulting in defects such as dislocations, yielding poor photostability as well as low fluorescence QY [52]. Besides other different optimizations of the synthesis conditions [51, 141, 176], an efficient approach developed by Lim et al. is incorporating

ZnSe as a buffer layer to reduce the lattice mismatch down to 3.4%. The as-prepared robust InP/ZnSeS QDs allow a thicker shell growth of ZnS and reveals a high fluorescence QY (above 80%) [52].

2.2 Preparation of quantum dot oligomers

The methods used for preparation of nanoparticle oligomers in this thesis represent routes which fall into the categories of “self-assembly” and “separation”. They are discussed below.

2.2.1 Self-assembly and separation of nanoparticles

According to the synthetic strategy, self-assembly here is roughly divided into indirect and direct ones. The indirect self-assembly involves connections of the monomers¹ by molecular bridges (linkers) while by direct self-assembly the monomers are connected directly by altering the conditions of the system.

2.2.1.1 Indirect self-assembly

An example of the indirect self-assembly of nanoparticles is shown in Figure 2.16, Novak et al. used rigid thiol-functionalized phenylacetylenes as linkers or assembly templates which had different lengths and different numbers of arms to connect silver or gold particles [34]. Basically they simply mixed the raw noble metal nanoparticles and the linkers with proper ratio under stirring, and thus the different nanoparticle oligomers were obtained as designed. By TEM and absorption spectra they characterized the resulting dimers, trimers and tetramers. The corresponding yields are about 50, 30, and 10%, respectively. Theories of electromagnetic interactions between metallic spheres based on the corresponding structures were also tested by absorption spectra.

Additionally, because complementary single-strand DNA molecules possess the unique Watson-Crick base-pairing interactions, they are very widely used for the connection of nanoparticles, not only for the noble metal, but also for QDs [44, 178–180]. One of the most successful works which produced very well defined oligomer systems was done by Tikhomirov and co-workers [44]. They prepared mercaptopropionic acid (MPA)-capped QDs with different sizes by a one-pot synthesis in aqueous solution and functionalized

¹The term “monomer” here means single nanoparticles as the basic elements or building blocks of the assembled nanostructures. This should be distinguished from the term “monomer” used in the synthesis of nanoparticles which means the molecular species for the nucleations in solution.

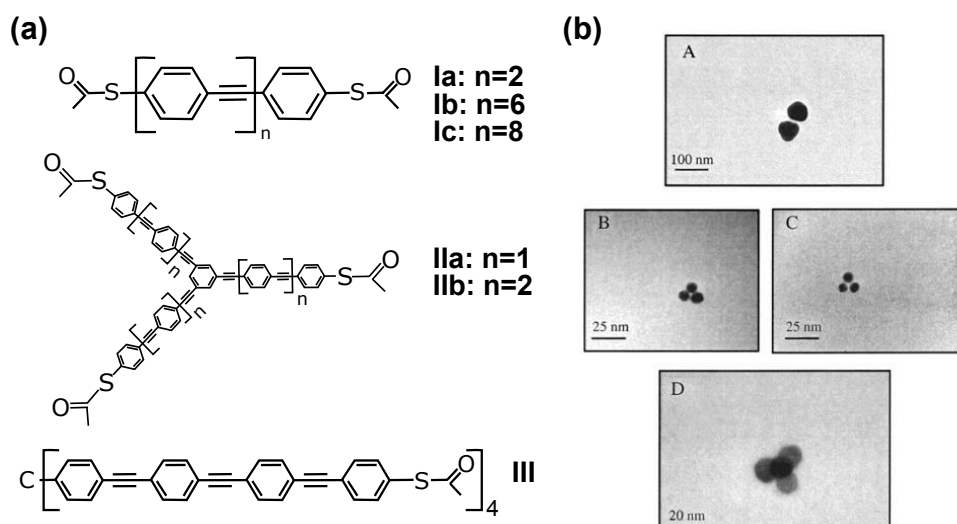


Figure 2.16: (a) Chemical structures of molecules used as linkers with different numbers and lengths of “arms”. (b) Transmission electron microscope images of (A): Silver particle dimers linked by structure Ia. (B) and (C): Gold particle trimers linked by structures IIa and IIb, respectively. (D) A gold particle tetramer linked by structure III. From Ref. [34].

the QDs with DNA ligands. The DNA ligands consisted of three domains: a quantum-dot-binding domain; a spacer and a DNA-binding domain. With a one-pot synthesis, some of DNA molecules will be bound to the QDs. By subsequent titration with the sequences complementary to the quantum dots binding domain and monitoring by size exclusion chromatography, the so-called valency of the QDs (meaning the number of binding sites on the QD surface) can be determined. With this rational design, quantum dot assemblies/oligomers have been made. The TEMs in Figure 2.17 show the corresponding kinds of QD oligomers. Gel filtration chromatography was taken as the separation technique in this example, and the yields for different complexes typically approached 70%. With the configuration shown in Figure 2.17(b)(middle panel), even obvious pH dependent Förster resonance energy transfer (FRET) was realized.

Although various different configurations can be formed by the use of templates (linkers), the indirect assembly increases the complexity of the oligomer system and the study of the direct interactions among the components is inevitably influenced by the linkers. In addition, the inter-particle separation distance has a lower limit in this case, which constrains some investigations, e.g., the electronic coupling among the components [35, 47]. These drawbacks highlight the importance of the direct self-assembly.

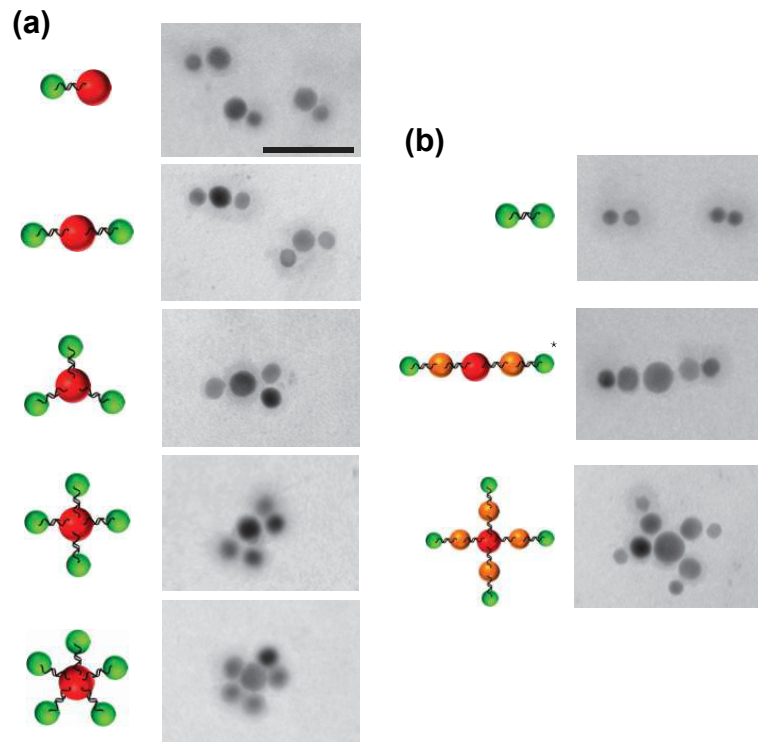


Figure 2.17: High-resolution TEM images of DNA-programmed quantum dot complexes. (a) Quantum dot assemblies built using red dots with valencies of 1–5 and green dots with valencies of 1. (b) Symmetric binary system made from the same green dots (top); complex structure made from three different dots: linear ternary complex (middle) and cross-shaped ternary complex (bottom). Scale bar: 10 nm. From Ref. [44].

2.2.1.2 Direct self-assembly

In a general frame, the colloidal stability of particles in a solvent is analyzed by the Derjaguin–Landau–Verwey–Overbeek (DLVO) theory [181]. The total interaction potential between particles V_{total} is the sum of the electrostatic repulsion potential V_{elec} , the van der Waals attraction potential V_{vdW} ¹, the dipolar interaction potential V_{dipole} and the charge–dipole interaction potential $V_{\text{charge–dipole}}$, i.e.,

$$V_{\text{total}} = V_{\text{elec}} + V_{\text{vdW}} + V_{\text{dipole}} + V_{\text{charge–dipole}} \quad (2.19)$$

¹Here the van der Waals interaction refers in particular to the interaction between two instantaneously induced dipoles, i.e., London dispersion force.

For monodisperse spherical nanoparticles, we have [46, 182]:

$$V_{\text{elec}}(r) = 2\pi\epsilon_s\epsilon_0a\Psi_0^2 \cdot \ln(1 + e^{-a(R-2)/L_e})$$

$$\text{with } L_e = \sqrt{\frac{\epsilon_s\epsilon_0k_B T}{2e^2 I}} \quad (2.20)$$

$$V_{\text{vdW}}(r) = -\frac{A_H}{6} \left[\frac{2}{R^2 - 4} + \frac{2}{R^2} + \ln \frac{R^2 - 4}{R^2} \right] \quad (2.21)$$

$$V_{\text{dipole}}(r) = -\frac{\mu^2}{2\pi\epsilon_s\epsilon_0R(R^2 - 4a^2)} \quad (2.22)$$

$$V_{\text{charge-dipole}}(r) = -\frac{Q^2\mu^2}{6(2\pi\epsilon_s\epsilon_0)^2k_B T r^4} \quad (2.23)$$

where r is the center-to-center separation of neighboring nanoparticles of radius a ($R = r/a$), ϵ_s is the relative dielectric constant of the solvent, ϵ_0 is the dielectric constant of vacuum, Ψ_0 is the surface potential of the particle, L_e is the Debye screening length, I is the ionic strength, μ is the dipole moment, Q is the effective surface charge of the nanoparticles, k_B is the Boltzmann constant, T is the absolute temperature, and A_H is the Hamaker constant of the particles. For noble metal nanoparticles (e.g., citrate-stabilized gold nanoparticles), V_{dipole} is derived from surface defects and nonuniform ligand capping and is usually negligible [182, 183]. Thus, the stability of the colloidal noble metal particles is mainly determined by the balance between V_{elec} and V_{vdW} . Particularly, adding a tiny amount of salt increases the ionic strength of the medium, therefore reduces the Debye screening length, and leads to a smaller repulsion potential V_{elec} . Eventually, the probability of effective collision is improved, inducing the aggregation of nanoparticles. Based on this principle, Chen and co-workers [45, 46] triggered the aggregation of gold nano-spheres by the addition of NaCl. To prevent dissociation of as-formed oligomers, a diblock copolymer was used to encapsulate the resulting assemblies. By fine tuning the electrostatic interaction with the concentration of the salt, they obtained monomers, dimers and trimers with purities of 71%, 24% and 3.5%, respectively. The oligomers were subsequently further purified by density gradient (11 + 62% CsCl gradient) centrifugation. The final purities of the dimers and trimers were enriched to be as high as 95.1% and 81%, respectively (Figure 2.18).

When aggregation of quantum dots is considered, there are three main differences compared with metal nanoparticles: (1) Due to the small dielectric constant, the electrostatic repulsion potential is no longer dominant; (2) As a long range interaction,

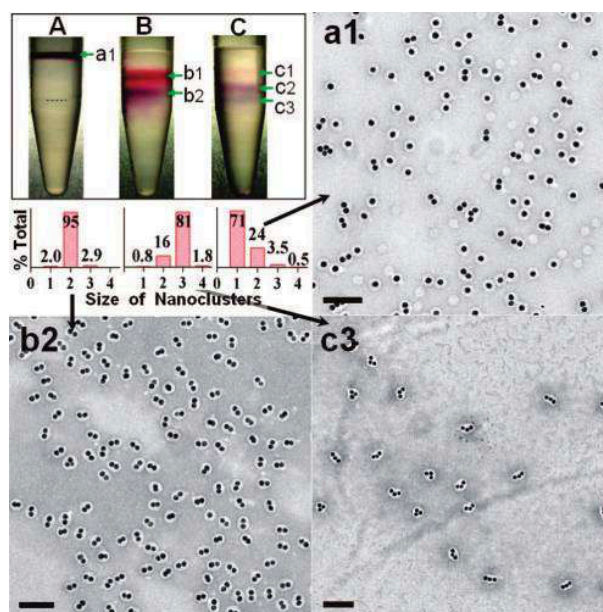


Figure 2.18: (A) A typical setup for centrifugation, where 62% and 11% aq. CsCl and then AuNPn@PSPAA in water were layered from bottom to top. (B) The result of (A) after 20 min centrifugation. (C) Separation result of a pre-enriched trimer sample. (a1, b2, and c3) TEM images of the respective fractions indicated in A-C; Insets: the statistical histograms. Scale bars: 100 nm. From Ref. [45].

the dipole-dipole attraction of QDs is considerably strong. In particular, experimentally the magnitude of the II-VI QD dipoles was observed to be very high for both wurtzite hexagonal and zinc blende cubic nanocrystals, despite the apparent lack of crystal lattice asymmetry of the cubic phase. This effect was attributed to charged chalcogen surface states [183, 184]. In contrast, the energy of van der Waals interaction between anisotropic QD cores was considered to be less than $0.5RT$ [33]. Tang et al. reported linear spontaneous assembly of single CdTe nanoparticles into nanowires and attribute this to dipole interactions. According to Equation 2.22, the energy of nanoparticle dipole attraction of two CdTe QDs with a diameter of 3.4 nm and a center-to-center interdipolar separation of 4 nm was estimated to be 8.8 kJ/mole (0.091 eV) [184]. A linear dependence of dipole moment on the size of semiconductor QDs was also reported: the dipole moment varies from 41 D to 98 D with an increase of QD diameter from 2.7 nm to 5.6 nm [183].

Colloidal QDs in a non-polar organic solvent are stabilized by surface ligands which usually have long chained structures [185]. The ligands with long chains provide steric repulsion between particles, which plays an most important role to obtain monodisperse nanoparticles. Taking this principle from the opposite direction, Xu et al. in the Basché group realized the controllable aggregation of QDs by removal of ligands. CdSe/CdS/ZnS QDs were precipitated by a bad solvent and re-dispersed in a good solvent for several

times. The ligand removal during this process leads to an increasing number of QD oligomers. The QD oligomers were separated by density gradient ultracentrifugation and the fractions of QD dimers and trimers could be enriched up to 90% and 64%, respectively (Figure 2.19) [47].

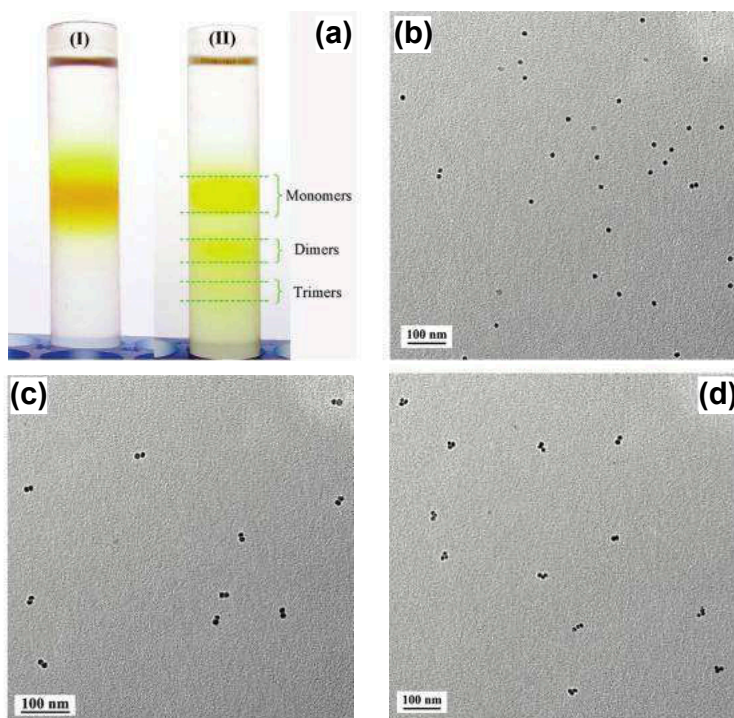


Figure 2.19: (a) Photograph of QD oligomers in the tube after density gradient ultracentrifugation. (I) QDs precipitated directly from the growth solution and redispersed in cyclohexane; (II) QDs precipitated again and redispersed in cyclohexane. TEM images of QD monomers (b), dimers (c), and trimers (d) from the corresponding bands. Scale bars: 100 nm. From Ref. [47].

2.2.2 Density gradient ultracentrifugation (DGU)

Besides other methods for purification/separation of nanoparticles according to size, shape and/or nanostructures [186] such as size exclusion chromatography, gel filtration chromatography [44], capillary or gel electrophoresis [180, 187, 188], magnetic field flow fractionation [189, 190], selective precipitation [191–193], membrane filtration [194, 195] and selective extraction [196, 197], density gradient (ultra)centrifugation as a fast, versatile and efficient technique was extensively applied for various nanoparticle solutions [45, 198–204].

First, considering the simple case that a nanoparticle suspends in a liquid medium in a gravitational field, as depicted in Figure 2.20(a), it receives gravity $G = mg$, where m

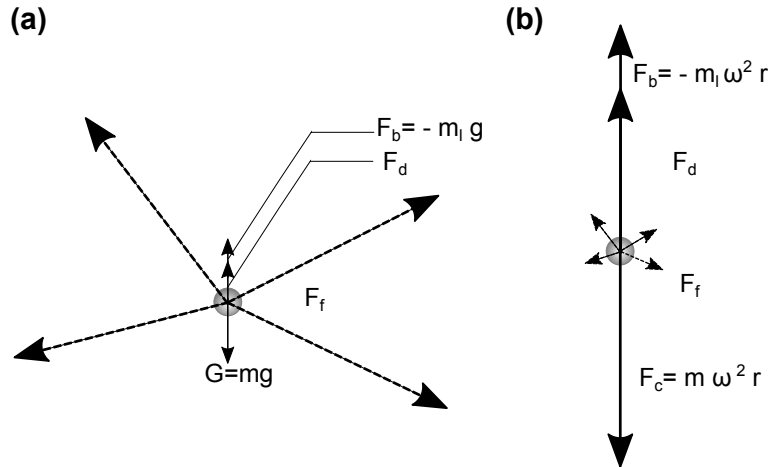


Figure 2.20: Sketch of force analyses of a particle in a liquid medium (a) in normal gravitational field and (b) in force field of ultracentrifugation. For meaning of symbols see text.

is the mass of the particle and g is the acceleration of gravity, buoyant force $F_b = -m_l g$, where m_l is the mass of the liquid displaced by the particle, Brownian fluctuating force F_f and possible viscous drag force F_d . Taking into account the very small gravity and buoyant force due to the small mass m , the random Brownian fluctuating force dominates, and therefore the particle is able to suspend in the liquid for very long time [205].

In order to separate different components of nanoparticles by sedimentation, the force field of ultracentrifugation was applied. The corresponding sedimentation-diffusion equilibrium can be roughly analyzed as follows. As shown in Figure 2.20(b), the force balance includes [202]: centrifugal force $F_c = m\omega^2 r$, buoyant force $F_b = -m_l\omega^2 r$, Brownian fluctuating force F_f and viscous drag force F_d , where ω is the angular speed, r is the distance from the center of the rotor to the location of the particle. Since the ultracentrifugal force can be as high as 100,000 to 1,000,000 times g , the Brownian fluctuating force is relatively small and negligible. Regarding the drag force F_d , the specific expression depends on the Reynolds number, which represents the ratio of characteristic magnitudes of inertial and viscous forces and is defined as: $Re \equiv \rho_1 U L / \eta$, where η is the viscosity, ρ_1 is density of the fluid, U is the characteristic speed and L is the characteristic length. In the scale of nanometer, the typical sedimentation problems meet $Re \ll 1$ [202] and the viscous drag force has the form of $F_d = -\zeta v$ with v denoting the sedimentation velocity and ζ is the friction or drag coefficient. It can be imagined that the particle will be accelerated first by the strong centrifugal force, but subsequently the increasing speed will give rise to increasing drag force F_d , which will decrease the acceleration. Eventually, the acceleration will approach zero and a sedimentation-diffusion equilibrium will be reached. Under this

condition, the total force should be zero and expressed as:

$$F_{\text{total}} = F_c + F_b + F_d + F_f = (m - m_l)\omega^2 r - \zeta v + 0 = 0 \quad (2.24)$$

This results in the so-called *Svedberg coefficient*:

$$S_v = \frac{v}{\omega^2 r} = \frac{m - m_l}{\zeta} \quad (2.25)$$

The low Reynolds number implies that the inertial effects are negligible and the Stokes flow equations can be applied. For a spherical particle, $F_d = 6\pi a\eta v$, where a is the radius of the particle, i.e.,

$$\zeta = 6\pi a\eta \quad (2.26)$$

Combining Equation 2.25 and Equation 2.26, we have [206],

$$v_{\text{sph}} = \frac{(\rho - \rho_l)d^2}{18\eta}\omega^2 r \quad (2.27)$$

where d is the diameter of the spherical particle, ρ and ρ_l are the mass densities of the particle and the fluid, respectively. In fact, the friction coefficients are similar for spherically isotropic objects, and the dynamics of other polyhedral bodies can be described in the same form with a correction factor [207], i.e.,

$$v = \frac{K(\rho - \rho_l)d_{\text{eq}}^2}{18\eta}\omega^2 r \quad (2.28)$$

with $K = 0.843 \cdot \log_{10} \frac{A_{\text{eq}}}{0.065 \cdot A}$

where d_{eq} and A_{eq} represent the diameter and the area of the sphere with the same volume as the particle, respectively, A is the real surface area of the particle and K (usually between 2 and 4) is the correction factor. Therefore, Equation 2.28 suggests that particles with larger size and density will travel faster in the sedimentation process if other conditions are the same.

For particle separation, there are two types of centrifugal techniques: differential centrifugation and density gradient centrifugation. The term “differential centrifugation” here refers to multiple centrifugation in a uniform medium. As illustrated in Figure 2.21(a) and according Equation 2.28, due to the different sedimentation rates of various components, the big and “heavy” particles precipitate first. After each centrifugation for an appropriate time, the supernatant is transferred to another tube for the next round of centrifugation which is usually done with an increasing speed, until the complete

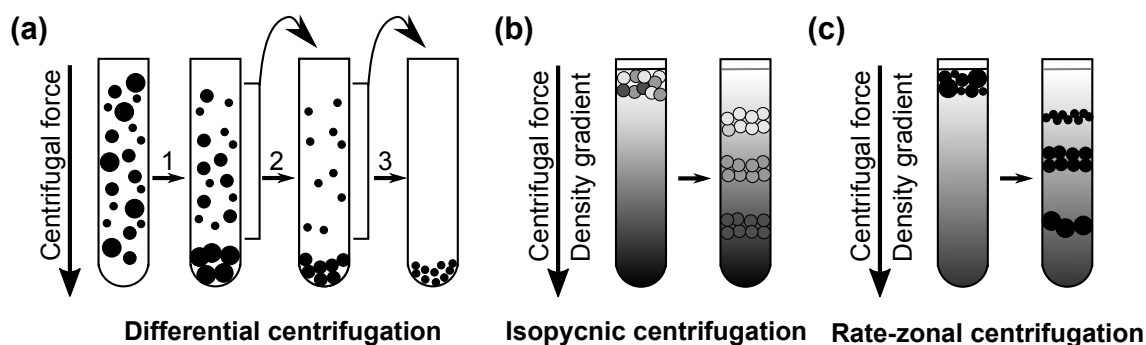


Figure 2.21: Schematic diagrams of (a) differential centrifugation (b) isopycnic centrifugation (c) rate-zonal centrifugation. The gray level represents mass density (darker color represents larger density).

separation of all components. Differential centrifugation is commonly used in the separation or purification of nuclei of cells and viral particles [208, 209].

If the particles are similar, it is obvious that the quality of separation will be poor with respect to differential centrifugation. Therefore, density gradient centrifugation is required. The variation of the buoyant force within the tube is realized by the medium supporting a density gradient. Density gradient centrifugation can be divided into isopycnic and rate-zonal centrifugations. Figure 2.21 (b) illustrates the principle of the isopycnic centrifugation, in which the densities of the particles must be within the range of the densities of the medium. The principle of the separation is merely based on the difference of their buoyant densities. Each of the particles with a specific density will eventually sediment at the position where its density is the same as the gradient media (i.e., the equilibrium position). Sufficient centrifugation time is necessary for the particles to travel to their isopycnic positions, while excessive running time has no further effect on the position of the bands. Isopycnic centrifugation has been applied for the separation of nanoparticles with relatively small densities such as single-walled carbon nanotubes (SWNT) [198, 203, 210]. However, for objects such as metallic or semiconductor inorganic nanoparticles whose densities are higher than the available upper limit of any liquid densities ($\sim 1.7 \text{ g/cm}^3$), this method is not applicable [211]. In this case or the case of separation of particles with the same density, the rate-zonal centrifugation has to be used [45, 47, 201, 212, 213]. As shown in Figure 2.21(c), in the rate-zonal centrifugation, the sample is usually loaded as a thin layer on top of a density gradient of the medium before centrifugation in order to avoid the cross-contamination of particles with different sedimentation velocities. The particles then sediment through the medium gradient into distinct bands/zones according to their sizes, shapes, and densities. The medium gradient provides a viscosity/density gradient which improves particle resolution and

the stability of the whole system, e.g., preventing convection currents, especially in the vertical direction [214]. In contrast to the isopycnic centrifugation, the separation must be terminated before the separated particles precipitate down to the bottom of the centrifuge tube [186]. Particles from different bands are usually taken out by a needle or a pipette syringe. Several centrifugation-redispersion cycles can be applied with an appropriate solvent for a better purification of the fractions [45, 47]. In addition to separation of nanoparticles with different sizes [201] and shapes [202], rate-zonal centrifugation has also been used for the separation/enrichment of nanoparticle oligomers (Figure 2.18 and Figure 2.19) [45, 47].

Compared with the normal centrifuge, an ultracentrifuge consists of a refrigerated, low-pressure chamber containing a rotor which is driven by an electrical motor and is able to rotate at extremely high speed, e.g., as high as 10,000-100,000 revolutions per minute (rpm). Since the technique for separation of QD oligomers in this thesis was the rate-zonal density gradient ultracentrifugation, the term “density gradient ultracentrifugation (DGU)” below in this thesis refers particularly to the rate-zonal density gradient ultracentrifugation, unless otherwise specified.

2.3 Single particle spectroscopy of quantum dots

Due to variations in size, lattice stoichiometry, morphology, crystal habit, ligand adsorption and local environments, single QD particles within the ensemble may exhibit substantially different behaviors from the ensemble properties [24]. In addition, practical applications such as biological fluorescent labelling [12, 13, 25], single particle tracking [26], quantum cryptography [27] and single-photon sources [28] can only be realized at the single particle level. Therefore, the investigation of the fluorescence of single QDs is of great significance. In this thesis, single particles were studied by confocal fluorescence microscopy which is introduced below.

2.3.1 Confocal fluorescence microscopy

2.3.1.1 The basic principle of confocal fluorescence microscopy

The basic setup of confocal fluorescence microscopy can be schematically illustrated in Figure 2.22(a): the excitation light passes through a pinhole aperture, and is focused on a small spot on the sample in a defined focal plane of the microscope objective. Then the secondary fluorescence emission light from the same focusing point in the focal plane is collected by the objective, transmits back through the dichroic mirror and is focused

as a confocal point at the detector pinhole aperture. Fluorescence light rays which occur at points above and below the objective focal plane are not confocal with the pinhole. Therefore, these out-of-focus emitting light rays are blocked by the pinhole and not detected. As the excitation light scans relatively across the sample, which can be realized either by moving the sample (translating the stage) or scanning the excitation light, the information of fluorescence intensities at different points is temporarily recorded by the detector, and the confocal image of the sample is subsequently reconstructed point by point. In confocal microscope, much of the stray light passing through the optical system is eliminated by the pinhole aperture. Thus, compared to the conventional widefield optical microscopy, the confocal microscopy reduces the background fluorescence and increases the signal-to-noise ratio, and therefore dramatically improves the contrast [215].

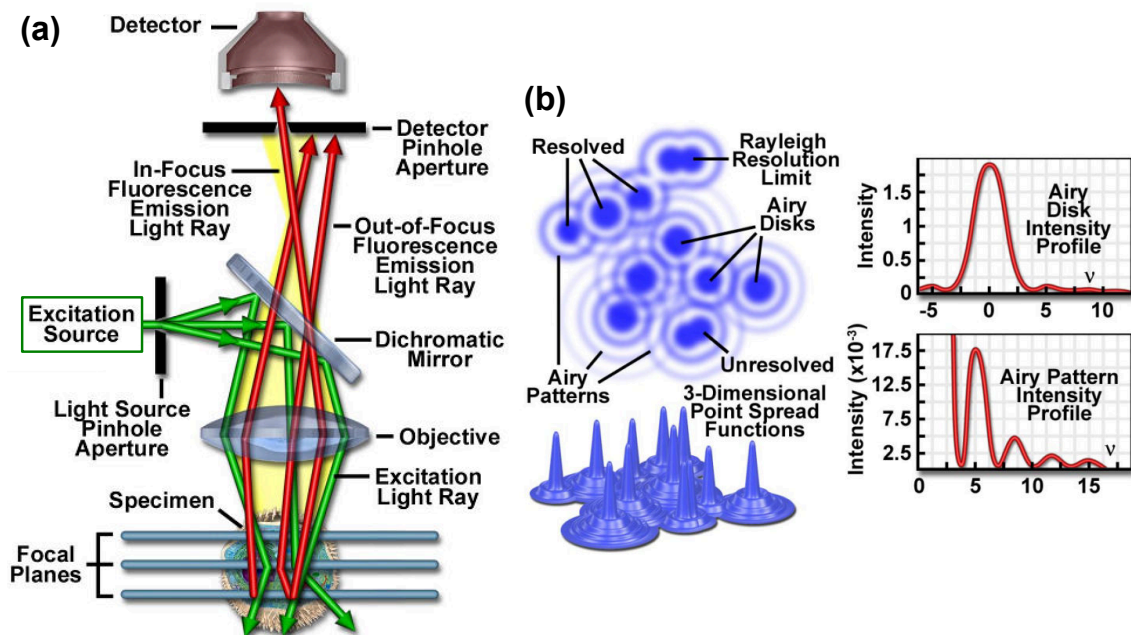


Figure 2.22: Schematic diagrams of (a) the optical pathway and principal components in a confocal microscope and (b) the Airy disk diffraction pattern and the corresponding three-dimensional point spread functions for image formation in confocal microscopy. Adapted from Ref. [29].

2.3.1.2 Spatial resolution and excitation intensity

As illustrated in Figure 2.22(b), the image formed by a point-like light at the focal plane is represented by the point spread function (PSF) [216, 217]. This intensity distribution can be described by the rotationally symmetric *Airy pattern* (the principal bright spot

in the center is termed *Airy disk*). The sample which is considered as a superposition of an infinite number of emitting points therefore produces the superposition of the corresponding Airy patterns. The resolution of a microscope mainly depends on the properties of the intensity point spread function in the image plane. In a given microscope, the numerical aperture (NA) of the microscope objective is defined as:

$$\text{NA} = n \sin \theta \quad (2.29)$$

where θ is the half-angle of the maximum cone of light that can enter or exit the lens and n is the index of refraction of the surrounding medium. Applying the Rayleigh criterion which means that two point sources are regarded as just resolved when the principal diffraction maximum of the one image coincides with the first minimum of the other (the radius of the Airy disk) [218], the lateral spatial resolution limit is calculated to be [216]:

$$\Delta r_{\text{Ray}} = 0.61 \frac{\lambda}{\text{NA}} \quad (2.30)$$

In the case of a confocal microscope, because single-point illumination scanning and detection are employed, only part of the sample in the shared volume of the excitation and detection point spread functions is detected. Hence, in the confocal case, the intensity point spread function is the product of the independent illumination intensity and detection intensity point spread functions [29]. As discussed in Ref. [101], due to the narrower intensity point spread function, ideally the lateral spatial resolution limit is decreased by a factor of $\sqrt{2}$, i.e.,

$$\Delta r_{\text{Conf}} \simeq 0.43 \frac{\lambda}{\text{NA}} \quad (2.31)$$

Axial resolution in the experiments of this thesis is negligible because the samples used are thin and transparent [219]. The lateral intensity distribution (Airy function) can be described in good approximation by a Gaussian function [220]:

$$I(r) = I_0 e^{-2r^2/w^2} \quad (2.32)$$

where r is the radial coordinate with respect to the center of the beam spot, I_0 is the maximum intensity at the center and w is the radius of the beam waist at which I dropped to I/e^2 . This Gaussian distribution is also the beam profile in the focal plane of the excitation light source. Hence, if the lateral focus width is known/measured, the excitation intensity can be estimated using the following equation containing the excitation power P

after the microscope objective [221, 222]:

$$I_0 = \frac{2P}{\pi w^2} \quad (2.33)$$

Since for a Gaussian distribution, the full width at half maximum meets $\text{FWHM} = \sqrt{2 \ln 2} w$, the excitation intensity can be also written as:

$$I_0 = \frac{4 \ln 2}{\pi} \frac{P_0 \eta_{\text{trans}}(\lambda_{\text{ex}})}{\text{FWHM}^2} \quad (2.34)$$

where P_0 is the original excitation power in front of the microscope objective and $\eta_{\text{trans}}(\lambda_{\text{ex}})$ is the transmission factor of the microscope objective at the excitation wavelength λ_{ex} . Therefore, $P = P_0 \eta_{\text{trans}}(\lambda_{\text{ex}})$.

2.3.2 Detection of a single particle (QD)

2.3.2.1 Signal to noise ratio

The fundamental prerequisite for the implementation of any single particle experiment is a sufficiently high signal-to-noise ratio (SNR). The achievable SNR can be approximated as follows [223]:

$$\text{SNR} = \frac{N}{\sqrt{N + CP\Delta t + N_d\Delta t}} \quad (2.35)$$

Here, C is the scattered light background (Rayleigh and Raman scattering), P is the incident laser power, Δt is the integration time, N_d is the dark count rate of the detector and N is the number of photons, which is calculated as follows:

$$N = \eta_{\text{det}} \phi_{\text{fl}} \frac{P}{h\nu} \frac{\sigma}{A} \Delta t \quad (2.36)$$

in which η_{det} is the detection efficiency of the confocal microscope, ϕ_{fl} is the quantum yield, $h\nu$ is the photon energy, σ is the absorption cross section and A is the area of the laser spot.

2.3.2.2 Detection efficiency

The detection efficiency of a confocal microscope setup resulting from the efficiencies of all components in the optical path is [219]:

$$\eta_{\text{det}}(\lambda) = \eta_{\text{geo}} \eta_{\text{trans}}(\lambda) \prod_{i=1}^N \eta_i^{\text{Opt}}(\lambda) \eta_{\text{Detector}}(\lambda) \quad (2.37)$$

In addition to the transmissions of the microscope objective, the detector and other optical elements, a limiting factor is the spatial geometric collection efficiency η_{geo} of the microscope objective used. This is special in microscopes which are operated at cryogenic temperatures, since there no immersion oil can be used, constraining the accessible NA from being larger than one. The collection efficiency η_{geo} results from the ratio of the NA dependent maximum acceptance solid angle $\Omega_{\text{geo}} = 2\pi(1 - \cos\theta)$ and full solid angle $\Omega_0 = 4\pi$, i.e.,

$$\eta_{\text{geo}} = \frac{\Omega_{\text{geo}}}{\Omega_0} = \frac{1 - \cos\theta}{2} \quad (2.38)$$

where $\theta = \sin^{-1}(\text{NA}/n)$.

2.3.3 Fluorescence blinking

2.3.3.1 Blinking: “on” and “off” states in fluorescence

In 1996 Nirmal et al. first observed that under continuous illumination, the fluorescence intensity of a single CdSe/ZnS QD detected as a function of time consists of a series of abrupt changes, meaning intermittently flickering on and off, which is termed fluorescence intermittency or more humbly, fluorescence blinking [54]. Similar fluorescence blinking behavior was subsequently also found in other nanocrystal systems such as CdS [224], CdS/HgS [225], CdTe [57], InP [85], Si [226] and PbS [227], and became one of the most studied photo-physical properties of individual semiconductor QDs [24, 228–230]. As revealed in Figure 2.23, to analyze the dynamics responsible for the blinking phenomenon, the most common method is to extract the durations of *on* and *off* events (*on* and *off* times) from the fluorescence time trace and compile the corresponding histograms. Under the approximation of binary blinking, a proper threshold is set to discriminate the two events, and the *on/off* times are thus obtained. In contrast to the blinking of single molecules which originates from a transition to a triplet state [231], a typical feature of the blinking found in QD systems is that the statistic histograms of lengths of *on* and *off* times reveals a non-exponential character. The probability distribution extracted from such histograms is empirically best described by an inverse power law (a linear distribution in log-log plots as shown in Figure 2.23(c) and Figure 2.23(d)) with the form [232]:

$$P(t) = At^{-m} \quad (2.39)$$

The exponent m has usually been found to be in the range between one and two. This distribution of the *on* or *off* times extends over a large time scale from several 100 μs up to

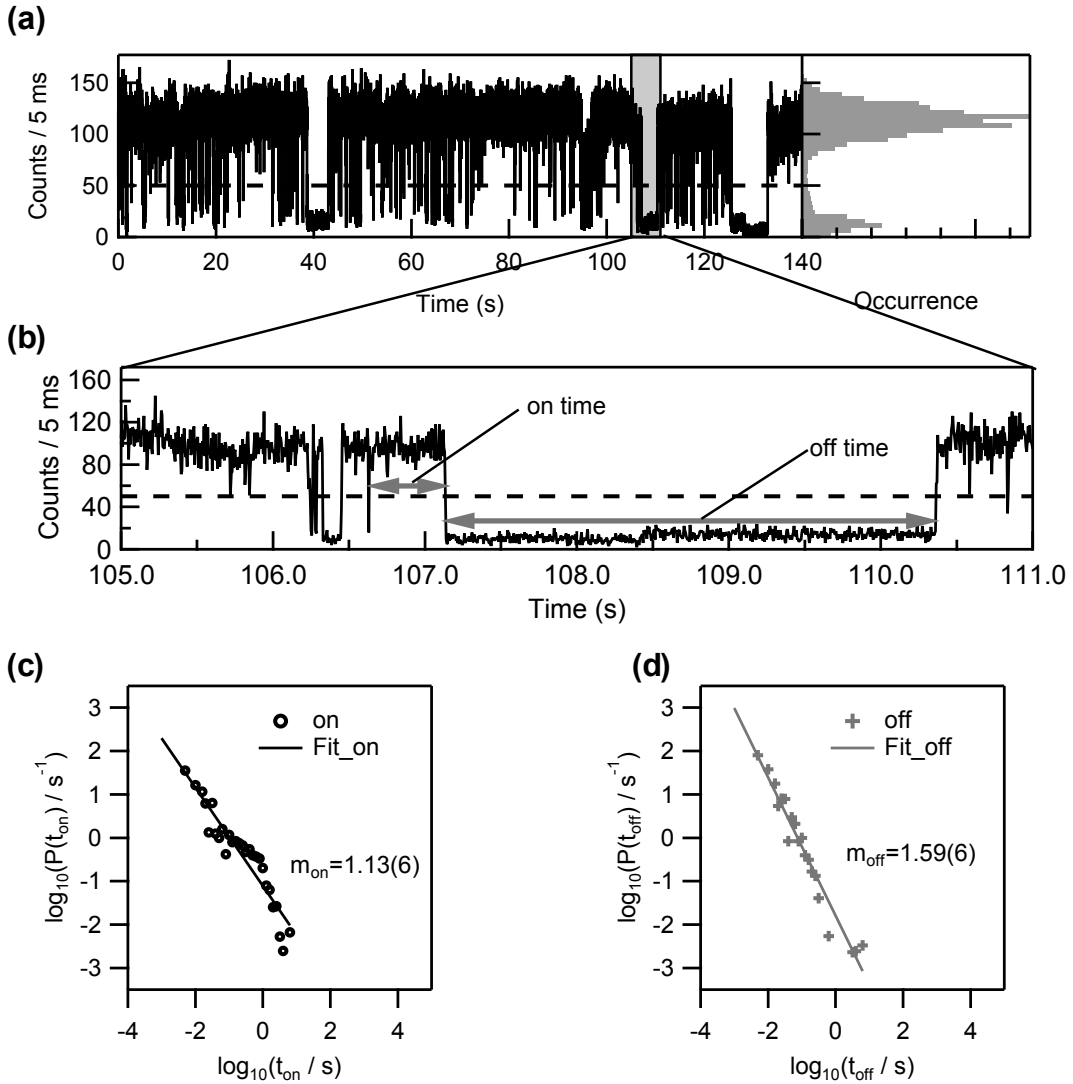


Figure 2.23: (a) Fluorescence time trace of a single InP/ZnSeS QD under excitation by 488 nm laser light. The dashed horizontal line is the adopted threshold to discriminate the *on* and *off* events. The gray histogram on the right panel is the corresponding intensity distribution. (b) Enlarged view of part of the time trace with the definition representation of *on* and *off* times. (c) and (d) are the log-log plots of the histograms of the lengths of *on* and *off* times, respectively. The lines are the corresponding least squares linear fittings.

the total observation time such as several 100 s or 1000 s. Therefore, the integral

$$\langle t \rangle = \int_{t_{min}}^{\infty} t P(t) dt \quad (2.40)$$

diverges and there is no characteristic time scale in blinking behavior since the mean *on* and *off* times are both observation time dependent. Thus, the description of blinking with

any single rate process is not possible, because any single rate process will predict a single exponential distribution for *on* or *off* times [24].

2.3.3.2 Mechanism of blinking: proposed physical models

Although up to now the exact mechanism of blinking still remains ambiguous, a lot of effort has been made in the past decades. The model first proposed by Efros and Rosen assumes that the non-emitting period of a single QD is due to a light-induced ionization process [55]. As shown in Figure 2.24, an electron–hole pair (exciton) is excited in a neutral QD by a photon and subsequently recombines, generating emission, which corresponds to an *on* state. For some reason such as tunneling or Auger autoionization, one of the carriers (either an electron or a hole) is ejected from the QD core into the surrounding matrix or surface traps, resulting in a charged QD. This ionized QD is not fluorescent any more due to the very fast Auger process (usually orders of magnitude faster than the rate of radiative recombination [233]) between the remaining carrier and a subsequent exciton. This Auger process means that the energy of the exciton is completely transferred to the remaining carrier and excites this carrier up to a higher excited energy level, therefore without any fluorescent emission, corresponding to an *off* state. The QD will emit again when charge neutrality is regained. This model provided the first intuitive picture for blinking, but failed to explain the power law distributions of *on* and *off* times. Therefore, numerous other modified mechanisms have been proposed as follows:

- **Spectral diffusion.** The hypothesis by the group of Bawendi [56, 57] involves a resonant tunneling between an excited state in the QD and an acceptor trap state which diffuses at the surface or outside the particle. Whenever the trap state becomes in resonance with the energy levels of the QD, a charge carrier tunnels out or back into the QD, rendering switching between *on* and *off* states of the fluorescence. Applying the one-dimensional random-walk theory, the probability density was calculated to be naturally in the form of a power law and the exponent should be $m = 1.5$ for both *on* and *off* times. Interestingly, by assuming spectral diffusion of both QD and the acceptor state, Tang et al. found the exponent changed to be $m = 0.5$ [58].
- **Spatial diffusion.** Another diffusion mechanism is proposed by Margolin et al. [59]. In contrast to spectral diffusion, it suggested spatial diffusion, meaning either by tunneling or thermal activation, the ejected carrier diffuses in three-dimensional space around the QD and hops back from the matrix. The model also predicts power law distribution of *on* and *off* times. In addition, ergodicity breaking and

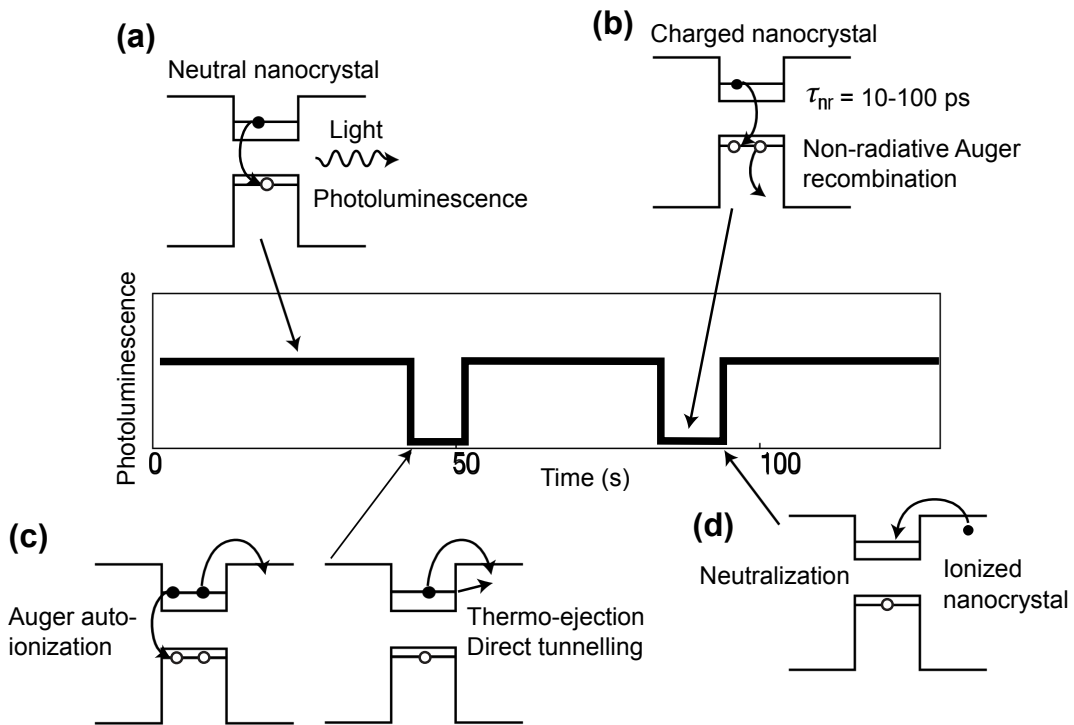


Figure 2.24: Schematic diagrams of fluorescence blinking and classic charging model of a QD. (a) An optical excited neutral QD corresponds to photoluminescence. (b) Excitation of the charged QD leads to fast non-radiative Auger recombination. (c) Ionization processes induces the *on* to *off* transition. (d) Neutralization process induces the *off* to *on* transition. Adapted from Ref. [79].

anomalous diffusion are involved in the model, by which the probability of the carrier which leaves the QD permanently in the limit of long observation times have been explained.

- **Static multiple trap distribution.** Instead of a single trap, Verberk et al. [60] postulated a uniform static distribution of a series of electron traps near the QD. With a distance and/or trap depth dependent exponential distribution of trapping and de-trapping rates, power-law *off* time distributions were obtained. This model suggests sensitivity of the power law exponent to the dielectric of the environment [228].
- **Tunneling barrier fluctuation.** Alternatively, Kuno et al. [61] suggested a dynamic tunneling process between an electron within a QD and an trap state outside, where the corresponding height or width of the tunneling barrier varies between each transition of *on-off* events.

- Non-radiative rate fluctuation.** Differently from the mechanisms above, the model proposed by Frantsuzov and Marcus [62] does not invoke the presence of the long-lived electron traps. The quenching of the QD fluorescence is attributed to the direct non-radiative recombination of the exciton through the Auger assisted formed deep surface states. Based on this assumption, the naturally obtained continuous distributed hole-trapping rate is then governed by the energetic diffusion of the transition between the first two excited electron states ($1S_e - 1P_e$). However, both *on* and *off* time distributions are predicted in this case to be power law with an exponent of 1.5, which is independent of the chosen threshold and not consistent with the fact of divergence obtained from different data [63]. Hammers reported a similar theory and compared it with the experimental data to explain the blinking suppression after ligand exchange [74].

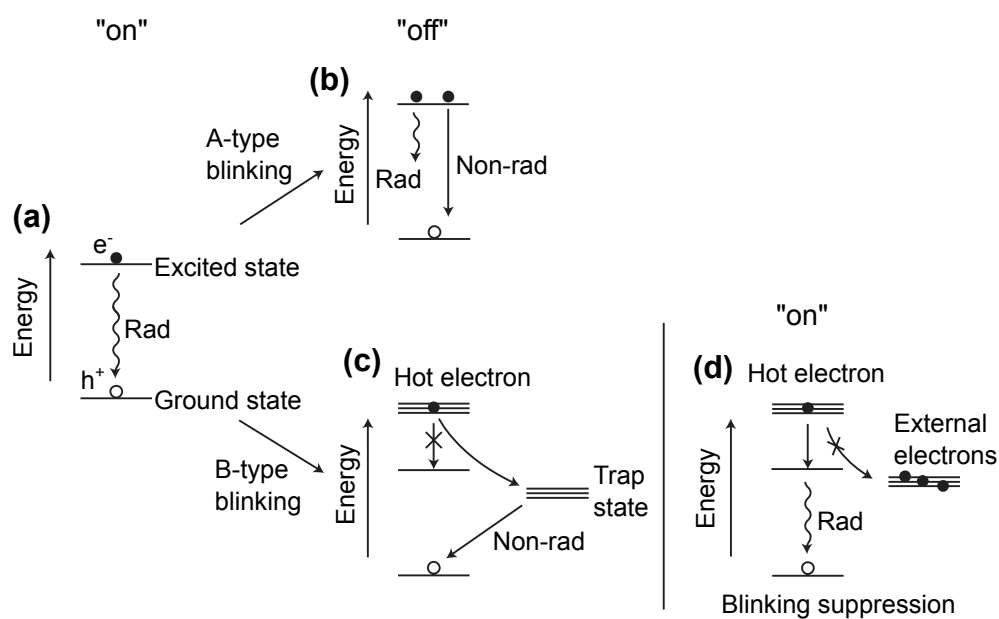


Figure 2.25: Schematic diagrams for *on* and *off* states in A- and B-type blinking events. (a) An *on* states contains a photoexcited electron-hole pair and emits efficiently. (b) In an A-type blinking event, the *off* state contains an additional electron in an excited state and is dark due to the increasing of non-radiative relaxation rate. (c) In a B-type event, the “hot electron” is trapped by surface states immediately after photoexcitation and combines non-radiatively with the remaining hole. (d) Addition of external charges in the trap states deactivates the trapping pathway, and thus causes B-type blinking suppression. From Ref. [234].

Both experimental observations and data analyses for the blinking phenomenon become complicated due to many factors involved. For example, Nirmal et al. [54] and Banin et al. [235] found a linear decrease of the *on* time with the increase of the

excitation intensity. In contrast, the *off* time is independent of the intensity. Shimizu et al. later observed truncation times (cutoffs) in *on* time distributions which decreased with the increase of excitation intensity and may imply some competing physical process interrupting power-law blinking [57]. Moreover, some reports highlighted the strong dependence of the power law exponents and the truncation times on the chosen threshold and the experimental bin time, pointing out the truncated power-law distributions of *on* times may not reflect a real trend [24, 63]. In addition, Spinicelli et al. reported gray states in CdSe-CdS nanocrystals involving a trion emission (one electron-hole pair in a ionized QD) [236]. Zhang et al. even found continuous distribution of emitting states from single CdSe/ZnS QD and a nonlinear correlation of lifetime and intensity fluctuations [237]. As an experimental result of Zhao et al., the intensity of the *off* state is found to be at least 10 times smaller than would be predicted by the charging model of blinking in the strong confinement limit [238]. These observations accompanied by some other investigations of the *off* state behavior challenges the charging-Auger-recombination and “*on/off*” discrete state model, implies that charged quantum dots are also able to be emissive, and suggests that other complicated processes such as time-dependent charge migration or multi-exciton emission might be responsible for some observed fluorescence dynamics [237–240]. More recently, a finding by Galland et al. with the technique of spectroelectrochemistry revealed that there are two types of blinking [241]. With the relatively bright *off* state from their QDs, they measured the fluorescence lifetime and found the first type (termed A-type) blinking with an accompanying decreased fluorescence lifetime was consistent with the charging model, whereas when the other type (B-type) blinking happened, the fluorescence lifetime remained constant. The B-type blinking was explained by the activation and deactivation of an efficient capture of the photoexcited “hot electrons” (electrons occupying energy levels well above the lowest energy state in the conduction band) by the electron-accepting surface sites. By applying an external electrochemical potential, B-type blinking could be suppressed (Figure 2.25) [234]. In addition, a recently reported non-blinking (Zn)CuInS/ZnS QDs prepared by *in situ* interfacial alloying approach highlighted the contribution of interior traps to the blinking behavior [84]. Up to now, no single theoretical model is able to explain all experimental observations, and therefore the physical nature of blinking remains partly a mystery.

2.3.3.3 Blinking Suppression: towards non-blinking quantum dots

Despite the lack of a complete understanding of the exact physical origin of fluorescence blinking, various methods have been developed to reduce and suppress blinking:

- **Experimental conditions.** Some groups found a dependence of blinking on temperature [57] and excitation energy [64, 65, 242], and therefore to some extent, the corresponding experimental conditions can be tuned to minimize the blinking.
- **Plasmon resonance.** Plasmon resonance from metallic nanostructures was used to cause a change in the fluorescence properties [66–68]. Energy transfer to the metal could play an essential role in the observed blinking suppression.
- **Surface modification.** Another important method to modify blinking is the surface modification of QDs with organic molecular ligands or polymers serving as charge compensators/mediators [69–75]. Hohng et al. found near complete suppression of quantum dot blinking when thiol-containing chemicals were added under ambient conditions [69]. The authors believed that the thiol moiety which plays a role as an electron donor, can donate electrons to the surface electron traps of a QD. Therefore, it prevents the traps accepting electrons from the QD itself. Thus, the blinking is suppressed [69]. The function of thiol group for blinking suppression has also been reported in aqueous solutions [243, 244].
- **“Giant” QDs.** The group of Hollingsworth and Mahler et al. developed the so-called “giant” QDs by overcoating QD cores with very thick shells [76–78, 245]. The strategy is clear: no matter how ionization of the QD occurs, the thick potential barrier around the core should decrease the possibility of the escape of the carriers to the surface [79]. It is worth noting that growth of the thick shell took days. Furthermore, the quantum yield of the “giant” QDs appeared to be low (10%–40%), which was speculated to be related to the recombination through defects within the thick, imperfect shell [76].
- **Confinement potential design.** As demonstrated by Efros, if the Auger non-radiative recombination time becomes longer than the radiative recombination time of a charged electron-hole pair (that is, a trion), which is several nanoseconds, there will be no photoluminescence *off* periods (even if the nanocrystal becomes charged) [79]. Wang et al. indeed observed alloyed CdZnSe/ZnSe QDs with relatively small size (~5 nm) exhibiting no blinking at all [80]. They attributed it to a trion emission resulting from a gradually changing potential energy function and the relatively soft confinement. Furthermore, it is reported that compared to an abrupt and step-like confining potential corresponding to the traditional core/shell structure, a “smooth” confining potential which could result from a graded alloy

core/shell structure can efficiently increase the rates of Auger recombination, and thus blinking can be suppressed [81, 246].

- **High crystallinity.** In 2013, new high-quality CdSe-CdS core-shell QDs with narrow emission linewidths and suppressed blinking have been synthesized by Chen et al. [82]. The authors ascribed the strong blinking suppression as well as other high qualities (high particle uniformity, high quantum yields, narrow and symmetric emission spectral lineshapes) of their new kind QDs to good crystallinity. Similar results were found in zinc-blende CdSe/CdS system as well [83]. In a recent report by Zhang et al., (Zn)CuInS/ZnS QDs prepared by *in situ* interfacial alloying approach exhibited non-blinking behavior, and the main mechanism was believed to be the modification of QDs traps from interior to exterior [84].

Almost all the above-mentioned investigations with respect to the suppression of fluorescence blinking have focused on group II-VI QDs (CdSe or CdTe based). Taking into account the increasing requirements of low toxicity in QD applications, a new type of non-blinking Cd-free QD is urgently needed. Although as promising alternatives, InP based QDs have been synthesized and characterized [4, 51, 141, 175, 177, 247], there are very few reports on the fluorescence blinking and blinking suppression of InP based QDs, and no InP based QDs without blinking have ever been observed [85–87].

2.3.4 Spectral diffusion

As discussed in the beginning of Section 2.3, the linewidth of the emission spectrum of an ensemble of QDs is broadened due to inhomogeneous broadening. Yet, even the emission spectra of single QDs at low temperatures often do not exhibit the homogeneous linewidth (Equation 2.50) or the experimental resolution limited linewidth as originally expected. This can be attributed to spectral diffusion, which means that the wavelength of the emission peak of a single QD is not constant but varies with time under constant excitation. Spectral diffusion occurs on all time scales of observations. The one occurring on a timescale which is smaller than the acquisition time of the experiment results in broadening of the emission spectra as mentioned above and is only possible to be resolved by high resolution spectroscopies [248] whereas the one which occurs at larger time scales results in discrete jumps of the spectral position [249]. Although the fundamental cause of spectral diffusion remains uncertain, the classic model proposed by Empedocles and Bawendi has been widely accepted [24, 250]:

Unlike the case of single molecules which are exquisitely sensitive to changes in their surrounding environment [251], a lack of dependence of energetics of the radiative

recombination on surface modification for CdSe QDs was reported by Kuno et al. [252]. Therefore, the excitonic energy in QDs is not sensitive to the chemical nature of the nanocrystal surface and should be relatively unaffected by small changes in the surrounding environment [250]. In addition, the magnitude and frequency of small spectral shifts such as several meV have been observed to increase with increase of excitation intensity and energy (shorter excitation wavelength) [253, 254], which implies that the contribution of excitation is in the form of energy released as the exciton relaxes to its emitting state. Heating is considered not to be the main factor due to rapid heat dissipation. However, changes of local electric fields which result from charges trapped on or near the surface of the nanocrystal are thought to be responsible for the spectral diffusion of QD. The released excess excitation energy may facilitate the movement of the charges among different local trap sites, inducing local electric field fluctuations and eventually generating observable spectral shifts [253]. Similar spectral shifts can be realized by applying an electric field (Stark effect), which further confirms the model [255].

2.3.5 Single particle spectroscopy at cryogenic temperature

At cryogenic temperature, the emission spectra of single particles collapse to narrow lines, exhibiting an abundant spectroscopic landscape and unexpected physical properties, which are hidden at the ensemble level and the single particle level at room temperature. With the technique of single particle spectroscopy at cryogenic temperatures, the fundamental excitonic structure of the band edge can be revealed.

2.3.5.1 Electron-phonon coupling

A phonon, as an energy quantum, is a collective excitation in a periodic, elastic arrangement of atoms or molecules in condensed matter. In a solid, it represents an excited state of a quantized collective oscillation mode of the interacting lattice atoms. By analogy with transverse and longitudinal waves, phonons as quasi-particles can also be classified into transverse phonons and longitudinal phonons. The transverse phonons oscillate perpendicularly to the direction of propagation whereas the oscillation of longitudinal phonons is along the propagation direction. From another point of view, phonons can be divided into optical and acoustic phonons. Optical phonons show movements of cations and anions in the opposite directions, while those in acoustic phonons move in the same direction. The term *optical* in this case has no meaning with respect to the optical activity, but refers to the oscillation frequencies in the visible or infrared spectral range. Therefore, as depicted in Figure 2.26(a), with the combination

of directions and motions, the resulting types of phonons are: longitudinal optical (LO), transverse optical (TO), longitudinally-acoustic (LA) and transverse-acoustic (TA). Furthermore, the dispersion relations of LO- and LA-phonons in an anisotropic three-dimensional crystal are shown in Figure 2.26(b). The LO-branch is usually almost dispersionless.

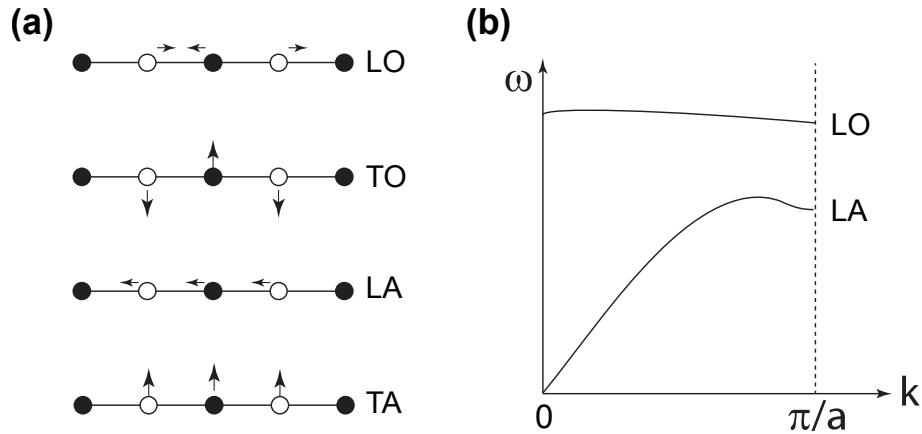


Figure 2.26: (a) Schematic diagrams of different types of phonons based on the directions of motion of the ions in a crystal: longitudinal optical (LO), transverse optical (TO), longitudinal acoustic (LA) and transverse-acoustic (TA). (b) The dispersion of longitudinal optical and longitudinal acoustic phonons. From Ref. [256].

The properties of optical and acoustic phonons and their contributions to electron-phonon coupling in semiconductor QDs are discussed below:

The coupling of optical phonons, especially LO phonons, to an exciton in a semiconductor is believed to be caused by the polar Fröhlich mechanism [102]. As shown in Figure 2.27, after excitation, the spatial separation of the electron and hole wavefunctions leads to an electric polarization field, resulting in a distortion of the ionic lattice as cations and anions move to the opposite directions. With the recombination of the exciton, the electric field disappears and the ions return to their initial positions, exhibiting vibrational motion. The frequencies of optical phonons are mainly material dependent.

Acoustic phonons in optical transitions are generated by piezoelectric coupling (induced by acoustic vibration induced electric polarization) or deformation of the lattice-periodic potential (shift of the band energies due to a change in the atomic positions), where the latter has a greater influence [258]. In contrast to the optical phonons whose frequencies are weakly size dependent, the frequencies of acoustic phonons are strongly size dependent and reveal an inversely proportional relationship with the radius R of the QD [97, 259]. Unlike the optical phonons which are usually quite flat in the entire first Brouillon zone, the acoustic phonons show a dispersion (Figure 2.26(b)). Therefore,

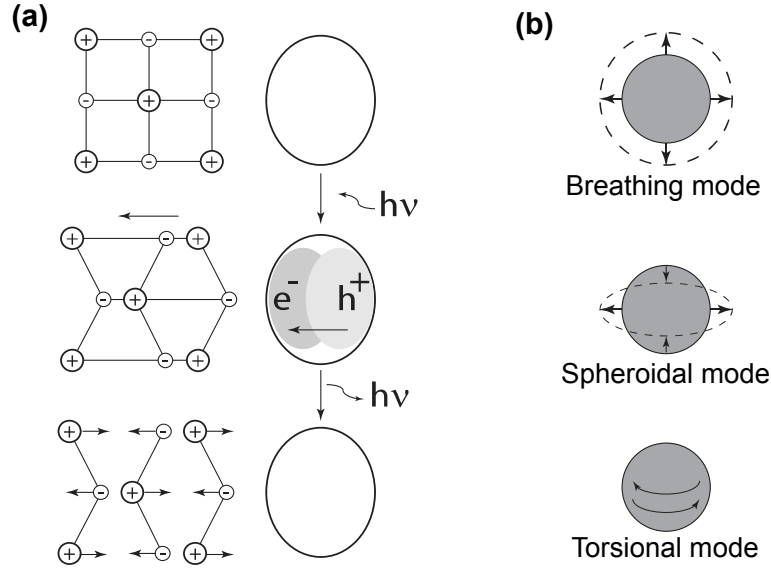


Figure 2.27: (a) Fröhlich coupling at an optical excitation to optical phonons: The crystal lattice is initially at equilibrium position without excitation (up); A photoexcited exciton with a separation between the wavefunctions of the electron and the hole creates a temporary internal electric field, distorting the (ionic) crystal lattice (middle); The internal field disappears and the atoms relax to their equilibrium positions after the recombination of the exciton, inducing lattice vibrations (bottom). Adapted from Ref. [257]. (b) Schematic diagrams of vibrational modes of an elastic sphere: breathing mode ($l = 0, n = 1$) (up), spheroidal mode ($l \geq 0, n = 0$) (middle) and torsional mode ($l = 1, n = 0$) (down), according to Ref. [102].

the acoustic phonon energy varies significantly with different symmetry points of the Brillouin zone in bulk materials. The Lamb theory [260] considers the acoustic vibrations of a particle as a whole from a classical point of view [261]. The theory based on the model of a spherical elastic body was first described by Lamb [260] and applied to the calculations of acoustic phonon energies by Tamura et al. [262], Tanaka et al. [263], Saviot et al. [264], etc.

The model is valid when the wavelengths of the acoustic phonons are sufficiently larger than the lattice constant of the semiconductor [102]. The computed vibrational frequencies have reached consistency with the experimental data in many nano-structured systems with different environments and various boundary conditions [261, 265–268].

In Lamb's theory, the equation of motion of a three-dimensional elastic body is given by [102, 269]:

$$\rho \frac{\partial^2 \mathbf{u}}{\partial t^2} = (\lambda + \mu) \nabla(\nabla \cdot \mathbf{u}) + \mu \nabla^2 \mathbf{u} \quad (2.41)$$

where \mathbf{u} is the lattice displacement vector, ρ is the mass density and the two parameters μ and λ are Lamé constants, which connect the diagonal and off-diagonal elements of the

deformation tensor ϵ_{ik} with that of the strain tensor σ_{ik} as:

$$\sigma_{ik} = 2\mu\epsilon_{ik} + \lambda\delta_{ik}\epsilon_{ll} \quad (2.42)$$

Using these two constants, the longitudinal and transverse sound velocities can be respectively expressed as:

$$v_l = \sqrt{\frac{2\mu + \lambda}{\rho}} \quad \text{and} \quad v_t = \sqrt{\frac{\mu}{\rho}} \quad (2.43)$$

Under stress-free boundary conditions, Equation 2.41 can be solved by introducing a scalar potential and a vector potential. Thus, two types of vibrational modes, which are defined as spheroidal modes and torsional modes are obtained. The eigenvalues of both are described by orbital angular momentum quantum number l and harmonic n . For the spheroidal modes, we have:

$$\begin{aligned} & 2 \left[\eta^2 + (l-1)(l+2) \left[\frac{\eta j_{l+1}(\eta)}{j_l(\eta)} - (l+1) \right] \right] \frac{\xi j_{l+1}(\xi)}{j_l(\xi)} - \frac{1}{2}\eta^4 \\ & + (l-1)(2l+1)\eta^2 + [\eta^2 - 2l(l-1)(l+2)] \frac{\eta j_{l+1}(\eta)}{j_l(\eta)} = 0 \quad (l \geq 0) \end{aligned} \quad (2.44)$$

where ξ and η are dimensionless eigenvalues and $j_l(\eta)$ is the spherical Bessel function of first kind. The spheroidal modes are vibrations with dilatation. Their eigenvalues are material dependent via the ratio v_l/v_t and given by:

$$\xi_l^s = \frac{\omega_l^s d}{2v_l} \quad \text{and} \quad \eta_l^s = \frac{\omega_l^s d}{2v_t} \quad (2.45)$$

where ω_l^s is the angular frequency and d is the diameter of the particle. Particularly, the mode with $l = 0$ and $n = 0$ which is called breathing mode is purely radial with spherical symmetry. In contrast to the spheroidal modes which have mixed longitudinal and transverse components, the torsional modes are purely transverse without dilatation, independent of material, and the corresponding eigenvalues are:

$$j_{l+1}(\eta) - \frac{l-1}{\eta} j_l(\eta) = 0 \quad (l \geq 1) \quad (2.46)$$

which can be further written as:

$$\eta_l^t = \frac{\omega_l^t d}{2v_t} \quad (2.47)$$

Hence, the $(n + 1)th$ eigenvalues corresponding to the angular momentum l are denoted as ξ_l^s , η_{ln}^s and η_{ln}^t . Only the lowest modes ($n = 0$) are the surface modes and higher modes ($n \geq 1$) are the inner modes [270]. Since these eigenvalues are simple numbers, the eigenfrequencies ω_l^s and ω_l^t , or the energies of these spherically confined acoustic modes reveal a $1/d$ dependence on size.

The strength of the electron-phonon coupling is described by the Huang-Rhys factor S , which is defined as

$$S_i = \frac{\Delta_i^2}{2} \quad (2.48)$$

where Δ_i is the shift of the potential minima of the ground and excited state in dimensionless normal coordinates of phonon mode i . The reorganization energy λ_i is the energy recovered as the system relaxes along this mode, given by $\lambda_i = \omega_i S_i$, where ω_i is the phonon frequency [271]. At cryogenic temperatures, since all absorptions and emissions originate from the $\nu = 0$ state, the Huang-Rhys factor can be obtained directly from the ratio of the intensities of the one-phonon transition and the zero-phonon line [271].

Experimentally, there is great variation in the strength of electron-phonon coupling from QD to QD. Taking CdSe QDs as an example, the Huang-Rhys factor shows a large distribution for both the longitudinal optical modes (S_{LO} : 0.06-1.3) [253] and acoustic phonons ($S_{ac} = 0.016$ -0.09) [272]. Considering the variation of the size among individual QDs, it is not surprising that various experiments gave different results.

2.3.5.2 Fluorescence spectra at cryogenic temperature

The spectral properties of QDs are temperature dependent. When the temperature is decreased from room temperature to cryogenic temperatures, the contribution of phonons to electronic transitions becomes smaller and smaller, and the absorption and emission spectra are strongly narrowed. For some materials, a purely electronic transition without phonon participation which is called zero-phonon line (ZPL) can be observed [273].

According to the Heisenberg uncertainty principle, the energy level above ground state with energy E and lifetime Δt has an uncertainty in energy [274, 275]:

$$\Delta E \Delta t \simeq \hbar \quad (2.49)$$

which means that with a finite lifetime τ of the excited state, any transition energy cannot have infinitely narrow line frequency distribution, but contains a range of possible frequencies. Then if dephasing effects can be neglected, the corresponding homogeneous

linewidth in the spectrum is:

$$\Delta\nu_{\text{hom}} = \frac{\Delta E}{h} \simeq \frac{1}{2\pi\Delta t} = \frac{1}{2\pi\tau} \quad (2.50)$$

Therefore, neglecting spectral diffusion, the ZPL at cryogenic temperatures has the line profile of a Lorentzian curve based on this natural broadening [276]:

$$I(\nu) = \frac{1}{2\pi} \frac{\Delta\nu_{\text{hom}}}{(\nu - \nu_0)^2 + (\frac{\Delta\nu_{\text{hom}}}{2})^2} \quad (2.51)$$

Here, ν is the frequency, ν_0 is the frequency of the optical transition with the highest intensity and $\Delta\nu_{\text{hom}}$ is the full width at half maximum (FWHM). At temperatures above 0 K, the homogeneous linewidth $\Gamma(T)$ of a transition for a single QD becomes [256]

$$\Gamma(T) = \Gamma_0 + \sigma T + \frac{\Gamma_{\text{LO}}}{e^{E_{\text{LO}}/k_{\text{B}}T} - 1} \quad (2.52)$$

where $\Gamma_0 = \frac{1}{2\pi\tau}$ is the homogeneous linewidth at 0 K, σ is the electron-acoustic phonon coupling coefficient, Γ_{LO} represents the strength of electron-LO-phonon coupling and E_{LO} is the LO-phonon energy.

Experimentally, at cryogenic temperatures, the purely electronic transition (ZPL) and acoustic and longitudinal-optical phonon sidebands (PSBs) of some QDs such as CdSe can be resolved, as shown schematically in Figure 2.28.

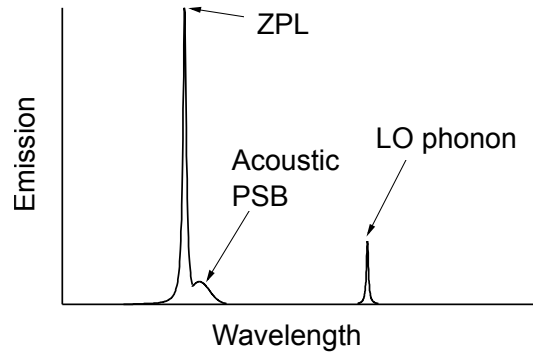


Figure 2.28: Schematic emission spectrum of a single CdSe QD at cryogenic temperatures with a zero-phonon line (ZPL), acoustic phonon sideband (PSB) and the longitudinal-optical (LO) phonon.

In addition to the spectral line shape, the band gap of a semiconductor also changes with the temperature. A reduction of the temperature leads to a reversible blue-shift of the spectra for both bulk semiconductor crystals and nanocrystals. This can be rationalized by the interaction resulting from changes of bond length and electron-phonon coupling

with temperature, whereby the bonding energy, and thus the band gap are modified. The temperature dependence of the band gap of a bulk semiconductor crystal is generally described with the empirical Varshni equation [277]:

$$E_g(T) = E_g(0) - \frac{\alpha T^2}{T + \beta} \quad (2.53)$$

where $E_g(0)$ is the band gap at 0 K, α is a temperature coefficient and the temperature β is close to the Debye temperature of the corresponding material. However, these parameters from different literatures are not consistent [278].

As an improvement of the Varshni equation, a further description of the temperature dependence of the band gap of semiconductors proposed by O'Donnell and Chen takes into account the influence of the electron-phonon coupling on the binding and the resulting energy band gap [279]. In contrast to Equation 2.53, no empirical variables from temperature dependent experiments are required, but the Huang-Rhys factor S and the average phonon energy $\langle \hbar\omega \rangle$ are involved [279]:

$$E_g(T) = E_g(0) - \frac{2S \langle \hbar\omega \rangle}{e^{\langle \hbar\omega \rangle / k_B T} - 1} \quad (2.54)$$

where k_B is the Boltzmann constant. This equation can also be applied to the estimation of Huang-Rhys factor and the average phonon energy if the transition energies have been experimentally obtained. For example, Narayanaswamy et al. extracted the Huang-Rhys factor S from experimental fitting based on this equation, revealing that the electron-phonon coupling increases as the diameter of the nanocrystal decreases for InP/ZnS QDs [280, 281]. A similar trend has also been observed for CdSe QDs through fluorescence line narrowing experiment [282].

Experimental materials and methods

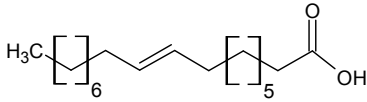
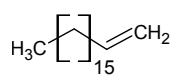
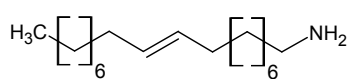
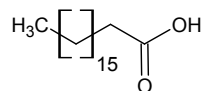

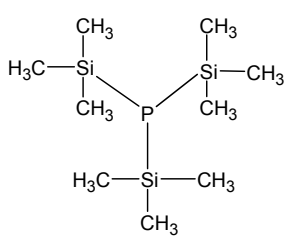
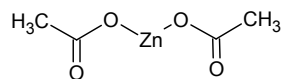
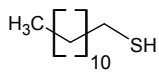
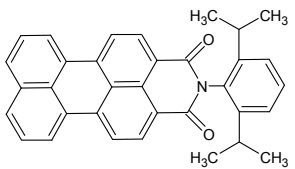
3.1 Materials

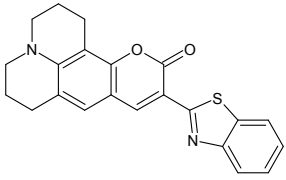
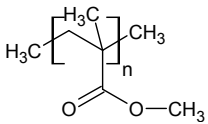
Chemicals (Table 3.1) were purchased from *Merck*, *abcr*, *Sigma-Aldrich*, *Alfa*, *Strem Chemicals*, *Exciton*, *Goodfellow* or lab-prepared. Perylene-monoimide (PMI) was supplied by the group of Prof. Dr. Klaus Müllen (Max Planck Institute for Polymer Research, Mainz, Germany). All chemicals were used without further purification.

Table 3.1: Chemicals used in this thesis.

Chemical	structure	Molecular Weight	Supplier
Trioctylphosphine oxide (TOPO, 98%)		387	Merck
Trioctylphosphine (TOB, 97%)		371	abcr
Tetradecylphosphonic acid (TDPA)		278	Lab ¹

¹Prepared by Michaela Wagner in the Basché group according to Ref. [283].

Chemical	structure	Molecular Weight	Supplier
Oleic acid (OA, 90%)		282	Sigma-Aldrich
1-Octadecene (ODE, 90%)		252	Sigma-Aldrich
Oleylamine (70%)		267	Sigma-Aldrich
Stearic acid (SA, 98.5%)		284	Sigma-Aldrich
Tetrahydrofuran (THF, 99.9%)		72	Sigma-Aldrich
Tris(trimethylsilyl)- phosphine (P(TMS) ₃ , 98%) (10 wt% in hexane)		250	Strem-Chemicals
Zinc acetate (Zn(ac) ₂ , 99.99%)		183	Sigma-Aldrich
1-Dodecanethiol (DDT, 98%)		202	Sigma-Aldrich
Perylene-monoimide (PMI)		482	AK Müllen

Chemical	structure	Molecular Weight	Supplier
Coumarin 545		374	Exciton
Polymethyl-methacrylate (PMMA)		—	Good-fellow
Cadmium oxide (CdO, 99.5%)		128	Sigma-Aldrich
Selenium (Se, 99.5%)		79	Alfa
Zinc oxide (ZnO, 99.999%)		81	Sigma-Aldrich
Sulfur (S, 99.98%)		32	Sigma-Aldrich
Indium chloride (InCl ₃ , 99.999%)		222	Sigma-Aldrich

3.2 Synthetic methods

3.2.1 Synthesis of CdSe/CdS/ZnS quantum dots

The synthetic procedures to prepare CdSe/CdS/ZnS core-shell QDs in this thesis are based on the methods developed by the group of Peng [18, 20, 125] and the group of Basché [21]. As shown in Figure 3.1, all reactions were carried out in an air-free and water-free system with a continuous inert argon gas flow of 20–30 mL/min realized by a standard Schlenk

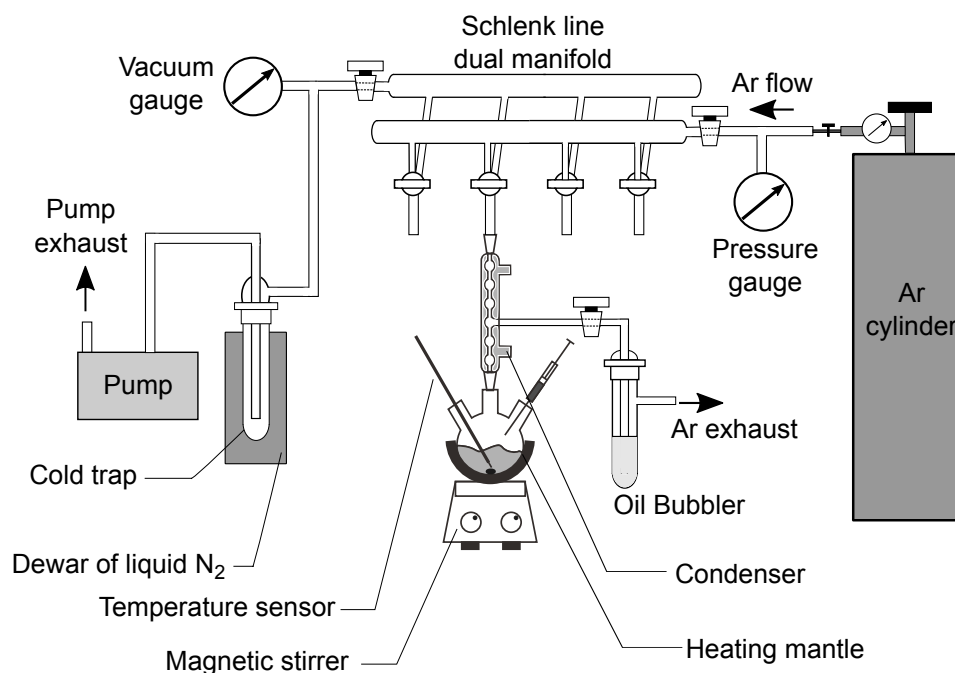


Figure 3.1: Experimental setup for quantum dot synthesis.

line setup in a fume hood. The vacuum achieved was about 1–5 mbar during the degassing processes. The reaction temperature was controlled with a heating rate of 10–15°C/min.

3.2.1.1 Precursor solution

All the precursor solutions were prepared under Ar atmosphere protection. The Se-TOP precursor solution (0.2 M) was prepared by dissolving 79 mg Se powder in 5 mL TOP at room temperature in an ultrasonic bath. The Cd-OA-ODE precursor solution (0.2 M) was prepared by dissolving 160.5 mg CdO in 2.5 mL OA and 3.75 mL ODE at 200°C. The Zn-OA-ODE precursor solution (0.1 M) was prepared by dissolving 203.4 mg ZnO in 7 mL OA and 18 mL ODE at 310°C. The S-ODE precursor solution (0.1 M) was prepared by dissolving 32 mg sulfur in 10 mL ODE at 180°C.

3.2.1.2 Synthesis of CdSe core QDs

The hot injection approach was used for the synthesis of CdSe QDs [20, 21].

CdSe core synthesis in TDPA, TOPO and TOP In a typical reaction, 26 mg CdO, 112 mg TDPA and 2 g TOPO were loaded in a three-neck flask and degassed at 100°C for 15 min. Then the mixture was heated up to 310°C until the reddish CdO powder was gradually dissolved resulting in optical clear solution. Subsequently, the temperature was adjusted

to 270°C (or 310°C, 380°C) and 1 mL as prepared Se-TOP precursor solution (0.2 M) was swiftly injected. Immediately after the injection, the temperature decreased and was kept at 250°C (or 290°C, 360°C). The growth time was determined according to the desired size and morphology (see Section 4.3.1). When the reaction was completed, the heating mantle was removed and the solution was cooled to room temperature. To remove the unreacted precursors and excess ligands, the QDs were precipitated by adding ethanol/methanol (v/v 3:1), subsequent centrifugation and decantation. The resulting CdSe QDs were re-dissolved in toluene and stored at 4°C in the dark for further processing.

CdSe core synthesis in SA, TOPO and TOP To synthesize large spherical CdSe QD cores (see Section 4.3.5.1), stearic acid (SA) was introduced. 13 mg CdO and 1 g SA were mixed and heated to about 130°C under Ar protection until the solution was clear. Then the mixture was cooled to room temperature. After that, 2 g TOPO was added and the system was re-heated up to 360°C under Ar flow. Subsequently, the solution was cooled slowly and the temperature was set to 270°C. At this temperature, 1 mL as prepared Se-TOP precursor solution (0.2 M) was swiftly injected and the QDs were allowed to grow at 250°C for 1 min. To stop the reaction, the heating mantle was removed and the solution was cooled to approximately 70°C and diluted with 10 mL of toluene. The QDs were precipitated by adding acetone, centrifugation and decantation. The QDs with large size could be re-dissolved in toluene and also be stored at a relatively muddy state at 4°C in the dark for further processing. The resulting size is 4.7 ± 0.6 nm, and other characterizations can be found in Section 4.3.5.1.

3.2.1.3 Concentration estimate of the CdSe core

Although many approaches have been reported for the determination of the extinction coefficient/absorption cross section and the concentration of CdSe QDs in solution, such as atomic absorption spectroscopy [114, 284], osmotic pressure [285], comparison with a known amount of precursor solution [286] and inductively coupled plasma atomic emission spectroscopy [287], it is widely recognized that the results in the literatures revealed large discrepancies [288, 289]. The discrepancies may be derived from the differences of both the synthetic methods and the uncertainties of the characterization techniques. In this thesis, the widely applied method by Yu et al. in Ref. [114] was adopted.

Typically, 10 μ L of the prepared CdSe solution was taken and diluted with 3 mL toluene. Then the absorption spectrum of this solution was measured. According to the procedures and the empirical functions described by in Ref. [114], both the size and the molar extinction coefficient of the CdSe QDs can be estimated from the wavelength of

the first excitonic absorption peak. The CdSe molar concentration was then determined by Beer-Lambert's law:

$$A = \epsilon \cdot C \cdot L \quad (3.1)$$

where A is the absorbance at the first excitonic absorption peak, ϵ ($\text{L} \cdot \text{mol}^{-1} \cdot \text{cm}^{-1}$) is the molar extinction coefficient, C (mol/L) is the molar concentration of the QDs and L (cm) is the path length of the cuvette. In the measurements in this thesis, L was fixed to 1 cm.

3.2.1.4 Shell coating of CdSe core QDs

The CdSe/CdS/ZnS core shell QDs were synthesized via *successive ion layer adsorption and reaction (SILAR)* method [20, 21]. First, the size of the CdSe core was calculated by the empirical formula Equation 2.15. Then, with the estimated concentration by Equation 3.1, the amount of the precursor solutions for each injection was calculated by assuming the growth of a concentric spherical shell with a thickness of one monolayer (ML). Based on the wurzite structure of the nanocrystals, the average thicknesses of one ML of CdS and ZnS were estimated as 0.35 nm and 0.31 nm, respectively. It is worth noting that the best results were achieved by the procedure as follows: for the first ML, the actual injection amount was 50% of the theoretical amount, and from the second ML, 50% of the theoretical amount was used after the equivalent diameter correction based on the actual injection volume of the last injection.

As a typical shell coating procedure of the SILAR method, $\sim 1.5 \times 10^{17}$ CdSe QDs dissolved in a minimum amount of toluene (e.g., 0.5 mL) were mixed with 4 mL ODE and 1 mL oleylamine and loaded in a three-neck flask. Evacuation was conducted at 60°C for 30 min to thoroughly remove the toluene. Then the mixture was heated to 240°C under Ar flow. During this process, Cd-OA-ODE precursor solution for the first ML was injected at about 100°C. After 10 min growth at 240°C, S-ODE precursor solution for the first ML was added. The subsequent injections of Cd-OA-ODE (or Zn-OA-ODE) and S-ODE precursor solutions were performed alternately within time intervals of 10 min at 240°C. Thus, multi-epitaxial growth of shells was possible to be carried out. After cooling down to room temperature, acetone was added for the precipitation of the CdSe/CdS/ZnS QDs by centrifugation. The particles were re-dispersed in toluene and stored at 4°C for further characterizations and applications.

3.2.2 Assembly and enrichment of quantum dot oligomers

3.2.2.1 Assembly of QDs into QD oligomers

The assembly procedure of QDs is based on Xu's method [47]: A toluene solution containing $\sim 10^{15}$ CdSe/CdS/ZnS QDs was diluted to 0.5 mL. Then 15 mL methanol as a bad solvent was added. With slight shaking, the mixture instantly became turbid. Subsequently, the QD monomers and oligomers were precipitated by centrifugation (4000 revolutions per minute (rpm), 30 min) and re-dispersed in 0.3 mL cyclohexane. This was defined as a cycle of assembly. If most of the QDs in solution at this time was still monomers (can be characterized by TEM), an additional cycle of assembly was required, until the formation of the desired amount of oligomers.

3.2.2.2 Enrichment and separation of QD oligomers

The enrichment and separation of QD oligomers were carried out by the density gradient ultracentrifugation (DGU) technique using an ultracentrifuge from *Beckman* (SW-60 Ti rotor (swing)). The density gradient was built with a cyclohexane- CCl_4 solution system from the bottom to top 90%, 80%, 70%, 60%, 50%, 40% with respect to the volume ratio of CCl_4 in an 11×60 mm uncapped thick wall polyallomer tube (the inner diameter of the tube is 8 mm). The volume of each layer was 0.35 mL. The solvent with the smallest density was loaded firstly. Then successively, the solvent layer with larger density was injected to the bottom of the tube using a syringe to lift the former solvent layer. After all layers of solvent were injected, approximately 0.15 mL QD cyclohexane solution was carefully added on top of the solution gradient. According to the QD size, different times (e.g., 10–40 min) were used for the ultracentrifugation which was performed at 50000 rpm, 4°C , with the centrifuge chamber evacuated. The distinct bands corresponding to different oligomers could be observed by eye under room light and/or UV lamp (312 nm). The fractions were taken successively by a pipette or an 1 mL syringe from top to bottom.

3.2.3 Synthesis of InP/ZnSeS quantum dots

The synthetic procedure is based on the modification of the previous route developed by Lim et al. [7, 52].

3.2.3.1 Precursor solution

InCl_3 -tetrahydrofuran (InCl_3 -THF) precursor solution was prepared by dissolving 25 mg InCl_3 in 1.13 mL THF. Zn-OA-ODE precursor solution was prepared by dissolving 5.50 g

zinc acetate in 19 mL OA and 41 mL ODE at 200°C under Ar atmosphere protection. P-ODE precursor solution was prepared by mixing 0.4 mL $P(\text{TMS})_3$ solution (10 wt% in hexane) with 1 mL ODE in a glove box. Se-TOP-ODE precursor solution was prepared by dissolving 31.6 mg Se in 1 mL TOP and 1 mL ODE.

3.2.3.2 Synthesis of InP/ZnSeS QDs

Modified from the routes of Ref. [52] and Ref. [7], synthesis of InP/ZnSeS QDs was developed. Two main series of samples labeled as *H* and *L* respectively (see also Section 5.2) were synthesized as follows:

1 mL InCl_3 -THF precursor solution, 2 mL Zn-OA-ODE precursor solution and 8 mL ODE were loaded in a 100 mL three-neck-flask and degassed for 30 min at 100°C. Then the temperature of the system was increased to 280°C (for *H* series) or 220°C (for *L* series) under Ar gas flow. At this temperature, 1.4 mL of P-ODE precursor solution was swiftly injected into the solution. The solution was allowed to react for 20 s (for *H* series) or 7 min (for *L* series) before a proper amount of Se-TOP-ODE precursor solution was added dropwise and reacted for 10 min (for *H* series) or 13 min (for *L* series). Subsequently, 4 mL $\text{Zn}(\text{OA})_2$ solution and 0.18 mL 1-dodecanethiol (DDT) were added and the solution was then heated up to 300°C. After 90 min, the heating mantle was removed and the reaction was therefore terminated. The as-prepared QDs were dissolved in chloroform and purified by precipitation via centrifugation after adding an excess amount of acetone. The final product was re-dissolved in chloroform.

For the *HLim* series samples prepared by Dr. Jaehoon Lim, besides the route for *H* series samples, additional 6 mL (3 mmol) $\text{Zn}(\text{OA})_2$ stock solution were swiftly injected and then 0.72 mL (3 mmol) 1-dodecanethiol were drop-wise injected, and the mixture was reacted for 120 min at 300°C.

3.3 Characterization techniques

3.3.1 Ensemble absorption and fluorescence spectroscopy

3.3.1.1 Absorption spectroscopy

UV-visible absorption spectra were measured with an Omega-20 spectrometer from *Bruins Instruments*. Cuvettes with four quartz windows and thickness of 1 cm were used. The absorption spectra were recorded against the corresponding pure solvent reference with

a slit width of 0.5 mm. Samples were diluted until the absorbance was below 0.05 at the excitation wavelength.

3.3.1.2 Fluorescence spectroscopy

Fluorescence emission (photoluminescence) and fluorescence excitation spectra were taken with a FluoroMax-2 fluorometer from *Horiba Jobin Yvon*. Cuvettes with four quartz windows and thickness of 1 cm were used. The samples were diluted until $\sim 10^{-7}$ – 10^{-6} mol/L to make sure the measured spectral intensities were within the linear range of the spectrometer.

3.3.1.3 Quantum yield determination

The fluorescence quantum yield (QY) of QDs was determined by comparison of the integral fluorescence intensity of the QD solution with a standard dye solution at the same excitation wavelength according to the following formula [290–292]:

$$\Phi_{\text{QD}} = \left(\frac{A_{\text{dye}} \cdot I_{\text{QD}} \cdot n_{\text{solv.QD}}^2}{A_{\text{QD}} \cdot I_{\text{dye}} \cdot n_{\text{solv.dye}}^2} \right) \Phi_{\text{dye}} \quad (3.2)$$

where Φ is the quantum yield, A is the absorbance (optical density) at the selected wavelength in the absorption spectrum which is taken as the excitation wavelength for the fluorescence spectrum, I denotes the integrated fluorescence intensity, $n_{\text{solv.QD}}$ and $n_{\text{solv.dye}}$ are the respective refractive indices of the solvents in which the QDs and dye are dissolved. The subscript “dye” refers to the used reference dye whose absolute quantum yield is known. Sample were diluted until the absorbance was below 0.05 at the excitation wavelength for the fluorescence emission spectrum in order to minimize the inner filter effect. For the CdSe/CdS/ZnS QDs in toluene, the reference dye perylene-monoimide (PMI) in toluene whose QY is 90% was used [293]. The absorption spectra of both the sample and the reference dye were measured. Then the wavelength corresponding to the intersection of the two absorption spectra (i.e., where the optical density of the QD is equivalent to that of the reference dye) was taken as the excitation wavelength for fluorescence spectra. For the InP/ZnSeS QDs in chloroform, the reference dye Coumarin 545 whose QY is 95% in ethanol was used [7]. The refractive indices of chloroform and ethanol were 1.4459 and 1.3624, respectively. The chemical structures, absorption and fluorescence spectra of PMI and Coumarin 545 are shown in Table 3.1 and Figure 3.2.

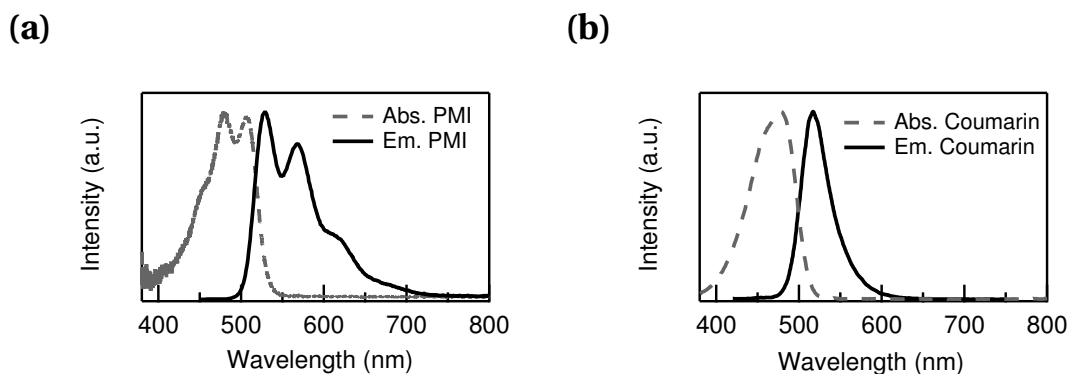


Figure 3.2: Absorption (dashed gray line) and fluorescence emission (solid black line) spectra of PMI (a) and Coumarin 545 (b).

3.3.2 Transmission electron microscopy (TEM)

Philips EM-420 transmission electron microscope operated at an accelerating voltage of 120 kV (for low resolution images), *Carl Zeiss LIBRA-120* energy-filtered transmission electron microscope operated at an accelerating voltage of 120 kV (for low resolution images) and *JEOL JEM-2100* operated at an accelerating voltage of 200 kV (for high resolution images) were used to analyze the morphology, size distribution and the structure of QDs. Samples were purified by precipitation/re-dispersion with bad solvent and good solvent. The QD solutions were diluted and drop-casted onto copper grids covered with a carbon film. The TEM grids were dried in air after removing the excess liquid with filter paper. The size distributions were obtained by measurements of hundreds of QDs for each sample with a program written by the author in *AutoHotkey* language.

3.3.3 Energy dispersive X-ray spectroscopy (EDS)

For elemental analysis, a *JEOL JEM-3010* high-resolution transmission electron microscope operated at an accelerating voltage of 300 kV equipped with EDS (*Oxford*) and a Gatan digital camera (MSC-794) was used.

3.3.4 X-ray diffraction (XRD)

In order to investigate the crystal structure of QDs, XRD measurements were performed with a powder diffractometer (*Bruker* New D8 Advance), using $CuK_{\alpha 1}$ ($\lambda = 0.15406$ nm) as the radiation source. Measurements were carried out in a 2θ range from 20 to 80 degrees. The QD samples were thoroughly purified, drop-casted onto glass substrates for several

times and dried at room temperature. The XRD patterns of the samples were corrected by the data of the bare glass substrate measured under the same experimental condition.

3.3.5 Fluorescence lifetime measurements

Time resolved fluorescence measurements were performed by time-correlated single photon counting (TCSPC) with a FluoroLog-3 spectrometer (*Horiba Jobin Yvon*). The samples were excited at 450 nm with a repetition rate of 1 MHz by a tunable FIANIUM fiber laser. A hybrid photomultiplier detector assembly (PMA Hybrid 50, *PicoQuant*) was used as a detector. The photon counts from the APD and the trigger pulse from the laser were fed into a PicoHarp 300 TCSPC module (*PicoQuant*) to record the rise/decay time profiles. The instrumental response function (IRF) was recorded at 450 nm, employing light scattered by the sample.

3.4 Experimental setups for single particle investigations

3.4.1 Sample preparation

A glass coverslip (*Hecht*, borosilicate glass, $d = 20$ mm, thickness 0.13–0.16 mm) was first cleaned in the ultrasonic bath of Hellmanex dilute solution (5 mL special cleaning concentrate Hellmanex II from *Hellma* diluted in 150 mL deionized water) and subsequently cleaned with pure deionized water. Then the glass coverslip was heated in a furnace at 520°C for 4 hours.

A freshly prepared QD solution was diluted by toluene (for CdSe/CdS/ZnS QDs) or chloroform (for InP/ZnSeS QDs) until the concentration was about 10^{-8} mol/L and further diluted by 100 times with poly(methyl methacrylate) (PMMA, chemical structure shown in Table 3.1)/toluene solutions (~ 20 g/L). Finally, 30 μL of the obtained ultra-diluted solution was spin-coated onto a clean glass coverslip at 3000 rpm for 120 s. This results in a QD is doped polymer film with a thickness of ~ 100 nm [294].

3.4.2 Excitation light sources

For the single particle emission spectroscopy of CdSe/CdS/ZnS QDs and InP/ZnSeS QDs at cryogenic temperatures, OPSSL (optically pumped semiconductor laser) with a wavelength of 487.6 nm and an output power of 20 mW (Sapphire 488-20 CDRH, *Coherent*) was used. For the single particle spectroscopy of InP/ZnSeS QDs at room temperature, diode laser

with a wavelength of 445.4 nm and an output power of 75 mW (OBIS 445 LX, *Coherent*) was used.

3.4.3 Confocal microscope for cryogenic temperature measurement

The confocal fluorescence microscope for the operation at cryogenic temperatures mainly modified by Dr. Anne Boos from the commercial confocal microscope Attocube CFM1 (*Attocube systems*) [219] was used for the measurements of CdSe/CdS/ZnS QDs and InP/ZnSeS QDs at 4.5 K. The basic structure of the setup is described below. More detailed

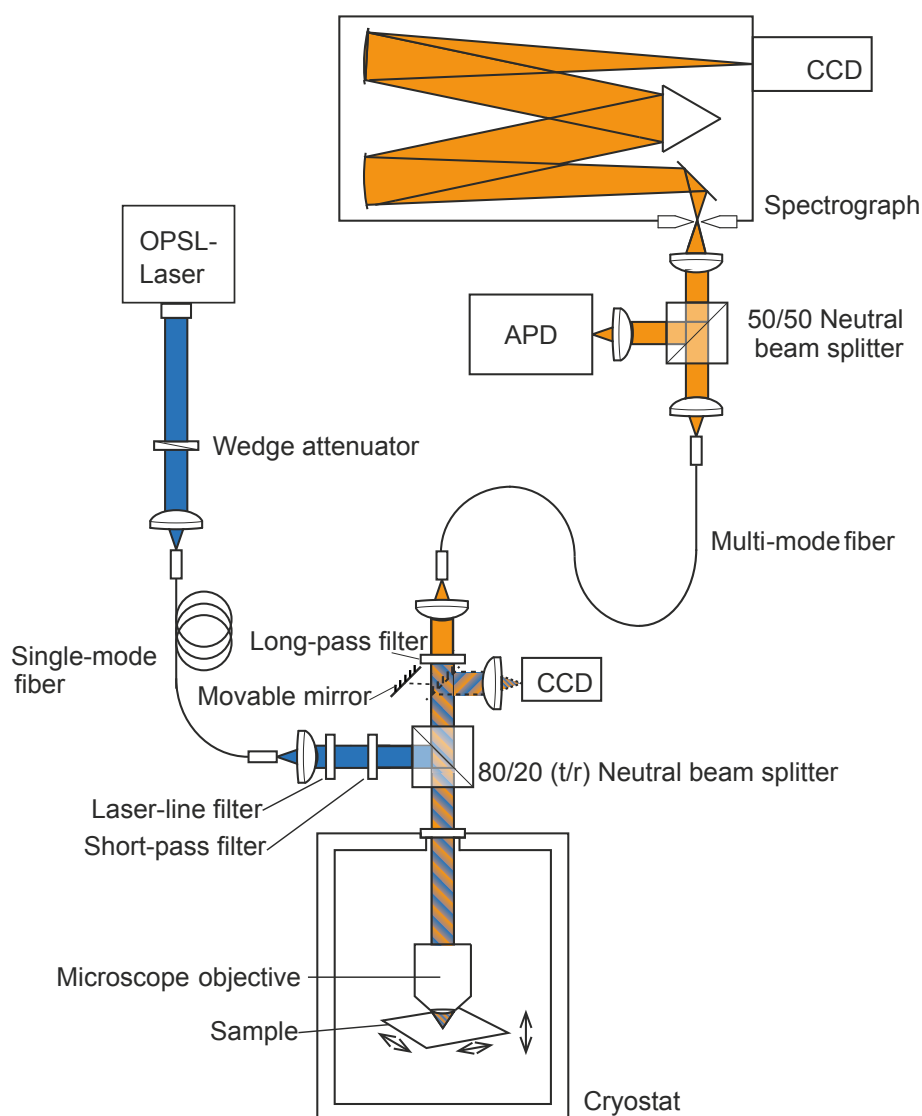


Figure 3.3: Schematic diagram of the confocal fluorescence microscope setup for cryogenic temperature measurement.

introduction can be found in Ref. [295] and Ref. [219]. Figure 3.3 shows a schematic representation of the principal components of the setup.

The excitation light passed through a polarization-maintaining single-mode fiber (PM 460 HP, *Nufern*, this fiber also served as a pinhole) and reached an optical head mounted on the cryostat. Here the filters removed unwanted wavelength components (fiber fluorescence) before a neutral beam splitter cube (*Linos* Type 746 908, 20R/80T), by which 20% of the light was reflected through an optical window (N-BK7 Broadband Precision Window, *Thorlabs*) into the cryostat in the direction of the microscope objective. The objective focused the excitation light onto the sample in the cryostat and collected the fluorescence light. The emitting light went back along the same path as the excitation light until the beam splitter, which transmitted 80% of the intensity. After the beam splitter, a movable mirror could be inserted and served for focus checking by the reflection of the excitation light from the sample plane to a CCD (charge coupled device) camera. After this movable mirror, remaining excitation light was removed by an optical long-pass filter before the emission light was focused on the conjugate focal plane of the focal plane in the sample, where a multi-mode fiber (AFS50/125Y Custom Patch Cord 2.5 m, *Thorlabs*) was located. Then the emission light was guided by means of the multi-mode fiber to a detection system mounted on an optical table and composed of an APD (avalanche photo diode) and a spectrograph equipped with an EMCCD (electron multiplying charge coupled device). Some important elements are introduced in more detail below:

3.4.3.1 Cryostat and sample tube

The Supervari-Temp-Cryostat which allows experiments at variable temperatures from 1.4 K to room temperature from *Janis Research* was used for cryogenic temperature measurement in this thesis. The schematic diagram in Figure 3.4 illustrates the details of the cryostat. The cryostat consisted of several insulating vacuum chambers and three containers for cryogenic liquids: 1) A liquid nitrogen reservoir of a capacity of 50 L was used for pre-cooling the system and reducing the consumption of liquid helium. 2) A 50 L liquid helium reservoir, in which the helium level was monitored by a level indicator (liquid cryogen level meter, model LM-500, *Cryomagnetics*), allowed continuous measurements for several days and the exemption from frequent liquid helium refilling. 3) The third container mounted in the helium reservoir was called variable temperature insert (VTI). It included a vacuum-insulated tube which could be filled with liquid helium from the helium reservoir through a needle valve. The so-called “cryogenic temperature” in this thesis realized by this setup is 4.5 K.

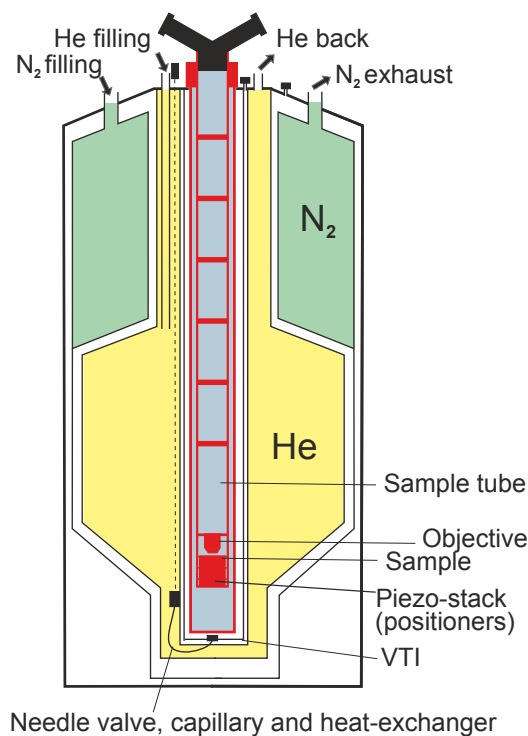


Figure 3.4: Schematic diagram of the cryostat in Figure 3.3 Adapted from Ref. [219].

The sample, the objective and the piezo-stack were mounted in a cylindrical titanium sample tube and not directly in liquid helium in the VTI due to the requirements of the piezo actuators and sensors. After sample loading, the sample tube needed to be degassed until $\sim 10^{-4}$ mbar for 2 hours for QD samples and refilled with ~ 10 mbar of helium gas for sufficient and fast temperature setting.

3.4.3.2 Sample movement

The sample movement was based on a combination of coarse and fine adjustable piezo-actuators under a stationary microscope objective in the cooled cryostat with liquid helium. The combination of these two positioning principles allowed both relatively far distances of the sample travel and a precise control of a position. The piezo-actuators, which could be moved even at cryogenic temperatures, realized the movement of the laser beam on the sample in a telecentric system by sample scanning instead of laser scanning. By moving the sample, the paraxial approximation of the light was satisfied and thus the aberrations were minimized [219].

3.4.3.3 Avalanche photodiode (APD)

An avalanche photodiode (APD), whose high sensitivity allows even single-photon detection, is a semiconductor analog of a photomultiplier that converts light into electricity based on the photoelectric effect. By applying a high reverse bias voltage, the electron was accelerated by an electric field such that further electrons were generated due to impact ionization (avalanche effect). By a single photon, a steady stream via this internal current gain effect could be generated and detected. The current depended on the spectral sensitivity of the APD, the internal amplification as well as the incident light power [219]. In this work, as represented in Figure 3.3, the emitting light was focused by an achromatic lens ($f = 50$ mm) on the active area (diameter = $170 \mu\text{m}$) of an APD SPCM-AQR-14 (*Perkin Elmer*), which had a time resolution of 690 ps [294].

It is worth noting that the APD was on the optical head before November of 2012. The former setup can be found in Ref. [295]. However, this configuration induced a poor mechanical stability of the system. In addition, since the APD had a relatively large active area ($170 \mu\text{m}$ in diameter), a higher background was observed. As an improvement, when the APD was moved onto the optical table behind the multi-mode fiber, the mechanical stability of the system was dramatically enhanced and the background was reduced.

3.4.3.4 Spectrograph and EMCCD-camera

The fluorescence emission spectra from single QDs were recorded by a spectrograph (SR-750-B1-R, *Andor Technologies*) with a focal length of 750 mm in Czerny-Turner configuration and an EMCCD camera (Newton EMCCD O DU970N-BV 1600 x 200 pixels with an edge length of 16 microns per pixel, *Andor Technology*). The emitted light was

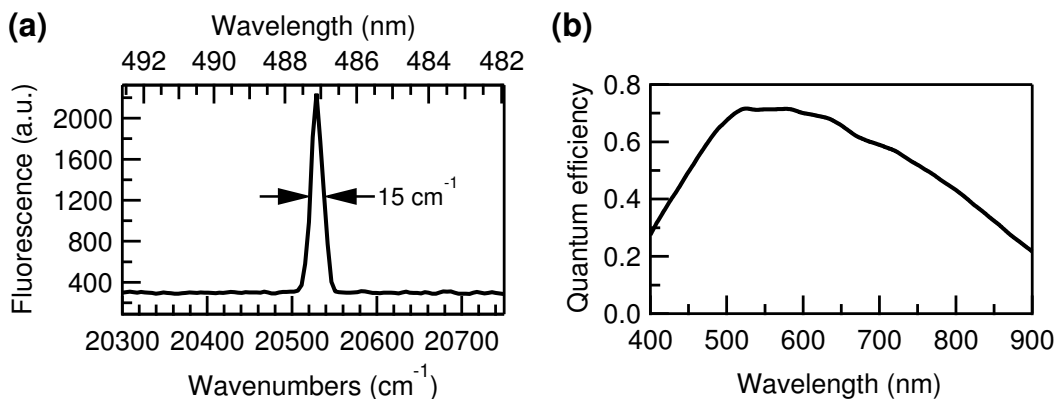


Figure 3.5: (a) Spectrum of a 488 nm laser whose FWHM indicates the spectral resolution of the spectrograph. (b) Wavelength dependent quantum efficiency of the EMCCD camera in combination with a grating with 150 grooves/mm, provided by *Andor Technologies*.

focused by an achromatic lens ($f = 80$ mm) on the entrance slit of the spectrograph and parallelized by a concave mirror. Parallel light beam hit a diffraction grating which reflected dispersed light on a further concave mirror. The concave mirror focused the light eventually onto a EMCCD camera. The grating with 150 grooves/mm allowed a spectral range as large as 200 nm displayed on the EMCCD camera. As revealed in Figure 3.5(a), spectral resolution of the spectrograph was measured to be ~ 15 cm^{-1} with a 488 nm laser. The wavelength dependent quantum efficiency of the EMCCD camera in combination with a grating with 150 grooves/mm is shown in Figure 3.5, and the obtained emission spectra were corrected accordingly.

3.4.4 Confocal microscope for room temperature measurement

The confocal microscope developed in the Basché group for room temperature measurement is shown in Figure 3.6. The excitation laser light was coupled into a single-

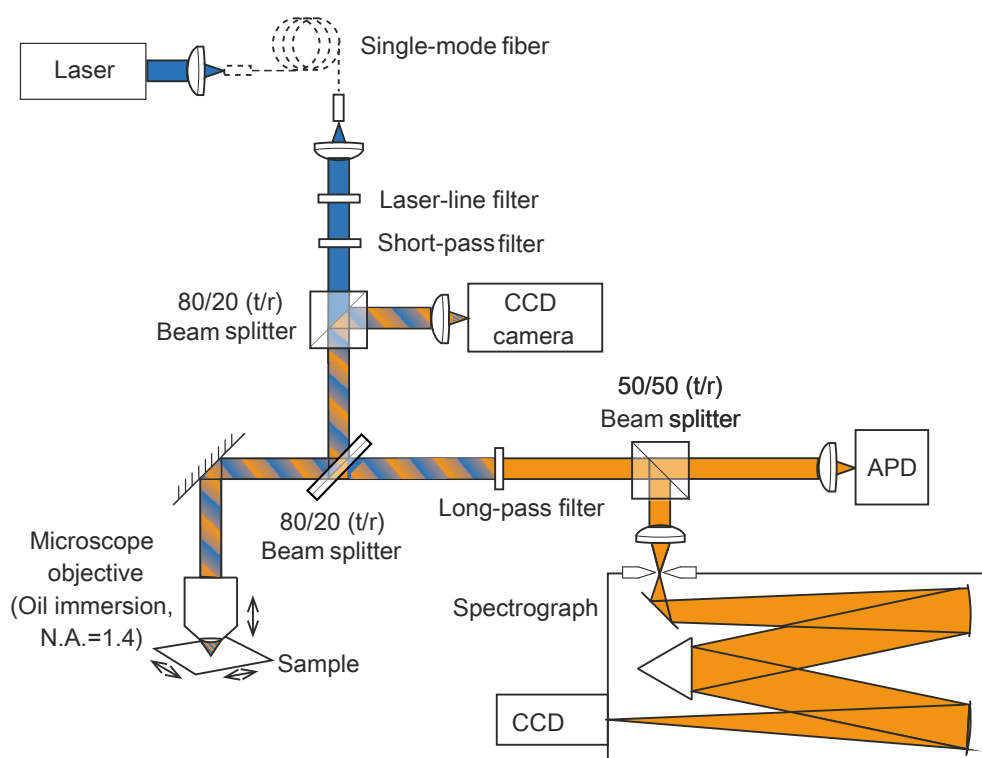


Figure 3.6: Schematic diagram of the confocal fluorescence microscope setup for room temperature measurement.

mode fiber and subsequently passed through filters for spectral filtering. Then the light transmitted through a neutral beam splitter cube and was reflected by a beam

splitter plate (the transmittance and reflectivity of both beam splitters were 80% and 20%, respectively). The incident light further went into an oil immersion microscope objective (Zeiss Plan-Apochromat, NA = 1.4) and was eventually focused on the sample. The fluorescence light of the sample as well as the reflected excitation light was collected by the same microscope objective and 4% of the intensity was delivered along the same path as the excitation light and eventually focused onto a CCD camera, by which the focus of the sample plane could be monitored. The other 80% of the intensity of the returning light passed through the beam splitter plate and the component of remaining excitation light was removed by a long-pass filter. Eventually the emission light reached a detection system composed of an APD (SPCM-AQR-14, *Perkin Elmer*, time resolution: 690 ps) and a spectrograph ($f = 300$ mm, SpektraPro 300i, *Acton Research*) equipped with an EMCCD (Newton EMCCD O DU970N-BV 1600 x 200 pixels with an edge length of 16 microns per pixel, *Andor Technology*). An achromatic lens with a focal length of 50 mm was used to focus the collimated light on the entrance slit of the spectrograph, and a grating with 50 grooves/mm was selected for the measurements of InP/ZnSeS QDs at room temperature. The fluorescence image was performed by successively scanning the sample mounted on a piezoelectric XY-translation stage (P-731-8C). Combined with another piezoelectric element (P-721, PIFOC), the microscope objective could be moved in Z-direction for focusing. The high NA of the microscope objective in this setup and the absence of the multi-mode fiber in the detection path increased the signal of the fluorescence.

3.4.5 Experimental conditions for single particle measurements

Experimental conditions for single particle measurements in this thesis such as excitation source, excitation power, excitation intensity, filter combinations, objective, grating and spectral resolution (defined by FWHM of the corresponding excitation laser light) are tabulated in Table 3.2. All experimental spectral data were analyzed by procedures on the platform of software *WaveMetrics Igor Pro*.

Table 3.2: Overview of experimental conditions for single particle measurements in this thesis. RT: 295 K; LT: 4.5 K. AFM-CFM: atomic force and confocal fluorescence microscope.

Conditions	CdSe/CdS/ZnS QDs at RT & LT	AFM-CFM CdSe/CdS/ZnS QD dimers at RT	InP/ZnSeS QDs <i>H/In</i> series at RT	InP/ZnSeS QDs <i>H & L</i> series at RT	InP/ZnSeS QDs at LT
Excitation source	Coherent Sapphire 488 -20 CDRH	PicoQuant LDH-P-C-470 + PDL 800-B	Coherent Sapphire 488 -20 CDRH	Coherent OBIS 445 LX	Coherent Sapphire 488 -20 CDRH
Ex. Power (μW)	2.8 & 8.4	0.7	0.5	0.5	2.8
Ex. Intensity (W/cm^2)	1045 & 3135	300	285	344	1045
Filter(s) in Ex. Path	Semrock LL01 488 25 & Semrock LL01 488 25	AHF/Chroma LL z 470/635 M & AHF Dichr. 510 DCXRU	Semrock LL01 488 25 & Omega 3rd 490 SP	Chroma ZET 445/10 & Semrock BP 417/60	Semrock LL01 488 25 & Semrock LL01 488 25
Filter(s) in Em. Path	Semrock LP01 514 RU	Semrock LP02 488 RU & Semrock FF01 770 SP	Naneo LP 488	Semrock LP02 458 RU	Semrock LP02 488 RU
Objective	Olympus PLC (NA = 0.65)	Zeiss EC Plan-Neofluar (NA = 0.95)	Zeiss Plan-Apochromat (NA = 1.4)	Zeiss Plan-Apochromat (NA = 1.4)	Olympus PLC (NA = 0.65)
Grating	150 l/mm	300 l/mm	50 l/mm	50 l/mm	150 l/mm
Spectral resolution (cm^{-1})	15	50	96	100	17

4

Monomers, homo- and hetero-dimers of CdSe/CdS/ZnS QDs

4.1 Motivation and approaches

Assembly of nanoparticles into oligomers and larger structures is of current interest, since the properties of the assembled structures may differ from those of the isolated components [33–39]. For instance, creating three dimensional superlattices via coupling of nanoparticles leads to a shift of their emission energy [40–42]. To quantitatively investigate the fundamental mechanism of specific interactions (e.g., electronic coupling) among the components, the first challenge is to find an effective coupling approach to build a well-defined system containing particle oligomers. As introduced in Section 2.2.1, various methods of indirect self-assembly were developed for inorganic nanoparticles, including noble metal nanoparticles and semiconductor quantum dots (QDs) [34, 35, 44]. However, since a strong interaction requires a short inter-particle distance, the direct assembly is more important. Unfortunately, well-defined nanoparticle oligomer systems obtained by direct assembly can only be found in a few reports, most of which are limited to metal particles [45, 46]. Although Xu et al. in the Basché group developed the direct assembly of semiconductor QDs into QD dimers and trimers [47], the corresponding property studies are still in their infancy. In addition, new systems like QD hetero-oligomers are more easily amenable to quantitative studies of the electronic couplings among QDs, and therefore, needed to be prepared.

The motivation of this project was to construct a well-defined QD oligomer (dimer) system by direct assembly of individual (monomer) CdSe/CdS/ZnS QDs for future optical investigations on the electronic coupling between the neighboring QDs at the single particle level.

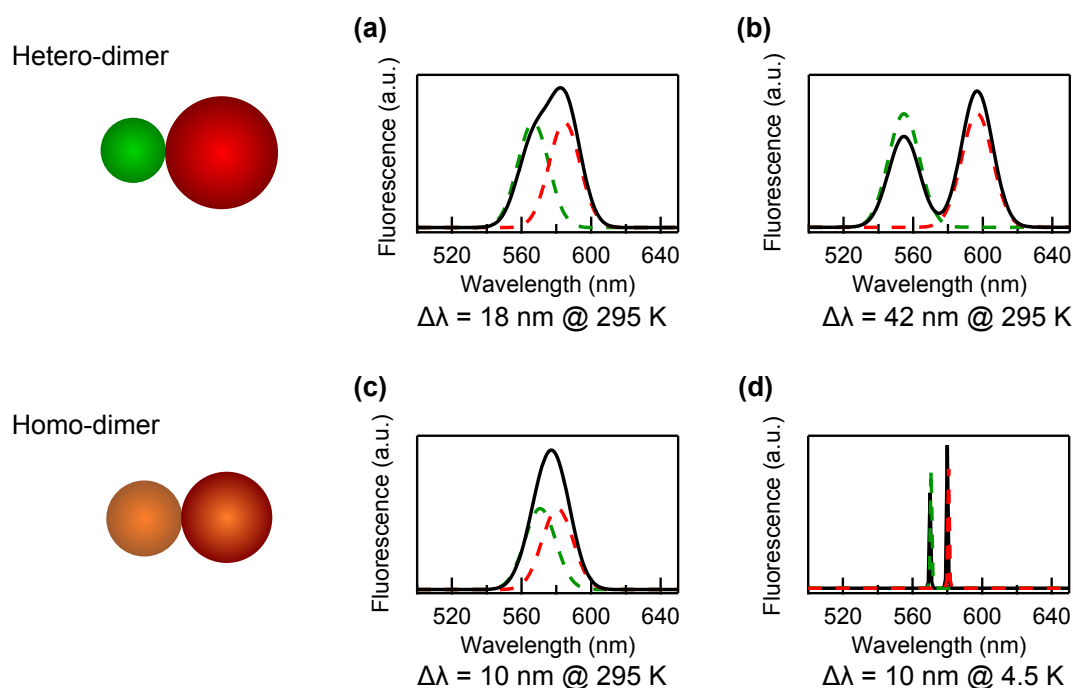


Figure 4.1: Simulated fluorescence emission spectra of single QD hetero-dimers and homo-dimers at 295 K and 4.5 K with Gaussian line shape: (a) Hetero-dimer with an emission wavelength difference of 18 nm at 295 K. (b) Hetero-dimer with an emission wavelength difference of 42 nm at 295 K. (c) Homo-dimer with an emission wavelength difference of 10 nm at 295 K. (d) Homo-dimer with an emission wavelength difference of 10 nm at 4.5 K. Under the assumption that the FWHM of a single QD is 21 nm and 0.5 nm (spectral resolution limited) at 295 K and 4.5 K, respectively, the green and red dashed lines represent the emission spectra of the green and red QDs, respectively. The solid black line is the the dimer fluorescence under the assumption that energy transfer from green QD to red QD is 20%.

Possible approaches for the investigation were analyzed and illustrated in Figure 4.1. Regarding the emission wavelengths of the QD components, there are two possible QD dimer configurations at the single particle level:

- **Hetero-dimer:** The two components, i.e., the green QD (denoted as *gQD*, since in many cases in this thesis it is green-emitting) and the red QD (denoted as *rQD*, since many cases in this thesis it is red-emitting) were prepared separately with different emission wavelengths before assembly.

- **Homo-dimer:** The QD dimer which assembled from the same batch of the raw QD solution. However, since a size distribution exists in any ensemble QD system, the two QDs at the single particle level within a dimer do not have exactly the same emission wavelength. In this sense, a gQD and rQD can also be defined according to the slightly different emission wavelengths.

The fluorescence components of the two QDs within a dimer are required to be spectrally differentiable in order to probe them individually at the same time. Considering that the full width at half maximum (FWHM) of a single CdSe/CdS/ZnS particle is around 21 nm (see Section 4.2.5) at room temperature (295 K), according to Rayleigh criterion [218], the minimum separation of the emission maxima of gQD and rQD should be above 20 nm in order to obtain a visible discrimination. In Figure 4.1(a), dimer spectra with a spectral separation of 18 nm are shown exemplarily. Furthermore, a complete separation of the two emission peaks, which is important for the optical measurement of the components individually, requires an emission wavelength difference as big as about 42 nm at room temperature (Figure 4.1(b)), which can only be realized in a hetero-dimer. Although it is difficult to resolve the contributing spectra for homo-dimers at room temperature (Figure 4.1(c)), they can be well separated at cryogenic temperatures (e.g., 4.5 K). As introduced in Section 2.3.5.2, at cryogenic temperatures, the emission peaks of the CdSe/CdS/ZnS QDs are expected to be strongly narrowed and become a sharp line (the so-called zero-phonon line (ZPL)). The sharp ZPL allows very fine discrimination of the two peaks of gQD and rQD, even if they are derived from the same QD batch, as represented in Figure 4.1(d).

In conclusion, two different approaches have been attempted in this project: 1) the cryogenic temperature measurement of a homo-dimer sample; 2) the room temperature measurement of hetero-dimers whose QD components exhibit large wavelength difference (near 40 nm).

4.2 CdSe/CdS/ZnS QD monomers and homo-dimers

4.2.1 CdSe cores and CdSe/CdS/ZnS QDs

The synthetic procedure for CdSe/CdS/ZnS QDs can be found in Section 3.2.1. Briefly, the CdSe core QDs were synthesized by hot injection of Se-TOP precursor solution into Cd solution in TDPA and TOPO. Then the *successive ion layer adsorption and reaction (SILAR)* method [20, 21] was applied for the respective coating of CdS and ZnS shells onto the CdSe core, resulting in a CdSe/CdS/ZnS core/shell/shell system.

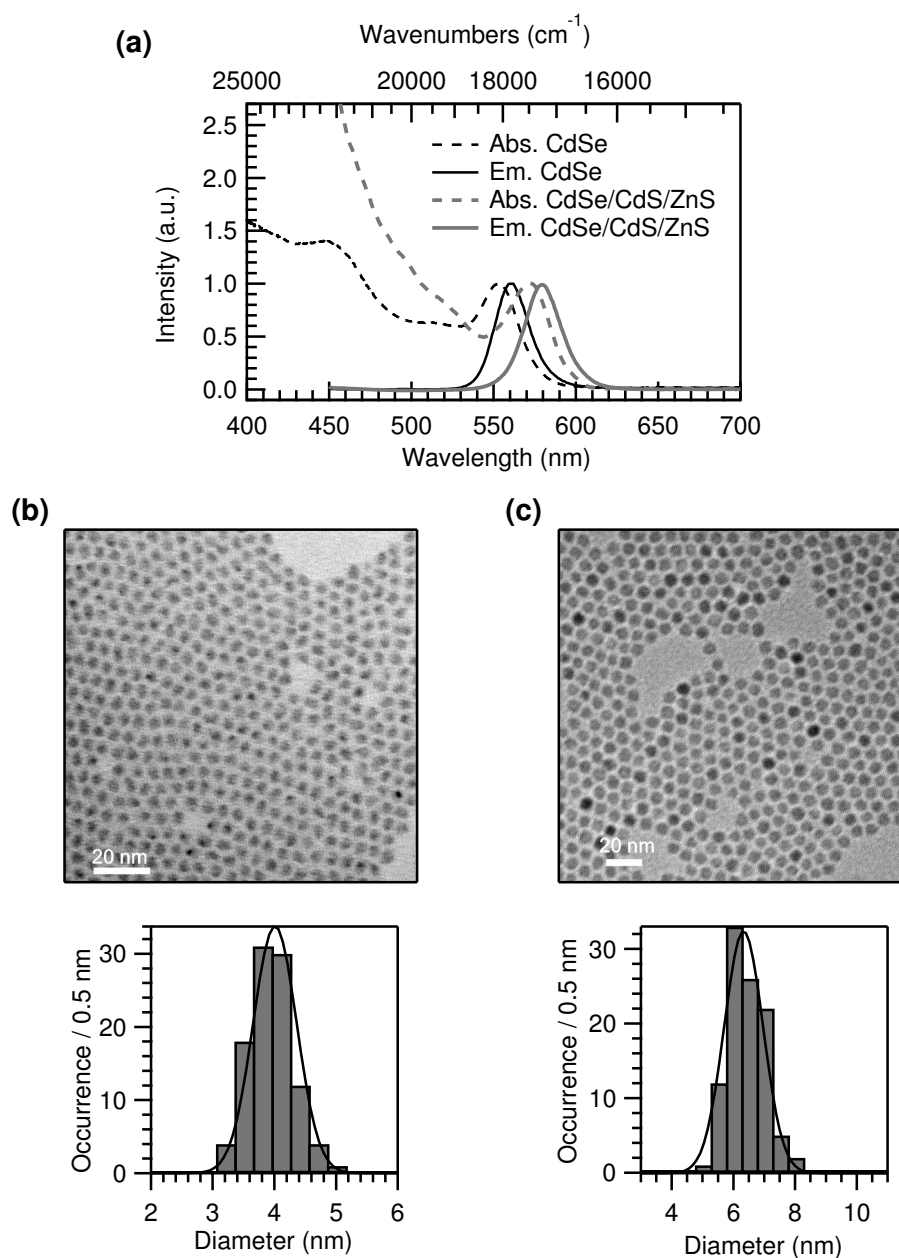


Figure 4.2: Characterizations of CdSe core QDs and CdSe/CdS/ZnS core-shell QDs: (a) The absorption (dashed lines) and emission spectra (solid lines) of CdSe cores (black curve) and CdSe/CdS/ZnS QDs (gray curve), respectively; TEM images and the corresponding size distributions of (b) CdSe core QDs (4.0 ± 0.3 nm) and (c) CdSe/CdS/ZnS core-shell QDs (6.3 ± 0.6 nm). The solid curves in the histograms are the corresponding Gaussian fits.

A representative example is shown in Figure 4.2: the CdSe core QDs with a diameter of 4.0 ± 0.3 nm were prepared at an injection temperature of 310°C , growth temperature of 290°C and with a growth time of 3 min. Subsequently, 4 monolayers (MLs) CdS and 1 ML

ZnS were overcoated. From Figure 4.2(a), it can be observed that after the epitaxial growth of the shell, both the absorption and fluorescence emission spectra exhibit explicit red shifts, with the first excitonic absorption peak shifting from 553 nm to 572 nm and the emission maximum from 562 nm to 579 nm, respectively. This suggests an extension of the exciton wavefunctions from the core into the shell [150, 151]. The FWHMs of the emission peaks of the core and core-shell particles are 24.7 nm and 26.6 nm, indicating narrow emissions. In addition, the quantum yield of the QDs is dramatically enhanced from 20% to 62% by the coating of the CdS/ZnS shell, which can be explained by the increasing confinement of the wavefunctions of the charge carriers away from the surface, thereby reducing the probability of non-radiative de-excitation processes from the surface-related trap states (e.g., surface dangling bonds and defects) [148–151].

The transmission electron microscopy (TEM) images and the size statistics are represented in Figure 4.2(b) and Figure 4.2(c), for the core sample and CdSe/CdS/ZnS QDs, respectively. The respective sizes are 4.0 ± 0.3 nm and 6.3 ± 0.6 nm, indicating narrow size distributions. In addition, the QDs become more spherical and more regular after shell-coating.

4.2.2 Assembly of CdSe/CdS/ZnS QDs

To prepare QD oligomers, a procedure based on the method developed by Xu et al. [47] was adopted. “A cycle of assembly process” is defined and depicted in Figure 4.3: Methanol as a bad solvent was added to a toluene solution containing CdSe/CdS/ZnS QDs. The aggregated QDs were precipitated by centrifugation and re-dispersed in cyclohexane. If most of the QDs in solution are still monomers, which can be checked by TEM analysis, an additional cycle of assembly was conducted. For details see Section 3.2.2.1.

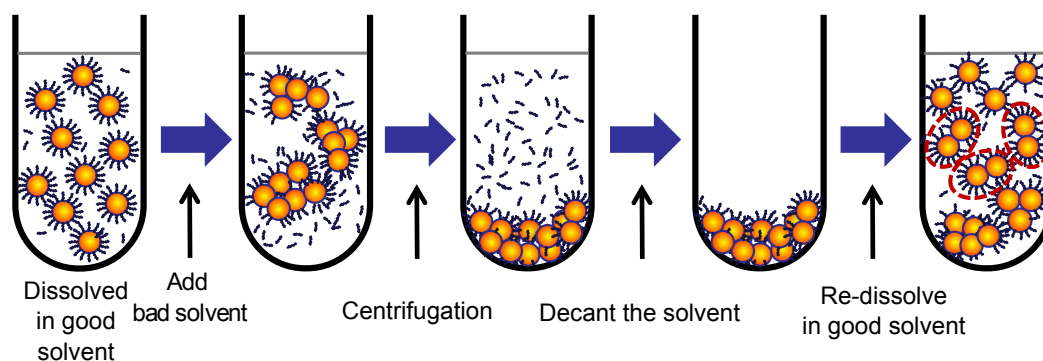


Figure 4.3: Schematic diagrams of a cycle of assembly procedure of QDs from monomer to oligomers. The red dashed ellipses in the last tube indicate QD dimers.

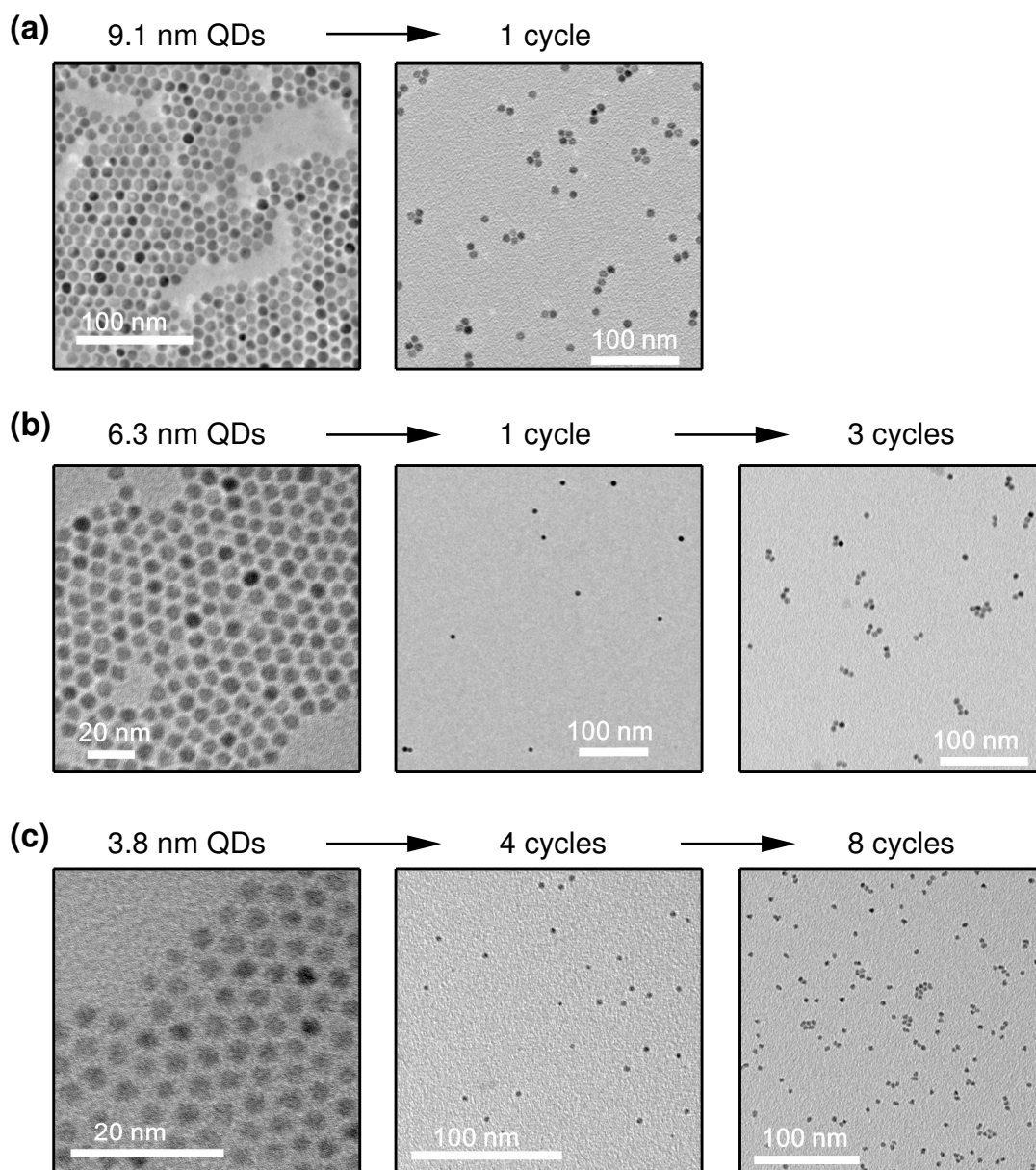


Figure 4.4: TEM images after different numbers of cycles of assembly process of CdSe/CdS/ZnS QDs with various sizes (diameters): (a) 9.1 ± 0.9 nm, (b) 6.3 ± 0.6 nm and (c) 3.8 ± 0.5 nm. The required number of cycles of the assembly to obtain an appropriate proportion of oligomers is strongly size dependent.

To characterize the assembly of QDs, TEM measurements were performed. Regarding the sample preparation for TEM, QD solutions with high concentrations (e.g., absorbance above 0.2) can self-assemble to result in ordered close packed QD arrays on the carbon film on the TEM grid evaporation of the solvent. This is an indication that the QDs are uniform in size and morphology, as shown in Figure 4.2(b) and (c). However, it has to

be pointed out that these self-assembled close packed arrays are not the desired stable oligomers formed in solution, because they are still fully covered with ligands and will disassemble when they are re-dissolved in a good solvent. Therefore, to avoid this self-assembly (induced by evaporation of the solvent on TEM grids), the samples have to be diluted to very low concentrations (absorbance below 0.05) for the TEM characterization of the oligomers. As a compromise, the number density of particles in TEM image has to be drastically reduced.

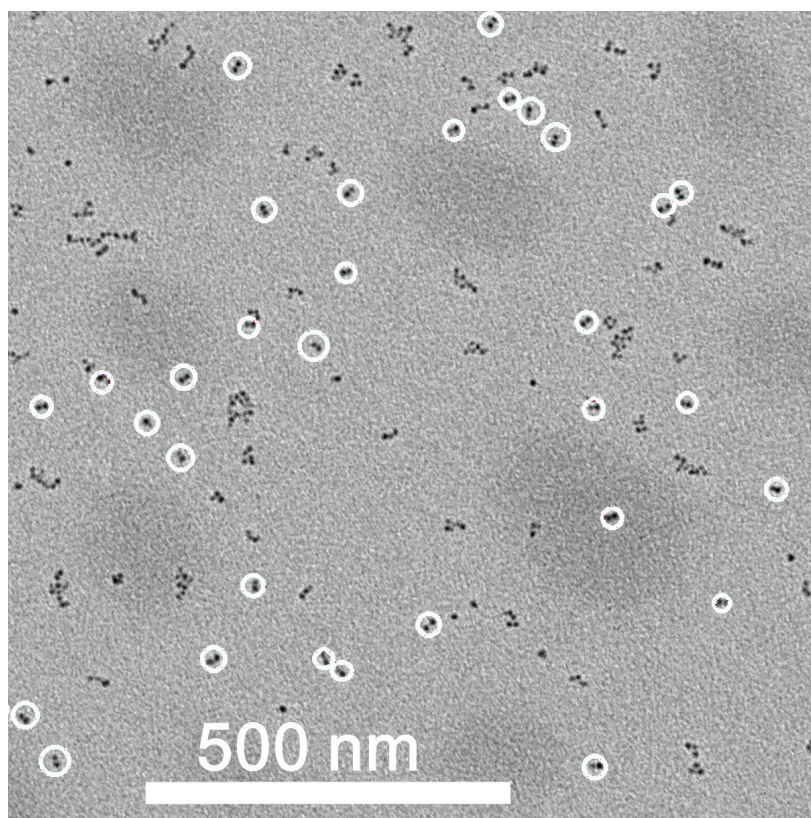


Figure 4.5: A large-area TEM image of oligomers assembled from CdSe/CdS/ZnS QDs with a diameter of 6.3 nm. The particles marked with white circles are QD dimers.

An interesting phenomenon is that the required cycles of assembly were found to be QD size dependent. To demonstrate this, three batches of CdSe/CdS/ZnS QDs with different sizes were compared. As revealed in Figure 4.4(a), for big QDs with a diameter of 9.1 nm, after one cycle of assembly, some oligomers were formed. In contrast, aggregation is more difficult for smaller QDs. For instance, after a cycle of assembly with the same procedure, the particles in the sample of 6.3 nm QDs (the same sample shown in Figure 4.2(c)) were mostly monomers (Figure 4.4(b), middle). To obtain an enlarged fraction of oligomers, two more cycles had to be performed (Figure 4.4(b), right). More

seriously, for the QDs as small as 3.8 nm, even 4 cycles were not sufficient to trigger efficient assembly, but oligomers appeared only after 8 cycles (Figure 4.4(c)). Several factors are speculated to be responsible for this experimental observations: 1) A linear dependence of dipole moment on size of QDs as was reported by Shim et al. [183]; 2) After the removal of excess ligands by purification, more surface ligands might be lost for larger QDs during the assembly process; 3) The effect of steric repulsion might be also size dependent.

As an example, a large-area TEM image of assembled oligomers from CdSe/CdS/ZnS QDs with a diameter of 6.3 nm is shown in Figure 4.5. Particles marked with white circles are dimers. Generally, the fraction of QD dimers obtained at this stage is about 20%–30% for all particle sizes.

4.2.3 Enrichment and separation of QD oligomers

To further enrich the required QD dimers, density gradient ultracentrifugation (DGU) was applied. As described in Section 3.2.2.2, a cyclohexane–CCl₄ solution system was

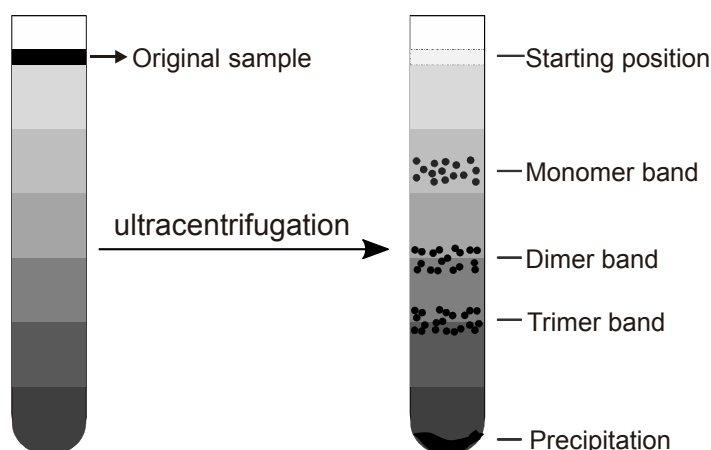


Figure 4.6: A schematic diagram of the principle of density gradient ultracentrifugation. The gray level represents the mass density (darker color corresponds to larger density).

used to build the density gradient. The volume fractions of CCl₄ are 90%, 80%, 70%, 60%, 50%, 40% from the bottom to top. As discussed in Section 2.2.2, since the density of the QDs is much larger than any available organic solvent, the isopycnic centrifugation is impossible to be conducted. According to the principle of rate-zonal centrifugation which was applied here and is schematically depicted in Figure 4.6, with a proper time of ultracentrifugation, distinct monomer, dimer and trimer bands in the tube can be obtained due to the size difference among them. According to Equation 2.28, the required time is strongly QD size dependent. Since Equation 2.28 is based on the force equilibrium

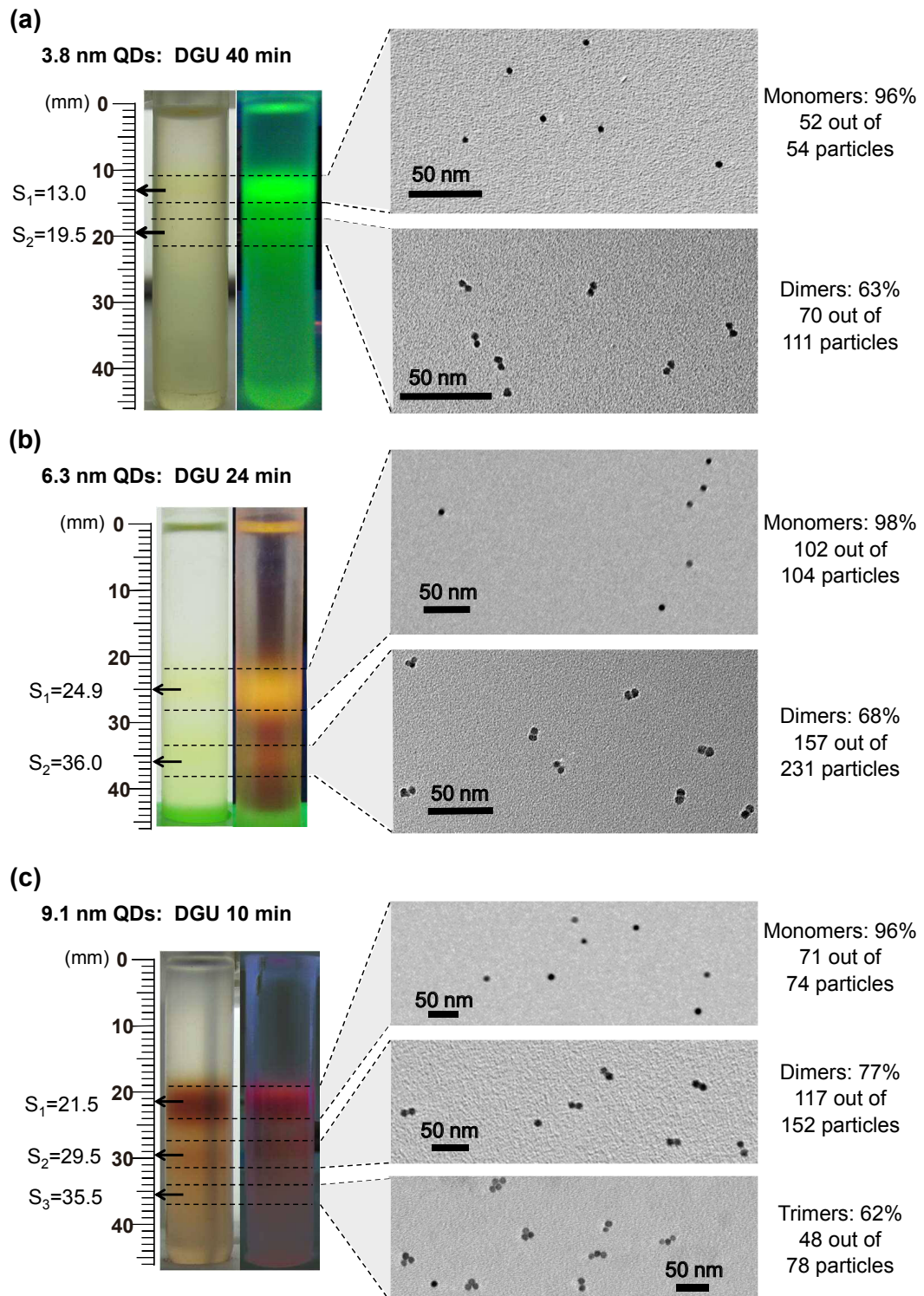


Figure 4.7: Photographs of centrifuge tubes after DGU containing solutions of the QDs with different sizes: (a) 3.8 nm, (b) 6.3 nm and (c) 9.1 nm. The left photographs were taken under room light while the right ones were taken under UV lamp. The right panels show typical TEM images of samples taken from the various bands and the corresponding fractions of the particles expected.

condition of small nanoparticles (the inertial effects are negligible [202]), if it is applied directly to the uniform linear motion, the sedimentation distance s should be calculated as $s = vt$, i.e.,

$$s = vt = \frac{K(\rho - \rho_l)d_{\text{eq}}^2}{18\eta}\omega^2 r t \quad (4.1)$$

with $K = 0.843 \cdot \log_{10} \frac{A_{\text{eq}}}{0.065 \cdot A}$

where v is the velocity of the particle, ρ and ρ_l are the densities of the particle and the liquid medium, respectively, ω is the angular speed, r is the distance from the rotation axis of the rotor to the location of the particle, η is the viscosity, and d_{eq} and A_{eq} represent the diameter and the surface area of the sphere which has the same volume as the particle, respectively. A is the surface area of the real particle and K , usually between 2 and 4, is a correction factor. Figure 4.7 shows three sets of photographs of the centrifuge tubes after DGU containing solutions of oligomers assembled from QDs with sizes of 3.8 nm, 6.3 nm and 9.1 nm, respectively. Indeed, the resulting solutions exhibited two or three distinct bands, separated by dark gaps. Subsequently, the fractions in the centrifuge tube were taken carefully by a pipette or an 1 mL syringe from top to bottom. In this thesis, the fractions taken from the monomer, dimer or trimer band are defined as “monomer sample”, “dimer sample” and “trimer sample”, respectively, and the QD monomers, dimers, trimers and higher oligomers are collectively termed “particles”. The right panels in Figure 4.7 present TEM images of samples taken from the various bands and the corresponding fractions of the particles expected. It can be concluded from the TEM images that almost all particles in the monomer samples are monomers, and the neighboring QDs within a dimer or a trimer are in closely contact, which is consistent with the directly coupled QD dimers reported in Ref. [47]. A large-area TEM image of the obtained 6.3 nm CdSe/CdS/ZnS QD dimer sample is shown in Figure 4.8. The fraction of the QD dimers in this sample is ~68% (157 out of 231 particles). In general, the fraction of QD dimers in a dimer sample depends on various factors, such as the initial fraction of dimers before DGU, the stability of the solution in the centrifuge tube (e.g., turbulence and diffusion due to mechanical vibration disturbance), the skills in extracting the fraction from the centrifuge tube after DGU and the volume of the solution extracted. The highest dimer fraction is 81% (356 out of 439 particles). Thus, the QD dimers are separated from as assembled oligomer mixture and therefore, enriched. Additionally, as revealed by the photographs in Figure 4.7, to arrive at similar positions in the centrifuge tube, the smaller QDs requires longer time of ultracentrifugation than the bigger QDs.

Even if only the position of the QD monomers is taken into account, the predicted sedimentation distance by Equation 4.1 reveals difference from the experimental

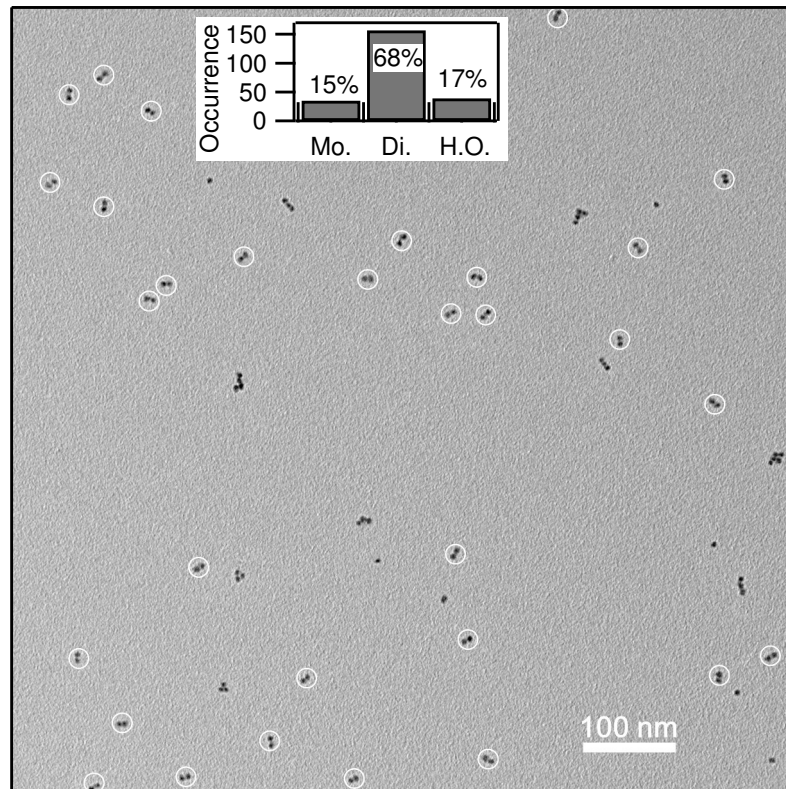


Figure 4.8: A large-area TEM image of the sample which is taken from the dimer band shown in Figure 4.7(b). The particles marked with white circles are QD dimers. The inset shows the particle distribution. Mo.: monomers; Di.: dimers; H.O.: trimers, tetramers and higher oligomers.

observations (see columns of “Calc. s_1^* ” and “Exp. s_1 ” in Table 4.1). This difference becomes very severe when comparing the positions of the dimer and trimer bands (see columns of “Calc. s_2^* ” and “Exp. s_2 ” for dimer bands, and “Calc. s_3^* ” and “Exp. s_3 ” for trimer bands in Table 4.1). The specific parameters were taken as follows:

- The mass density of the CdSe/CdS/ZnS QDs $\rho = 5 \times 10^3 \text{ kg/m}^3$, considering that the density of CdSe, CdS and ZnS (wurtzite structure) are $5.81 \times 10^3 \text{ kg/m}^3$, $4.82 \times 10^3 \text{ kg/m}^3$ and $3.98 \times 10^3 \text{ kg/m}^3$, respectively.
- The mass density of the liquid medium $\rho_1 = 1.338 \times 10^3 \text{ kg/m}^3$, which is the average density of the cyclohexane– CCl_4 gradient solvent system used.
- The viscosity $\eta = 1 \times 10^{-3} \text{ Pa}\cdot\text{s}$, since the viscosities of cyclohexane and CCl_4 are $1 \times 10^{-3} \text{ Pa}\cdot\text{s}$ and $0.97 \times 10^{-3} \text{ Pa}\cdot\text{s}$, respectively.

- As depicted in Figure 4.9(b), when the rotor is processing, the particles are moving in the centrifuge tube, therefore, as the first approximation, the average radius of the rotor $r_{av} = 91.7$ mm was taken as the rotation radius r in Equation 4.1.
- The angular velocity ω is calculated with the rotation speed of 50000 rpm.

Table 4.1: DGU experimental conditions and sedimentation distances of QD oligomers with different sizes. s_1 , s_2 and s_3 represent the sedimentation distances of the monomers, dimers and trimers, respectively. “Calc.” with star stands for calculation results based on Equation 4.1 while “Calc.” without star stands for the calculation results based on Equation 4.11. “Exp.” denotes the experimental observations. “Time” means the time of ultracentrifugation.

QD size (nm)	Time (min)	Calc. s_1^* (mm)	Calc. s_1 (mm)	Exp. s_1 (mm)	Calc. s_2^* (mm)	Calc. s_2 (mm)	Exp. s_2 (mm)	Calc. s_3^* (mm)	Calc. s_3 (mm)	Exp. s_3 (mm)
3.8	40	17.7	13.9	13.0	28.1	21.0	19.5	36.9	26.7	–
6.3	24	29.2	24.2	24.9	46.4	37.3	36.0	60.8	48.2	–
9.1	10	25.4	20.7	21.5	40.3	31.6	29.5	52.9	40.7	35.5

The significant disagreement between the calculations based on Equation 4.1 and experimental results can be explained by the over-simplifications with regard to the following two aspects:

(1) As mentioned above, the position of QDs in the tube changed during the DGU. As a result, the rotation radius r which was related to the centrifugal force should not be taken as a constant, but should vary between r_{min} and r_{max} as shown in Figure 4.9(b). Since at the beginning the sample was loaded at the top of the centrifuge tube, the r is directly related to the sedimentation distance s of the QDs, i.e., $s = r - r_{min}$.

(2) The density of the medium differs at different positions/depths. Therefore, the use of an average solvent density for the calculation may be inappropriate. Since the liquid layers with different densities could also diffuse with the proceeding of DGU, a quasi-continuous variation of the density along the tube can be assumed. From the geometry of the centrifuge tube and the amount of solvent for each layer, the density gradient was calculated to be $c_\rho = 10 \text{ kg} \cdot \text{m}^{-3} \cdot \text{mm}^{-1}$. Consequently, the density ρ_1 should be corrected to be $\rho_1(r) = \rho_0 + c_\rho(r - r_{min})$, where $\rho_0 = 1.16 \times 10^3 \text{ kg/m}^3$ is the smallest density of the solvent (40% CCl_4).

Based on the two considerations above, an improvement of Equation 4.1 was developed as follows:

$$v = \frac{K [\rho - \rho_1(r)] d_{eq}^2}{18\eta} \omega^2 r \quad (4.2)$$

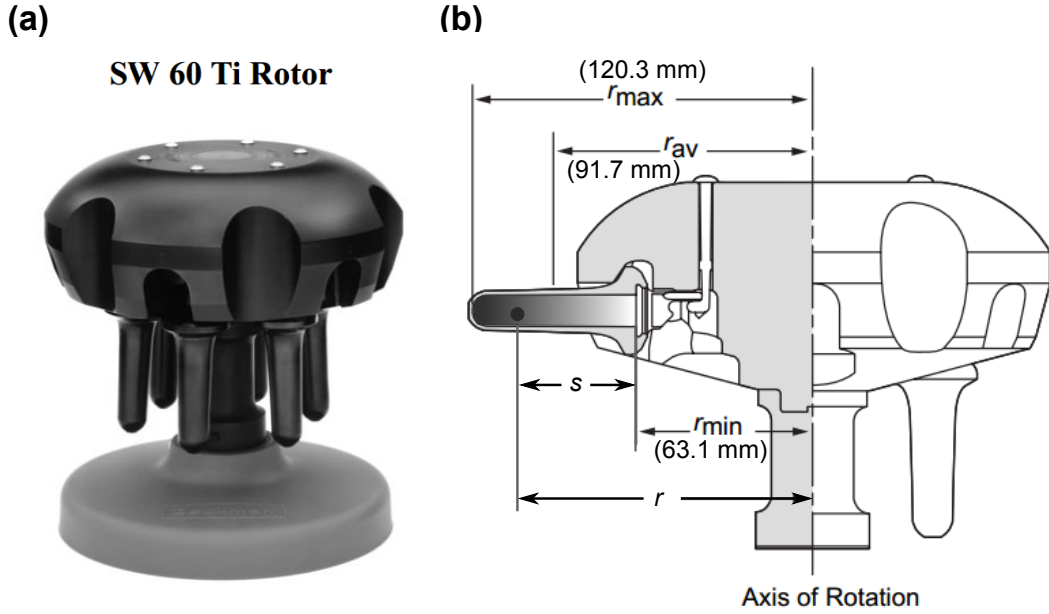


Figure 4.9: (a) A photograph and (b) profile chart of *Beckman* SW-60 Ti rotor (swing), adapted from the manual of the device. The black dot in the centrifuge tube schematically denotes the position of a QD. The color gradient in the centrifuge tube stands for the density gradient of the solvent (darker color corresponds to larger density).

where $\rho_1(r) = \rho_0 + c_\rho(r - r_{\min})$. For simplicity, we define

$$\alpha \equiv \frac{K\omega^2 d_{\text{eq}}^2}{18\eta} \quad (4.3)$$

Therefore, Equation 4.2 can be re-written as:

$$v = \alpha(\rho - \rho_0 - c_\rho r + c_\rho r_{\min}) \cdot r = \alpha(\rho - \rho_0 + c_\rho r_{\min}) \cdot r - \alpha c_\rho r^2 \quad (4.4)$$

Then, further defining

$$p \equiv \alpha(\rho - \rho_0 + c_\rho r_{\min}) \quad \text{and} \quad q \equiv -\alpha c_\rho \quad (4.5)$$

we have

$$v = \frac{dr}{dt} = p \cdot r + q \cdot r^2 \quad (4.6)$$

i.e.,

$$dt = \frac{1}{pr + qr^2} dr \quad (4.7)$$

Using

$$\int \frac{1}{ax + bx^2} dx = -\frac{1}{a} \ln \left| \frac{a + bx}{x} \right| + C$$

the integration of Equation 4.7 yields:

$$t = \int dt = -\frac{1}{p} \ln \left| \frac{p + qr}{r} \right| + C \quad (4.8)$$

Therefore,

$$r = \frac{p}{e^{-p(t-C)} - q} \quad (4.9)$$

where C is the integration constant, which can be determined by the initial conditions.

$$r(t=0) = r_{\min} = \frac{p}{e^{cp} - q}$$

Thus,

$$C = \frac{1}{p} \ln \left(\frac{p}{r_{\min}} + q \right) \quad (4.10)$$

Eventually, the expected sedimentation distance is:

$$s = r - r_{\min} = \frac{p}{e^{-p(t-C)} - q} - r_{\min}$$

where

$$\begin{aligned} p &= \frac{K\omega^2 d_{\text{eq}}^2}{18\eta} (\rho - \rho_0 + c_\rho r_{\min}) \\ q &= -\frac{K\omega^2 d_{\text{eq}}^2}{18\eta} c_\rho \\ K &= 0.843 \cdot \log_{10} \frac{A_{\text{eq}}}{0.065 \cdot A} \\ C &= \frac{1}{p} \ln \left(\frac{p}{r_{\min}} + q \right) \end{aligned} \quad (4.11)$$

Concerning the situation of a QD dimer or trimer, as introduced above, the equivalent diameter d_{eq} and equivalent area A_{eq} , which correspond to the sphere with the same volume as the oligomers, were calculated and substituted into Equation 4.11. The obtained sedimentation distances of the particles are denoted as s_1 , s_2 , s_3 for monomers, dimers and trimers, respectively.

Table 4.1 lists the calculated and experimental sedimentation distances of QDs with various sizes and DGU times, experimental results of which are shown in Figure 4.7. In contrast to the values calculated based on Equation 4.1 (Calc. s_1^* and Calc. s_2^*), the

predicted sedimentation distances by Equation 4.11 for both monomers (Calc. s_1) and dimers (Calc. s_2) are well consistent with the experimental observations (Exp. s_2), although the equivalence of a dimer to a sphere which has the same volume is a very rough approximation. As shown in Figure 4.7(c), a trimer band can also be seen for 9.1 nm QDs. However, the prediction of this trimer position Calc. s_3 exhibits relatively big difference from the reality (although better than Calc. s_3^*). This might be attributed to the imperfect “equivalent sphere” approximation for trimers, considering that they possess more kinds of geometrical configurations.

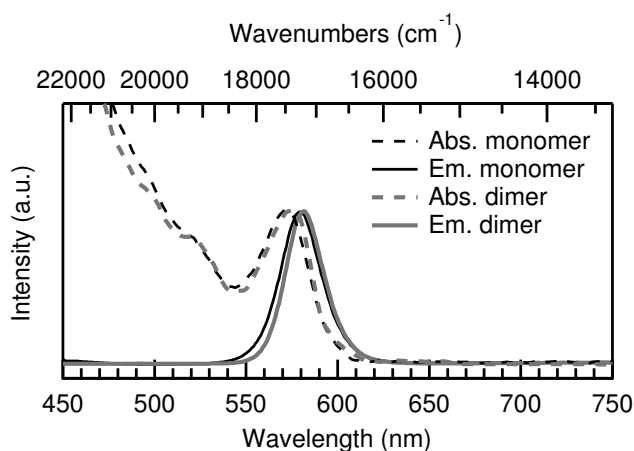


Figure 4.10: Absorption (dashed lines) and emission (solid lines) spectra of the monomer sample (black curves) and the dimer sample (gray curves) which are taken from the monomer band and the dimer band shown in Figure 4.7(b), respectively.

Ensemble absorption and emission spectra of 6.3 nm monomer and dimer samples are shown in Figure 4.10(c). Compared to the monomer sample spectra, the absorption spectrum of QD dimer sample exhibits a small red-shift of the first excitonic peak (from 572 nm to 575 nm), and the fluorescence peak in the emission spectrum also slightly shifts to the lower energy direction (from 579 nm to 583 nm), which implies that possible electronic coupling within homo-dimers in the dimer solution exists. Both the emission peak FWHM of the monomer and the dimer samples are quite narrow, i.e., 26.6 nm and 24.6 nm, respectively. However, the quantum yield drops from 61.9% to 36.5% after dimerization, which might be due to ligand loss during the assembly process.

4.2.4 Fluorescence imaging of single QDs

Single particle measurements of as-prepared 6.3 nm CdSe/CdS/ZnS QDs at room temperature (295 K) and cryogenic temperature (4.5 K) were both performed with the

setup described in Section 3.4.3. Both samples were embedded in PMMA films. The scanning speed for recording fluorescence images was 10 ms per pixel. The time resolution (time bin) for fluorescence time traces was 100 ms. Regarding the emission spectra, every QD was measured for 25 s with the shortest spectral integration time of 5 s. The excitation intensity was about 1 kW/cm^2 (1045 W/cm^2).

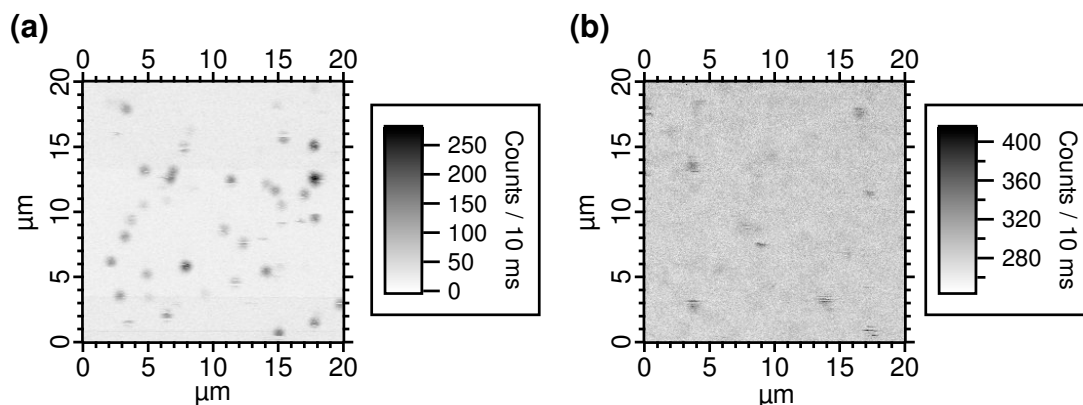


Figure 4.11: Confocal fluorescence microscopic images of 6.3 nm CdSe/CdS/ZnS QDs in a PMMA film at (a) 295 K (b) 4.5 K, excited by a 488 nm laser with an excitation intensity of 1 kW/cm^2 at both temperatures.

Table 4.2: Comparison of the results from the fluorescence microscopic images at 295 K and 4.5 K. The QD density here is defined by the number of QDs per image which show single in spectrum.

Temperature	background counts	signal amplitude	SNR	QD density (#/image)
295 K	30	170	6.8	27
4.5 K	280	50	2.4	14
Ratio (4.5 K/295 K)	9.3	0.29	0.35	0.52

In general, as an example shown in Figure 4.11, for both monomer and dimer samples, the fluorescence images measured by the same setup at room temperature and cryogenic temperature exhibited large differences, including an increase of the background counts and decreasing signal amplitude, signal to noise ratio (SNR) and QD density from 295 K to 4.5 K. These changes can be quantitatively characterized by a series of ratios of values at 4.5 K and 295 K, as listed in Table 4.2. These ratios are qualitatively consistent with results from Ref. [219], where the reason was speculated to be related to a loss of QD ligands during the evacuation process of sample preparation, since different evacuation times and ligands led to different results [219].

4.2.5 Single particle spectroscopy of QD monomer and dimer samples at room temperature ($T = 295$ K)

4.2.5.1 Typical emission spectra

Figure 4.12 shows typical emission spectra of individual particles in QD monomer and dimer samples at 295 K, respectively. In this case the emission peak of the particle in dimer sample is slightly broader than that of the particle in monomer sample. Even if the particle whose emission spectrum is shown in Figure 4.12(b) is a QD dimer, it is not possible to spectrally resolve the two QD components within it.

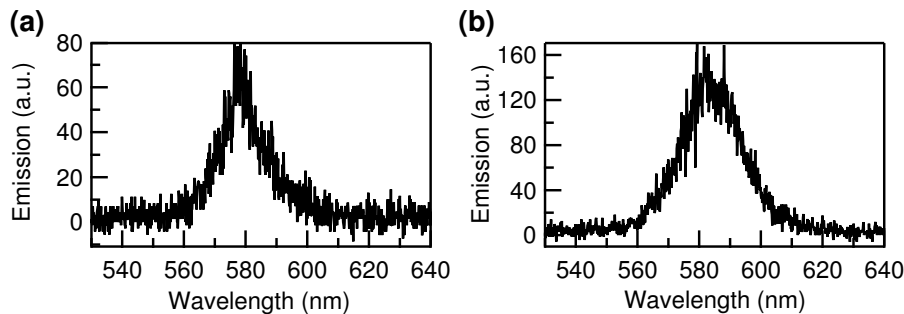


Figure 4.12: Typical emission spectra of a single particle (in a PMMA film) from (a) monomer sample and (b) dimer sample at 295 K, excited by a 488 nm laser with an excitation intensity of 1 kW/cm^2 . The integration time is 5 s.

4.2.5.2 Statistics of the emission spectra at 295 K

As a more quantitative study, spectral positions and FWHMs of the emission peaks of the particles in monomer and dimer samples at room temperature were collected and analyzed statistically. As presented in Figure 4.13(a) and Figure 4.13(b), the distributions of the spectral positions of emission maxima follow Gaussian functions, with resulting average values of 17288 cm^{-1} (i.e., 578 nm) and 17130 cm^{-1} (i.e., 584 nm) for monomers and dimers under the excitation intensity of 1 kW/cm^2 , respectively. These values give good agreement with the ensemble emission wavelengths, which are 579 nm and 583 nm for monomers and dimers, respectively. The FWHM of the emission peaks of monomers and dimers are similar at room temperature, both around 600 cm^{-1} (~ 20 – 21 nm), further revealing that it is not possible to spectrally discriminate two neighboring QDs in a homo QD dimer at room temperature. Therefore, cryogenic temperature measurement is indispensable.

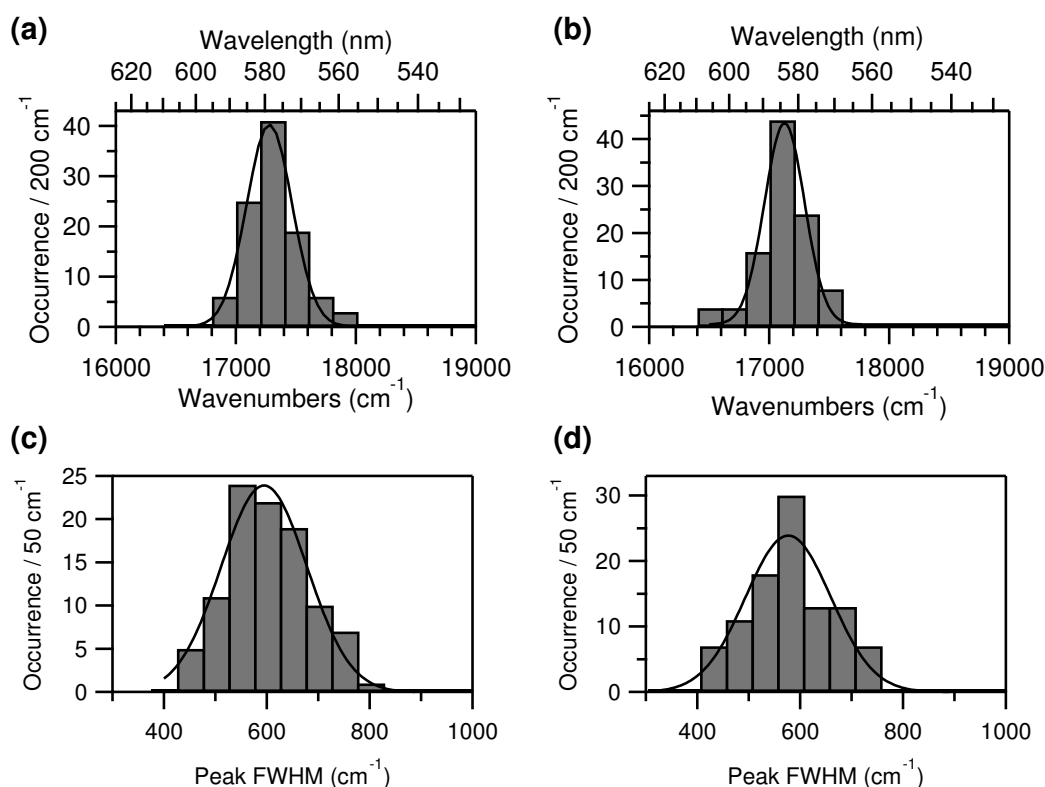


Figure 4.13: Distributions of spectral positions of peak maxima in emission spectra of single particles (in a PMMA film) from (a) monomer sample and (b) dimer sample at 295 K. Lower panels are the corresponding FWHM distributions of single particles in (c) the monomer sample and (d) the dimer sample at 295 K, respectively. The solid curves in the histograms are the corresponding Gaussian fits.

4.2.6 Single particle spectroscopy of CdSe/CdS/ZnS QD monomers at cryogenic temperature ($T = 4.5$ K)

4.2.6.1 Typical emission spectra

Single particle spectroscopy of QD monomers at 4.5 K was performed. As expected, the FWHM of the emission of a single QD was extremely narrowed and a sharp ZPL accompanied by phonon sidebands (PSBs) appeared when the temperature was reduced to the cryogenic temperature. Figure 4.14 shows a typical emission spectrum of a single bright CdSe/CdS/ZnS QD at 4.5 K which was excited with excitation intensity of 1 kW/cm^2 . In conjunction with the zero-phonon line (ZPL), the transitions of the replicas of acoustic phonons, longitudinal optical (LO) phonons of CdSe (210 cm^{-1}) and CdS (302 cm^{-1}), and even second harmonic of the LO-phonon of CdSe (423 cm^{-1}) can be observed in the spectra. The results of the LO phonons are in good agreement with the literature (LO_{CdSe}

= 206 cm^{-1} [253], $\text{LO}_{\text{CdS}} = 305 \text{ cm}^{-1}$ [296]). For QDs of inferior quality, the 2LO_{CdSe} is invisible. However, almost all the principal peaks and CdSe LO PSBs exhibit obvious asymmetry, suggesting the presence of an electron-phonon coupling to acoustic modes and the participation of the electron-LO-phonon coupling of CdS, respectively. In contrast, the peaks corresponding to the LO-phonon replicas in the spectra of single CdSe/ZnS QDs are symmetrical due to the absence of CdS, as described in Ref. [219].

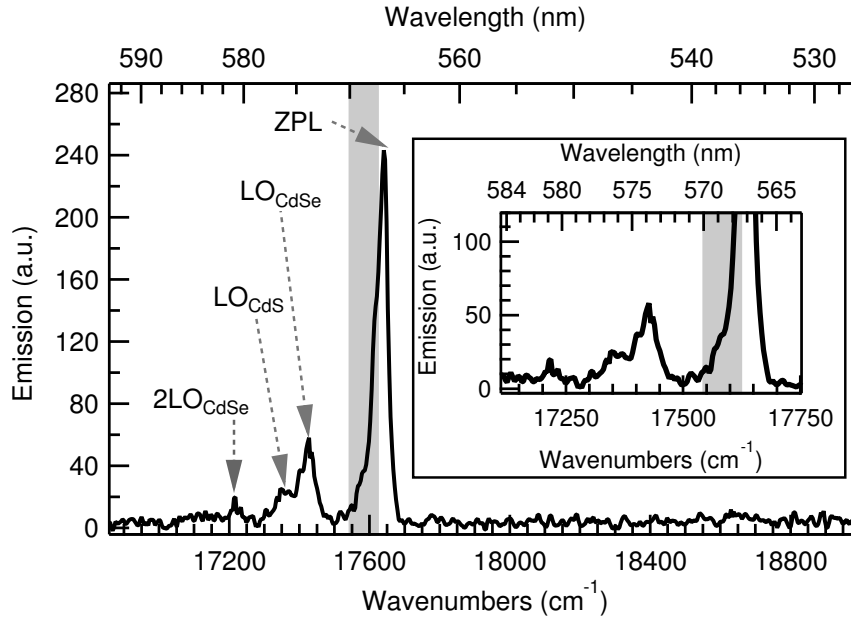


Figure 4.14: A typical emission spectrum of a single bright CdSe/CdS/ZnS QD in a PMMA film at 4.5 K with excitation intensity of 1 kW/cm^2 . The emission energy range which approximately corresponds to transitions of acoustic phonon replicas are highlighted with gray background. LO_{CdSe} , LO_{CdS} and 2LO_{CdSe} denote the LO phonon replicas of CdSe, CdS and second harmonic of the LO-phonon of CdSe, respectively. The inset shows an enlarged view. The integration time is 5 s.

4.2.6.2 Statistics of the LO phonon replica

As it is one of the most important features of a single QD spectrum at low temperature, the LO phonon energy of CdSe was further studied. The peak-to-peak distance between the ZPL and CdSe LO replica was measured and analyzed, since this distance is supposed to be the energy of CdSe LO phonons [253]. Figure 4.16(a) reveals the statistical correlation of the CdSe LO phonon energy to the ZPL spectral position. It can be seen that most of the values concentrate in the region between 200 cm^{-1} and 220 cm^{-1} . The average value was calculated to be 207 cm^{-1} . Noting that for a single CdSe QD with a diameter of 4.5 nm without passivation shell, the LO_{CdSe} phonon energy has been reported to be 25.6 meV

(206 cm^{-1}) [253] and the size of the CdSe core used here in the core-shell QD (4.0 nm), it exhibits very good agreement. From the left panel in Figure 4.16(a), it can be concluded that the LO phonon energy is insensitive to spectral position of the emission peak of the single QDs.

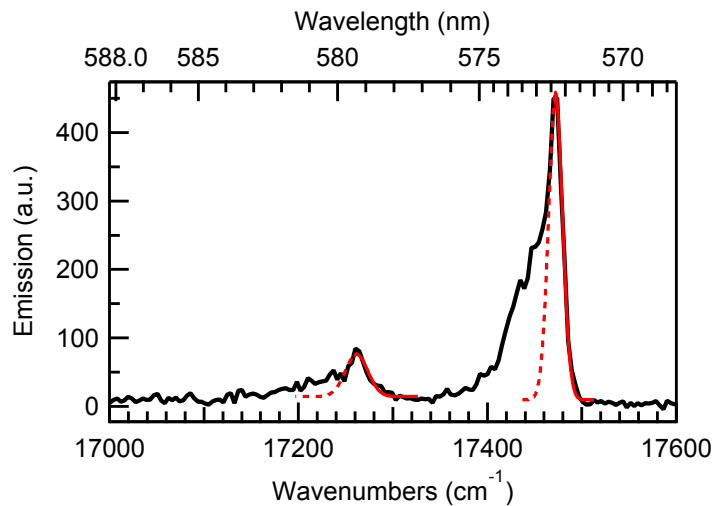


Figure 4.15: Gaussian fits (red lines) of the ZPL and the CdSe LO replica of an emission spectrum (solid black line) belonging to a single CdSe/CdS/ZnS QD in a PMMA film at 4.5 K with excitation intensity of 1 kW/cm^2 . The integration time is 5 s. The Gaussian fits are done based on the high-energy side of the corresponding peaks (the energy range corresponding to the solid red lines).

As introduced in Section 2.3.5.1, the Huang-Rhys factor describes the strength of the linear electron-phonon coupling and can be obtained directly from the intensity ratio of the one-phonon- and zero-phonon-transitions in the emission spectrum at cryogenic temperatures [271]. In order to extract the ZPL and the CdSe LO replica from the principal peak and PSB respectively, Gaussian fits based on the high-energy side of the corresponding peaks were conducted (Figure 4.15). Then the integrated intensities of these Gaussian fits were considered as the integrated intensities of the ZPL and the CdSe LO replica. Results are shown in Figure 4.16(b). The S_{LO} (CdSe) varies from 0.20 to 0.82 with an average value of 0.40, which exhibits no obvious dependence on spectral position of the emission (or particle size). The values are generally consistent with literature values of Empedocles et al. ($S_{\text{LO}} = 0.06\text{--}1.3$ with an average value of 0.49 for single CdSe and CdSe/ZnS QDs [253]) and Norris et al. ($S_{\text{LO}} = 0.36$ and 0.45 for sub-ensemble CdSe QDs with diameters of 4.2 nm and 3.8 nm, respectively [297]). In addition, both CdSe LO phonon energy and S_{LO} of CdSe reveal a lack of excitation intensity dependence, which is consistent with the observations in Ref. [219].

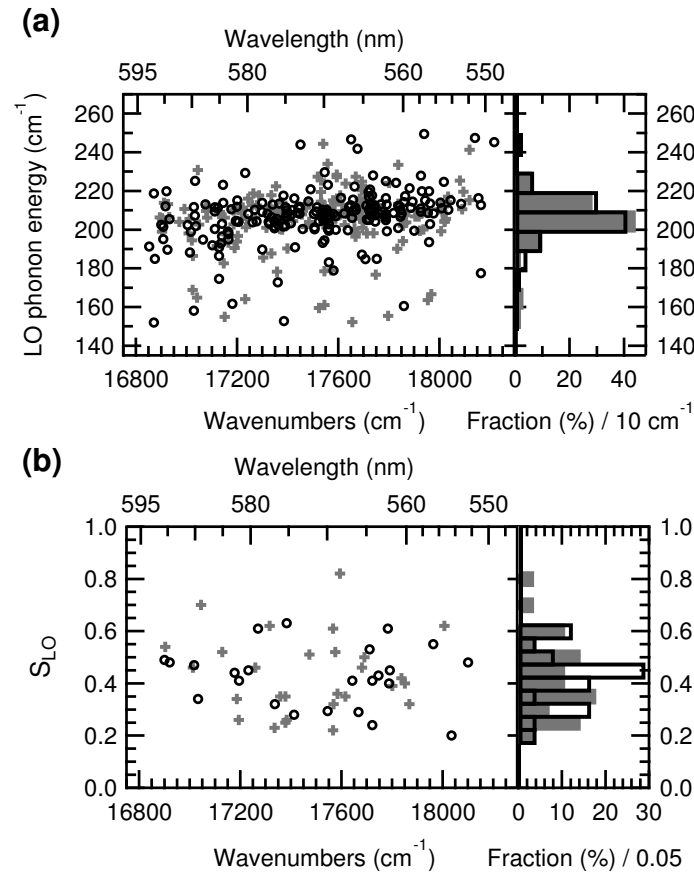


Figure 4.16: Statistical correlations of (a) CdSe LO phonon energy (peak-to-peak distance between ZPL and PSB of CdSe LO, 405 spectra) and (b) The Huang-Rhys factor of CdSe LO phonon (from 52 QDs) to the ZPL spectral positions. The gray cross (+) and black circle (o) stand for the results of QDs excited with 1 kW/cm² and 3 kW/cm², respectively. The bars filled with gray color and the ones with black frame without filling are the respective statistics.

4.2.6.3 Statistics of the band edge emission peak at 4.5 K

The spectral positions of the ZPLs, i.e., the maximum of the band edge transitions were statistically analyzed. As introduced in Section 2.3.5.2, when the temperature is decreased to cryogenic temperatures, an explicit spectral blue-shift is expected. Experimentally, as seen in Figure 4.17(a), the average wavenumber of the band edge transition is 17518 cm⁻¹. Compared with the ensemble emission wavelength at 295 K which is 579 nm (17271 cm⁻¹) and the maximum of the distribution of the single particle emission spectra which is 578 nm (17288 cm⁻¹), the energy increased by 247 cm⁻¹ and 230 cm⁻¹, respectively. As a commonly used formula (see Section 2.3.5.2), the empirical Varshni equation $E_g(T) = E_g(0) - \alpha T^2 / (T + \beta)$ predicts an increase of the band edge transition of 825 cm⁻¹ from 295 K to 4.5 K, when the coefficients of bulk CdSe semiconductor $\alpha = 1.7 \cdot 10^{-3}$ eV/K and

$\beta = 1150$ K are used [298]. This is much larger than the experimental values 247 cm^{-1} and 230 cm^{-1} found here. Nevertheless, when applying the equation of O'Donnell and Chen $E_g(T) = E_g(0) - \frac{2S\langle\hbar\omega\rangle}{e^{\langle\hbar\omega\rangle/k_B T} - 1}$ (details see Section 2.3.5.2) which is an alternative without empirical variables [279], the calculated blue-shift energy differs significantly. The Huang-Rhys factor S and the average phonon energy $\langle\hbar\omega\rangle$ are involved in this formula. In case of our CdSe/CdS/ZnS QDs, as a first approximation, when only the LO phonon of CdSe is taken into account, meaning $S = 0.40$ and $\langle\hbar\omega\rangle = 207\text{ cm}^{-1}$ based on the results in Section 4.2.6.2, a blue-shift of 95 cm^{-1} should be expected. Obviously, the experimental results are smaller than the value based on the Varshni equation but larger than the value from the equation of O'Donnell and Chen. This could be due to the complexity in composition of the core-shell system and a model in which more details are taken into account might be needed.

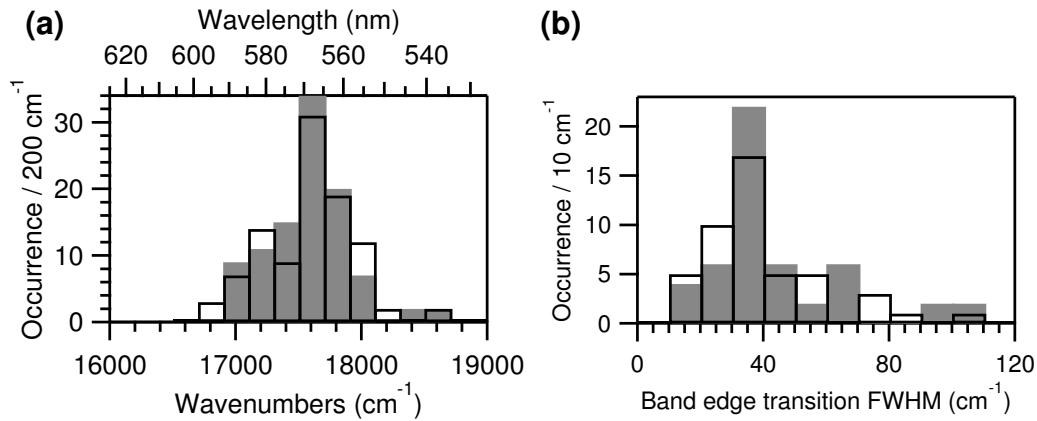


Figure 4.17: Distributions of (a) spectral positions and (b) FWHMs of the band edge transition peaks in emission spectra of single QDs in a PMMA film at 4.5 K. The bars filled with gray color and the ones with black frame without filling are the statistics of QDs under the excitation of 1 kW/cm^2 and 3 kW/cm^2 , respectively.

The FWHMs of the band edge transitions were also studied. As revealed in Figure 4.17(b), the width of the principal peak is distributed in a range of $10\text{--}110\text{ cm}^{-1}$ and concentrates on $30\text{ cm}^{-1}\text{--}40\text{ cm}^{-1}$. The emission ZPL of a single CdSe/CdS/ZnS QD has been observed by Chilla et al. to be as narrow as $220\text{ }\mu\text{eV}$ (1.77 cm^{-1}) corresponding to the resolution limit [299]. Since the spectral resolution in the measurements here was about 15 cm^{-1} , most of the limited widths observed here definitely do not reflect the natural broadening of the zero-phonon transition state and fast spectral diffusion might be involved. However, the width of the peak provides a feature of the QD monomers, which could be useful for the comparison with the QD dimer sample (see Section 4.2.7).

4.2.6.4 Statistics of the spectral diffusion

Spectral diffusion of CdSe/CdS/ZnS QDs was investigated at 4.5 K. As shown in Figure 4.18(a), for every QD, 5 spectra were consecutively measured with the integration time of 5 seconds for each spectrum. Then the largest peak-to-peak spectral position shift of the band

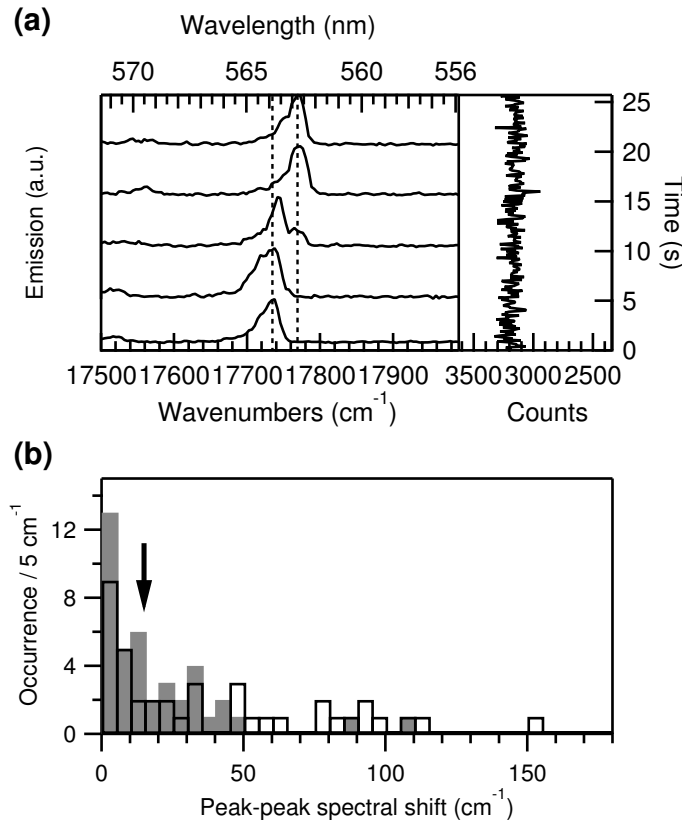


Figure 4.18: (a) Five consecutive emission spectra (left panel) and the corresponding fluorescence time trace (right panel, time bin: 100 ms) of a single QD in a PMMA film at 4.5 K. The dashed lines represent the minimum and maximum energy edge to define the magnitude of spectral diffusion, i.e., maximum peak-to-peak shift in a series, which is about 35 cm^{-1} in this specific case. (b) Spectral diffusion distributions of the QDs in a PMMA film at 4.5 K. The integration time is 5 s for each spectrum. The bars filled with gray color and the ones with black frame without filling stand for the results under the excitation of 1 kW/cm^2 and 3 kW/cm^2 , respectively. The vertical arrow denotes the experimental spectral resolution (15 cm^{-1}).

edge transition within the series of every QD was recorded and used to characterize the magnitude of spectral diffusion (in the situation of Figure 4.18(a) the value is $\sim 35 \text{ cm}^{-1}$). Figure 4.18(b) illustrates the distribution of the spectral diffusion under this definition. One can see that the spectral shifts of most of the QDs are smaller than 50 cm^{-1} , especially for the cases when an excitation intensity of 1 kW/cm^2 was applied. It is interesting that the

excitation power exhibits an influence on the behavior of spectral diffusion. With larger excitation intensity (3 kW/cm^2), a slightly bigger extent of spectral diffusion (spectral position of peak maximum jumps within a bigger energy range) was observed. The excitation power dependence is consistent with the experimental results by Empedocles et al. [253, 254].

4.2.7 Single particle spectroscopy of QD dimer sample at cryogenic temperature ($T = 4.5 \text{ K}$)

4.2.7.1 Spectral categories of particles in the dimer sample

The as-prepared CdSe/CdS/ZnS QD homo-dimer sample (containing 68% QD dimers) spectra of which are shown in Figure 4.10 was used to make a sample for single particle statistics at 4.5 K. In this experiment, different kinds of spectral series were observed, which were categorized into four types, denoted by *M*, *D*, *H* and *MD*, respectively. Although it is not possible to exclude the presence of particles which may not emit during the measurement, spectral series of different categories probably correspond to different kinds of particles (monomer, dimer, trimer, or higher oligomers), as explained as follows:

- (1) Type *M* (Figure 4.19(a)) is a series in which each spectrum shows only one principal band edge emission peak whose FWHM is smaller than 50 cm^{-1} , and the spectral diffusion is also smaller than 50 cm^{-1} . This feature indicates a high probability that the corresponding QD is a single QD monomer.
- (2) Type *D* is a spectral series which exhibits two sharp principal peaks with a relatively large spectral position difference (larger than 100 cm^{-1}), either within one spectrum or in two spectra of the same series. Two examples are shown in Figure 4.19(b) and Figure 4.19(c): the separations of the two peaks emitting at different wavelengths in these two cases are $\sim 198 \text{ cm}^{-1}$ and $\sim 260 \text{ cm}^{-1}$, respectively. Considering that two distinct peaks (difference larger than 100 cm^{-1}) and spectral diffusion (larger than 100 cm^{-1}) have very rarely been observed on the experimental time scale in the QD monomer sample (see Section 4.2.6.4), the possibility of a monomer can be largely excluded for the QDs of type *D*. Thus, particles of this type are most likely to be QD dimers.
- (3) In very few cases, multiple peaks could be observed in the spectral series, as revealed in Figure 4.19(d). These series are labeled as type *H*. This may imply that the corresponding QD oligomers are higher oligomers (trimers, tetramers or even aggregates consisting of more QDs).

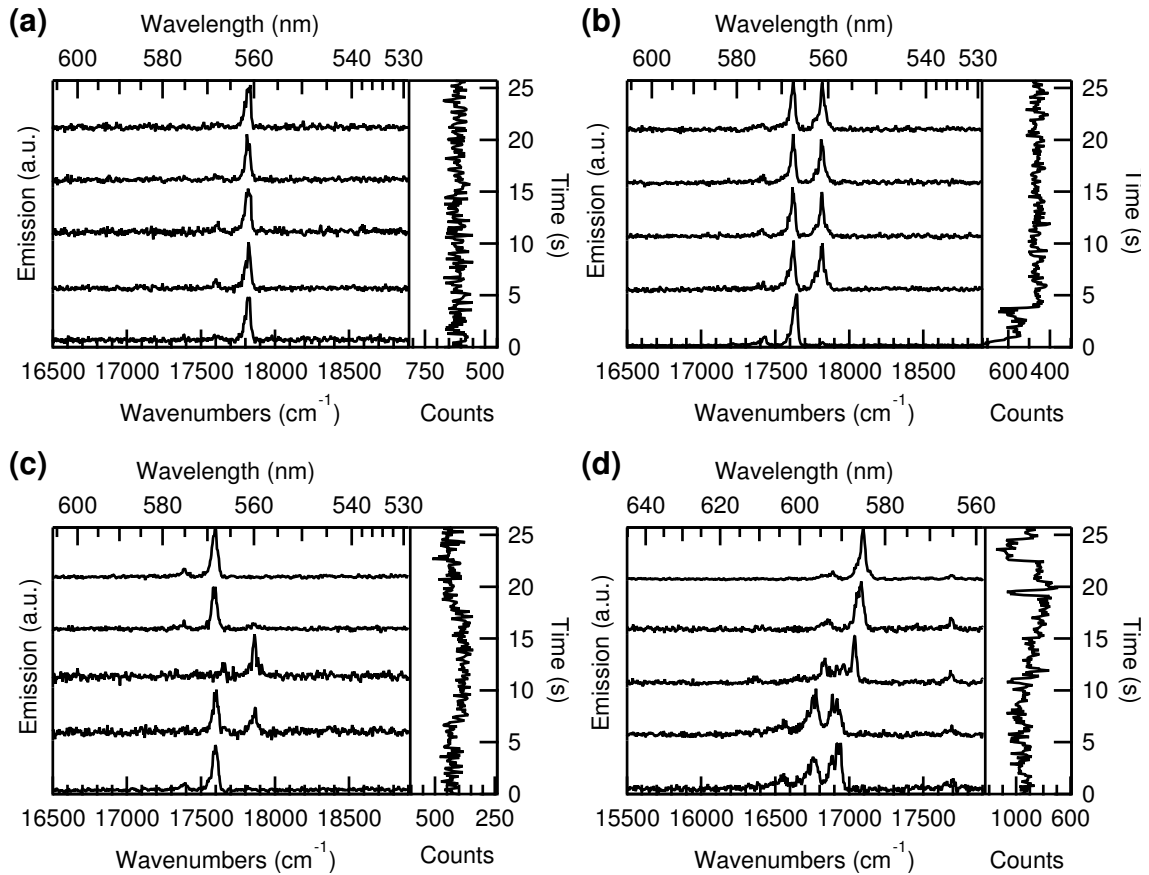


Figure 4.19: Representative spectral series (left panels) and the corresponding fluorescence time traces (right panels, time bin: 100 ms) of the particles (in a PMMA film) taken from the dimer sample and measured at 4.5 K: (a) *M* type; (b) *D* type with small peak separation ($\sim 198 \text{ cm}^{-1}$); (c) *D* type with big peak separation ($\sim 260 \text{ cm}^{-1}$); (d) *H* type. The integration time of each spectrum is 5 s.

(4) Moreover, there are spectral series which are difficult to be categorized into any of the three types mentioned above. These series are labeled as *MD*. For this type, it is difficult to distinguish between monomers and dimers:

- CASE 1: As shown in Figure 4.20(a), the signal to noise ratio is too low for the extraction of spectral positions of the possible emission peaks.
- CASE 2: There are no adequate spectra in a series due to the short survival time of the particle against photo-bleaching. Figure 4.20(b) shows an example. The emissions of the first and second spectra are close to each other in wavelength and no additional spectra are available for analysis due to the photo-bleaching.
- CASE 3: As revealed in Figure 4.20(c), two emission peaks can be resolved in the spectra. However, the spectral position separation is $\sim 62 \text{ cm}^{-1}$. This value is at

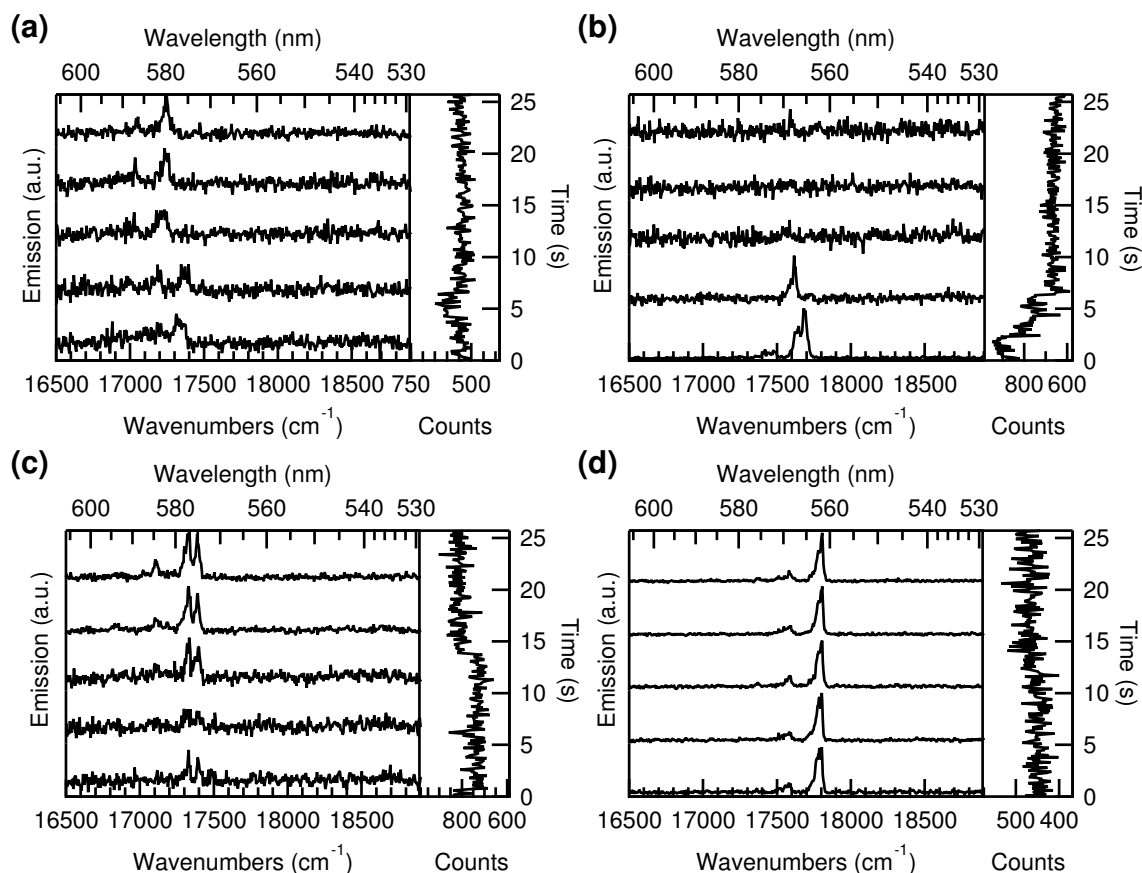


Figure 4.20: Representative spectral series (left panels) and the corresponding fluorescence time traces (right panels, time bin: 100 ms) of particles (in a PMMA film) belonging to type *MD* taken from the dimer sample and measured at 4.5 K: (a) Low signal to noise ratio. (b) Short survival time against photo-bleaching. (c) Two close peaks ($\sim 62 \text{ cm}^{-1}$). (d) Broadened peak ($\sim 57 \text{ cm}^{-1}$). The integration time of each spectrum is 5 s.

the border of the criterion for monomer and dimer discrimination ($\sim 50 \text{ cm}^{-1}$ as discussed above). Considering the statistics of the linewidth (Figure 4.17(b)) and spectral diffusion on the time scale of the measurement (Figure 4.18) of the QD monomer sample at 4.5 K, the probability of spectral diffusion induced dual emissions from a monomer in this case is low. To be on the safe side, this kind of spectral series was categorized into type *MD*, not type *M*.

- **CASE 4:** Although only one single principal peak in each spectrum of the series was found, the FWHM of the emission peaks are larger than the value corresponding to the monomer sample. An example is shown in Figure 4.20(d), whose biggest FWHM is $\sim 57 \text{ cm}^{-1}$. Similar to the CASE 3 above, it also cannot be surely assigned to a monomer or a dimer.

4.2.7.2 Category distribution and discussion

The category distribution of the spectral series mentioned above is presented in Figure 4.21. Type *D* is dominant with a fraction of 43%. However, it is not appropriate to conclude that the observed QD dimer purity is 43%, since the following possibilities should be taken into account:

- (1) As briefly discussed above, the cases belonging to type *MD* might also correspond to QD dimers.
- (2) In fact, particles corresponding to type *M* should not be surely assigned to QD monomers, since dimers whose two QD components emit extremely close in wavelength will exhibit the same spectrum. As a consequence, there is always the possibility that some QDs of type *M* are actually QD dimers.
- (3) In addition, blinking behavior of QDs makes the system even more complicated. As mentioned above, taking into account QDs which were in an *off* state or did not fluoresce at all during the measurement, assigning a single particle to monomer or dimer is not possible only by means of spectroscopy.

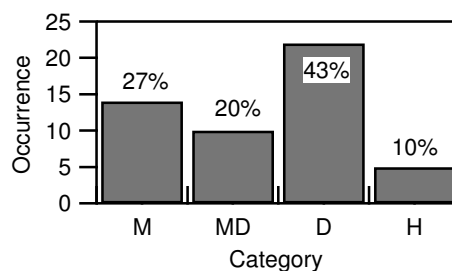


Figure 4.21: Category distribution of emission spectral series of single particles (in a PMMA film) from the QD dimer sample at 4.5 K.

Compared with the results of the monomer sample at 4.5 K mentioned above, since explicit differences have been observed for the particles in the dimer sample, the types and type distributions derived from spectral series definitely provide evidence of the existence of QD dimers in the dimer sample. As a very rough estimate, the dimer fraction could be in the range of 40%–70%, although this should not be quantitatively compared with the ensemble result (~68%) from TEM measurement.

4.3 CdSe/CdS/ZnS QD hetero-dimers

Although some qualitative proof of the existence of QD dimers in single particle measurement have been obtained at 4.5 K, an obvious disadvantage of the experiments at cryogenic temperature mentioned above is that the components were not spatially resolved in nanoscale. In contrast, with a setup combining atomic-force microscopy and confocal fluorescence microscopy (AFM-CFM) developed by the Basché group, AFM images (topography) and the corresponding fluorescence spectra of QDs can be recorded simultaneously [47, 300]. Taking advantage of this technique, the dimers can be spatially characterized at room temperature. However, to distinguish the fluorescence components spectrally, hetero-dimers have to be used instead of homo-dimers. Therefore, the synthesis of the hetero-dimer was attempted.

4.3.1 Size dependent fluorescence of CdSe core particles

The relationship between the fluorescence emission wavelength and the size of CdSe QDs has been investigated experimentally. With an injection temperature of 270°C and a growth temperature of 250°C, a series of CdSe QDs was synthesized following the procedure “CdSe core synthesis in TDPA, TOPO and TOP” described in Section 3.2.1.2. As shown in Figure 4.22(a) and Figure 4.22(b), both absorption and emission wavelengths of CdSe QDs reveal a red-shift with growth time. Figure 4.22(c) and Figure 4.22(d) display two typical TEM images corresponding to the CdSe core growing for 3 min (diameter: 2.6 ± 0.3 nm) and 15 min (diameter: 3.1 ± 0.4 nm), respectively, which were used for the further synthesis of core-shell structures in this work.

4.3.2 QD hetero-dimers whose QD components have different sizes

4.3.2.1 QD components

As discussed before, the strategy of hetero-dimer preparation is to dimerize two QDs with large difference in their emission wavelengths. Since the fluorescence is strongly size dependent, the first intuitive idea is to synthesize and assemble two QDs with different sizes (denoted as structure *I*). CdSe QDs mentioned above with the growth time of 3 min and 15 min were selected as cores for the green QDs (gQDs) and red QDs (rQDs). Considering that CdS shell coating will lead to emission red-shift, in order to eventually obtain adequate wavelength separation between gQDs and rQDs, different thicknesses of CdS shells were chosen. The CdSe cores for gQDs were coated with 4 monolayers

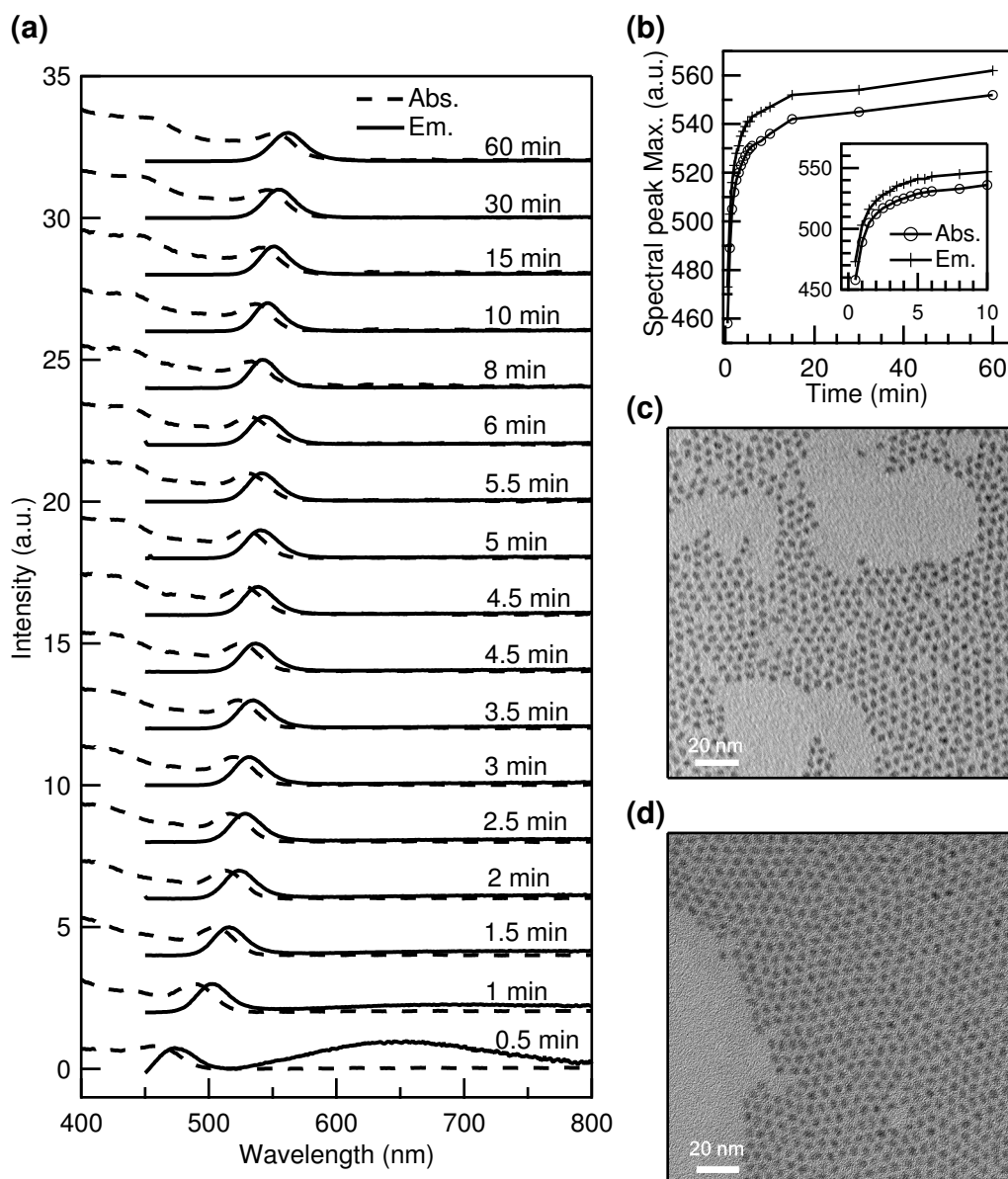


Figure 4.22: (a) Temporal evolution of absorption and emission spectra of CdSe QD cores. (b) The maxima of the first excitonic peak of the absorption spectra (o) and the maxima of the peaks (+) of the emission spectra at different growth times. The inset shows an enlarged view for the first 10 min and solid lines are only a guide for the eye. TEM images of the CdSe QDs growing for (c) 3 min and (d) 15 min. The diameters are measured to be 2.6 ± 0.3 nm and 3.1 ± 0.4 nm, respectively.

CdS and 1 monolayer ZnS (written as “CdSe/4ML CdS/ZnS” for short) while the rQDs were prepared to give CdSe/8ML CdS/ZnS. Corresponding characterizations are shown in Figure 4.23. From TEM images, it can be seen that not only the size distribution of

rQDs is broader than that of gQDs, but also the average size of rQDs is much larger than that of gQDs, namely 8.4 ± 1.0 nm versus 5.3 ± 0.6 nm. More importantly, as revealed in Figure 4.23(d), the emission wavelength separation is about 42 nm, which can be spectrally well resolved.

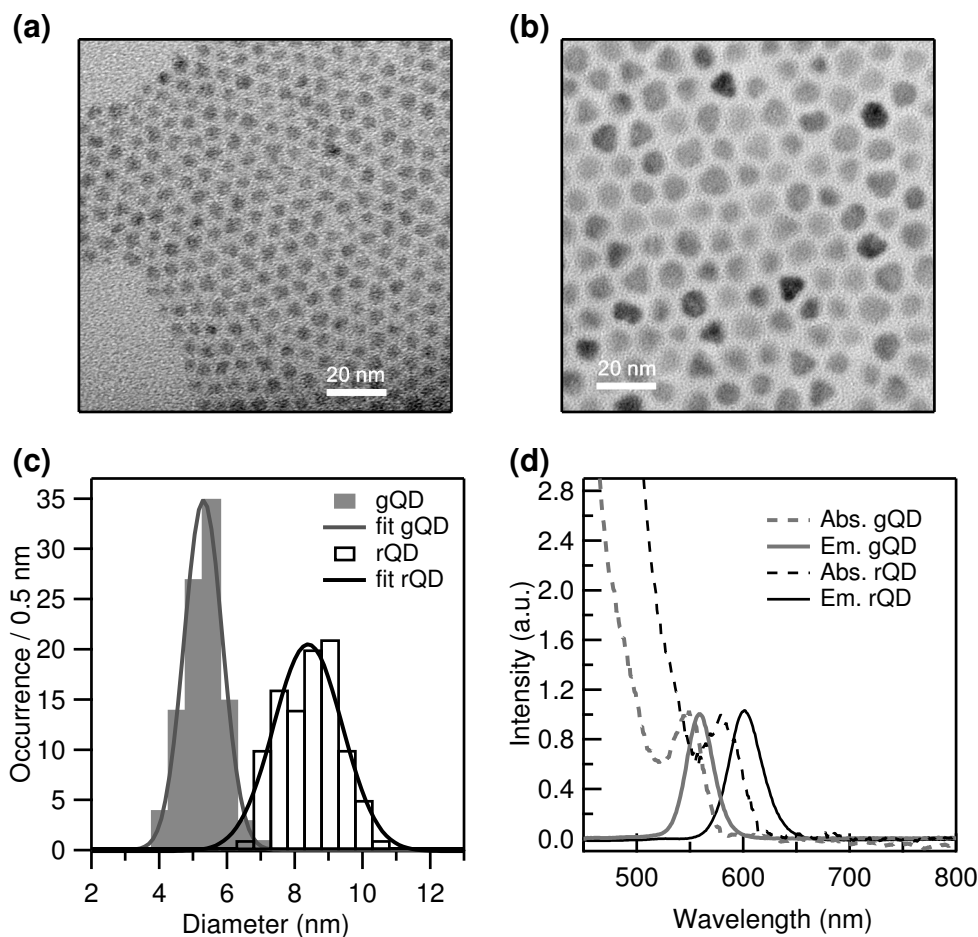


Figure 4.23: Characterizations of QD components with different sizes: TEM images of (a) gQDs and (b) rQDs. (c) The size distributions of gQDs (diameter: 5.3 ± 0.6 nm) and rQDs (diameter: 8.4 ± 1.0 nm). Solid lines in the histograms are the corresponding Gaussian fits. (d) Absorption and emission spectra of gQDs and rQDs.

4.3.2.2 Dimerization and characterizations

The gQDs and rQDs were mixed and assembled for three cycles to form QD oligomers. The as assembled particles are characterized by TEM. As shown in Figure 4.24, the QD size varies over a wide range, probably due to the contribution from the size distributions of both gQD and rQD batches. Figure 4.24 also reveals that: 1) The homo-dimers composed of two rQDs (marked with red circles) are more than the ones composed of two gQDs

(marked with green circles); 2) The homo-dimers composed of two gQDs are more than the hetero-dimers whose components have different sizes (marked with blue circles). The dependence of the required cycles of assembly on QD size (see Section 4.2.2) may explain the former but not the latter. To understand the mechanism of the second phenomenon, a model of assembly of QDs with different sizes is proposed here.

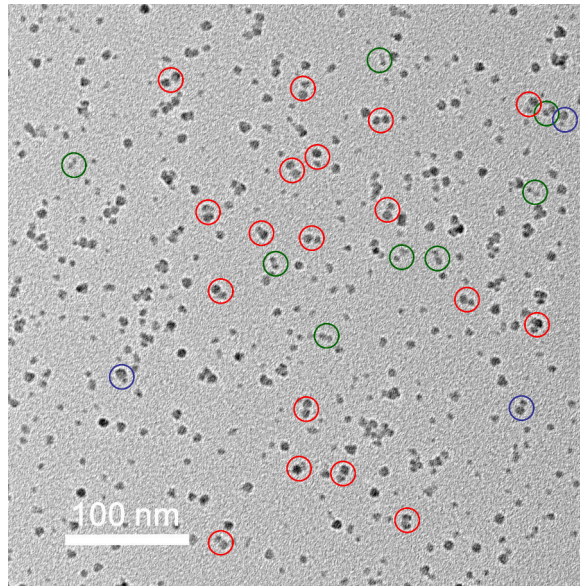


Figure 4.24: TEM image of as assembled oligomers from 5.3 nm gQDs and 8.4 nm rQDs. The particles marked with green, red and blue circles are homo-dimers composed of two gQDs and two rQDs, and hetero-dimers, respectively.

Specifically, as depicted in Figure 4.25(a), QDs with two sizes (for simplicity, small QDs and big QDs denoted as “sQD” and “bQD”) are mixed immediately after synthesis and the surface sites for chemical bondings are fully covered with ligands. During the process of assembly, ligand loss is induced, accompanied by the formation of oligomers. Because of detachment of ligands, some exposed free surface sites (red dots in Figure 4.25) are left, available for QD attachment to form QD oligomers. The essential hypothesis of this model is that the surface site density ρ is QD size independent, and the assembly of oligomers is realized by the connection of exposed surface sites from different QDs. Under this condition, the numbers of total surface sites are $4\pi\rho R^2$ and $4\pi\rho r^2$ for bQD and sQD, respectively, where R and r are the respective radii of the particles. Then if the ligand loss is also uniformly distributed, the ratio of the numbers of exposed free sites for bQD and sQD should be R^2/r^2 , which means that the free sites of bQD can be much more than that of sQD, as represented by red dots in Figure 4.25(b). Considering the initial stage of the assembly process (the onset of dimer formation), along with the desired hetero-dimer (D_{sb}) composed of one sQD and one bQD, homo-dimers D_{bb} (the dimer of two bQDs)

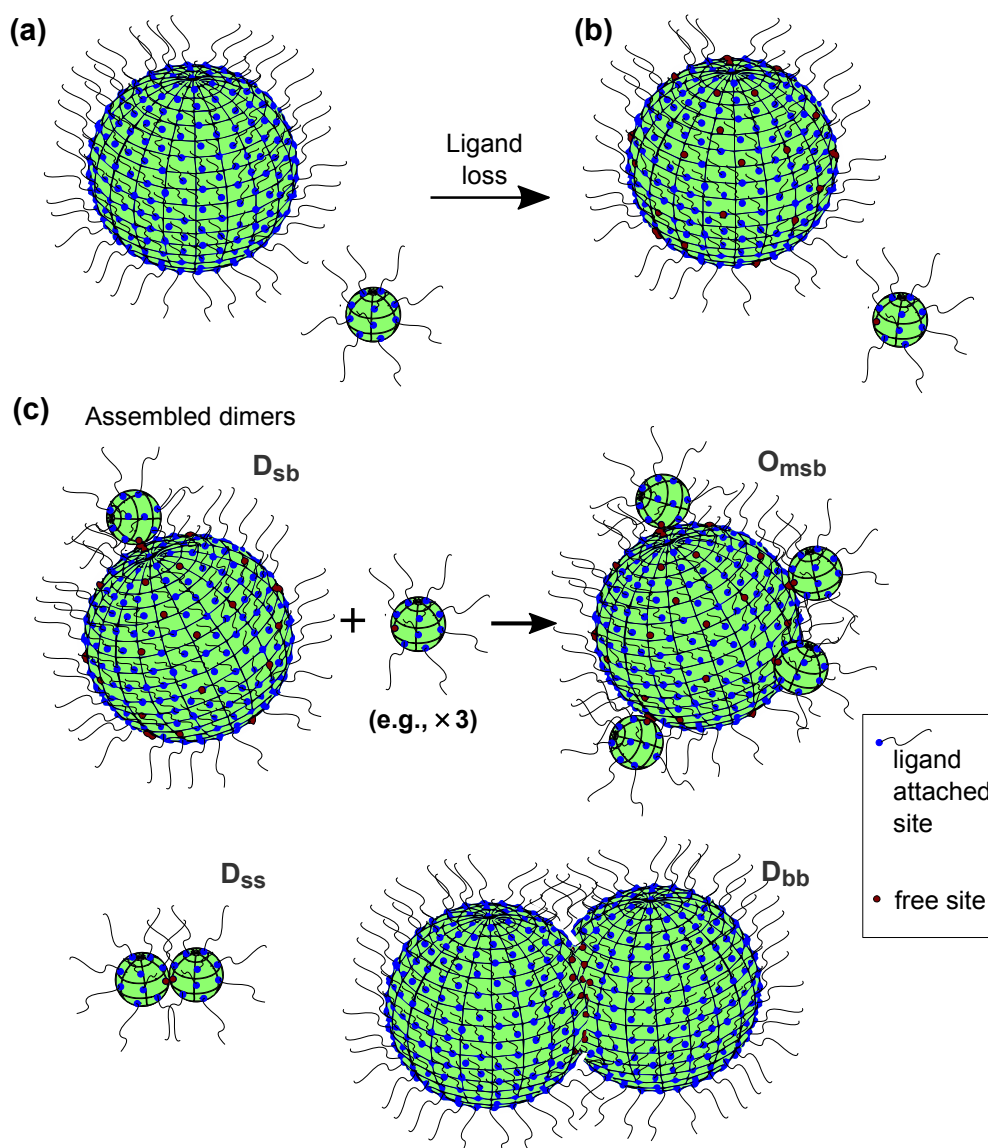


Figure 4.25: Schematic diagram of mechanism of the assembly from QDs with different sizes. (a) Original state of the as-synthesized QDs. (b) The state of QDs after ligand loss. (c) Possible assembled QD dimers: D_{sb} , D_{ss} and D_{bb} .

and D_{ss} (the dimer of two sQDs) are also possible to be created. However, the stability of the hetero-dimers and homo-dimers is likely to be significantly different. As illustrated in Figure 4.25(c), since numerous free surface sites of the bQD in a hetero-dimer are exposed, which have high activity, there is a high probability that the surrounding sQD monomers collide with the hetero-dimer D_{sb} and assemble to form an oligomer containing multiple sQDs and one bQD (O_{msb}). In contrast, since QDs with the similar sizes have similar numbers of free sites in a system, either the as formed D_{bb} or D_{ss} have few numbers of

exposed surface sites, corresponding to a lower free energy of the system compared to the case of D_{sb} . As a consequence, QD dimers which are most likely to form are homo-dimers rather than hetero-dimers.

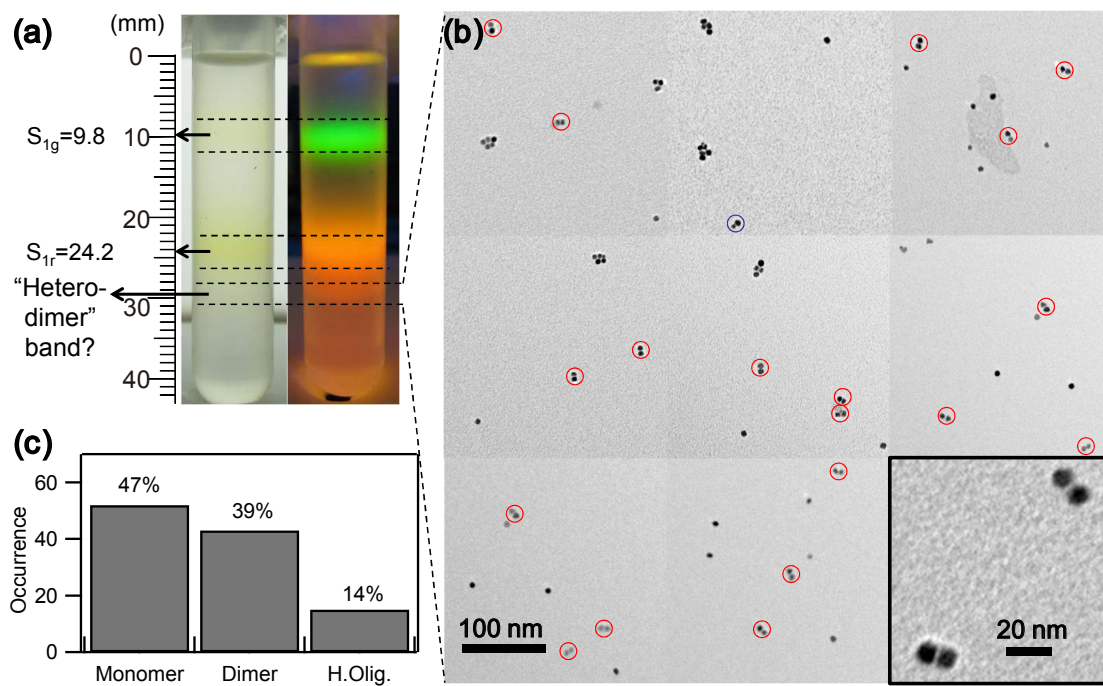


Figure 4.26: (a) Photographs of a centrifuge tube after DGU containing QD oligomers assembled from 5.3 nm gQDs and 8.4 nm rQDs. The left photo was taken under room light while the right one was taken under UV lamp. The gQD monomer, rQD monomer and suspected “hetero-dimer” bands were marked. (b) TEM images of the particles from the suspected “hetero-dimer” band. All images have the same scale bar of 100 nm except for the right bottom inset which shows an enlarged view with scale bar of 20 nm. The homo-dimers are marked with red circles while a hetero-dimer is marked with a blue circle. (c) Particle distribution of the sample taken from the suspected “hetero-dimer” band. H.Olig.: trimers, tetramers and higher oligomers.

DGU at 50000 rpm for 14 min was performed subsequently. Figure 4.26(a) shows photographs of the centrifuge tube after DGU under room light and UV light, respectively. The gQD monomer and rQD monomer bands can be clearly observed from the distinct colors. The sedimentation distances measured are 9.8 mm and 24.2 mm, respectively. Considering the sizes of the particles (5.3 nm for the gQDs and 8.4 nm for the rQDs), the corresponding calculated results based on Equation 4.11 are 9.2 mm and 25.2 mm, respectively, giving relatively good agreement with the observations. When a QD hetero-dimer composed of 5.3 nm and 8.4 nm QDs is converted to an equivalent spherical particle, Equation 4.11 predicts a sedimentation distance of 27.6 mm. In the experiment, at the corresponding position below the rQD monomer band, a relatively blurred band under

a small dark gap was observed. This band is a suspect for the desired hetero-dimers (simply denoted as “hetero-dimer” band), which was therefore extracted from the tube and characterized by TEM. Figure 4.26(b) shows a typical TEM image. Not only the fraction of dimers is relatively low (39%, 43 out of 110 particles), but also most of visible dimers are homo-dimers, meaning that the sizes of the two QD components are quite close (generally in the range of 7.5 nm–8.5 nm).

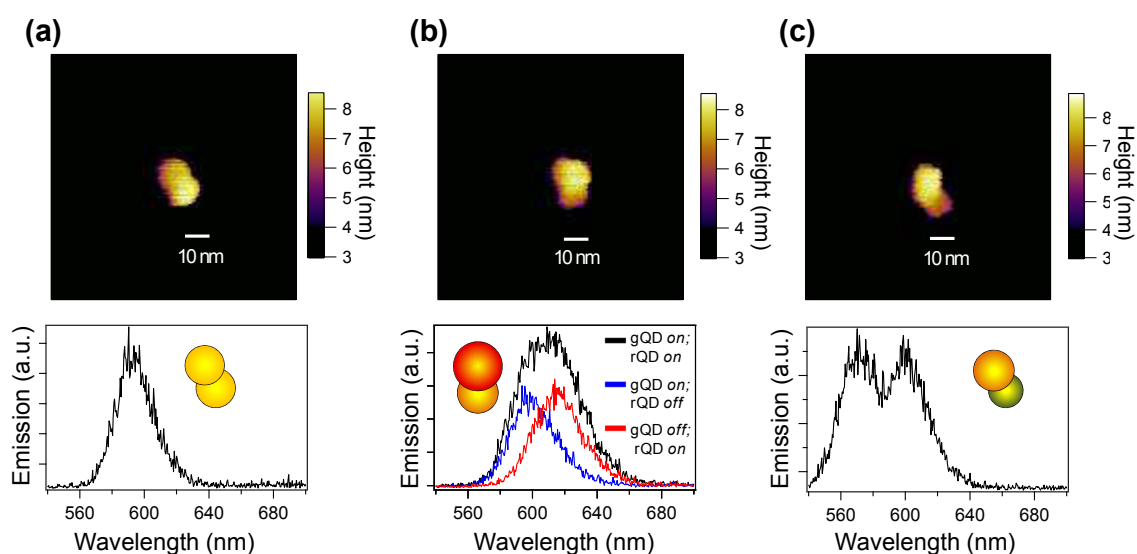


Figure 4.27: Three representative combinations of AFM images (upper panels) and corresponding fluorescence spectra (lower panels) of the QD dimers from the “hetero-dimer” band in Figure 4.26. Data provided by Sven Stöttinger.

Furthermore, single particle measurements of the sample from the “hetero-dimer” band in Figure 4.26 were performed with the AFM-CFM setup by Sven Stöttinger. Three examples are illustrated in Figure 4.27. From Figure 4.27(a) to (c), the examples were arranged in accordance with the order of increasing spectral distance of the two peak components. However, even for the situation of Figure 4.27(c), it is not possible to probe the emissions from the two components separately at the same time. An interesting phenomenon is that the emission of a single component could be observed sometimes when the other component is *off* due to fluorescence blinking. In the case represented in Figure 4.27(b), when the gQD (rQD) turned to *off* state while the rQD (gQD) was still in *on* state, a solitary spectrum of rQD (gQD) emerged. The brighter emission spectra obtained under the circumstance that both QDs were *on* is similar to the superposition of the two isolated spectra. Nevertheless, when the gQD and rQD are both *on*, the simultaneous independent measurements of fluorescence of each is infeasible.

As a conclusion from both TEM and AFM-CFM characterizations, the obtained QD dimers from the so-called “hetero-dimer” band in Figure 4.26 are typically not the real desired hetero-dimers as originally designed, but homo-dimers mainly from the batch of big rQDs. An obvious reason is that the sample before DGU had a small fraction of hetero-dimers, as discussed above. In addition, if the attachment between the components in a dimer was relatively weak, the sQD (gQD) and bQD (rQD) in a hetero-dimer might detach during DGU since the sedimentation velocity was strongly size dependent. This might be another reason for the lack of observation of QD hetero-dimers in the experiment.

4.3.3 QD hetero-dimers whose QD components have similar sizes

Since it turned out that the method used so far for the assembly of hetero-dimers was inefficient, a new strategy was invented, which rests on the dimerization of QD components with similar sizes. For a spherical CdSe QD, the emission wavelength is size dependent. However, when the QD is coated with a CdS shell, a red-shift is expected due to the wavefunction extension of the excitons into the CdS shell. In contrast, since ZnS has a much wider energy band gap, theoretically coating ZnS onto CdSe or CdSe/CdS QDs will not influence the emission wavelength. Therefore, as illustrated in Figure 4.28(b), with particular combinations of core-shell compositions, QD components with similar sizes but different emission wavelengths (structure *II*) were prepared.

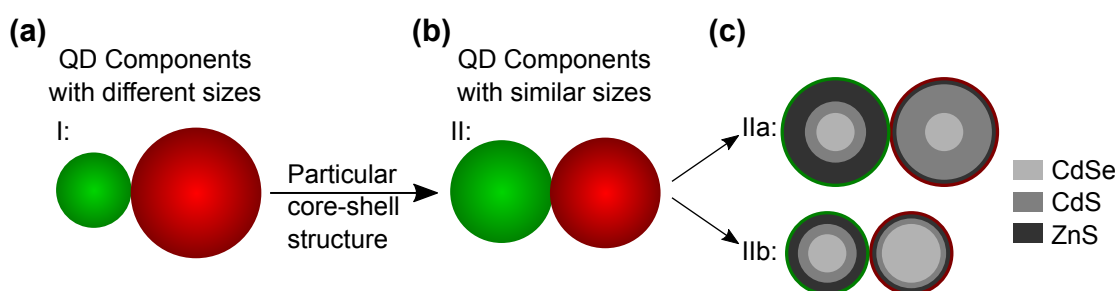


Figure 4.28: Schematic diagram of QD hetero-dimers with different structures. (a) QD components with different sizes (structure *I*). (b) QD components with different fluorescence emissions but similar sizes by particular core-shell structure design (structure *II*). (c) Two specific approaches to structure *II*. The outermost contours denote the colors of fluorescence.

Two approaches will be further discussed, which are schematically depicted in Figure 4.28(c). For structure *IIa*, the same CdSe core but different ratios of the amount of CdS-shell and ZnS-shell for the two QD components were used, while for structure *IIb*, different CdSe cores were used as well.

4.3.4 Structure *Iia*: QD components with the same CdSe core

For simplicity, structure *Iia* was attempted first: CdSe QD cores injected at 270°C with the growth time of 3 min (Figure 4.22(c)) were chosen for the cores of both gQDs and rQDs. After subsequent shell overgrowth, CdSe/5ML CdS/1ML ZnS QDs and CdSe/2ML CdS/4ML ZnS QDs were obtained as rQDs and gQDs, respectively.

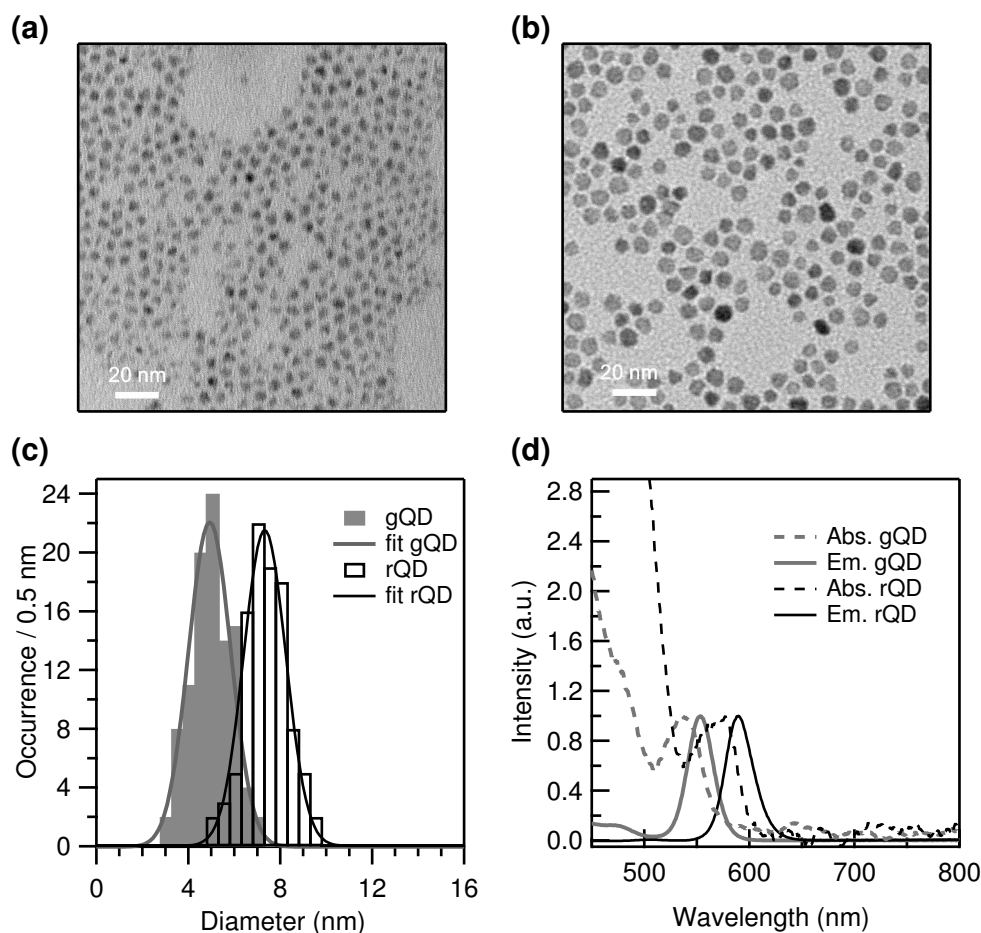


Figure 4.29: Characterizations of the QD components of structure *Iia*: TEM images of (a) gQDs and (b) rQDs. (c) The size distributions of gQDs (diameter: 4.9 ± 0.9 nm) and rQDs (diameter: 7.3 ± 0.9 nm). Solid lines in the histograms are the corresponding Gaussian fits. (d) Absorption and emission spectra of the gQDs and rQDs.

Although the lattice constants of CdS and ZnS are different (0.35 nm versus 0.31 nm), the theoretical size discrepancy between gQDs and rQDs with the structures mentioned above should be rather small, i.e., 0.24 nm in diameter. From this point of view, the experimental observations are surprising. As shown in Figure 4.29(c), the synthesized gQDs (4.9 ± 0.9 nm) and rQDs (7.3 ± 0.9 nm) exhibit a large difference in size. This

originates from the bad quality in morphology of the gQDs, shown in Figure 4.29(a). The QDs appear irregular and the size varies strongly from one to another. Probably, the growth of multiple ZnS shells was not successful due to the large lattice mismatch between either ZnS and CdSe or ZnS and CdS [21]. Since either ZnS and CdSe or ZnS and CdS have a large lattice mismatch [21], the ZnS shell may grow in ways such as coherent epitaxial with a large distortion or strain, incoherent epitaxial with dislocations, or highly disordered [151], which makes it difficult to overgrow thick ZnS shell. In conclusion, the resulting sizes of the two QD components prepared by this method were not sufficiently close.

4.3.5 Structure *Iib*: QD components with different CdSe cores

A sufficient emission wavelength separation of the two QD components which have similar sizes can be realized either by the size difference of CdSe cores or by the different magnitude of red-shifts in emission resulting from different shell compositions. Since the latter could not be achieved due to the difficulties from the ZnS coating, CdSe cores with smaller and bigger sizes have to be synthesized and used for gQDs and rQDs, respectively. Thus, the hetero-dimers shown as structure *Iib* in Figure 4.28(c) are required. For gQDs, the 2.6 nm QDs whose TEM image is shown in Figure 4.22(c) can be directly used. However, in order to obtain a sufficiently long emission wavelength (> 590 nm) and spherical core-shell QDs with a narrow size distribution, the QD cores for rQDs have to be big (> 4.5 nm) and spherical.

4.3.5.1 Synthesis of big spherical CdSe cores

In order to synthesize big spherical CdSe cores, the first strategy was to increase the reaction time. For the procedure discussed in Section 4.3.1 whose spectral temporal evolution is shown in Figure 4.22(a) and Figure 4.22(b), the spectral position of emission peak maximum tended to saturate after 15 min, and the longest emission wavelength 562 nm which was achieved by a growth time of 60 min is still much smaller than the required 590 nm. Furthermore, the morphology of the as-prepared QDs became elliptical with an aspect ratio of ~ 2.0 , which can be found in Figure 4.30(a) (middle and bottom panels).

Increasing the temperature is another approach to prepare bigger CdSe QDs. The injection temperature of the precursor solution was therefore raised. Figure 4.30(b) (middle panel) displays the TEM image of CdSe cores when the system was hot-injected at 310°C and reacted for 15 min at 290°C . Compared with the results at lower temperature with the same growth time, a much longer emission wavelength was obtained (593 nm), which is

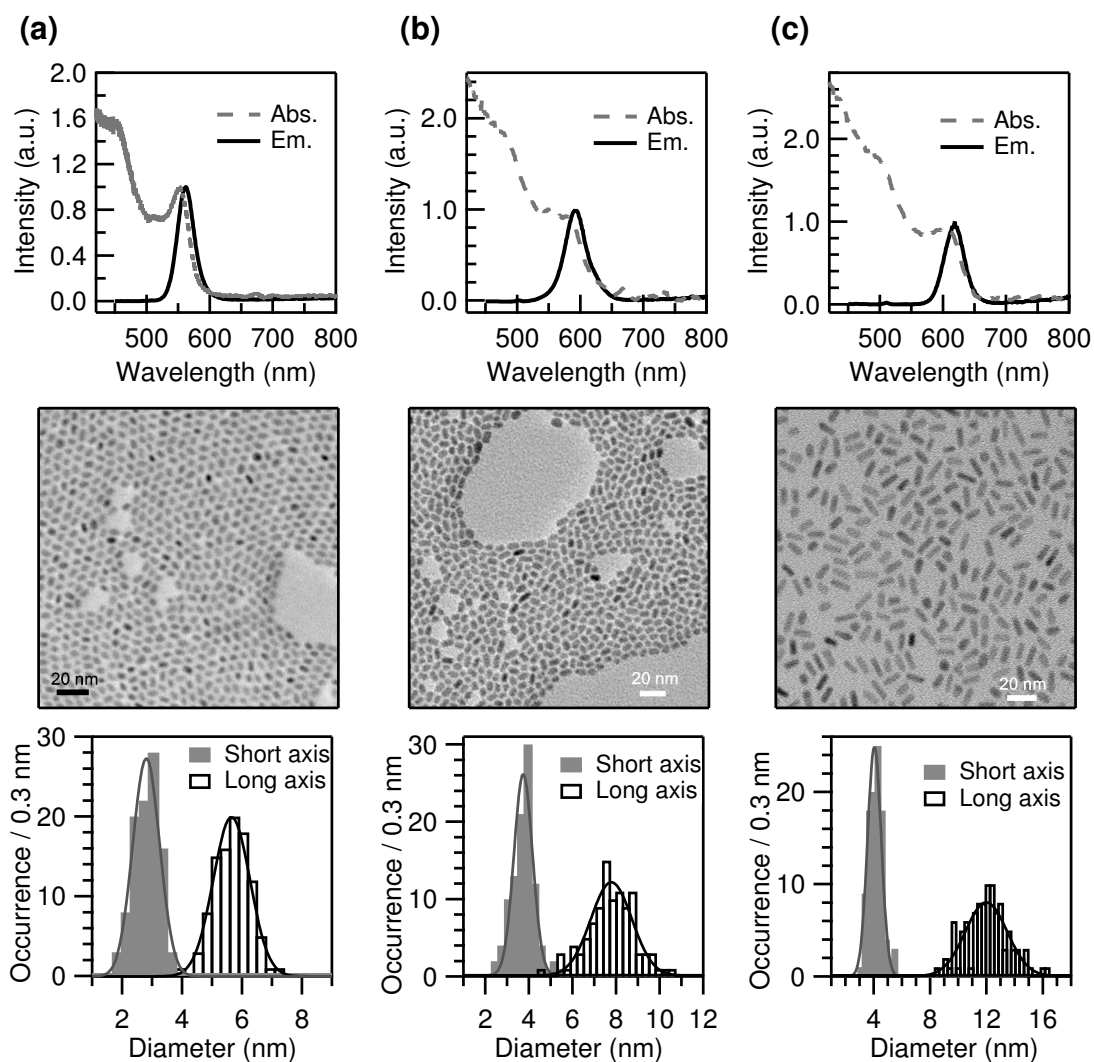


Figure 4.30: The absorption and emission spectra (upper panels), TEM images (middle panels) and the corresponding size distributions (lower panels) of CdSe QDs (a) hot-injected at 270°C and growing at 250°C for 60 min, (b) hot-injected at 310°C and growing at 290°C for 15 min, and (c) hot-injected at 380°C and growing at 360°C for 1 min. The respective QD diameters of short axes and long axes are: (a) 2.8 ± 0.4 nm and 5.7 ± 0.6 nm; (b) 3.7 ± 0.4 nm and 7.8 ± 0.9 nm; (c) 4.0 ± 0.5 nm and 12.0 ± 1.5 nm. Solid lines in the histograms are the corresponding Gaussian fits.

suitable for the core of rQD. However, the QDs were elliptical as well with a short axis of only 3.7 nm and an ellipticity of 2.1.

The size comparison of the QDs growing for 3 min at different hot-injection temperatures (270°C and 310°C, 3.1 ± 0.4 nm and 4.0 ± 0.3 nm) revealed a hint that higher temperature with shorter growth time favored the synthesis of big spherical cores. Inspired by this phenomenon, hot-injection at temperatures as high as 380°C was carried

out. However, as shown in Figure 4.30(c), even with the growth time as short as 1 min at 360°C, the particles exhibited rod-shaped with an aspect ratio of ~ 3.0 .

The ellipticity of the CdSe QDs can be explained by a mechanism proposed by Peng et al. [136]: It is well recognized that CdSe QDs grow in wurtzite (hexagonal) structure at high temperatures, and a permanent dipole moment has been observed along the unique c -axis [301]. Since the ligands used in the solution are usually electron-donating which should bind to cationic species exclusively, the (001) facet, either has to be terminated by negatively charged Se atoms and remains basically uncoated, or with surface Cd atoms which have more dangling bonds and are more active. Both cases induce a significant high chemical potential at this unique facet. As a result, especially considering the condition that the monomer concentration in our procedure was kept at relatively high value to prevent Ostwald ripening, the growth reaction rate along the c -axis is supposed to be much faster than that along any other axes. Therefore, elliptical QDs or even nanorods are expected to be formed.

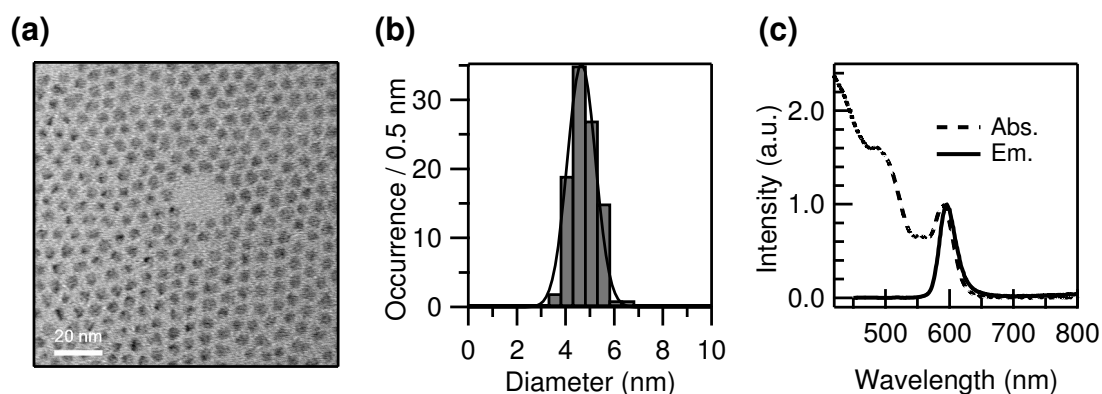


Figure 4.31: (a) TEM image, (b) size distribution (4.7 ± 0.6 nm) and (c) the absorption and emission spectra of the CdSe QDs synthesized with stearic acid, TOPO and TOP as ligands. Solid line in the histogram is the corresponding Gaussian fitting.

An alternative approach to produce big spherical CdSe QDs is to use other ligands. Qu et al. reported that fatty acids are excellent candidates to synthesize relatively large-sized CdSe QDs (above 4 nm) [125]. By a slight modification of their procedure, stearic acid (SA) has been introduced for the synthesis (details can be found in “CdSe core synthesis in SA, TOPO and TOP” in Section 3.2.1.2). The results are illustrated in Figure 4.31. From the TEM image, it can be seen that the CdSe core with new ligands are spherical and the size is 4.7 ± 0.6 nm. The emission maximum is at ~ 595 nm. Both characteristics completely meet the requirements of the CdSe cores for rQDs.

4.3.5.2 QD components

The as-synthesized big CdSe cores were coated with 1 ML CdS and 1 ML ZnS to produce rQDs. For the gQD, the 2.6 nm CdSe QD cores shown in Figure 4.22 were chosen and coated with 2 ML CdS and 2 ML ZnS. Figure 4.32 represents the characterization results of the gQD and rQD samples. The TEM images and size distributions explicitly indicate that the gQDs and rQDs are spherical and very similar in size (5.4 ± 0.4 and 5.6 ± 0.5 nm, respectively). Moreover, from Figure 4.32(d), it can be concluded that the ensemble emission wavelengths are also very well separated, as it was originally desired.

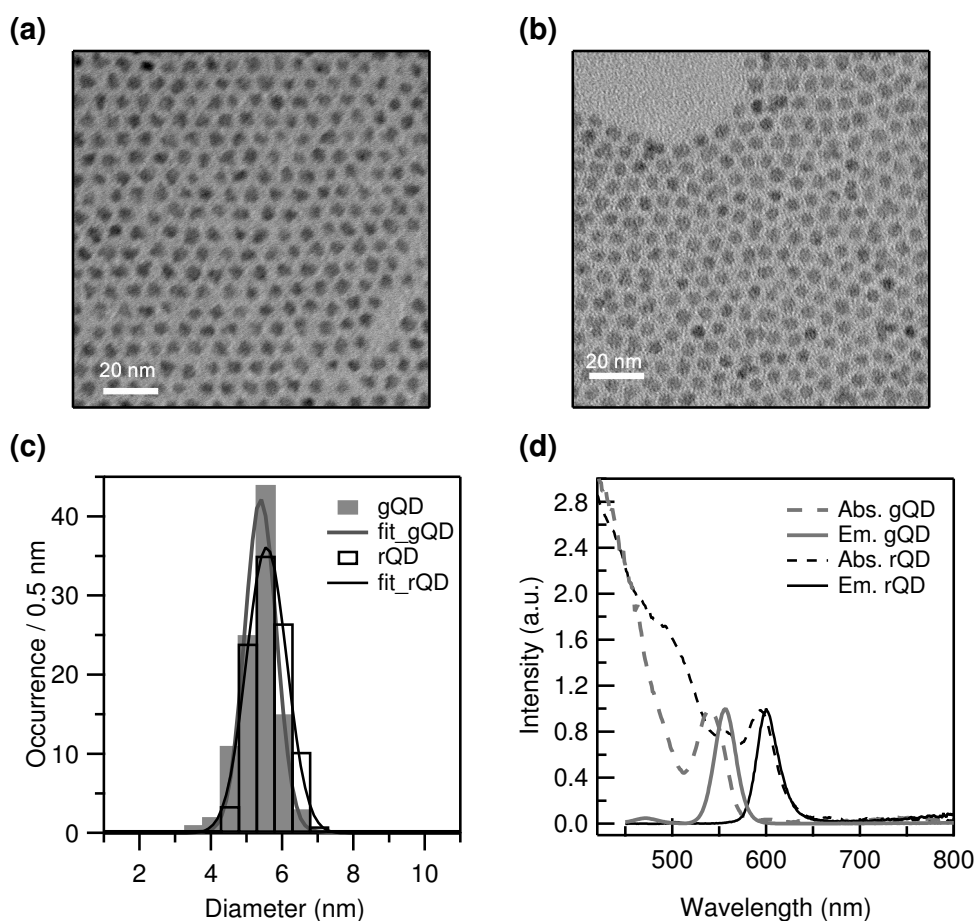


Figure 4.32: Characterizations of QD components of structure *Iib*: TEM images of (a) gQDs and (b) rQDs. (c) Size distributions of gQDs (diameter: 5.4 ± 0.4 nm) and rQDs (diameter: 5.6 ± 0.5 nm). Solid lines in the histograms are the corresponding Gaussian fits. (d) Absorption and emission spectra of the gQDs and the rQDs.

4.3.5.3 Dimerization and characterizations

Subsequently, the obtained gQDs and rQDs were mixed and assembled. As expected, in contrast to the case demonstrated in Section 4.3.2.2 (TEM images of assembled oligomers shown in Figure 4.24), here the QD components of the oligomers after assembly exhibited similar sizes, as displayed in TEM images in Figure 4.33.

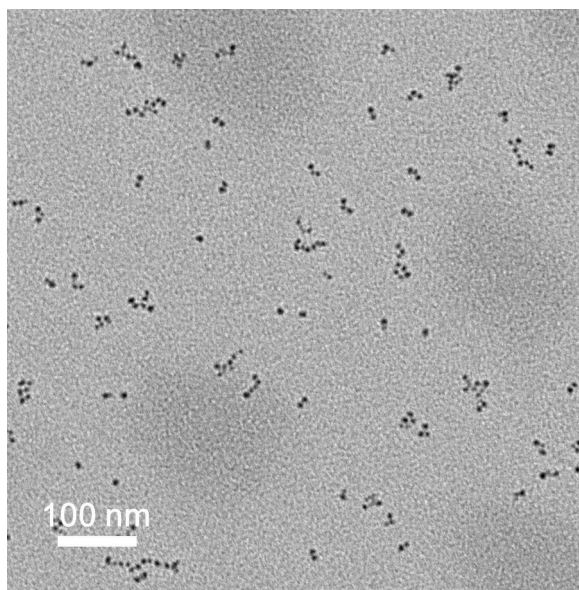


Figure 4.33: TEM image of as assembled oligomers from 5.4 nm gQDs and 5.6 nm rQDs.

To enrich the fraction of QD hetero-dimers, DGU at 50000 rpm for 19 min was conducted. Because of the slight difference of the average sizes of gQDs and rQDs, the overall size distribution of either monomers or dimers in a hetero-dimer sample is expected to be broader than that of monomers or dimers in a homo-dimer sample. Accordingly, in this experiment, broad bands were observed in the centrifuge tube after DGU, which is shown in Figure 4.34(a). A dark gap can still be resolved in the tube by the naked eye, which indicates where the monomer and dimer bands divide. Also due to the small size difference of gQDs and rQDs, the bands corresponding to homo-dimers and hetero-dimers are impossible to be differentiated. The center positions of the monomer band and dimer bands are measured to be 13.5 mm and 21.0 mm, respectively. According to Equation 4.11, the theoretical sedimentation distances of 5.4 nm and 5.6 nm QD monomers are expected to be 13.3 mm and 14.4 mm, respectively. The position of the hetero-dimer band is calculated to be 20.9 mm. Hence, the theoretical positions of the monomer bands and hetero-dimer band give good agreement with the experimental results. Figure 4.26(b) shows a TEM image of particles extracted from the dimer band. QD dimers whose neighboring QD components have similar sizes can be found in the image.

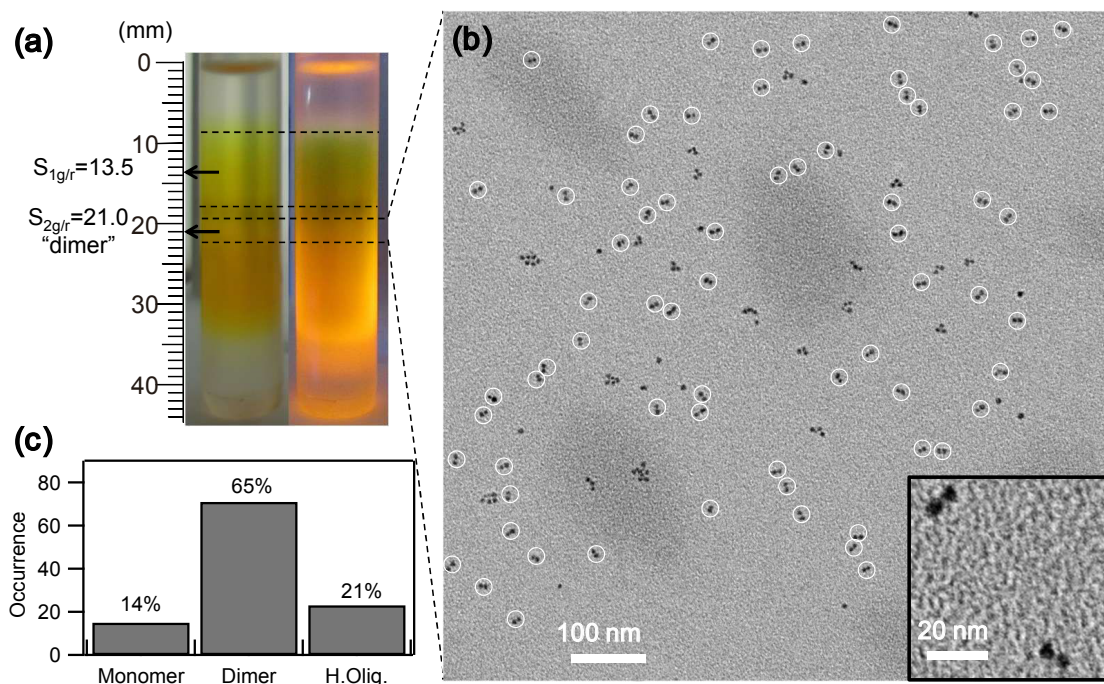


Figure 4.34: (a) Photographs of a centrifuge tube after DGU containing QD oligomers assembled from 5.4 nm gQDs and 5.6 nm rQDs. The left photo was taken under room light while the right one was taken under UV lamp. The QD monomer and hetero-dimer bands were marked. (b) A large-area TEM image of particles in the dimer band. The inset shows an enlarged view. The dimers are marked with white circles. (c) Particle distribution of the sample taken from the dimer band. H.Olig.: trimers, tetramers and higher oligomers.

The dimer fraction was $\sim 65\%$ (71 out of 109 particles). It should be emphasized that it was not possible to assign the observed QD dimers to homo-dimers or hetero-dimers by TEM, since the gQDs and rQDs are not differentiable by size.

Thanks to the capacity of simultaneous measurements of topography and fluorescence, a more comprehensive characterization of the dimer band sample was performed at the single particle level by Sven Stöttinger with the AFM-CFM technique. Figure 4.35 displays the results of two observed hetero-dimers. AFM images identify QD dimers spatially while the corresponding spectra confirm the emission wavelength difference of the two QD components of the same dimer. Thus, the existence of hetero-dimers can be verified. Furthermore, as revealed in the lower panels in Figure 4.35, the emission bands from the gQD and rQD in this hetero-dimer are spectrally completely separated. With a proper dichroic optical filter, the fluorescence of the two QD components within a dimer can be independently measured. This provides perspectives for the investigations of electronic couplings among QDs.

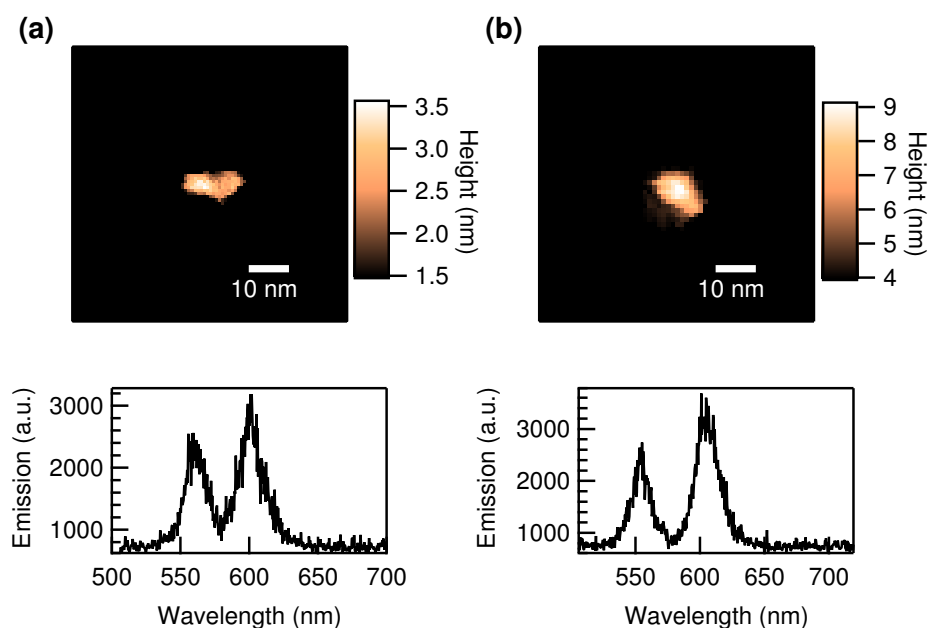


Figure 4.35: Two examples of combinations of AFM images (upper panels) and corresponding fluorescence spectra (lower panels) of QD dimers from the dimer band shown in Figure 4.34. Data provided by Sven Stöttinger.

4.4 Summary

Homo-dimers and hetero-dimers assembled from CdSe/CdS/ZnS QDs have been prepared to build a simple and well-defined system for the investigation of electronic interactions between two closely attached QDs. The assembly was performed by repeated precipitation of the QDs from a good solvent by adding a bad solvent. A size dependence of the assembly has been observed, meaning that smaller QDs require more cycles of assembly for effective formation of QD oligomers. The fraction of QD dimers among oligomers was found to be about 20%–30%. Subsequently, the fraction of QD dimers was enhanced by density gradient ultracentrifugation. The sedimentation distances calculated by the traditional sedimentation formula based on uniform centrifugal force field and homogeneous fluid (Equation 4.1) were found to be quite different from the experimental values. Therefore, taking into account variations of the centrifugal force and the medium density at different depths in the centrifuge tube, an improved theoretical formula (Equation 4.11) was proposed, with which the calculations gave good agreement with the observed sedimentation distances, both for the QD monomers and dimers. After DGU purification, the fraction of the QD dimers in solution could be enhanced up to 81%.

Single particle measurements of the QD monomers and dimers were performed at 295 K and 4.5 K, respectively. When the temperature was reduced, the quality of the fluorescence images of single QDs was found to degrade, including an enhancement of background and a reduction of signal amplitude, signal to noise ratio and QD density. The emission spectra collapsed to narrow ZPLs accompanied by PSBs. Experimental results indicated that neither the CdSe LO phonon energy nor the Huang-Rhys factor of CdSe LO phonon revealed correlation to the ZPL spectral position, and the respective values 207 cm^{-1} and 0.40 were in good agreement with those reported in the literature. In addition, the blue-shift of the band gap energy with the temperature reduction was measured and compared with theoretical calculations. It was found that the experimental value is smaller than the result based on the Varshni equation but larger than that calculated by the equation of O'Donnell and Chen. An excitation intensity dependence of spectral diffusion has also been observed.

As for the fluorescence of a homo-dimer sample at 4.5 K, various types of spectra have been found. The spectral series were categorized and analyzed, and possible scenarios were discussed as well. A comparison of the results of monomer and dimer samples indicates the presence of QD homo-dimers in the dimer sample.

Considering the hetero-dimer approach which may provide more quantitative and rigorous evidence of QD dimers, QD hetero-dimers whose components have different and similar sizes were prepared. Although the sedimentation distances of both were consistent with the calculation based on Equation 4.11, very small fraction of the desired hetero-dimers was found in the former case. This can be explained by a mechanism based on the exposed free surface sites triggered QD assembly under the assumption of size independent surface site density. Therefore, QD hetero-dimers whose components have similar sizes were attempted. Taking into account the requirement of emission wavelength separation and difficulties from the ZnS coating, big spherical CdSe QD cores were prepared. This was realized by a synthesis in which stearic acid was used as one of the surface ligands. Eventually, rQDs and gQDs with the structures of CdSe/1 ML CdS/1 ML ZnS and CdSe/2 ML CdS/2 ML ZnS were synthesized and dimerized. Although it was not possible to distinguish homo- and hetero-dimers from TEM characterization, the AFM-CFM measurement at room temperature provided conclusive evidence of the existence of QD hetero-dimers as desired. Since the fluorescence emissions of the two QD components could be spectrally completely separated, this well-defined QD dimer system has laid a foundation for the further investigations of the interaction (e.g, electronic coupling) among quantum dots.

5

Investigations of InP/ZnSeS QDs

5.1 Introduction and motivation

Undoubtedly, “green” chemistry is one of the major topics of the current chemical industry [302]. Specifically in the research field of quantum dots (QDs), there are increasing requirements for new types of cadmium-free QDs which are more environmentally benign due to the intrinsic toxicity of cadmium [49]. This is not only reflected in applications of conventional optoelectronic devices such as light-emitting diodes (LED) [2, 5–7, 98, 171], lasers [99, 100] and solar cells [10, 11], but also in applications at the single particle level such as biological fluorescent labeling [12, 13, 25, 303, 304], single particle tracking [26], quantum cryptography [27] and single-photon sources [28]. As introduced in Section 2.1.4, with its low toxicity and proper spectral emission range which covers the visible and near infrared, InP QDs are becoming a promising alternative for toxic QDs such as CdSe or CdTe from group II-VI. However, compared to the situation of group II-VI QDs, on the one hand, people face greater challenge in synthesis of high quality InP QDs with narrow size distribution, small full width at half maximum (FWHM) and high quantum yield at the ensemble level (see Section 2.1.4) [134].

Since the pioneering work of Battaglia et al. [175], many efforts have been made to improve the quality of InP based QDs, by photo-assisted surface etching of InP QDs [177] and synthesis of InP QDs with a ZnS shell [51, 141, 176]. Furthermore, more complicated core-shell structures and a deeper analysis of the internal structure have been reported more recently [52, 84, 142, 171]. The work here is mainly based on the strategy developed

by Lim et al. [52], incorporating ZnSe as a buffer layer into the InP/ZnS system to alleviate the lattice mismatch between InP and ZnS. Thus, a high QY can be achieved.

At the single particle level, as discussed in Section 2.3.3.3, various approaches have been established to suppress the fluorescence blinking, including alteration of temperature [57] or excitation energy [64, 65, 242], utilization of the plasmon resonance from metallic nanostructures [66–68], surface modification of QDs with organic molecular ligands or polymers serving as charge compensators/mediators [69–75, 243], synthesis of particles with alloy composition [80] and overcoating QDs with very thick shells of another passivating semiconductor material [76–78, 245]. Among these approaches, “giant” QDs were considered to be an efficient method [76, 77]. It is worth noting that with respect to the CdSe based “giant” QDs, the thick shell has to be CdS or $\text{Cd}_x\text{Zn}_y\text{S}$ for effective blinking suppression [76] whereas CdSe/ZnS QDs were proven by Heyes et al. to exhibit shell-independent blinking [305]. In addition, Wang et al. reported that their small CdZnSe/ZnSe QDs (~5 nm) showed non-blinking emission due to the soft confinement potential of the alloy structure [80], and García-Santamaría also found that the formation of a graded layer can produce a “smooth” potential profile resulting in great reduction of the Auger recombination rate [306]. These two findings combined with the more recently reported studies of non-blinking zinc-blende CdSe/CdS [83] and (Zn)CuInS/ZnS QDs [84] have suggested that the crystallinity and internal structure of the particles play an important role in the blinking suppression.

Almost all of the above-mentioned studies on the suppression of fluorescence blinking have focused on group II-VI QDs (CdSe or CdTe as the core). There are in contrast very few reports on the fluorescence blinking of InP based QDs [85–87]. Zan et al. studied the effect of the synthetic conditions on the blinking of InP/ZnS QDs [86], and Dennis et al. observed slight suppression of fluorescence blinking and Auger recombination from their InP/CdS type-II QDs [87]. Unlike the QDs of the conventional CdSe/CdS system, it has been observed that InP based (InP/CdS) QDs lack a simple shell-thickness dependence on blinking, meaning that even the blinking of QDs with only one monolayer of a CdS shell could be effectively suppressed [87]. Their results have also implied that the core-shell interface and internal structure are expected to be at least as significant as (if not more significant than) the shell thickness to the blinking suppression, especially for InP based QDs.

In this chapter, the studies presented concentrate on the internal structure of the particles, not only with regard to ensemble synthesis and characterizations, but also to spectral properties of the individual particles.

5.2 Sample description

Three series (labelled with *HLim*, *H* and *L*) of samples with different injected amounts of precursors and reaction temperatures were investigated. The amount of the Se was systematically varied and compared in each set. The *HLim* series was prepared by Dr. Jaehoon Lim from the research group of Prof. Kookheon Char in Seoul National University and the *H* and *L* series were synthesized by the author of this thesis. Synthetic details are described in Section 3.2.3. Sample labels and the corresponding essential experimental conditions such as P-ODE precursor injection temperatures T_{inj} , the growth times of InP $t_{grow.InP}$ and Se $t_{grow.Se}$, and the amounts of Se and S injections are tabulated in Table 5.1. For experiments at the single particle level, about one hundred quantum dots of each sample were measured.

Table 5.1: Labels and essential synthetic parameters of the InP/ZnSeS samples.

Sample	Composition	T_{inj} (°C)	$t_{grow.InP}$	$t_{grow.Se}$	Se (mmol)	S (mmol)
<i>HLim1</i>	InP/ZnS	280	20 s	—	0	3.8
<i>HLim2</i>	InP/ZnSeS	280	20 s	10 min	0.2	3.8
<i>HLim3</i>	InP/ZnSeS	280	20 s	10 min	0.8	3.8
<i>H1</i>	InP/ZnS	280	20 s	—	0	0.8
<i>H2</i>	InP/ZnSeS	280	20 s	10 min	0.2	0.8
<i>L1</i>	InP/ZnS	220	7 min	—	0	0.8
<i>L2</i>	InP/ZnSeS	220	7 min	13 min	0.001	0.8
<i>L3</i>	InP/ZnSeS	220	7 min	13 min	0.05	0.8
<i>L4</i>	InP/ZnSeS	220	7 min	13 min	0.2	0.8
<i>L5</i>	InP/ZnSeS	220	7 min	13 min	0.4	0.8

5.3 Ensemble characterizations

5.3.1 *HLim* series

Ensemble absorption and emission spectra of the three InP/ZnSeS samples *HLim1*, *HLim2* and *HLim3* with different amounts of Se were measured. As shown in Figure 5.1 and Table 5.2, from sample *HLim1* to *HLim3*, both the absorption and emission spectra exhibit red-shifts, which can be interpreted by the increasing spatial extension of the wavefunctions of electrons and holes into the shell with the increase of the amount of Se incorporated. The FWHMs of the emission spectra are generally larger (above 50 nm) than those of the emission spectra of CdSe QDs, which has been commonly observed in

previous reports [51, 134, 141, 171, 176]. In addition, compared to the quantum yields of the other two samples (56% and 59% for *HLim1* and *HLim2*, respectively), a lower value of the sample *HLim3* was found (25%).

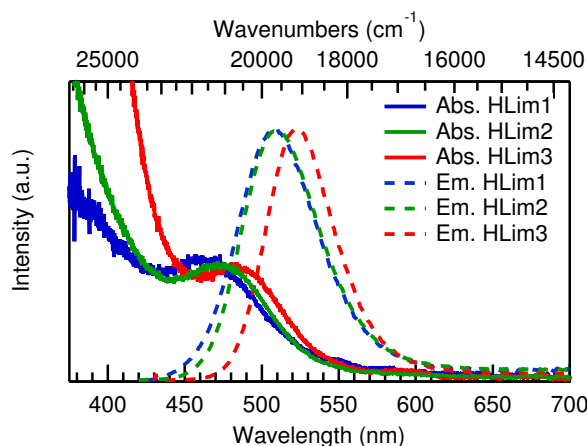


Figure 5.1: Absorption (solid lines) and emission (dashed lines) spectra of samples of the *HLim* series. The emission spectra were measured with an excitation wavelength of 400 nm.

Table 5.2: Results of the ensemble spectra of *HLim* series.

Sample	$\lambda_{\text{Abs.Max}}$ (nm)	$\lambda_{\text{Em.Max}}$ (nm)	FWHM (nm)	QY (%)
<i>HLim1</i>	464	507	63	56
<i>HLim2</i>	468	509	58	59
<i>HLim3</i>	479	520	53	25

Furthermore, these three samples were characterized by TEM. In the TEM images shown in Figure 5.2, it can be observed that the particles have irregular shapes for all three samples. Statistics reveal that the sizes of *HLim1*, *HLim2* and *HLim3* are 7.3 ± 0.8 nm, 7.5 ± 0.9 nm and 6.9 ± 1.1 nm, respectively.

5.3.2 H series

Since the work in Ref. [7] revealed that a shell with less sulfur of InP/ZnSeS QDs resulted in a higher quantum yield, two samples *H1* and *H2* were prepared with injections of less S-precursor solutions. Although no Se was added for *H1* and 0.2 mmol Se were injected for *H2*, the spectra of them are quite similar (Figure 5.3), both emitting at 513 nm. However,

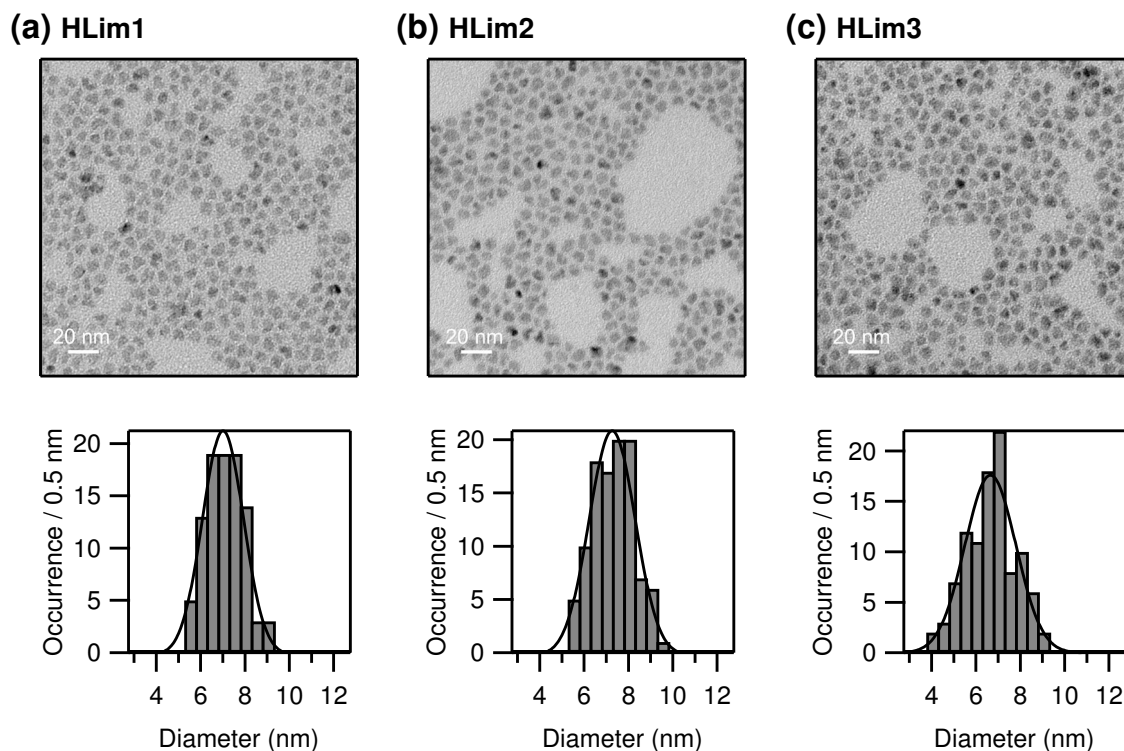


Figure 5.2: TEM images of samples (a) *HLim1*, (b) *HLim2* and (c) *HLim3*, respectively. The panels at the bottom show the corresponding size distributions: *HLim1*: 7.3 ± 0.8 nm; *HLim2*: 7.5 ± 0.9 nm; *HLim3*: 6.9 ± 1.1 nm. Solid curves in histograms are the corresponding Gaussian fits.

as listed in Table 5.3, with the addition of Se from sample *H1* to *H2*, the QY is dramatically increased, from 37% to 69%.

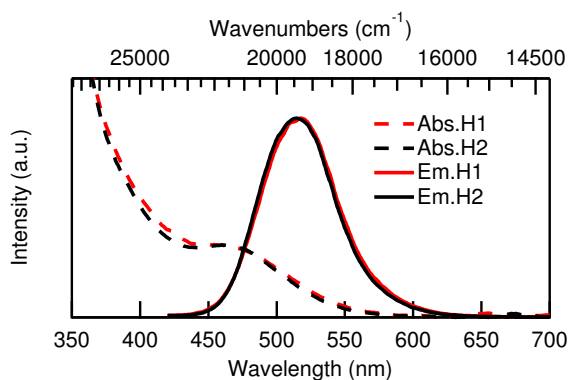


Figure 5.3: Absorption (dashed lines) and emission (solid lines) spectra of the *H* series.

Table 5.3: Results of the ensemble spectra of *H* series.

Sample	$\lambda_{\text{Abs.Max}}$ (nm)	$\lambda_{\text{Em.Max}}$ (nm)	FWHM (nm)	QY (%)
<i>H1</i>	466	513	66	37
<i>H2</i>	466	513	65	69

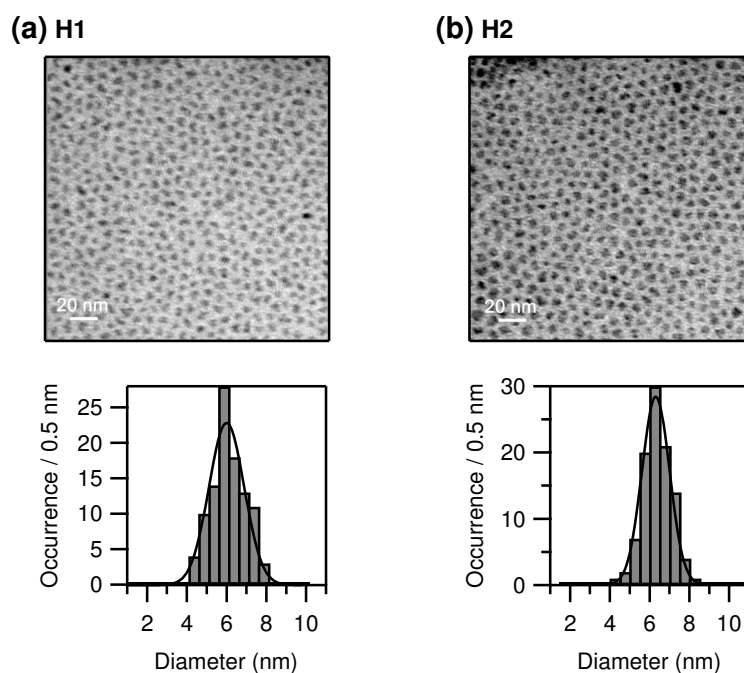


Figure 5.4: TEM images of samples (a) *H1* and (b) *H2*, respectively. The panels at the bottom show the corresponding size distributions: *H1*: 6.0 ± 0.8 nm; *H2*: 6.3 ± 0.7 nm. The solid curves in the histograms are the corresponding Gaussian fits.

TEM images of the samples *H1* and *H2* are shown in Figure 5.4. As expected, compared with *HLim* series, *H* series exhibits smaller sizes, since less amount of sulfur was added in the reaction. However, morphology and size uniformity are only slightly improved.

5.3.3 *L* series

As discussed in Ref. [52], at relatively high temperature (280°C), the fast growth of InP (20s) and ZnSe shells (10 min) are probably under kinetic control at a high monomer concentration. Therefore, procedures in which InP and ZnSe grow at lower temperature (220°C) have been attempted in order to allow the reaction to achieve a more controllable state, and more detailed and systematical investigations of the resulting *L* samples were performed. Taking *L4* as an example (the other *L* samples showed the similar behaviors),

at some crucial growth stages during synthesis, aliquots of the reaction solutions were extracted and characterized as follows.

5.3.3.1 Temporal evolution

Optical spectra Figure 5.5(a) shows the temporal evolution of the absorption and the fluorescence spectra of *L4*. Since Zn have been initially added to passivate InP cores, once

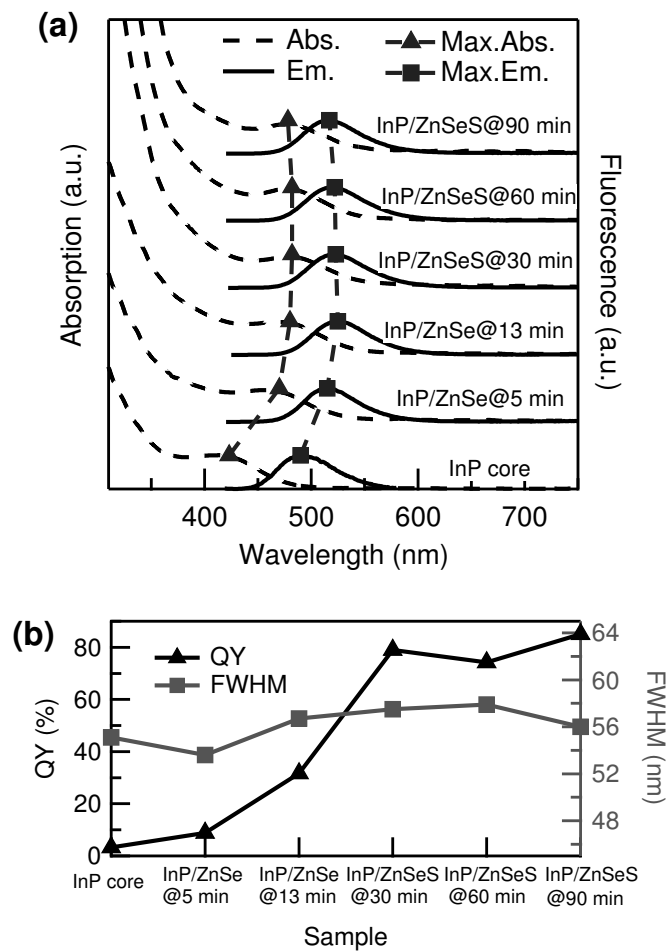


Figure 5.5: Comparison of QDs at different growth stages for sample *L4*. (a) Temporal evolution of the absorption (dashed lines) and the fluorescence (solid lines) spectra (excited at 300 nm for the InP core and 400 nm for the others). The maxima of the first excitonic absorption and fluorescence peaks are marked by triangles and squares, respectively. The dashed connection lines between the symbols serve as a guide for the eye. (b) Temporal evolution of fluorescence quantum yields and emission FWHM of sample *L4*.

Se injected, ZnSe will form at the surface of the InP cores. After Se injection, maxima of

both the first excitonic absorption peak and the fluorescence peak exhibit obvious red-shifts, indicating a delocalization of the charge carriers into the ZnSe buffer shell. After Zn and S precursor injections, in contrast, a slight blue-shift of peak maximum can be observed, which may be due to a slight alloying of ZnSe and ZnS at 300°C [7, 21, 307]. The fluorescence QY increases dramatically after Se and S injections and eventually ends up at ~85%, while FWHMs of the emission spectra remains at around 55 nm (Figure 5.5(b)). The fluorescence maximum of the final sample is located at 517 nm, corresponding to a green emission.

Structural characterizations In order to study the internal structure of the as-prepared *L4* QDs, the samples reacted for 13 min after Se injection (InP/ZnSe@13 min), reacted for 30 min, 60 min and 90 min after S injection (InP/ZnSeS@30 min, InP/ZnSeS@60 min and InP/ZnSeS@90 min, respectively) were characterized by TEM. The corresponding sizes of the QDs obtained from the TEM images displayed in Figure 5.6 are 2.9 ± 0.4 nm, 3.7 ± 0.4 nm, 4.2 ± 0.5 nm and 4.5 ± 0.4 nm, respectively. The size of the Zn-passivated InP core is estimated to be ~1.3 nm according to the wavelength of the first excitonic absorption peak (423 nm) based on the empirical formula (Equation 2.16). Compared with the *HLim* and the *H* series, the *L4* sample (Figure 5.6(d)) shows a more spherical morphology and a narrower size distribution.

In addition, the atomic contents of the samples at different growth stages of *L4*, which are considered to correspond to different radial positions of the InP/ZnSeS@90 min QDs, were measured by energy dispersive X-ray spectroscopy (EDS). The results show that with the proceeding of the shell coating, the atomic contents of Se and S gradually decrease and increase, respectively, as indicated in Figure 5.7(a). Combined with the corresponding sizes measured by TEM (Figure 5.6), the EDS results explicitly confirm the composition gradient of the alloy shell.

Furthermore, this set of samples was thoroughly purified and X-ray diffraction (XRD) measurements were performed for crystallographic analysis. Figure 5.7(b) reveals that although the XRD pattern of InP cores shows broad band due to the very small size of the InP QDs (1.3 nm), compared with the standard XRD lines (vertical sticks), all core/shell samples can be identified and indexed with the zinc blende crystal phase according to the strongest three distinct diffraction peaks. Unlike InP/CdS QDs which have zinc blende core (InP) and wurtzite shell (CdS) [87], the crystal phase of the InP/ZnSeS QDs is maintained after coating. This is believed to be more favorable for the compatibility of core and shell. Moreover, it has been observed that the positions of the diffraction peaks in the XRD patterns shift gradually towards higher angles with the shell overgrowth. The peaks of

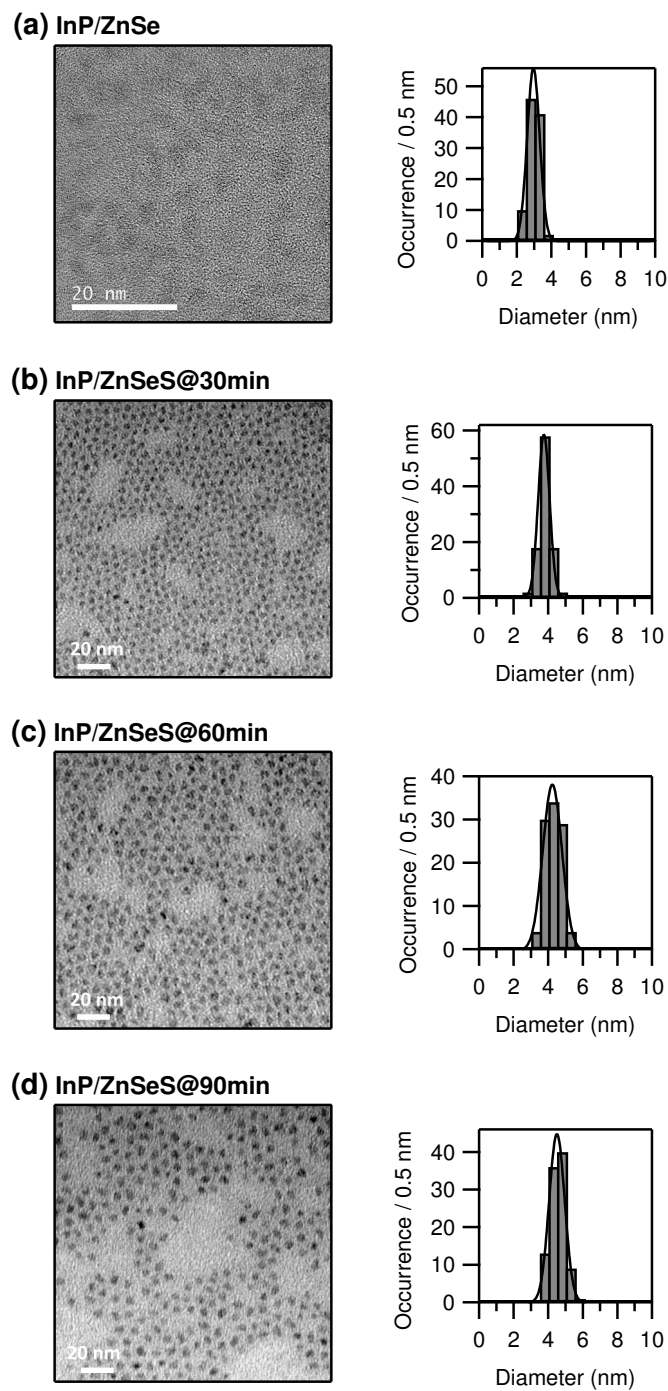


Figure 5.6: TEM images of QDs at different growth stages for sample *L4*. The right panels are size distributions and the corresponding Gaussian fits. (a) InP/ZnSe: 2.9 ± 0.4 nm; (b) InP/ZnSeS@30 min: 3.7 ± 0.4 nm; (c) InP/ZnSeS@60 min: 4.2 ± 0.5 nm; (d) InP/ZnSeS@90 min: 4.5 ± 0.4 nm.

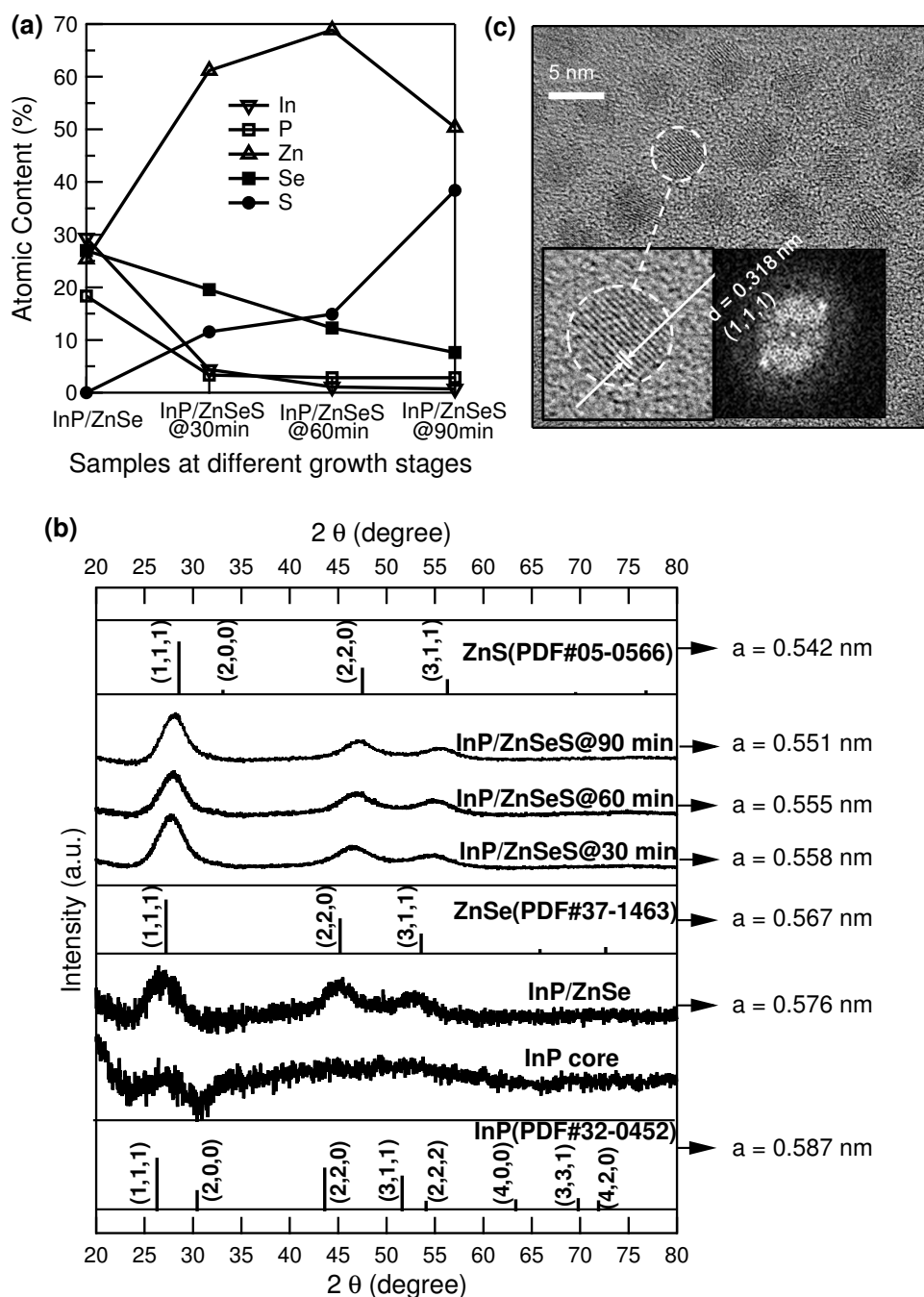


Figure 5.7: Structural characterization of QDs at different growth stages for sample *L4*. (a) Atomic contents at different growth stages of the InP/ZnSeS QDs from energy dispersive X-ray spectroscopy. (b) X-ray diffraction patterns of the samples at different growth stages. The standard diffraction lines of InP, ZnSe and ZnS of zinc blende structure from the ICDD PDF database indicated by vertical bars (|) are presented for comparison. The corresponding overall lattice constants are listed on the right side. (c) High resolution transmission electron microscopy images of the as-prepared InP/ZnSeS@90 min QDs. The insets are the enlarged view and the fast-Fourier transform (FFT) of the single QD marked with the dashed white circle.

the InP/ZnSe sample are located between the positions of the Bragg reflections for bulk InP (ICDD PDF¹ #32-0452) and ZnSe (ICDD PDF #37-1463), and similarly, the peaks of InP/ZnSeS samples are located between the positions of the Bragg reflections for bulk ZnSe (ICDD PDF #37-1463) and ZnS (ICDD PDF #05-0566). These data also illustrate a gradual decrease of the overall lattice constant from the center to the surface of the InP/ZnSeS QDs (listed on the right side of Figure 5.7(b)) based on formulas $2d \sin \theta = n\lambda$ (Bragg's law) and $d_{hkl} = a/\sqrt{h^2 + k^2 + l^2}$ (for cubic unit cell), where d is the interplanar spacing of the crystal, n (an integer) is the "order" of Bragg reflection, λ is the wavelength of the incident X-rays ($\lambda = 0.15406$ nm), θ is the angle of incidence and (hkl) denotes a generic Miller index. Furthermore, the InP/ZnSeS@90 min sample has been characterized by high resolution transmission electron microscopy. The electron micrograph in Figure 5.7(c) shows that the QDs have a relatively spherical shape. Based on the crystal lattice fringes and the corresponding fast-Fourier transform (FFT) (insets in Figure 5.7(c)), the exposed interplanar spacing has been measured to be 0.318 nm. This interplanar spacing is in good agreement with the value calculated by Bragg's law based on the peak position corresponding to crystal plane (111) in the XRD pattern. The lattice fringes also suggest a high crystallinity the InP/ZnSeS QDs.

5.3.3.2 Different amounts of Se

In order to study the influence of the ZnSe buffer shell on the photophysics, samples with different amounts of Se (varied from 0 to 0.4 mmol) have been synthesized, characterized and compared. As listed in Table 5.1, the samples were labeled as *L1*, *L2*, *L3*, *L4* and *L5* corresponding to Se amounts of 0, 0.001, 0.05, 0.2, 0.4 mmol, respectively. Figure 5.8(a) shows the absorption and emission spectra, from which it can be seen that the emission wavelengths of the samples are similar, except for *L5* which contains a large amount of Se. The fluorescence QYs increase from *L1* to *L4* and decrease for *L5* with increasing amount of Se, while the FWHM of the emission spectrum behaves in the opposite way, as displayed in Figure 5.8(b). The specific values can be found in Table 5.4.

Moreover, as represented in Figure 5.9, the fluorescence lifetimes of the samples of the *L* series were measured by means of time-correlated single photon counting (TCSPC) (for experimental details see Section 3.3.5). Histograms of photon arrival times had to be fit with a sum of four exponential functions convoluted with an instrumental response

¹ICDD: the International Centre for Diffraction Data; PDF: Powder Diffraction File.

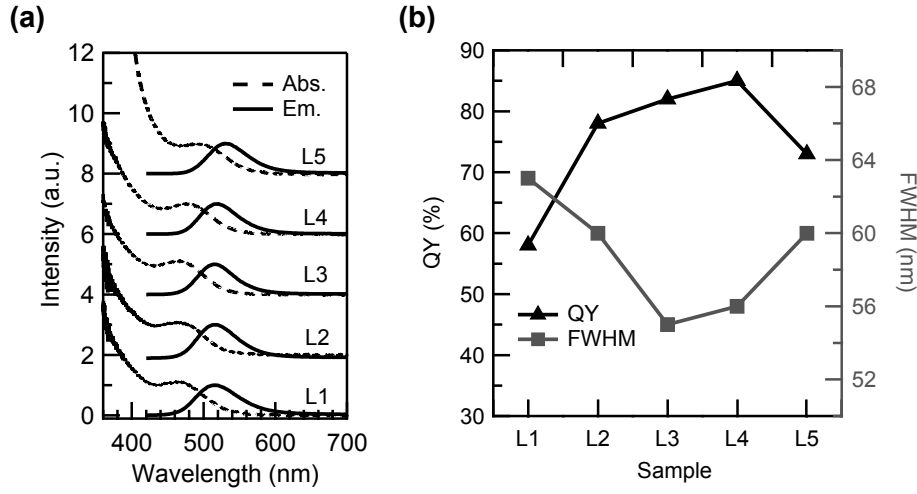


Figure 5.8: (a) Absorption and emission spectra of *L* series. (b) Comparison of fluorescence quantum yields and emission FWHMs of the InP/ZnSeS QD samples *L1-L5* with increasing amount of Se.

Table 5.4: Results of the ensemble spectra of *L* series.

Sample	$\lambda_{\text{Abs.Max}}$ (nm)	$\lambda_{\text{Em.Max}}$ (nm)	FWHM (nm)	QY (%)
<i>L1</i>	468	515	63	58
<i>L2</i>	468	516	60	78
<i>L3</i>	467	516	55	82
<i>L4</i>	478	517	56	85
<i>L5</i>	494	530	60	73

function (IRF) according to:

$$I_{fl}(t) = \left[\sum_n A_n e^{-\frac{t}{\tau_n}} \right] \otimes IRF(t) + B \quad (5.1)$$

The fitting parameters were listed in Table 5.5. Using the components of amplitudes A_n and lifetimes τ_n , the average fluorescence lifetime $\langle \tau \rangle$ of each sample was calculated based on:

$$\langle \tau \rangle = \frac{\sum_n A_n \tau_n^2}{\sum_m A_m \tau_m} \quad (5.2)$$

Moreover, together with the QY values in Table 5.4, according to

$$k_t = \frac{QY}{\langle \tau \rangle} \quad (5.3)$$

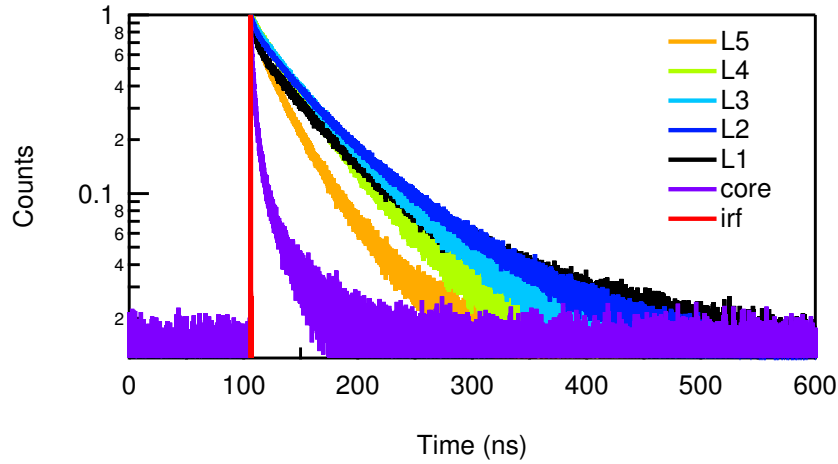


Figure 5.9: Fluorescence decay curves of the Zn-passivated InP core and InP/ZnSeS QDs with different amounts of Se in chloroform (*L* series). The red curve is the instrument response function (IRF) with an FWHM ~ 200 ps.

Table 5.5: Fluorescence lifetime fitting parameters of *L* series. k_r : radiative decay rate; k_{nr} : non-radiative decay rate.

	A_1	τ_1 (ns)	A_2	τ_2 (ns)	A_3	τ_3 (ns)	A_4	τ_4 (ns)	$\langle \tau \rangle$ (ns)	QY (%)	k_r ($10^6 s^{-1}$)	k_{nr} ($10^6 s^{-1}$)
core	0.42	0.34	0.41	2.58	0.14	11	0.03	49	23	3.3	1.4	42.0
L1	0.28	2.35	0.16	18	0.49	56	0.07	198	97	58	6.0	4.3
L2	0.17	2.45	0.22	25	0.54	63	0.07	199	93	78	8.4	2.4
L3	0.08	2.75	0.19	24	0.66	56	0.06	163	73	82	11.2	2.5
L4	0.05	2.68	0.2	22	0.69	48	0.06	125	58	85	14.6	2.6
L5	0.19	2.2	0.4	20	0.38	43	0.03	156	51	73	14.3	5.3

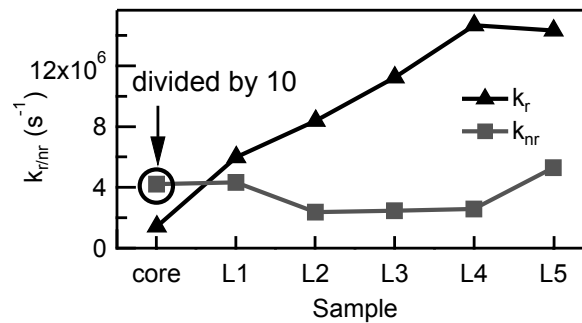


Figure 5.10: Comparison of radiative decay rates (k_r) and non-radiative decay rates (k_{nr}) of samples *L1-L5* with increasing amount of Se. In order to prevent the details being covered, k_{nr} of the core had been divided by a factor of 10 before it was plotted.

and

$$k_{\text{nr}} = \frac{1 - QY}{\langle \tau \rangle} \quad (5.4)$$

the radiative and non-radiative decay rate constants k_{r} and k_{nr} were obtained and are given in Figure 5.10. After the overgrowth of the shell, the radiative decay rate k_{r} increases almost linearly with increasing amount of Se and eventually saturates when using a large amount of Se in sample *L5* (0.4 mmol), while as a first approximation the non-radiative decay rate k_{nr} remains constant.

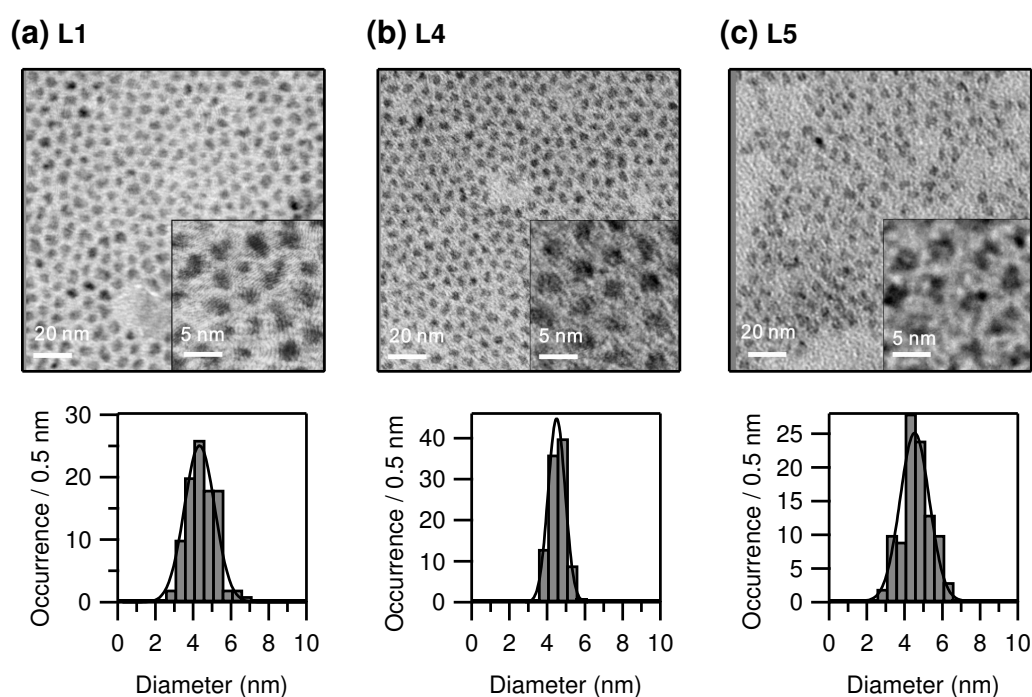


Figure 5.11: TEM images of samples (a) *L1*, (b) *L4* and (c) *L5*. The insets are enlarged views. The panels at the bottom show the corresponding size distributions: *L1*: 4.4 ± 0.8 nm; *L4*: 4.5 ± 0.4 nm; *L5*: 4.5 ± 0.8 nm. Solid curves in the histograms are the corresponding Gaussian fits.

Finally, the corresponding TEM images reveal that compared to the samples without Se (*L1*, Figure 5.11(a)) and with a large amount of Se (*L5*, Figure 5.11(c)), the QDs with 0.2 mmol Se (*L4*, Figure 5.11(b)) possess a more spherical morphology and a narrower size distribution. This correlation of the morphology and the optical properties (e.g., different fluorescence QYs) found here further reveals the importance of the crystal structure of the QDs on their photophysical properties, which can be controlled by the amount of Se.

5.4 Single particle measurements at room temperature (T = 295 K)

Single particle measurements at room temperature were performed with the setup described in Section 3.4.4. The different QDs were embedded in PMMA films. The time resolution (time bin) of the fluorescence time traces was 20 ms. The shortest spectral integration time was 1 second.

5.4.1 *HLim* series

For the measurement of the *HLim* series, a 488 nm OPSL laser was used. The excitation intensity was $\sim 285 \text{ W/cm}^2$. Other information such as optical filter combinations can be found in Table 3.2.

5.4.1.1 Photostability

The stability against photo-bleaching of the *HLim* series was tested in air and argon atmospheres. As revealed in Figure 5.12(a) and Figure 5.12(b), the survival time against

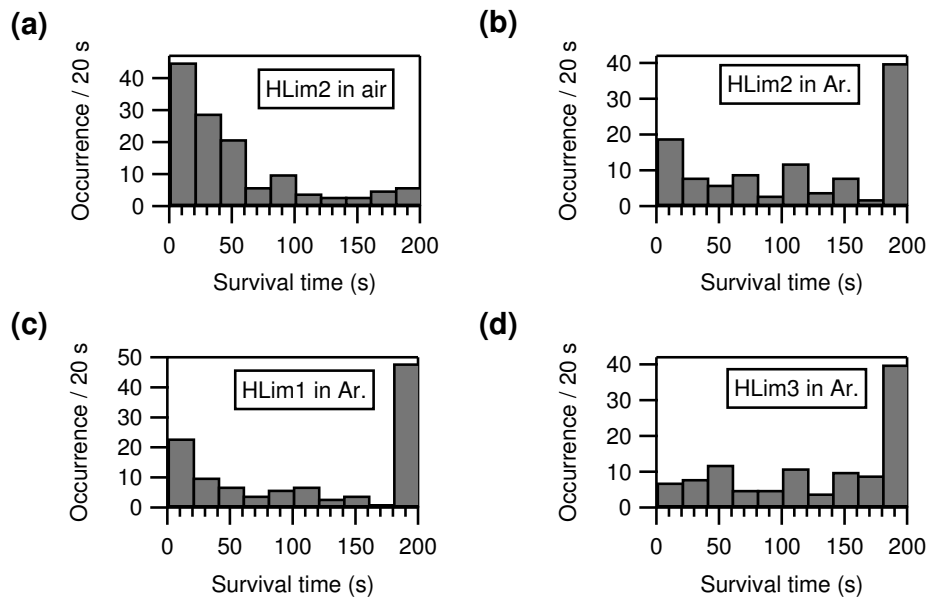


Figure 5.12: The survival times against photo-bleaching of sample (a) *HLim2* in air, (b) *HLim2* in argon, (c) *HLim1* in argon and (d) *HLim3* in argon.

photo-bleaching is strongly dependent on the surrounding atmosphere. Aa argon

atmosphere obviously plays an important role in the protection of samples from photo-bleaching, indicating that the bleaching may be mainly ascribed to a process which is related to the air environment (such as photo-oxidation), even though the QDs were embedded in the PMMA film.

Survival time distributions of sample *HLim1*, *HLim2* and *HLim3* in argon were compared as well (Figure 5.12(b)(c)(d)). In all three samples, QDs bleached in argon atmosphere. The fractions of the QDs whose survival time fell into the interval of 180-120 s were 48%, 36% and 35% for sample *HLim1*, *HLim2* and *HLim3*, respectively. This result suggests that the survival time against bleaching does not differ significantly from sample to sample under these experimental conditions.

5.4.1.2 Typical emission spectra

Since the 488 nm laser light was used as the excitation source, the wavelength of the edge of the long-pass filter used in the detection path in the experiment had to be longer than 488 nm. However, as seen in Figure 5.13(a), some blue part of the emission spectra of the bulk samples have been cut off by the filter. This induces two consequences: 1) Some bluer QDs would be excluded and absent in the single particle measurements; 2) The single particle emission spectra of some bluer QDs whose fluorescence could be detected may be partially cut off. The details are demonstrated below.

As displayed in Figure 5.13(b), the line shape of the emission spectrum of the single QD exhibits a substantial difference from the Gaussian fit. This spectral asymmetry could be easily attributed to the long-pass filter. But it is worth noting that the filter is at least not the exclusive contribution. An evidence is that another redder QD whose emission is far from the filter edge shows a similar line shape as well (Figure 5.13(c)). An asymmetry of emission spectra could be found for all the QDs measured, although it does not appear to be significant at room temperature. Since the ensemble spectrum is in principle equivalent to the convolution of single particle spectra of the contributing QDs and a symmetric Gaussian distribution of the emission spectral positions, the spectral asymmetry at the single particle level might be responsible for the asymmetry of the ensemble spectra.

5.4.1.3 Statistics of the emission spectra

The distributions of the emission maxima and FWHMs of the emission spectra of single particles belonging to the *HLim* series are shown in Figure 5.14 and the values are tabulated in Table 5.6.

The asymmetry of the histograms of the peak positions in Figure 5.14(a)(c)(e) are likely related to the long-pass filter used in the single particle measurement, meaning some

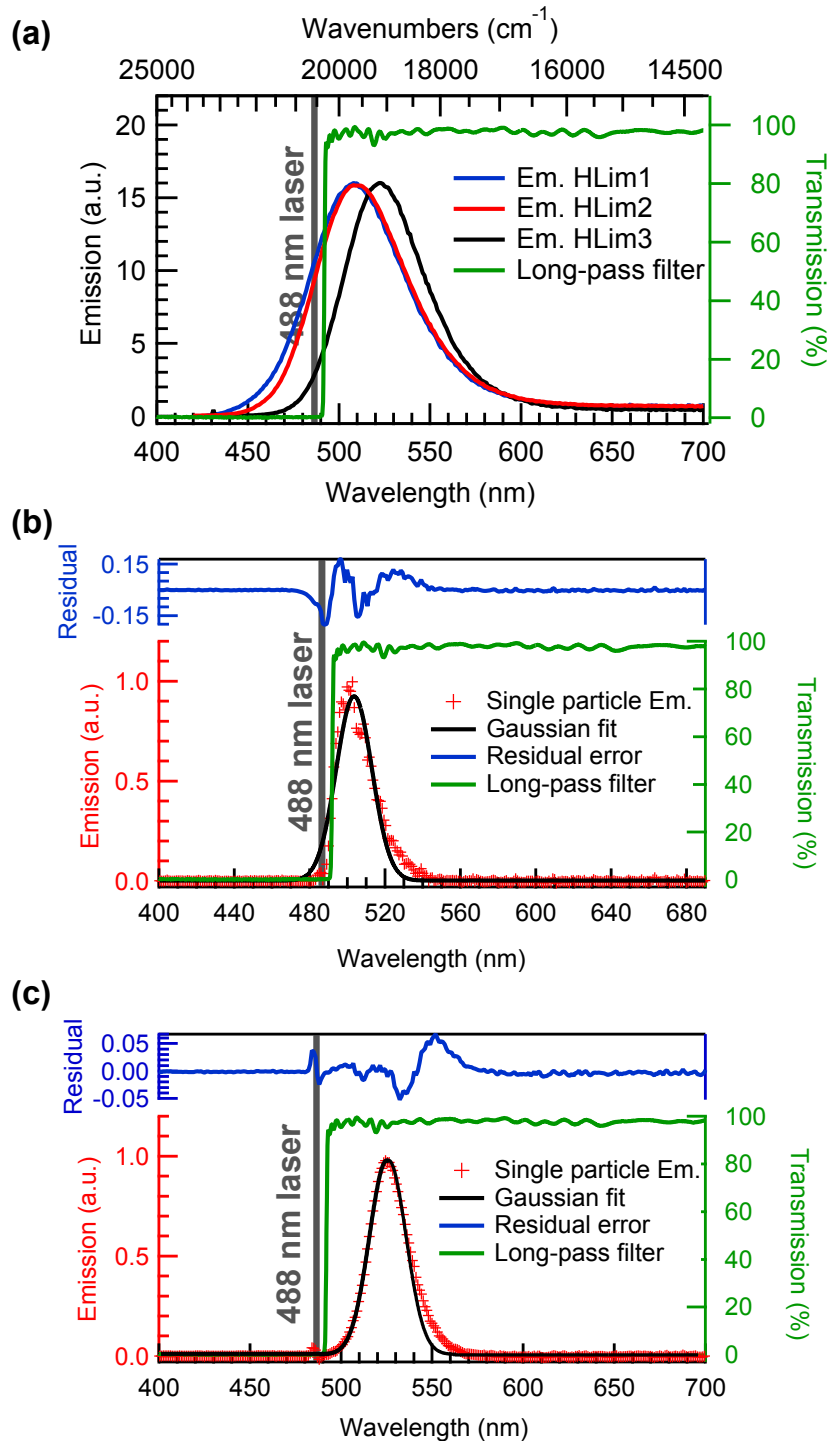


Figure 5.13: (a) Ensemble spectra of *HLim* series and the transmission curve of the 488 nm long-pass filter. Typical emission spectra of (b) a single QD and (c) another redder single QD with the transmission curve of the 488 nm long-pass filter used in the experiment. The black and blue solid curves are corresponding Gaussian fits and the residual error of the fits, respectively. Vertical lines indicate the spectral position of the 488 nm excitation light. The integration time of the single particle spectra is one second.

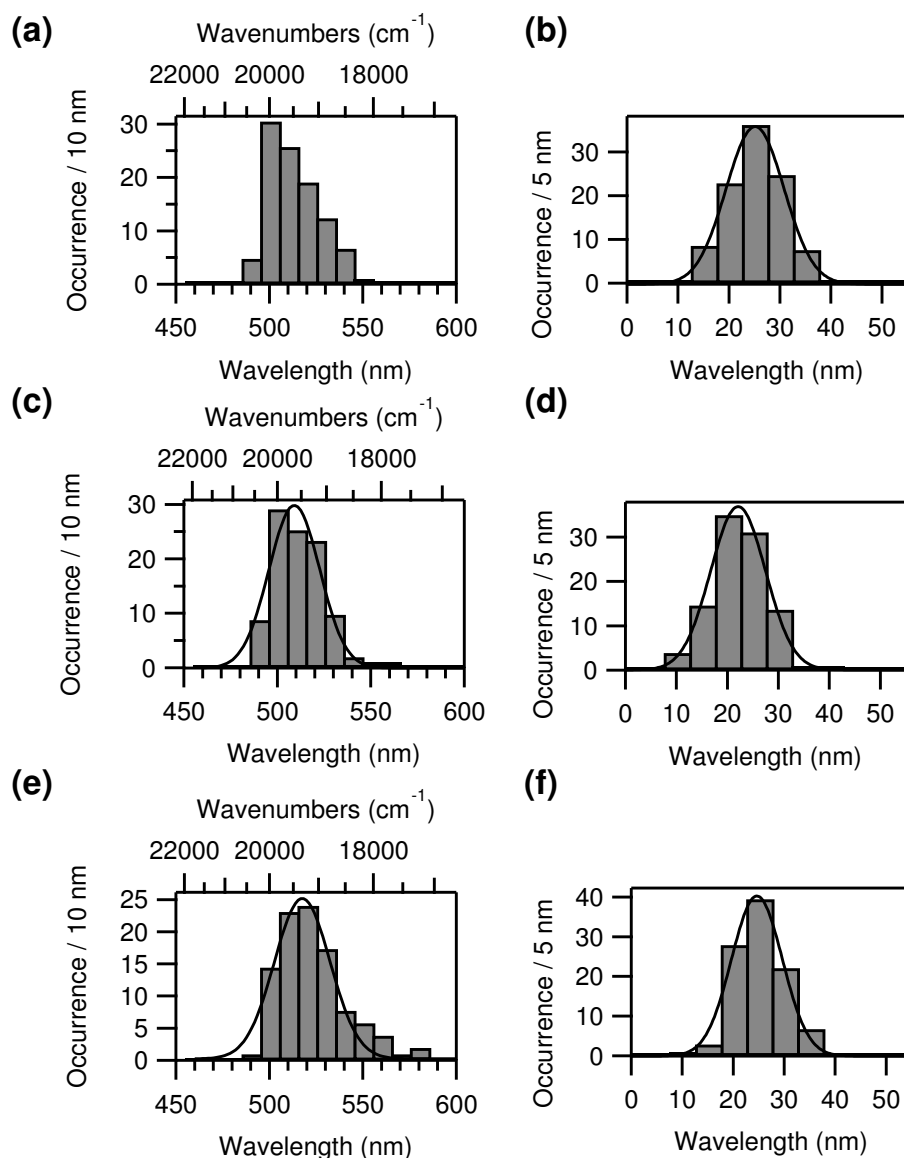


Figure 5.14: Distributions of emission maxima and FWHMs of the emission peaks in single QD spectra of *HLim* series. Spectral position distributions: (a) *HLim1*, (c) *HLim2* and (e) *HLim3*. FWHM distributions: (b) *HLim1*, (d) *HLim2* and (f) *HLim3*. The solid curves in the histograms are the corresponding Gaussian fits.

bluer QDs are filtered out artificially. Particularly, as revealed in Figure 5.14(a), a Gaussian fitting of sample *HLim1* is not possible. For the other two samples, despite of possible slightly over-estimations of red wavelengths due to the long-pass filter, the resulting values from the distributions of the spectral peak positions from single QDs (see Table 5.6) are in accordance with the ensemble emission maxima (Table 5.2).

To avoid any under-estimation of the FWHMs of emission peaks, only the QDs whose emission wavelengths are longer than 500 nm were taken into account for the FWHM statistics. The results shown in Table 5.6 from distributions in Figure 5.14(b)(d)(f) indicate that the emission peak widths of the single particles are all much narrower than those of the ensemble samples (22-25 nm versus 53–63 nm), suggesting the presence of inhomogeneous spectral broadening. Considering the spectral resolution (~ 96 cm^{-1}) of the spectra, the variation in peak FWHM among different samples is not significant.

Table 5.6: Statistical results of emission maxima and FWHMs of the emission peaks in single particle spectra of the *HLim* samples.

sample	Peak Max. (nm)	Peak FWHM (nm)	Peak FWHM (cm^{-1})
<i>HLim1</i>	—	25.1 ± 5.7	968 ± 220
<i>HLim2</i>	509.1 ± 13.6	22.1 ± 5.4	853 ± 208
<i>HLim3</i>	518.6 ± 14.8	24.6 ± 5.0	916 ± 186

5.4.1.4 Time traces and categorizations

For all three samples, four different types of single particle fluorescence time traces were observed, labeled with *F*, *N*, *B* and *M*, respectively. Representative time traces as well as the corresponding count rate distributions are displayed in Figure 5.15. Thresholds were set to define the *on* and *off* states according to the count rate distributions.

- Type *F* (Figure 5.15(a)): QDs which exhibit long *off* times and do not show well defined *on* state intensities in the time traces. Since it has been observed that even the fluorescence time trace with a time bin as small as 1 ms exhibits similar features (not shown here), the different intensities might be due to very frequent blinkings (fluctuations on the time scale smaller than 1 ms) [241]. From the count rate distribution (the right panel of Figure 5.15(a)), it can be seen that most of the time the QD is in *off* state at background intensities.
- Type *B* (Figure 5.15(b)): QDs featuring a binary blinking with relatively well defined intensities for both *on* and *off* states. The bimodal distribution of the fluorescence intensities indicate the photon counts from the bright state and the dark state.
- Type *M* (Figure 5.15(c)) is a category which embraces more complicated time traces: The single QDs show multiple levels of intensities, so that a threshold to distinguish

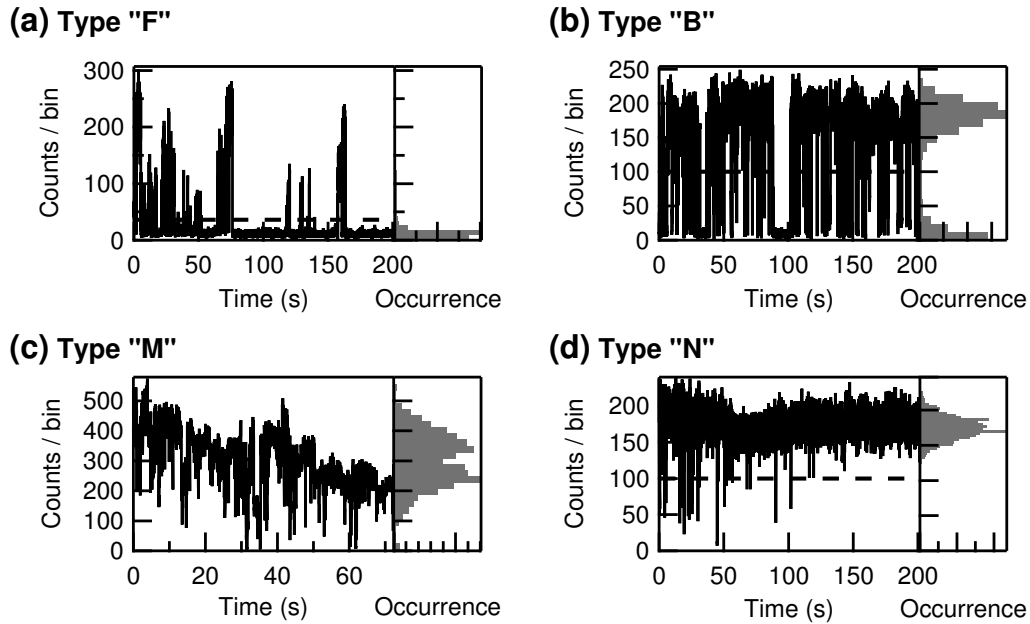


Figure 5.15: Four categories of fluorescence time traces of the *HLim* series, labeled with (a) *F*, (b) *B*, (c) *M* and (d) *N*. The histogram in the right panel in each sub-figure is the corresponding count rate distribution of the time trace. The horizontal dashed lines indicate the thresholds to discriminate between the *on* and *off* states. Time bin: 20 ms.

between *on* and *off* state is impossible to set. The states with intermediate intensities might correspond to some gray state, e.g., trion emissions [236].

- Type *N* (Figure 5.15(d)) is the category of critical importance, in which the QDs exhibit strong blinking suppression or nearly non-blinking behavior. Accordingly, the contribution from the *off* state to the count rate distribution is very small.

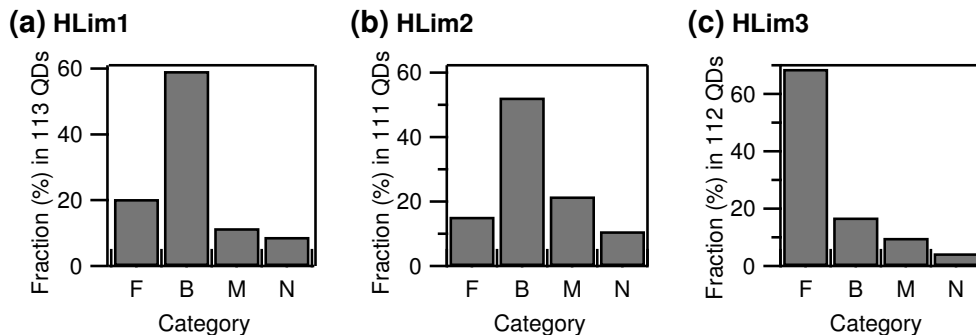


Figure 5.16: Category distributions of fluorescence time traces of *HLim* series: (a) *HLim1*, (b) *HLim2*, and (c) *HLim3*.

Single particle fluorescence time traces corresponding to these four categories can be found in all three samples of *HLim* series. The category distributions for sample *HLim1*, *HLim2* and *HLim3* are shown in Figure 5.16. Category *F* dominates (~69% of QDs) in sample *HLim3* whereas the category *B* dominates in the other two samples. This may explain why sample *HLim3* has the lowest quantum yield in solution. Moreover, too large amount of Se in InP/ZnSeS QDs is believed to reduce the crystallinity of the shell [52]. Thus, the presence of trap states in the shell may lead to non-radiative pathways and prevent a QD from emitting for a long time. In contrast, there are 9% and 11% nearly non-blinking QDs (category *N*) in *HLim1* and *HLim2* samples, respectively, implying that the blinking of some InP/ZnSeS QDs has been suppressed effectively.

5.4.1.5 Statistics of *on* and *off* times

The *on time fraction*, defined as the fraction of the total *on* time during the total measurement time, is extensively used to quantitatively characterize the blinking behavior of single QDs [71, 76, 82]. The *on* time fraction distributions of the *HLim* series were analyzed here. As illustrated in Figure 5.17, *HLim3* sample has more QDs which have a short *on* time fraction compared with *HLim1* and *HLim2* samples. This is consistent with the results of the category distributions, since category *F* obviously corresponds to a short *on* time fraction (generally below 40%). The overall *on* time fractions (the sum of *on* times from all QDs divided by the overall measurement time [305]) of *HLim1*, *HLim2* and *HLim3* are 63%, 69% and 42%, respectively. The fractions of QDs whose *on* time fraction is above 80% in *HLim1*, *HLim2* and *HLim3* samples are 33%, 43% and 22%, respectively. All these results show that *HLim2* possesses the strongest blinking suppression among the three samples.

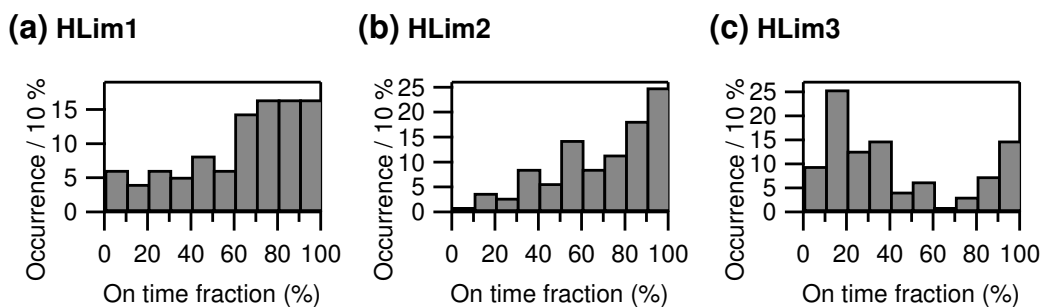


Figure 5.17: *On* time fraction distributions of fluorescence blinking of *HLim* series: (a) *HLim1*, (b) *HLim2*, and (c) *HLim3*.

The probability distributions extracted from the *on* and *off* time histograms were studied as well. As commonly found in QD blinking, introduced in Section 2.3.3.1, for

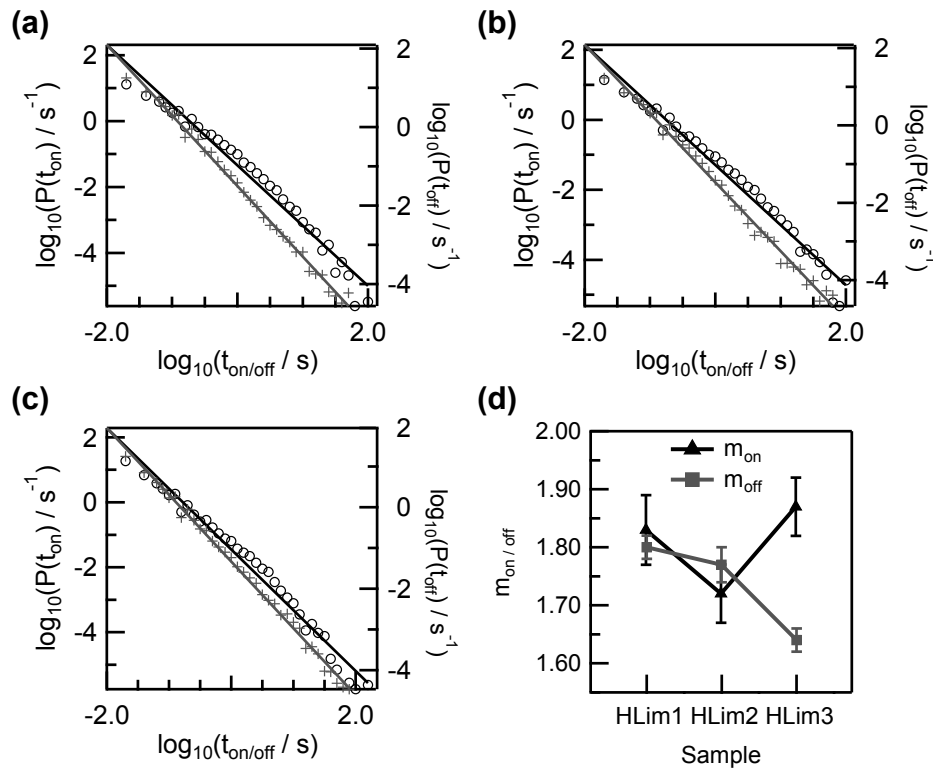


Figure 5.18: Probability distributions of the *on* (open circles) and *off* (gray crosses) times of the *HLim* series: (a) *HLim1*, (b) *HLim2* and (c) *HLim3*. The lines denote the least-squares fits. (d) Comparison of the inverse power law exponents m_{on} (black triangles) and m_{off} (gray squares) of different samples.

all three samples, the *on* or *off* time probabilities feature a linear distribution on a log-log scale as shown in Figure 5.18(a)–(c), namely that the distribution follows an inverse power law $P(t) = At^{-m}$. The exponents m_{on} and m_{off} of the power law distributions were determined by linear least-squares fits for the three samples and compared in Figure 5.18(d). *HLim3* has the largest m_{on} and smallest m_{off} , indicating large fraction of *on* times distributing in short times and large fraction of *off* times distributing in long times. The m_{on} of *HLim2* is smaller than that of *HLim1*, which means that *HLim2* has a higher probability for long *on* times. In contrast, no significant difference has been observed between the m_{off} of *HLim1* and that of *HLim2*. This implies a similar time scale of the “*off* to *on*” process for these two samples.

5.4.2 *H* and *L* series

In order to avoid cut by the long-pass filter, single particle measurements of sample series *H* and *L* excited by a 445 nm laser at room temperature were conducted, and a 458 nm

long-pass filter was used in the detection path of the setup to block the excitation light. The excitation intensity was $\sim 344 \text{ W/cm}^2$ (0.34 kW/cm^2) (also see Table 3.2).

5.4.2.1 Typical emission spectra

Single particle spectra of the *H* and the *L* series are similar to those of the *HLim* series. A typical spectrum is shown in Figure 5.19, in which obvious spectral asymmetry can also be observed. Since the spectral position of the edge of the long-pass filter (458 nm) for this measurement is far from the wavelength range of the emission, the spectral asymmetry cannot be attributed to the long-pass filter, but probably to some intrinsic optical properties of these InP/ZnSeS QDs. The rationale behind this phenomenon may be better understood with the results of the experiments at cryogenic temperature (see Section 5.5.1).

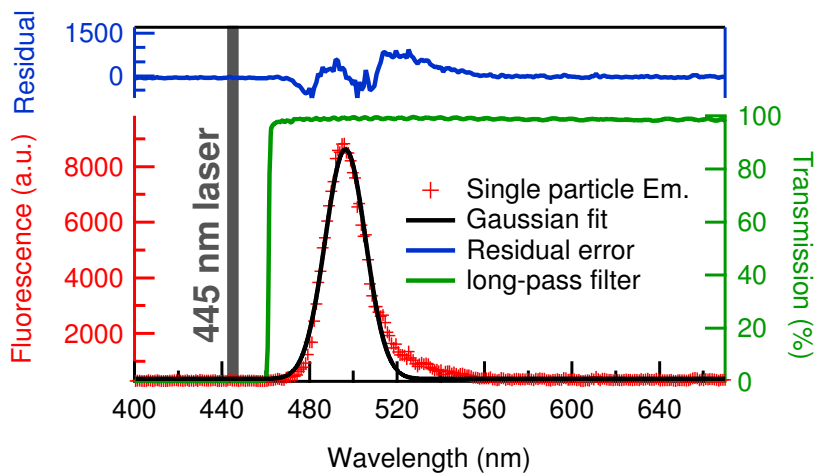


Figure 5.19: Typical emission spectrum of a single QD from *L4* excited at 445 nm and the transmission curve of the 458 nm long-pass filter used. The black solid curve is the Gaussian fit and the blue line is the residual error of the fit. The integration time of the spectrum was one second.

5.4.2.2 Statics of emission spectra

Because the long-pass filter was spectrally far away from the emission, the emission maximum of single particles belong to the *L* and *H* series showed symmetrical Gaussian distributions. As an example, distributions of emission maxima and FWHMs of the emission peaks in single QD spectra of *L4* sample are given in Figure 5.20. The values of the *L* and the *H* series are listed in Table 5.7. The average emission maxima of single particles were consistent with the ensemble results.

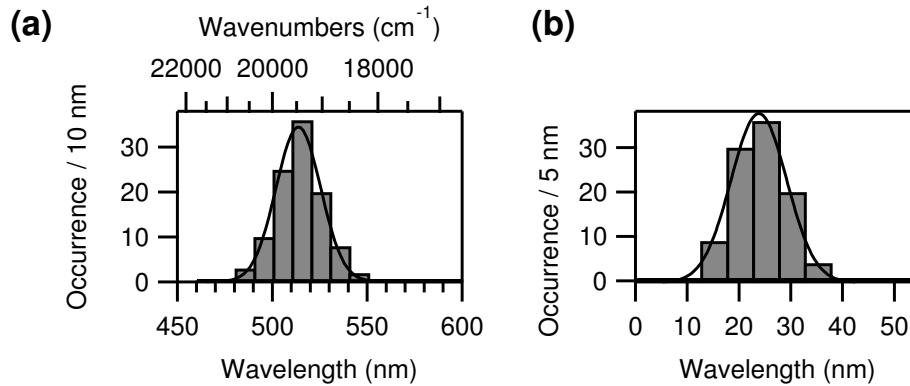


Figure 5.20: Distributions of emission maxima and FWHMs of the emission peaks in single QD spectra of *L4* sample. The solid curves in the histograms are the corresponding Gaussian fits.

Table 5.7: Statistical results of emission maxima and FWHMs of the emission peaks in single particle spectra of the *L* and the *H* series.

sample	Peak Max. (nm)	Peak FWHM (nm)	Peak FWHM (cm^{-1})
<i>H1</i>	514.7 ± 15.8	24.7 ± 8.1	959 ± 362
<i>H2</i>	514.0 ± 15.5	23.6 ± 8.6	894 ± 326
<i>L1</i>	512.5 ± 16.8	24.3 ± 9.7	926 ± 369
<i>L2</i>	514.0 ± 14.3	23.3 ± 7.8	882 ± 295
<i>L3</i>	516.6 ± 14.5	24.0 ± 6.5	900 ± 244
<i>L4</i>	513.9 ± 13.8	23.8 ± 6.3	902 ± 240
<i>L5</i>	530.8 ± 15.8	24.2 ± 9.1	859 ± 323

5.4.2.3 Time traces and *on/off* times

The fluorescence time traces of the *H* and the *L* series were analyzed. In contrast to the *HLim* series, almost all of the time traces in the *H* and the *L* series featured binary blinking behaviors, although a few “gray states” were also visible (Figure 5.22). Moreover, the *on* time fraction distributions of the *L* series were found to be quite different from those of the *H* series. As shown in Figure 5.21, the *on* time fractions are concentrated in the interval between 90% and 100% for the *L* series, whereas the *on* time fractions of the *H* series are more uniformly distributed, especially for that of sample *H1*. This implies that a synthesis at lower temperatures can suppress the blinking effectively for the system investigated.

Recently, the term *largely non-blinking* has been introduced by Vela et al. as a blinking behavior whose overall *on* time fraction is above 80% [305]. Regarding the distributions shown in Figure 5.21(a)–(e), largely non-blinking QDs dominate for all samples belonging to the *L* series. Figure 5.22 presents some representative time traces of these largely

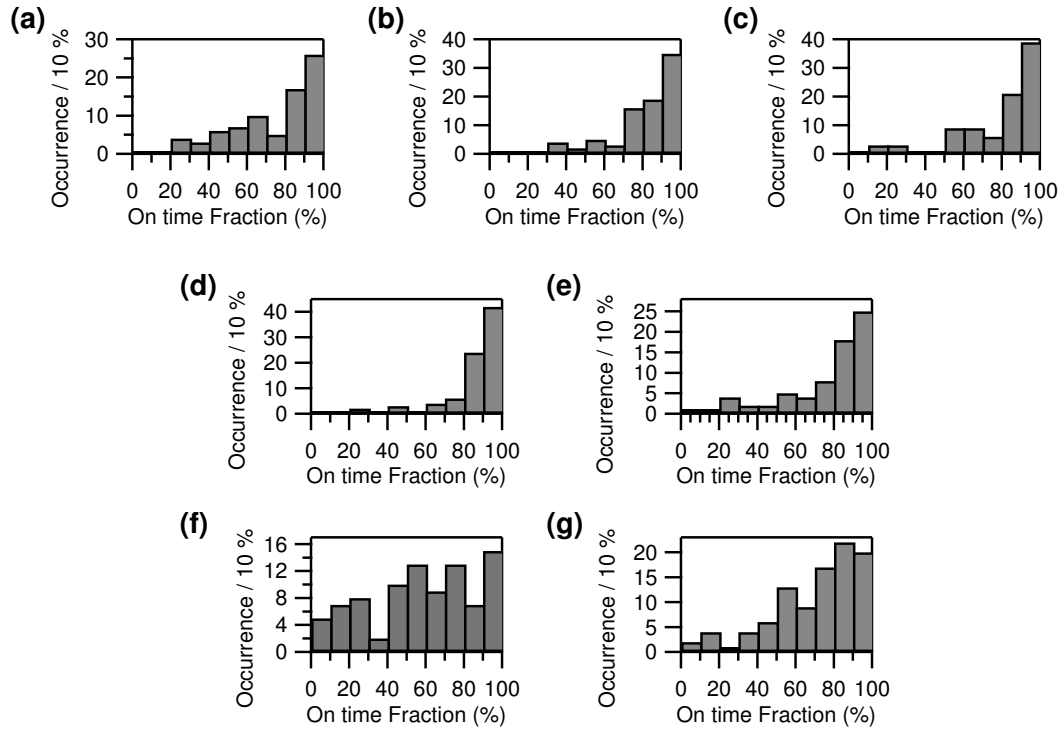


Figure 5.21: On time fraction distributions of sample (a) *L1*, (b) *L2*, (c) *L3*, (d) *L4*, (e) *L5*, (f) *H1* and (g) *H2*.

non-blinking QDs. From Figure 5.22(a) to Figure 5.22(d), the *on* time fractions of the corresponding QDs are 81%, 91%, 97%, 99%, respectively. Part of the time traces (marked with gray background) are expanded and plotted in the lower panels of the sub-figures. The combination of the figures in full range and a sub-range shows the self-similarity and complexity of the traces on different time scales. Considering that most of the QDs in the *L* series are largely non-blinking, it can be concluded that the blinking has been strongly suppressed in these samples.

As a more quantitative comparison of the samples with various amounts of Se in the *L* and *H* series, the percentage of QDs with an *on* time fraction over 80% and over 90% are displayed in Figure 5.23(a), respectively. Sample *L4* has the strongest blinking suppression, which means that about 80% and 51% of the QDs which have an *on* time fraction above 80% and above 90%, respectively. Samples with either less or larger amounts of Se lead to lower *on* time fractions. Additionally, the overall *on* time fractions reveal a similar trend (Figure 5.23(b)).

Furthermore, the samples of the *H* and *L* series also exhibit power law probability distributions of the *on* and *off* times. As an example, the result of *L4* is displayed in Figure 5.24(a). For comparison, *on* and *off* time coefficients (the power law exponents) of

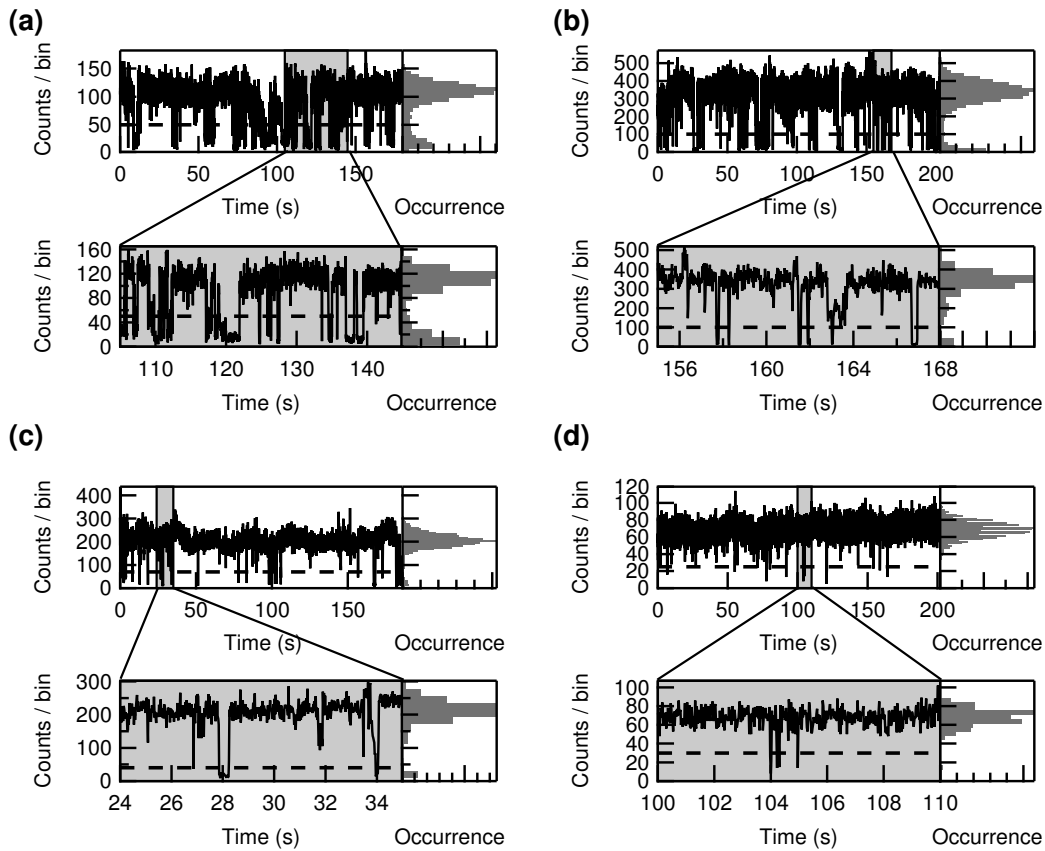


Figure 5.22: Representative fluorescence time traces with the corresponding distributions of count rates (right panels) of largely non-blinking InP/ZnSeS QDs (with the overall *on* time fraction over 80%). The calculated *on* time fractions are (a) 81%, (b) 91%, (c) 97% and (d) 99%, respectively. The lower panel in each sub-figure is the enlarged view of part of the time trace (the part marked with gray background), which shows the self-similarity and complexity of the traces on different time scales. Dashed lines denote the threshold values chosen for the discrimination of the *on* and *off* states. Time bin: 20 ms.

the *H* and *L* series are presented in Figure 5.24(b). For the *L*, m_{on} decreases from 1.48 to 1.28, while the *off* time coefficient m_{off} is rather insensitive to the Se amount and fluctuates around 1.55 in a narrow range. This trend is similar to the case of *HLim1* and *HLim2* (see Figure 5.18(d)) and has been observed by Zan et al. in InP/ZnS QDs synthesized under various conditions [86]. In conjunction with the ensemble characterizations, the single particle experiments have further emphasized the important function of the amount of Se as a buffer material. It seems that an appropriate amount of Se can optimize the internal structure of the QDs by reducing the interfacial strain and defects. Thus, the crystallinity has been improved, leading to a strong blinking suppression.

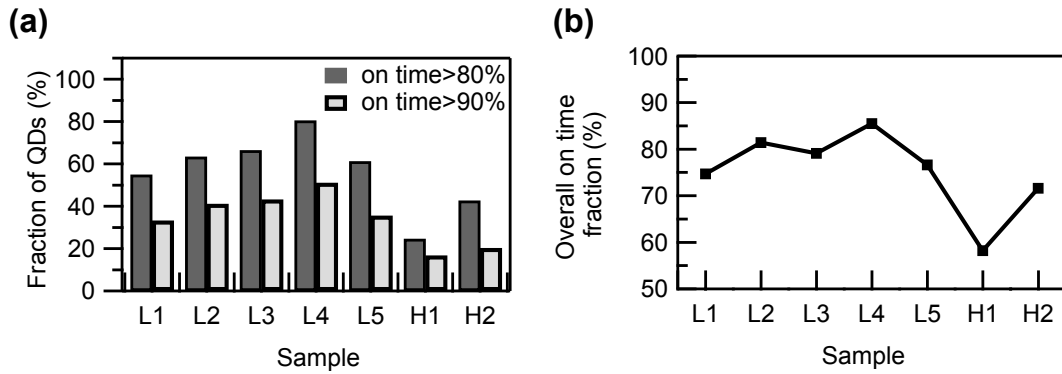


Figure 5.23: Comparison of the samples of *L* series and *H* series: (a) Fraction of QDs with an *on* time fraction $>80\%$ and $>90\%$, respectively. (b) Overall *on* time fraction.

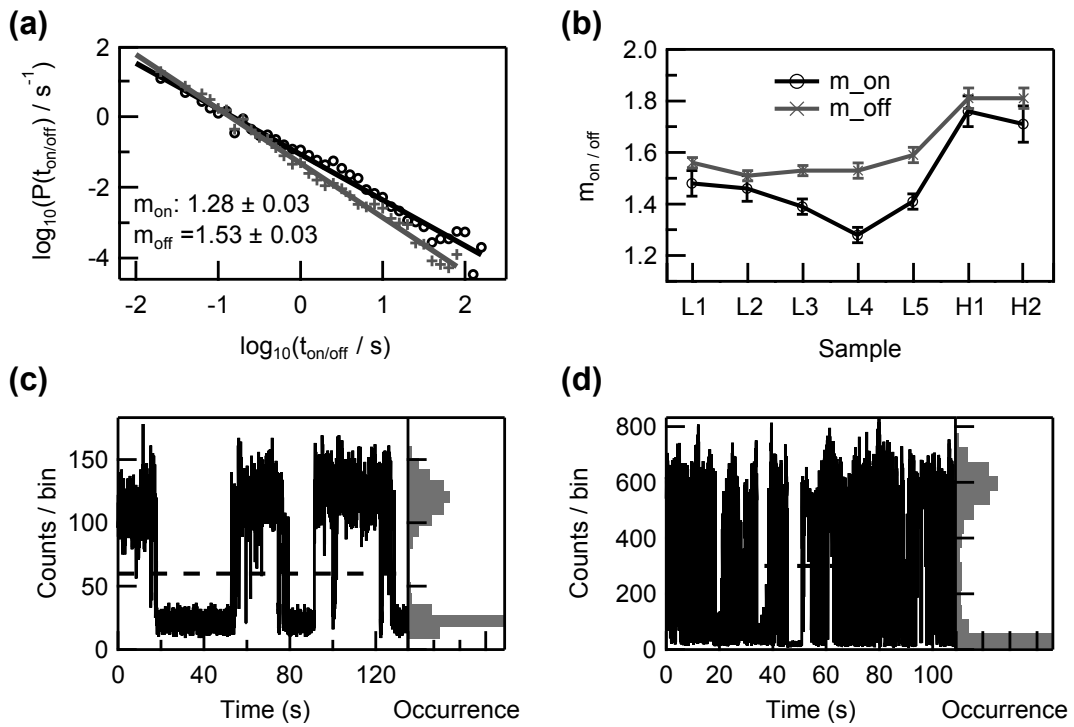


Figure 5.24: (a) Probability distributions of the *on* or *off* times of sample *L4*. (b) Comparison of the inverse power law exponents m_{on} and m_{off} of different samples. (c) A fluorescence blinking trace reveals a digital blinking behavior. $m_{on} = 1.15 \pm 0.08$ and $m_{off} = 1.26 \pm 0.13$ from 46 events. (d) A fluorescence blinking trace reveals a chaotic blinking behavior. $m_{on} = 1.54 \pm 0.16$ and $m_{off} = 1.80 \pm 0.11$ from 284 events.

Another interesting phenomenon which can be found in Figure 5.24(b) is that both *on* and *off* time coefficients of the *H* series are larger than those of the *L* series, but similar to those of the *HLim* series (Figure 5.18(d)). It is worth noting that even with the same *on* time fraction, m_{on} and m_{off} may be different for different particles relating to different

blinking behaviors. For example, with similar *on* time fractions ($\sim 63\%$), if both m_{on} and m_{off} are small ($m_{\text{on}} = 1.15$ and $m_{\text{off}} = 1.26$) as shown in Figure 5.24(c), the fluorescence time trace exhibits more digital blinking behavior, whereas if both m_{on} and m_{off} are large ($m_{\text{on}} = 1.54$ and $m_{\text{off}} = 1.80$) as shown in Figure 5.24(d), the fluorescence blinking is more chaotic. The different numbers of *on* or *off* events (46 versus 284) of the two time traces in this example further illustrate the different blinking behaviors. In addition, the analysis here also reflects that *on* time fraction and $m_{\text{on/off}}$ are two different ways to characterize the fluorescence blinking.

5.4.2.4 Influence of surface ligands

As mentioned in Section 2.3.3.3, the ligand related surface states have been considered as a crucial factor for the fluorescence quantum yield and blinking behavior of QDs [69–72, 75]. Therefore, the influence of surface ligands on quantum yield and blinking behavior of the as-prepared InP/ZnSeS QDs was studied. After harsh purification (six cycles with chloroform and an excess of ethanol), as shown in Figure 5.25(a), the average brightness (average value of the signal to noise ratios of QDs in the image) dropped by 18%. Meanwhile, the overall *on* time fraction of QDs decreased from 86% to 76%, and the fraction of the largely non-blinking QDs decreased from 81% to 50%. However, when additional 0.1 mL 1-dodecanethiol (DDT) was added, the intensity and blinking behavior basically recovered (brightness back to 0.91 of the original value).

Similar experiments were performed at the ensemble level. After harsh purification, some amount of ligands (DDT or OA) was added to the solution and the corresponding QYs were compared. The results shown in Figure 5.25(b) indicate that after ligand removal, addition of DDT may partially recover the QY of the QDs. In contrast, with an increasing amount of oleic acid (OA) added, the fluorescence was gradually quenched. These results implied that DDT may play an important role for the bulk emission quantum yield and blinking behaviors of InP/ZnSeS QDs. A tentative mechanism is outlined in the following:

In solution, ligands tend to reach a dynamic adsorption/desorption equilibrium with the QD surface. After harsh purification, the number of attached ligands per QD decreases dramatically. Thus, the passivation of QDs becomes worse, because of many surface defects and surface “dangling bonds”, which may quench the emission. Thiol-containing chemicals have been reported to be responsible for blinking suppression by mechanisms such as charge compensation at the surface traps [69, 82]. This may explain the different QYs when DDT and OA were added, since only the former compound contains a thiol group.

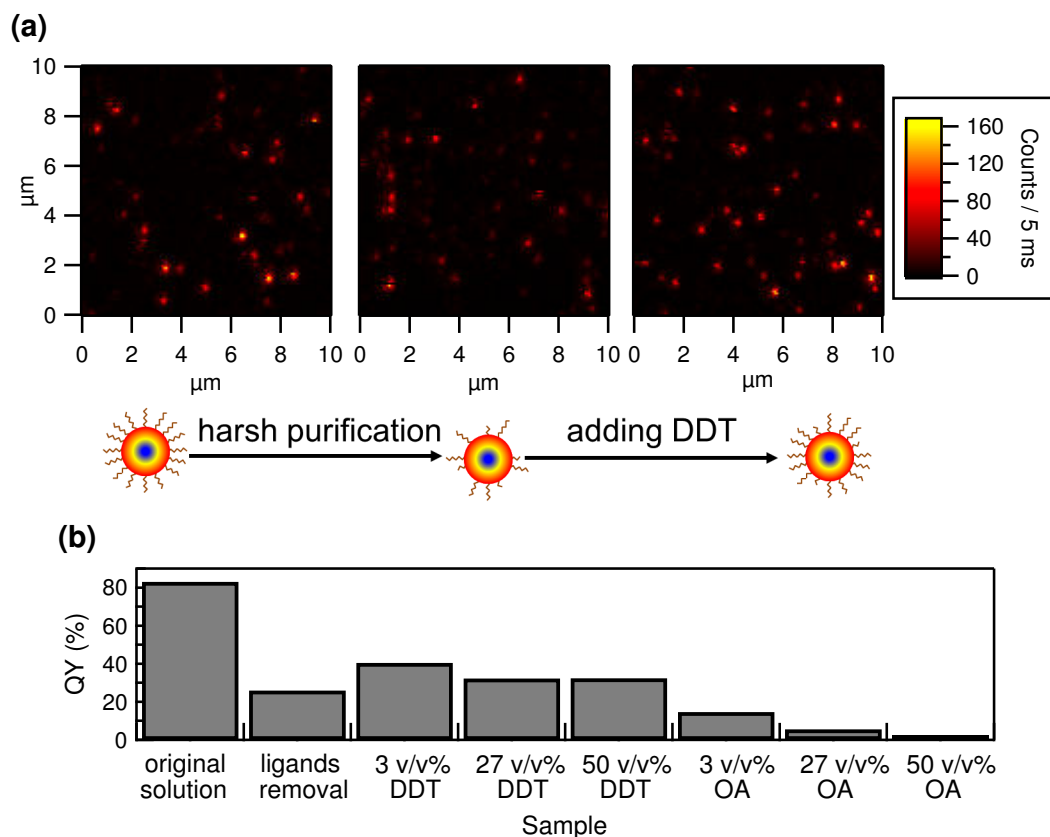


Figure 5.25: (a) Confocal fluorescence microscope images of the sample *L4* original (left), after harsh purification (middle) and after adding DDT again (right). The ratio of the average brightness of QDs among these three sample is about 1 : 0.66 : 0.91 from left to right. The illustration below shows the assumption with respect to the surface ligand states. (b) Quantum yield comparison of an original InP/ZnSeS QD solution, after ligand removal and when different amounts of ligands (1-dodecanethiol (DDT) or oleic acid (OA)) were added again.

5.5 Single particle measurements at cryogenic temperature ($T = 4.5$ K)

To further investigate the photophysical properties of InP/ZnSeS QDs, single particle measurements of *L* series samples *L1*, *L4* and *L5* at cryogenic temperature ($T = 4.5$ K) were performed with the setup described in Section 3.4.3. Because excitation with a 445 nm laser led to a low signal to noise ratio (approximately 3.1 with a time bin of 10 ms) and low signal to background ratio (about 1.08), a 488 nm OPSL laser was used as the excitation source. The excitation intensity was ~ 1045 W/cm². The samples were embedded in a PMMA film by spin-coating and measured in ~ 10 mbar helium atmosphere. Other experimental details are listed in Table 3.2.

5.5.1 Typical emission spectrum of InP/ZnSeS QDs at 4.5 K

A typical emission spectrum of a single InP/ZnSeS QD at 4.5 K with an integration time of 5 seconds is shown in Figure 5.26(a) (black curve). Compared with the spectrum of a single CdSe/CdS/ZnS QD at 4.5 K which has a zero-phonon line (ZPL) with a spectral resolution limited linewidth as displayed in Figure 5.26(b), the spectrum of a single InP/ZnSeS QD within the same magnitude of spectral range and the same integration time reveals no ZPL but a much broader main peak (band edge emission, $\sim 190 \text{ cm}^{-1}$) accompanied by a broad phonon sideband (PSB). The broad band edge emission implies that either significant coupling of the exciton to phonons with relatively low frequencies or very strong spectral diffusion are involved. Moreover, the asymmetrical broad peak observed at low temperature may have the same source as the slight spectral asymmetry of single InP/ZnSeS QD emission at room temperature.

5.5.2 Phonons contributions

In contrast to the situation of CdSe QDs, the reports on low temperature spectroscopy of InP based QDs are very rare, especially at the single particle level and/or measured at cryogenic temperatures [92, 110, 308]. Furthermore, considering the spectral resolution of the measurement ($\sim 17 \text{ cm}^{-1}$) and the composition of the InP/ZnSeS QDs, various phonon contributions coupled to the exciton will be discussed in the following.

5.5.2.1 Optical phonons

Since Fröhlich coupling involves the interactions between the longitudinal optical (LO) phonons and the polarization of the exciton (see Section 2.3.5.1), it is polar in nature. As a result, the magnitude of Fröhlich coupling is strongly dependent on the ionic polarization of the crystal, which is related to the static and high-frequency dielectric constants (ϵ_0 and ϵ_∞ , respectively) [298]. As listed in Table 5.8, both ϵ_0 and ϵ_∞ of InP are much larger than those of other semiconductors. This is not very surprising due to the more covalent character of the bonds in materials from group III-V. More specifically, a measurement of the coupling strength of the electrons and LO phonons can be represented by the Fröhlich coupling constant α_F defined as [309]:

$$\alpha_F = \frac{1}{2} \frac{e^2 / \sqrt{\hbar/2m_c^\alpha \omega_{LO}}}{\hbar\omega_{LO}} \left(\frac{1}{\epsilon_\infty} - \frac{1}{\epsilon_0} \right) \quad (5.5)$$

where e is the electron charge, m_c^α is the electron effective mass (conductivity mass) and ω_{LO} is the LO phonon frequency.

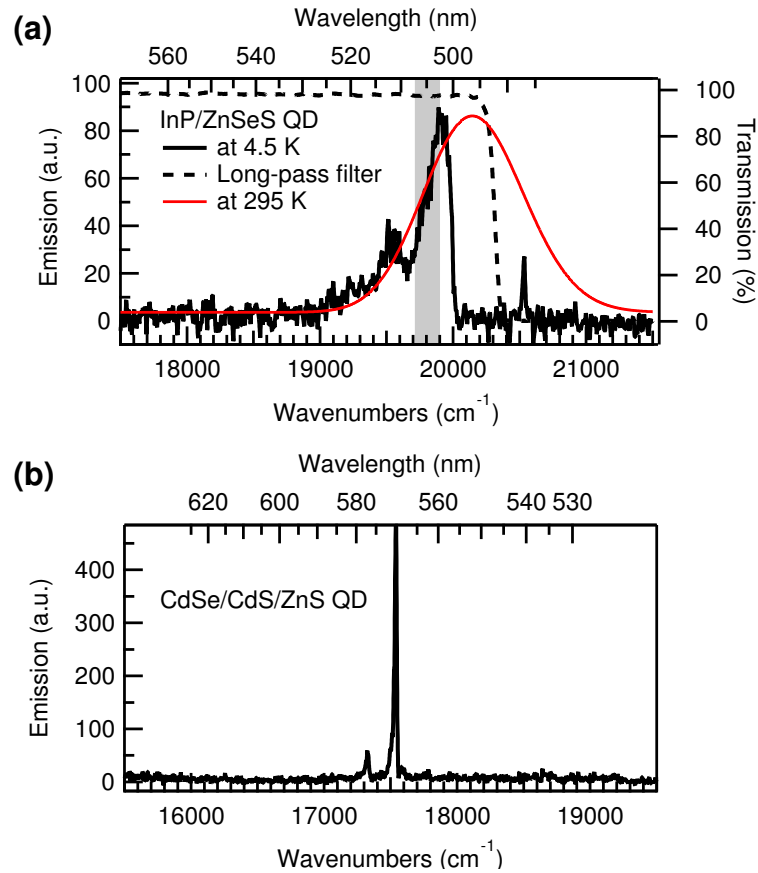


Figure 5.26: Typical emission spectra of (a) a single InP/ZnSeS QD (solid black curve) and (b) a single CdSe/CdS/ZnS QD in a PMMA film at 4.5 K excited at 488 nm with the same magnitude of spectral range. The region highlighted in gray with a width of 170 cm^{-1} denotes the transitions near the band edge at the lower energy side. The dashed line in (a) represents the transmission curve of the long-pass filter used at 4.5 K. The red curve in (a) is a typical emission spectrum of a single InP/ZnSeS QD in a PMMA film at 295 K excited at 445 nm. Integration time: 5 s.

Considering the smaller α_F of InP compared with those of other semiconductors shown in Table 5.8, weaker Fröhlich coupling is expected for InP. Moreover, the α_F values of zinc blende ZnSe and ZnS are comparable with the values of wurtzite CdSe and CdS, which indicates that the Fröhlich coupling strength is not determined by the crystal structure, but rather depends on the polarity of the bonds in the crystal. This suggests that the electron coupling to transverse optical phonons (TOs) for InP is also relatively strong and may contribute to the spectrum. Indeed, unlike for CdSe QDs, both the participation of LO ($\sim 342\text{ cm}^{-1}$) and TO ($\sim 310\text{ cm}^{-1}$) phonons in InP QDs (2.9 nm) have been observed by three-pulse photon-echo experiments in Ref. [110]. Another evidence is that the Huang-Rhys parameters S of the coupling to LO phonons obtained from the fitting based on the

Table 5.8: Static dielectric constants ϵ_0 , high-frequency dielectric constants ϵ_∞ and Fröhlich coupling constants α_F of some bulk semiconductor crystals [298].

Structures	Zinc blende			Wurtzite		
	InP	ZnSe	ZnS	CdSe	CdS	ZnS
ϵ_0	12.9	8.9	8.3	9.29	10.2	8.1
ϵ_∞	9.9	5.9	5.1	6.20	5.4	5.4
α_F	0.15	0.432	0.63	0.46	0.514	-

same experiment in Ref. [110] is 0.08, which is smaller than the value reported for CdSe QDs with a similar size ($S = 0.18$) [310].

Furthermore, Seong et al. studied the size-dependent Raman spectra of InP quantum dots [311]. They concluded that the LO phonon frequency decreases while the TO phonon frequency increases when the QD size is reduced, but only $\sim 2 \text{ cm}^{-1}$ difference in energy between QDs with diameters of 3.5 nm and 5.2 nm has been found. Therefore, as generally outlined in Section 2.3.5.1, the energies of optical phonons are almost size independent.

Based on Ref. [298], optical phonon energies of the relevant semiconductors are tabulated in Table 5.9. Since LO phonons dominate in the polar II-VI group semiconductors, TO phonons of the ZnSeS shell have not been considered in this study.

Table 5.9: Some optical phonon energies of InP, ZnSe and ZnS bulk semiconductors with zinc blende crystal structure [298].

Materials	$\hbar\omega_{LO} (\text{cm}^{-1})$	$\hbar\omega_{TO} (\text{cm}^{-1})$
InP	342	310
ZnSe	252	-
ZnS	350	-

5.5.2.2 Acoustic phonons

Unlike optical phonons, the frequencies of acoustic phonons are inversely proportional to the size of the nanocrystals according to Lamb theory (see Section 2.3.5.1). At the ensemble level, Narayanaswamy et al. have reported that both optical and acoustic phonons contributed to line broadenings in 1.8 nm and 3 nm InP/ZnS core-shell nanocrystals, and the acoustic phonon contributions were dominant at low temperatures [281], emphasizing the significant role that acoustic phonons play in the spectral linewidth at cryogenic temperature for InP based QDs. At the sub-ensemble level, Banin et al. [110] studied InP QDs smaller than 5 nm by nanosecond hole burning and femtosecond three-pulse phonon

echo experiments. Similar to the single QD emission spectrum shown in Figure 5.26(a), a broad main transition peak was found in the hole-burning spectra, and the authors observed narrow features the widths from 10 meV (80.6 cm^{-1}) to 20 meV (161.3 cm^{-1}) for the investigated InP QDs with diameters ranging from 4.1 nm to 2.2 nm. The line-widths have been attributed to coupling of the exciton to acoustic modes with low frequencies.

Table 5.10: Eigenvalues (η_{ln} based on Talati calculation [261] and η_{ln}^* based on Murray's method [264, 268]) and the corresponding energies ($\hbar\omega_{ln}$ and $\hbar\omega_{ln}^*$, respectively) of spheroidal and torsional modes of acoustic phonons of InP QDs with a diameter of 2.9 nm. The transverse velocity v_t : 3080 m/s of InP [261] was taken for the calculation.

Type	l	n	η_{ln}	η_{ln}^*	$\hbar\omega_{ln} \text{ (cm}^{-1}\text{)}$	$\hbar\omega_{ln}^* \text{ (cm}^{-1}\text{)}$
Spheroidal	0	0	3.283	–	37.1	–
Spheroidal	0	1	7.310	5.995	82.6	67.7
Spheroidal	1	0	–	3.647	–	41.2
Spheroidal	1	1	6.256	7.310	70.7	82.6
Spheroidal	2	0	–	2.653	–	30.0
Spheroidal	2	1	5.774	5.166	65.2	58.4
Torsional	1	0	5.184	5.764	58.6	65.1
Torsional	1	1	8.468	9.096	95.7	102.8
Torsional	2	0	–	2.502	–	28.3
Torsional	2	1	6.566	7.137	74.2	80.6

Based on Lamb's theory, the frequency of the acoustic phonon ω_{ln} should be calculated by $\omega_{ln} = 2\eta_{ln}v_t/d$, which is deduced from Equation 2.45 and Equation 2.47. The dimensionless eigenvalue η_{ln} here contains the ratio of longitudinal to transverse sound velocity (v_l/v_t) of the material. To estimate the acoustic phonon energies of InP/ZnSeS QDs, the QD diameter d chosen for the calculation needs to be considered. Since the exciton wavefunctions will extend into the shell which has a gradient composition, neither using the size of the core nor of the whole particle seems appropriate [281]. Therefore, as a rough estimate, an average diameter 2.9 nm (core (1.3 nm), core-shell QDs (4.5 nm)) was selected for the calculation. With the eigenvalues provided by Ref. [261], the energies corresponding to various acoustic phonon modes were calculated, as listed in Table 5.10. Unfortunately, it is not possible to assign any specific phonon energies to the spectrum shown in Figure 5.26(a). Nevertheless, the monotonous increase of the intensity within the range highlighted in gray in the spectrum implies that the breathing mode as well as other low frequency surface modes ($n = 0$) might contribute significantly. Taking into account the possibility of spectral diffusion and the linewidths of acoustic phonon replicas, a roughly estimated energy region with a maximum spectral distance of 170 cm^{-1} to the

purely electronic transition line is ascribed to the electron coupling to acoustic modes in this study (marked gray in Figure 5.26(a)).

5.5.3 Categories of single particle spectra

As shown in Figure 5.26(a), not only acoustic phonons are impossible to assign, but also the optical phonon replicas are difficult to be distinguished from each other. In order to have a better signal to noise ratio, a series of spectra from the same QD at different times were superposed after proper shifting every spectrum to avoid a possible broadening from spectral shifts. The shifts were determined such that the overlap of single spectra was maximized. As seen in Figure 5.27, the emission spectra of single InP/ZnSeS QDs can be categorized into three types:

- *A* type: The spectrum exhibits two distinct peaks, and the PSB corresponding to the LO and TO phonons of InP (or LO phonons of ZnS) can be distinguished from the main peak. At the spectral position where the LO phonon of ZnSe is expected (phonon energy 252 cm^{-1} , as marked by the rightmost vertical line in the spectra), an obvious dip appears instead of a peak, implying the absence of coupling to ZnSe LO phonons.
- *B* type: The spectral region where optical phonons are expected appears as shoulder. This might be ascribed to an increasing contribution from the ZnSe LO phonon (252 cm^{-1}) coupling to the exciton.
- *C* type: The PSB is more difficult to resolve in the spectrum and the entire range on the low energy side of the purely electronic transition in the spectrum shows a monotonous increase, which indicates that the coupling of ZnSe LO phonons to the exciton might be stronger compared with the situations of the other two types.

All three categories were observed in each of the three samples. Especially, the existence of type *B* and *C* in sample *L1* (InP/ZnS QDs without Se) indicates that this categorization may have a large error due to the lack of strict quantitative distinctions between the types. However, statistically, the category distributions of these three samples might still give some hints: As presented in Figure 5.28, the number of spectra belonging to type *A* decreases from *L1* to *L5* while the number of spectra of type *C* increases. Based on the speculations above, this is a hint that in *L1* sample, the excitons are mainly confined in the core, but with increasing amount of Se, the excitons extend more and more into the ZnSeS shell, and therefore the coupling to ZnSe phonons becomes stronger and more

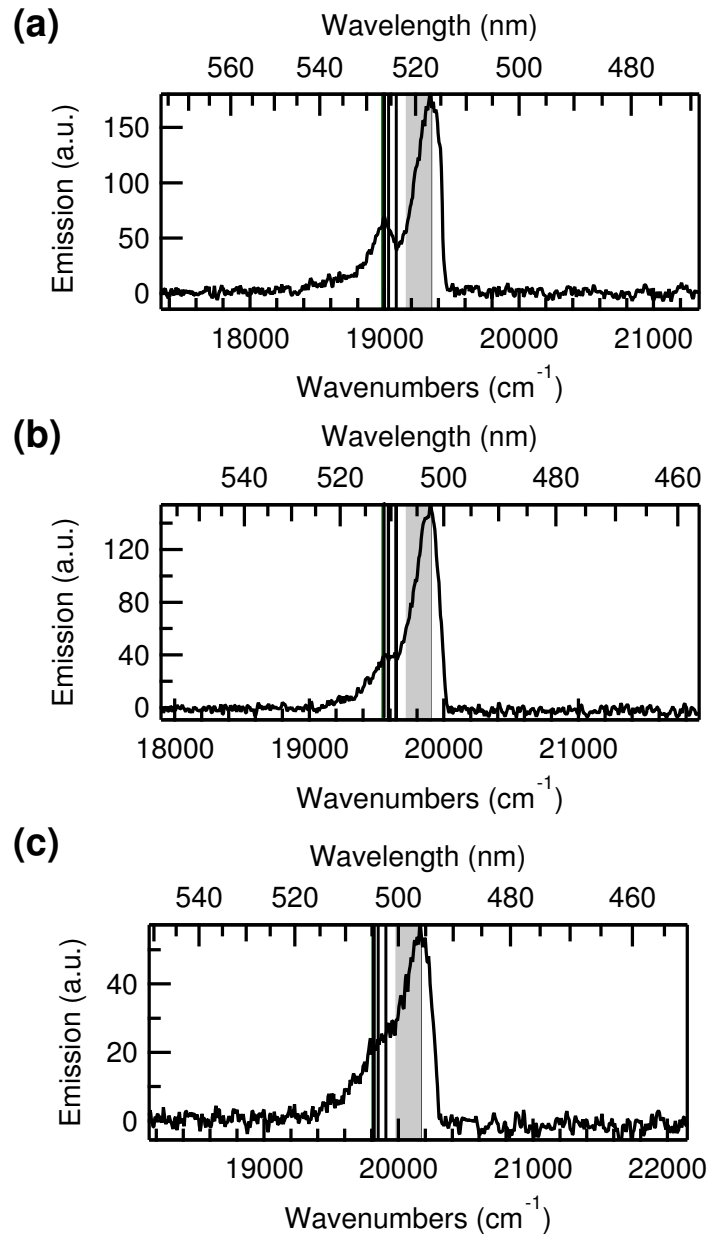


Figure 5.27: Representative emission spectra of single InP/ZnSeS QDs of (a) *A* type (b) *B* type and (c) *C* type. Spectra were obtained by the superposition of single spectra each with integration time of 5 s after proper shift as explained in the main text. The vertical lines mark the positions whose spectral distances to the main peak maxima are 350 cm^{-1} (LO phonon, ZnS), 342 cm^{-1} (LO phonon of InP, may not be able to distinguished by the eye from 350 cm^{-1}), 310 cm^{-1} (TO phonon, InP) and 252 cm^{-1} (LO phonon, ZnSe), from left to right, respectively. The region highlighted in gray having a width of 170 cm^{-1} denotes the transitions near the band edge which may originate from coupling to acoustic phonons.

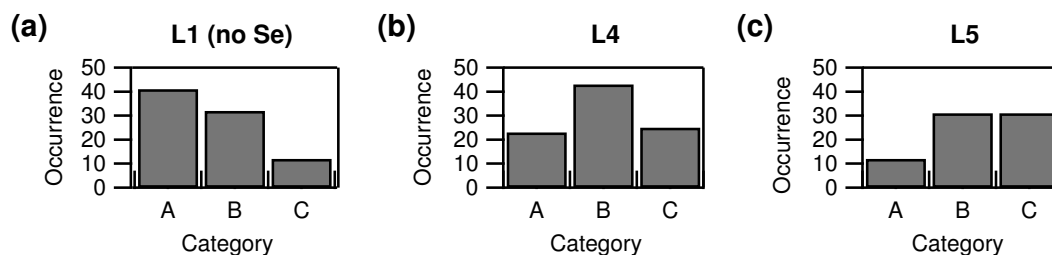


Figure 5.28: Spectral category distributions of InP/ZnSeS QDs at 4.5 K: (a) *L1*, (b) *L4* and (c) *L5*.

probable. It is worth noting that even in sample *L1*, the charge carriers may extend to the ZnS shell as it has been reported that InP/ZnS QDs can also form a (thin) radial composition gradient at 300°C or 260°C [4, 86]. In addition, for InP/ZnSeS QDs, the real phonon energies could be slightly different from the values of pure InP, ZnSe or ZnS, since the QDs have a radial gradient alloy structure.

5.5.4 Average optical phonon energies

Average optical phonon energies were calculated by identification of the spectral positions of the purely excitonic transitions and the PSBs. The spectral position of a PSB was defined by the position of the maximum of a resolved PSB (Figure 5.27(a)) or by the middle position of a flat PSB (Figure 5.27(b)), respectively. Most of the *C* type spectra were discarded for this analysis due to the difficulty in peak discrimination.

The results are represented in Figure 5.29(a)–(c). The resulting average optical phonon energies of *L1*, *L4* and *L5* are 332 cm⁻¹, 321 cm⁻¹ and 320 cm⁻¹, respectively. These values are all lie between the LO phonon energy (342 cm⁻¹) and TO phonon energy (310 cm⁻¹) of InP. However, the slightly smaller values of *L4* and *L5* may imply some contribution from the ZnSe shell, since the LO phonon energy of ZnSe is 252 cm⁻¹. Furthermore, there is no correlation between the average optical phonon energy and emission maximum position of all QDs.

5.5.5 Fluorescence blinking at 4.5 K

Due to the lower detection efficiency of the setup for cryogenic temperature measurements compared with the setup for room temperature measurements (see Section 3.4.3 and Section 3.4.4), the time resolution (time bin) of the fluorescence time trace at 4.5 K had to be increased up to 100 ms in order to acquire a sufficient signal to noise ratio. Since all possible blinking events within a time bin were smeared out and the corresponding intensities were converted to an average value, the increase of time bin may lead to some

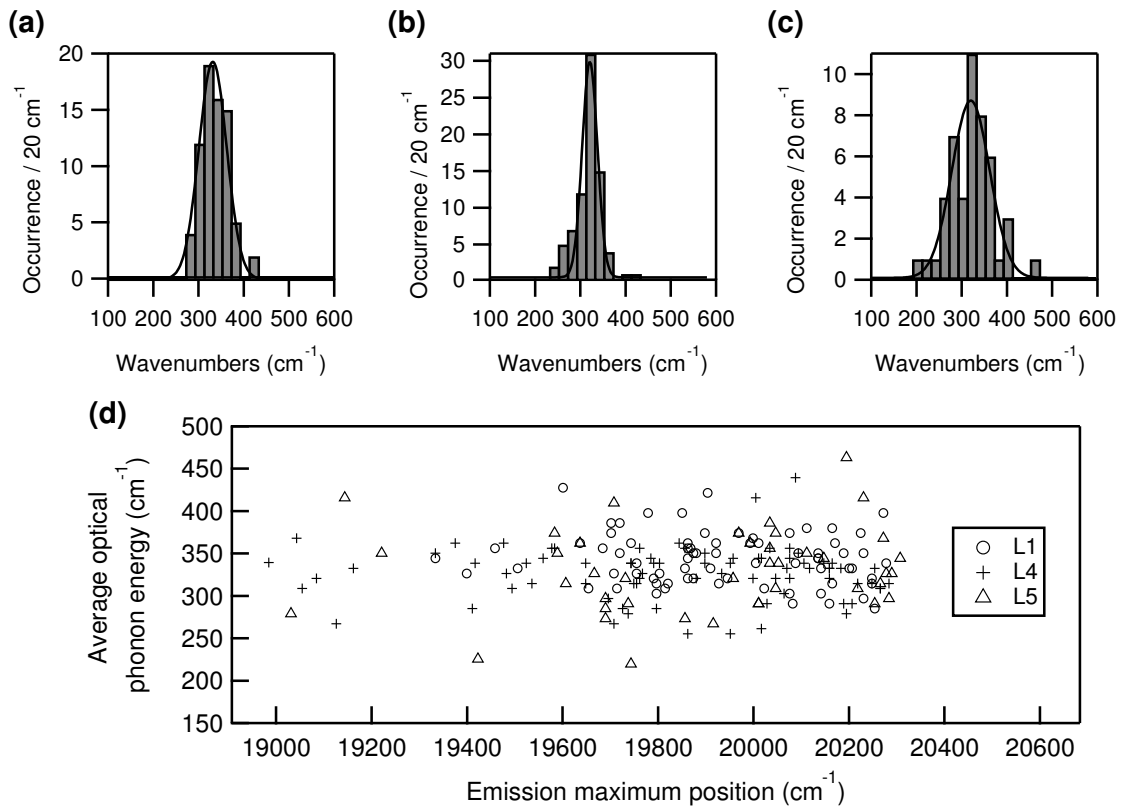


Figure 5.29: Average optical phonon energy distributions obtained by the spectral distance between the purely electronic transitions and PSBs (for details see the main text) of (a) $L1$, (b) $L4$ and (c) $L5$. The solid curves in the histograms are the Gaussian fits. (d) The correlation of the average optical phonon energy and the emission maximum position of all QDs investigated. The average optical phonon energies of $L1$, $L4$ and $L5$ are 332 cm^{-1} , 321 cm^{-1} and 320 cm^{-1} , respectively.

intermediate intensity levels between the levels of *on* and *off* states. To illustrate this, comparison of a simulated time trace with 10 ms time bin (blue crosses) and the time trace integrated from it with 100 ms time bin (red circles) is shown in Figure 5.30(a). Although the trace with 10 ms time bin was purely binary blinking (the dark count rate was 5 and the bright count rate was 100), when it was integrated to become the trace with a time bin of 100 ms, intermediate intensity levels appeared due to the different total counts summed up from different 100 ms time intervals. Accordingly, the distribution of the count rates was broadened. This effect has also been discussed in the literature [63]. Figure 5.30(b) shows a typical fluorescence time trace of InP/ZnSeS QDs in a PMMA film at 4.5 K, in which some intermediate intensity levels might be derived from the large time bin used (100 ms).

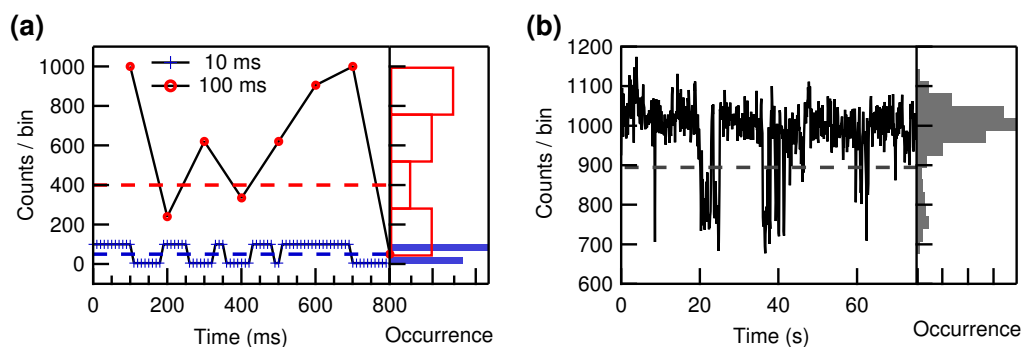


Figure 5.30: (a) A simulated time trace with a time bin of 10 ms (blue crosses, the dark count rate is 5 and the bright count rate is 100). Red circles denote the corresponding trace when the time bin is increased to 100 ms. The solid black connection lines between the symbols serve as a guide for the eye. The dashed lines are the thresholds and the histograms in the right panel are the count rate distributions. (b) A typical fluorescence time trace of InP/ZnSeS QDs from *L4* sample in a PMMA film at 4.5 K. Time bin: 100 ms. The *on* time fraction is 88%.

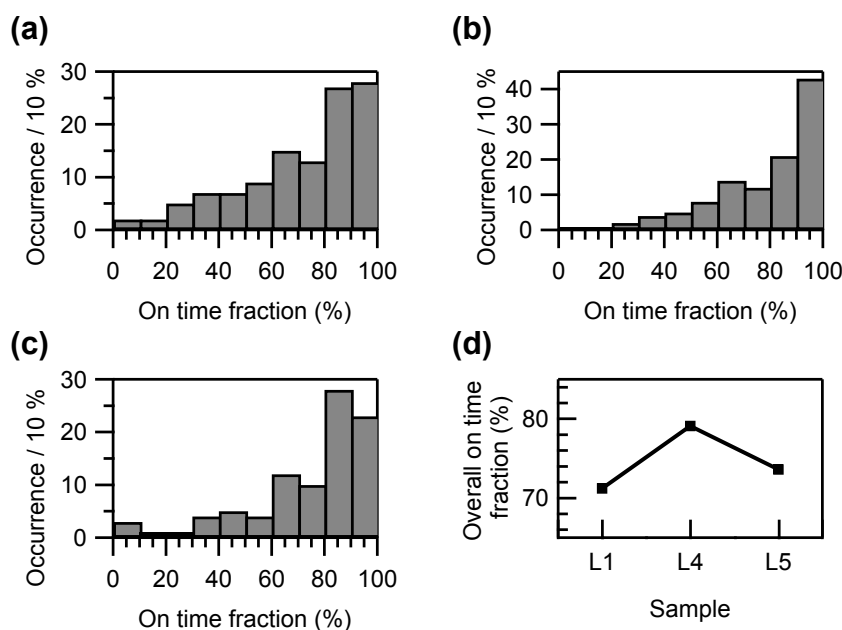


Figure 5.31: *On* time fraction distribution of: (a) *L1*, (b) *L4* and (c) *L5* samples at 4.5 K. (d) The overall *on* time fractions.

The *on* time fractions of sample *L1*, *L4* and *L5* at 4.5 K are shown in Figure 5.31. About 48%, 59% and 56% QDs are largely non-blinking QDs (*on* time fraction of >80%), and about 24%, 39% and 25% of QDs are the ones whose *on* time fractions are over 90%, for *L1*, *L4* and *L5*, respectively. The overall *on* time fractions of *L1*, *L4* and *L5* are 71%, 79% and 74%, respectively. Extracted from the histograms of the *on/off* time distributions, the probability distributions of the *on* or *off* times also follow inverse power-laws as it

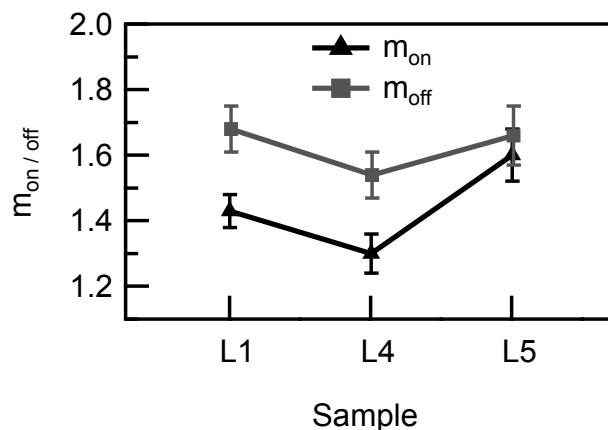


Figure 5.32: Comparison of the inverse power law exponents m_{on} and m_{off} of *L1*, *L4* and *L5* at 4.5 K.

is the case at room temperature. The power-law exponents m_{on} and m_{off} are displayed in Figure 5.32. The *on* (*off*) time coefficients of *L1*, *L4* and *L5* at 4.5 K are 1.43 (1.68), 1.30 (1.54), 1.60 (1.66), respectively. The trend of fluorescence blinking results at 4.5 K discussed above is similar to that at room temperature, indicating that sample *L4* reveals the strongest blinking suppression.

5.6 Comparison of the different samples

Within each series, a great many of experimental results presented before showed that the incorporation of 0.2 mmol Se improves the properties of the InP/ZnSeS QDs, including higher quantum yield, more spherical morphology, narrower size distribution, larger *on* time fraction and a smaller blinking coefficient m_{on} . Samples with either more or less Se induce more inferior properties. An overview of the experimental results is tabulated in Table 5.11.

Based on Table 5.11, the results among the different series can also be compared from another perspective. Generally, there are clear differences between the results of the high temperature series (*HLim* and *H* series) and those of the low temperature series (*L* series). This implies that a lower injection temperature and a relatively longer reaction time of InP and ZnSe lead to a higher quantum yield and a more effective blinking suppression of the final InP/ZnSeS QDs. In conjunction with the improvement of the *on* time fraction, the blinking coefficients m_{on} and m_{off} of the *L* series are obviously smaller than those of the high temperature series, leading to a more digital blinking behavior.

Since the chemical stability and diffusion rate of the reactive monomers (molecular species) as well as the binding strength of the organic ligands to the surface of the growing

QDs are all strongly temperature dependent, an appropriate growth temperature is crucial for the resulting quality of the synthesized quantum dots [312]. On the one hand, a too

Table 5.11: Overview of the experimental results of InP/ZnSeS QD samples at 295 K and 4.5 K (values in brackets). QY: quantum yield; FWHM: the FWHMs of the emission spectra of ensemble samples; QD size: particle diameters obtained from TEM images; LNB QD fraction: the fraction of largely non-blinking QDs (QDs with *on* time fractions over 80%).

Samples	QY (%)	FWHM (nm)	QD size (nm)	overall <i>on</i> time fraction (%)	LNB QD fraction (%)	m_{on}	m_{off}
<i>HLim1</i>	56	63	7.8 ± 0.8	63	33	1.83	1.80
<i>HLim2</i>	59	58	7.5 ± 0.9	69	43	1.72	1.77
<i>HLim3</i>	25	53	6.9 ± 1.1	42	22	1.87	1.64
<i>H1</i>	37	66	6.0 ± 0.8	58	24	1.76	1.81
<i>H2</i>	69	65	6.3 ± 0.7	72	43	1.71	1.81
<i>L1</i>	58	63	4.4 ± 0.8	75 (71)	55 (48)	1.48 (1.43)	1.56 (1.68)
<i>L2</i>	78	60	4.4 ± 0.7	81	64	1.46	1.51
<i>L3</i>	82	55	4.4 ± 0.5	79	67	1.39	1.53
<i>L4</i>	85	56	4.5 ± 0.4	86 (79)	81 (59)	1.28 (1.30)	1.53 (1.54)
<i>L5</i>	73	60	4.5 ± 0.8	77 (74)	61 (56)	1.41 (1.60)	1.59 (1.66)

low temperature is insufficient to overcome the energy barrier to trigger homogeneous nucleation and the subsequent crystallization [130], and a relatively small difference between temperatures before and after the injection of precursor solution may also adversely affect the separation of the nucleation and growth processes [131]. On the other hand, a too high temperature may induce an uncontrolled growth process during which it is difficult to exploit subtle kinetic or energetic effects to obtain precise control over the size and size distribution [312]. For the synthesis of InP/ZnSeS QDs, due to the relatively high reactivity of $\text{P}(\text{TMS})_3$ and Se-TOP, the reactions at high temperature (280°C) at short times are likely to be under kinetic control, which is an adverse condition to achieve good crystallinity and uniform shell growth [52]. In contrast, at a lower temperature (220°C) with longer reaction times, the thermodynamically controlled growth is favored, which might be responsible for the observed high QY and strong blinking suppression of the as-prepared QDs of *L* series.

5.7 Possible mechanisms of the strong blinking suppression

As mentioned at the beginning of this chapter, although the “giant” Cd-containing QDs with very thick shells (thickness above 6 nm) synthesized by Hollingsworth’s group succeeded in a reduction of fluorescence blinking [76, 162, 305], a thick shell is at least not the exclusive approach for blinking suppression in QDs. For instance, when applying ZnS as the shell instead of thick CdS or $\text{Cd}_x\text{Zn}_y\text{S}$ shells to synthesize “giant” QDs, the blinking behavior was found to be almost completely independent of the thickness of the ZnS shell [305, 313]. Similarly, blinking suppression of InP/CdS QDs was also found to be not strongly shell-thickness dependent [87], suggesting that both the composition and the internal structure are crucial factors for a successful blinking suppression. This has been further emphasized in Ref. [306], Ref. [83] and Ref. [84] with CdSe/CdS, zinc-blende CdSe/CdS and (Zn)CuInS/ZnS QD systems. In addition, the CdZnSe/ZnSe QDs synthesized by Wang et al. exhibited a complete non-blinking behavior even with a size of only ~ 5 nm [76].

The as-prepared InP/ZnSeS QDs (*L* series) are also quite small (~ 4.5 nm) with a relatively thin shell (~ 1.6 nm). Therefore, the isolation of the wavefunction of the core from the surface may not be the main reason for the blinking reduction. Considering that the InP/ZnSeS QDs have a radial gradient in both composition and crystal structure (see Figure 5.7), the strong blinking suppression should be more probably ascribed to the internal structure of the particles. Several mechanisms are tentatively suggested below:

- (1) **Less strain, fewer defects and better crystallinity resulting from the gradient crystal structure.** On the one hand, the reactivity difference between the Se and S precursor solutions during synthesis were chosen and utilized for the formation of a composition-gradient shell heterostructure [52]; on the other hand, even after the injection of Se precursor solution, there were still InP monomers remaining in the reaction system, which should lead to a growth competition with the subsequent ZnSe coating. Through this competition, the core and shell materials may form a very thin mixed layer at the interface. Therefore, the lattice mismatch at the core-shell interface could be further alleviated. It is worth noting that “giant” QDs with thick shells usually exhibit lower QYs, which is explained by the non-radiative recombination through defects (e.g., dislocations) within the thick and imperfect shell [76]. From this point of view, the low QY of InP/ZnS QDs made by Zan et al. [86] might also be rationalized by defects at the core-shell interface due to the large lattice mismatch. In contrast, for

the InP/ZnSeS QDs whose composition is shown in Figure 5.7, the gradually changing crystal structure may provide a favorable path to reduce the lattice mismatch and to improve the crystallinity. Thus, the fact that the InP/ZnSeS QDs show both high fluorescence QY (above 80%) and high *on* time fraction (~85%) appears to be at least partially attributable to the better crystallinity due to the gradient structure. This claim is similar to the explanations in the reports on phase-pure wurtzite and zinc blende CdSe/CdS QDs with high crystallinities [82, 83].

- (2) **Quasi-type-II electronic structure.** The electronic structure of the InP/ZnSeS QDs is schematically illustrated in Figure 5.33. Quite similar to the CdSe/CdS QD system, in conjunction with the energy offset between the very small InP core (1.3 nm) and the ZnSeS shell (conduction band minimum offset ~0.3 eV, valence band maximum offset ~0.8 eV) and the effective mass difference of the charge carriers ($m_e = 0.077$, $m_h = 0.64$ for InP), it is expected that a photoexcited hole should be mainly confined in the InP core whereas the electron wavefunction is able to delocalize into the gradient ZnSeS shell and thus spreads across the entire QD volume, resulting in a quasi-type-II structure (see also Figure 2.15) [7, 52, 314]. Another hint for this assumption is the existence of a relatively large effective Stokes shift (spectral separation between emission and absorption) in InP/ZnSeS QDs investigated here (1500–2000 cm^{-1}), which is similar to those of CdSe/CdS “giant” QDs, suggesting that an internal shell-to-core energy relaxation process may be involved [87, 315]. This quasi-type-II structure was analyzed for other systems and reported to be conducive to the blinking suppression through the reduction of the non-radiative Auger recombination [78, 161, 162]. Specifically, the extension of the wavefunction increases the effective particle size so that electrons and holes are spatially more separated, resulting in a reduction of the electron-hole overlap integral which can increase the non-radiative Auger lifetime [316, 317]. Thus, the fluorescence time is increased.
- (3) **Smooth energy potential and soft confinement.** Figure 5.33 also depicts the energy potentials near the band edge of the QDs with core/shell, core/shell/shell and radial gradient composition structures. It can be readily understood that the gradient structure provides a smooth and soft-confinement energy potential in comparison with the other two configurations. Because an efficient non-radiative Auger recombination has to satisfy the breaking of strict momentum conservation, which is suitable with the abrupt change at the core-shell interface in the case of core/shell or core/shell/shell structure, the more smooth energy potential with a

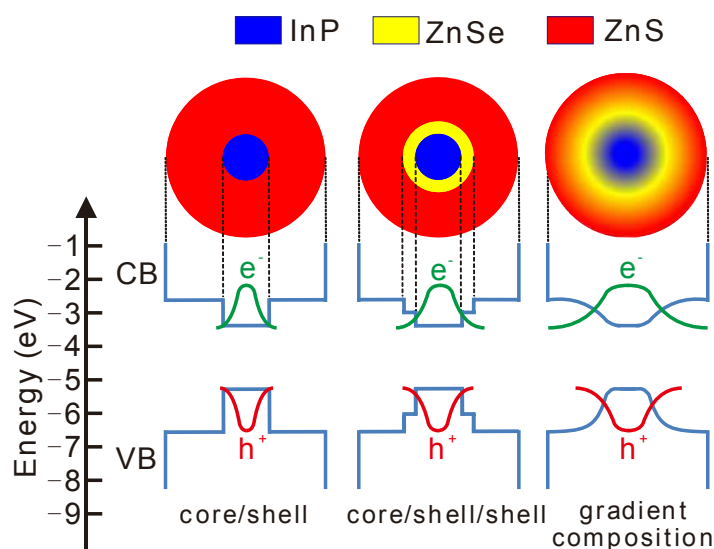


Figure 5.33: Schematic diagram to compare band energy functions and carrier wavefunctions of QDs with various compositions and structures: core/shell (left), core/shell/shell (middle) and gradient composition (right). The green curves denote the electron wavefunctions while the red curves denote the hole wavefunctions.

soft-confinement is expected to be critical for suppression of the non-radiative Auger recombinations [80, 318]. This view is supported by simulations and calculations by Cragg et al. [246], in which they have found that smoothing out the confinement potential could reduce the non-radiative Auger recombination rate by more than three orders of magnitude relative to the rate in structures with abruptly terminating boundaries.

- (4) **Ligand influence.** As shown in Figure 5.25 and discussed in Section 5.4.2.4, the ligands also have a strong influence on the optical properties of the InP/ZnSeS QDs. The comparison of OA and DDT has highlighted the particular role that DDT plays. As Hohng et al. pointed out, a thiol-moiety may serve as an electron donor, which can donate electrons to the surface electron traps, preventing the traps accepting electrons from the QD itself, and thus the blinking is suppressed [69]. The source of sulfur for the non-blinking high quality CdSe/CdS QDs synthesized by Chen et al. was also a thiol-containing chemical (1-octanethiol), whereas samples made from traditional sulfur precursor solution showed severe blinking [82]. Zhang et al. also synthesized nearly non-blinking CdSe/CdS and (Zn)CuInS/ZnS QDs with alkylthiols [84, 319]. It is believed that the decomposition process of alkylthiols at high temperature can slowly release the activated S by homolytic cleavage of the thiol and alkyl groups, and the activated S can subsequently bind to the surface traps of the QDs, inducing a

surface reconstruction and a blinking suppression [84, 319]. Moreover, as depicted in Figure 2.25, the so-called B-type blinking, which was proposed and reported by Galland et al., derived from the capture of hot electrons was able to be suppressed by applying an external electrochemical potential [241]. If this kind of blinking exists in InP/ZnSeS QDs, the DDT may provide electrons, which occupy the trap states, and thus reduce blinking of this type.

The significance of the internal structure has been further confirmed by the investigations of samples with an increasing amount of Se. For example, as revealed in Figure 5.11, the amount of Se influences the morphology/crystallinity of the samples, implying that the structure can be tuned by the amount of Se incorporated. As expected, not only the results at the ensemble level such as the fluorescence QY and FWHM of the emission spectra (Figure 5.8(b)), but also the results from single particle measurements such as the increase of the *on* time fraction (Figure 5.23(a) and (b)) and the decreasing *on* time power-law exponent m_{on} (Figure 5.24(b)) achieve the best value with the same tendency. Analysis of the time-resolved measurements (Figure 5.10) demonstrated that by adjusting the Se amount, the radiative rate k_r is enhanced. It is worth noting that, theoretically, if the non-radiative recombination time (e.g., Auger process) is always essentially longer than the radiative recombination time in a QD system, there will be no “dark” state at all, even if the QD is charged [79]. Although the lifetimes measured here are average results which may contain contributions from different pathways, generally the trend of the ratio k_r/k_{nr} is in good agreement with the observations of the blinking behavior, meaning that sample *L4* has the longest non-radiative recombination-time (smallest k_{nr}) compared with the radiative recombination-time (larger k_r), considering that $k_{\text{r/nr}} = 1/\tau_{\text{r/nr}}$. This implies that an optimized internal structure suppresses the non-radiative recombination pathways (including Auger recombination) efficiently.

5.8 Summary

Sample series *HLim*, *H* and *L* (for experimental conditions see Table 5.1) of green-emitting InP/ZnSeS QDs have been investigated both at the ensemble and the single particle level. Generally the *L* series exhibit higher QYs and stronger blinking suppression than the other two series synthesized at higher temperature. Within each series, the amount of Se has been proven to have a great impact on the photophysical properties of the samples. Specifically, in a series of QDs with increasing Se amount, the fluorescence QY, the radiative rate and blinking suppression increase.

The best sample with 0.2 mmol Se injection (*LA*) resulted in a very high fluorescence QY of ~85%. The radial gradient composition in the InP/ZnSeS QDs has been characterized and verified by energy dispersive X-ray spectroscopy. From the X-ray diffraction pattern, crystalline phases of both the Zn-passivated InP core and the ZnSeS shell were identified to be zinc blende. The similarity of the crystal structure at different growth stages and the gradually changed lattice constants further confirmed the radial gradient structure. Moreover, HRTEM images reveal a high crystallinity of the InP/ZnSeS QDs as well.

At the single particle level, strong suppression of fluorescence blinking of the as-prepared sample is characterized by the *on* time fraction and the *on/off* power law probability exponents. For the best sample, while the overall *on* time fraction was ~85%, about 80% and 51% of the QDs have an *on* time fraction of >80% and >90%, respectively. For the sample with 0.2 mmol Se, the power law exponent m_{on} can be as small as 1.28. In contrast, the *off* times seem to be insensitive to the Se amount. The strong fluorescence blinking suppression has been mainly attributed to factors caused by the internal structure of the InP/ZnSeS QD: gradient crystal structure induced reduction of defects, good crystallinity, and a quasi-type-II electronic structure in a smooth energy potential with soft confinement. As a thiol-containing ligand, DDT was also found to play a crucial role in the fluorescence performance.

Intensive spectral line broadening either originating from electron-phonon coupling or strong spectral diffusion in the fluorescence emission spectra of single InP/ZnSeS QDs has been observed at 4.5 K. The results have provided first indications that with an increasing Se amount, ZnSe optical phonons might contribute more and more to electron-phonon coupling, further implying the influence of the Se amount on the photophysical properties.

6

Summary and outlook

The thesis was devoted to investigations of two kinds of semiconductor quantum dot (QD) systems: CdSe/CdS/ZnS QDs (monomers and dimers) and InP/ZnSeS QDs. Core/shell/shell structured CdSe/CdS/ZnS QDs were synthesized in organic solvent and used as building blocks to build QD homo-dimers and hetero-dimers. The assembly was realized by repeated precipitation of the QDs from a good solvent (toluene or cyclohexane) by adding a bad solvent (methanol). For homo-dimers, a dependence of assembly cycles required to trigger effective dimer formation on the particle size was found. The QD dimer fraction in the samples after assembly was found to be typically about 20%–30%. To further enrich the dimers, rate-zonal density gradient ultracentrifugation (DGU) with a density gradient established by cyclohexane–CCl₄ mixtures was applied. After DGU, distinct monomer and dimer bands were observed. However, the sedimentation distances showed inconsistency with the results calculated by a sedimentation formula based on an assumption of a uniform centrifugal force field and a homogeneous fluid medium (Equation 4.1). Therefore, the variations of the centrifugal force and the medium density at different positions in the centrifuge tube were taken into account, and thus an improved sedimentation formula (Equation 4.11) was obtained. The calculated sedimentation distances of monomer and dimer bands according to the improved formula were found to be in good quantitative agreement with the experimental observations. By this method, the dimers could be enriched up to 81% as the best result. Subsequently, single particle measurements of the QD monomers and homo-dimers were performed at 295 K and 4.5 K, respectively. At room temperature, the emission spectra from the two components within QD homo-dimers were not distinguishable due to the small spectral separation and the broad linewidths. In contrast, the optical emission spectrum of a single CdSe/CdS/ZnS

QD features a narrow zero-phonon line (ZPL) accompanied by phonon sidebands (PSBs) at 4.5 K. Due to the narrow linewidths, replicas of CdSe and CdS LO phonons as well as the second harmonic of the LO-phonon of CdSe in the emission spectra of an individual CdSe/CdS/ZnS QD could be observed. The average energy and the Huang-Rhys factor of CdSe LO phonons were found to be 207 cm^{-1} and 0.40, respectively. Both values were in accordance with data reported in the literature and not correlated to the spectral position of the ZPL. Moreover, the band gap energy of a single QD showed a blue-shift with the decrease of temperature. The energy of this blue-shift was found to be smaller than the result based on the Varshni equation (Equation 2.53) but larger than that calculated by the equation of O'Donnell and Chen (Equation 2.54). In single particle spectroscopy at 4.5 K of a sample in which dimers have been enriched, different types of spectra were observed and categorized. Possible scenarios behind each type were analyzed as well. Moreover, as an alternative approach to the preparation of QD dimers, two batches of CdSe/CdS/ZnS QDs with different sizes were synthesized separately and assembled to form QD hetero-dimers. After further enrichment by DGU, most of the dimers at the position of the centrifuge tube where hetero-dimers were expected turned out to be homo-dimers with components having similar sizes. This result was explained by a model based on QD assembly triggered by exposed free surface sites under the assumption of a size independent surface site density. On a further attempt, QD hetero-dimers in which the components have similar sizes but different compositions were prepared. Eventually, the best hetero-dimers were built by the dimerization of CdSe/1 ML CdS/1 ML ZnS and CdSe/2 ML CdS/2 ML ZnS QDs. Although transmission electron microscopy (TEM) characterization was not able to distinguish between homo- and hetero-dimers, a combination of atomic force and confocal fluorescence microscopy provided an identification of QD hetero-dimers at room temperature.

Future research for this project may mainly concentrate on single particle spectroscopy of QD hetero-dimers. As concluded above, the hetero-dimers have been identified by the combined setup of atomic force and confocal fluorescence microscopy. Hence, with a proper dichroic optical filter, it will be possible to probe the photons emitted from the two QD components within a dimer individually at the same time, which allows their corresponding fluorescence intensities (therefore also blinking behaviors) and fluorescence decays to be measured separately. Thus, the electronic coupling between the two adjacent QDs can be studied and analyzed.

Concerning the InP/ZnSeS QDs, three series of samples with different InP and ZnSe growth temperatures and times were prepared. Generally, a lower growth temperature (220°C) with a longer reaction times led to better performance of the QDs such as better

crystallinity, higher quantum yield and stronger blinking suppression. Moreover, within each series, the amount of Se was also found to have a great impact on the properties mentioned above. A fluorescence QY as high as 85% was achieved by a sample which contained 0.2 mmol Se. The gradient composition in radial direction of the InP/ZnSeS QDs was corroborated by energy dispersive X-ray spectroscopy. Crystalline phases of the ZnSeS shell were identified to be zinc blende by X-ray diffraction. The results from X-ray diffraction also indicated that samples at different growth stages exhibited similar crystal structures and that the lattice constants also varied gradually with the epitaxial overgrowth of the shell. In addition, the results from high-resolution transmission electron microscopy revealed a good crystallinity of the InP/ZnSeS QDs. At the single particle level, strong suppression of fluorescence blinking was observed and characterized by the *on* time fraction and the *on/off* power law probability exponents. The sample with the best quality (*L4*) showed an overall *on* time fraction of ~85%, and the percentage of QDs which had an *on* time fraction >80% and >90% were 80% and 51%, respectively. The *on* time coefficient m_{on} was found to be as small as 1.28, indicating a high probability for long *on* times. The samples with more and less amounts of Se exhibited smaller *on* time fractions and bigger *on* time coefficients. However, the *off* times appeared to be insensitive to the Se amounts, which implied that the *off* to *on* transition process might be governed by a different mechanism from the *on* to *off* transition. Several factors related to the structure of the InP/ZnSeS QDs were tentatively suggested to be responsible for the observed strong fluorescence blinking suppression, such as gradient crystal structure induced good crystallinity and reduction of defects, a quasi-type-II electronic structure and a smooth energy potential with a soft confinement. The used 1-dodecanethiol (DDT), which served as S source and stabilizing ligand, also revealed a crucial influence on the bulk fluorescence quantum yield and blinking behavior. At cryogenic temperature (4.5 K), the emission spectra of single InP/ZnSeS QDs showed surprisingly broad linewidths, which could be due to strong electron-phonon coupling or spectral diffusion. The results suggested that with an increase of the Se amount, the coupling to ZnSe optical phonons increased, which further implied the impact of Se on the photophysical properties of the InP/ZnSeS QDs.

In the future, additional studies may be performed to gain a deeper insight into the rationale behind the blinking suppression, for instance, fluorescence lifetime measurement at single particle level, or single particle spectroscopy at various temperatures with high spectral resolution. From another perspective, experimental conditions might be further improved for a complete elimination of the blinking (i.e., non-blinking QDs). Moreover, the synthesis of red-emitting InP based QDs with a high quantum yield, which remains

a challenge so far, could be another direction of future work. In general, it is believed that further studies of these new Cd-free QDs will be beneficial for the fundamental understanding and applications of nanoparticles, especially at the single particle level.

References

- [1] Kim, J. Y., Voznyy, O., Zhitomirsky, D. and Sargent, E. H. 25th anniversary article: colloidal quantum dot materials and devices: a quarter-century of advances. *Adv. Mater.*, **25**, 4986–5010 (2013).
- [2] Colvin, V. L., Schlamp, M. C. and Alivisatos, A. P. Light-emitting diodes made from cadmium selenide nanocrystals and a semiconducting polymer. *Nature*, **370**, 354–357 (1994).
- [3] Kamat, P. V. Quantum dot solar cells. semiconductor nanocrystals as light harvesters. *J. Phys. Chem. C*, **112**, 18737–18753 (2008).
- [4] Li, L. and Reiss, P. One-pot synthesis of highly luminescent InP/ZnS nanocrystals without precursor injection. *J. Am. Chem. Soc.*, **130**, 11588–11589 (2008).
- [5] Bae, W. K., Kwak, J., Park, J. W., Char, K., Lee, C. and Lee, S. Highly efficient green-light-emitting diodes based on CdSe@Zns quantum dots with a chemical-composition gradient. *Adv. Mater.*, **21**, 1690–1694 (2009).
- [6] Yang, X., Zhao, D., Leck, K. S., Tan, S. T., Tang, Y. X., Zhao, J., Demir, H. V. and Sun, X. W. Full visible range covering InP/ZnS nanocrystals with high photometric performance and their application to white quantum dot light-emitting diodes. *Adv. Mater.*, **24**, 4180–4185 (2012).
- [7] Lim, J., Park, M., Bae, W. K., Lee, D., Lee, S., Lee, C. and Char, K. Highly efficient cadmium-free quantum dot light-emitting diodes enabled by the direct formation of excitons within InP@ZnSeS quantum dots. *ACS Nano*, **7**, 9019–9026 (2013).
- [8] Yang, Y., Zheng, Y., Cao, W., Titov, A., Hyvonen, J., Manders, J. R., Xue, J., Holloway, P. H. and Qian, L. High-efficiency light-emitting devices based on quantum dots with tailored nanostructures. *Nat. Photonics*, **9**, 259–266 (2015).
- [9] Bourzac, K. Quantum dots go on display. *Nature*, **493**, 283–283 (2013).
- [10] Gur, I., Fromer, N. A., Geier, M. L. and Alivisatos, A. P. Air-stable all-inorganic nanocrystal solar cells processed from solution. *Science*, **310**, 462–465 (2005).
- [11] Chuang, C.-H. M., Brown, P. R., Bulović, V. and Bawendi, M. G. Improved performance and stability in quantum dot solar cells through band alignment engineering. *Nat. Mater.*, **13**, 796–801 (2014).

- [12] Bruchez Jr., M., Moronne, M., Gin, P., Weiss, S. and Alivisatos, A. P. Semiconductor nanocrystals as fluorescent biological labels. *Science*, **281**, 2013–2016 (1998).
- [13] Gao, X., Cui, Y., Levenson, R. M., Chung, L. W. K. and Nie, S. In vivo cancer targeting and imaging with semiconductor quantum dots. *Nat. Biotechnol.*, **22**, 969–976 (2004).
- [14] Huang, Y., Kamoun, W. S., Martin, J. D., Chen, Y., Roberge, S., Cui, J., Margaret, R., Fukumura, D., Jain, R. K. and Bawendi, M. G. Quantum dot/antibody conjugates for in vivo cytometric imaging in mice. *Proc. Natl. Acad. Sci.*, **112**, E1048–E1048 (2015).
- [15] Murray, C. B., Norris, D. and Bawendi, M. G. Synthesis and characterization of nearly monodisperse CdE (E = S, Se, Te) semiconductor nanocrystallites. *J. Am. Chem. Soc.*, **115**, 8706–8715 (1993).
- [16] Hines, M. a. and GuyotSionnest, P. Synthesis and characterization of strongly luminescing ZnS-capped CdSe nanocrystals. *J. Phys. Chem.*, **100**, 468–471 (1996).
- [17] Talapin, D. V., Rogach, A. L., Kornowski, A., Haase, M. and Weller, H. Highly luminescent monodisperse CdSe and CdSe/ZnS nanocrystals synthesized in a hexadecylamine-trioctylphosphine oxide-trioctylphosphine mixture. *Nano Lett.*, **1**, 207–211 (2001).
- [18] Peng, Z. A. and Peng, X. Formation of high-quality CdTe, CdSe, and CdS nanocrystals using CdO as precursor. *J. Am. Chem. Soc.*, **123**, 183–184 (2001).
- [19] Yu, W. W. and Peng, X. Formation of high-quality CdS and other II-VI semiconductor nanocrystals in noncoordinating solvents: tunable reactivity of monomers. *Angew. Chemie Int. Ed.*, **41**, 2368–2371 (2002).
- [20] Li, J. J., Wang, Y. A., Guo, W., Keay, J. C., Mishima, T. D., Johnson, M. B. and Peng, X. Large-scale synthesis of nearly monodisperse CdSe/CdS core/shell nanocrystals using air-stable reagents via successive ion layer adsorption and reaction. *J. Am. Chem. Soc.*, **125**, 12567–12575 (2003).
- [21] Xie, R., Kolb, U., Li, J., Basché, T. and Mews, A. Synthesis and characterization of highly luminescent CdSe-core CdS/Zn_{0.5}Cd_{0.5}S/ZnS multishell nanocrystals. *J. Am. Chem. Soc.*, **127**, 7480–7488 (2005).
- [22] Reiss, P., Protière, M. and Li, L. Core/shell semiconductor nanocrystals. *Small*, **5**, 154–168 (2009).
- [23] Liang, Y., Thorne, J. E. and Parkinson, B. a. Controlling the electronic coupling between CdSe quantum dots and thiol capping ligands via pH and ligand selection. *Langmuir*, **28**, 11072–7 (2012).
- [24] Gómez, D. E., Califano, M. and Mulvaney, P. Optical properties of single semiconductor nanocrystals. *Phys. Chem. Chem. Phys.*, **8**, 4989–5011 (2006).
- [25] Medintz, I. L., Uyeda, H. T., Goldman, E. R. and Mattoussi, H. Quantum dot bioconjugates for imaging, labelling and sensing. *Nat. Mater.*, **4**, 435–446 (2005).

- [26] Marchuk, K., Guo, Y., Sun, W., Vela, J. and Fang, N. High-precision tracking with non-blinking quantum dots resolves nanoscale vertical displacement. *J. Am. Chem. Soc.*, **134**, 6108–11 (2012).
- [27] Michler, P., Imamoglu, A., Mason, M., Carson, P., Strouse, G. and Buratto, S. Quantum correlation among photons from a single quantum dot at room temperature. *Nature*, **406**, 968–970 (2000).
- [28] Brokmann, X., Messin, G., Desbiolles, P., Giacobino, E., Dahan, M. and Hermier, J. P. Colloidal CdSe/ZnS quantum dots as single-photon sources. *New J. Phys.*, **6**, 99 (2004).
- [29] Claxton, N. S., Fellers, T. J. and Davidson, M. W. Microscopy, Confocal. In *Encycl. Med. Devices Instrum.*, volume 1979, pages 1–37. John Wiley & Sons, Inc., Hoboken, NJ, USA (2006).
- [30] Buck, M. R. and Schaak, R. E. Emerging strategies for the total synthesis of inorganic nanostructures. *Angew. Chemie Int. Ed.*, **52**, 6154–6178 (2013).
- [31] Vanmaekelbergh, D. and Liljeroth, P. Electron-conducting quantum dot solids: novel materials based on colloidal semiconductor nanocrystals. *Chem. Soc. Rev.*, **34**, 299–312 (2005).
- [32] Lu, F., Yager, K. G., Zhang, Y., Xin, H. and Gang, O. Superlattices assembled through shape-induced directional binding. *Nat. Commun.*, **6**, 6912 (2015).
- [33] Korgel, B. a. and Fitzmaurice, D. Self-assembly of silver nanocrystals into two-dimensional nanowire arrays. *Adv. Mater.*, **10**, 661–665 (1998).
- [34] Novak, J. P. and Feldheim, D. L. Assembly of phenylacetylene-bridged silver and gold nanoparticle arrays. *J. Am. Chem. Soc.*, **122**, 3979–3980 (2000).
- [35] Koole, R., Liljeroth, P., de Mello Donegá, C., Vanmaekelbergh, D. and Meijerink, A. Electronic coupling and exciton energy transfer in CdTe quantum-dot molecules. *J. Am. Chem. Soc.*, **128**, 10436–10441 (2006).
- [36] Wang, X. and Li, Y. Monodisperse nanocrystals: general synthesis, assembly, and their applications. *Chem. Commun.*, pages 2901–2910 (2007).
- [37] Grzelczak, M., Vermant, J., Furst, E. and Liz-Marzán, L. Directed self-assembly of nanoparticles. *ACS Nano*, **4**, 3591–3605 (2010).
- [38] Kagan, C. R., Murray, C. B. and Bawendi, M. G. Long-range resonance transfer of electronic excitations in close-packed CdSe quantum-dot solids. *Phys. Rev. B*, **54**, 8633–8643 (1996).
- [39] Achermann, M., Petruska, M. a., Crooker, S. a. and Klimov, V. I. Picosecond energy transfer in quantum dot Langmuir–Blodgett nanoassemblies. *J. Phys. Chem. B*, **107**, 13782–13787 (2003).
- [40] Murray, C. B., Kagan, C. R. and Bawendi, M. G. Self-organization of CdSe nanocrystallites into three-dimensional quantum dot superlattices. *Science*, **270**, 1335–1338 (1995).

- [41] Shevchenko, E. V., Talapin, D. V., Kotov, N. a., O'Brien, S. and Murray, C. B. Structural diversity in binary nanoparticle superlattices. *Nature*, **439**, 55–59 (2006).
- [42] Maye, M. M., Kumara, M. T., Nykypanchuk, D., Sherman, W. B. and Gang, O. Switching binary states of nanoparticle superlattices and dimer clusters by DNA strands. *Nat. Nanotechnol.*, **5**, 116–120 (2010).
- [43] Kim, D., Tomita, S., Ohshiro, K., Watanabe, T., Sakai, T., Chang, I.-Y. and Hyeon-Deuk, K. Evidence of quantum resonance in periodically-ordered three-dimensional superlattice of CdTe quantum dots. *Nano Lett.*, **15**, 4343–4347 (2015).
- [44] Tikhomirov, G., Hoogland, S., Lee, P. E., Fischer, A., Sargent, E. H. and Kelley, S. O. DNA-based programming of quantum dot valency, self-assembly and luminescence. *Nat. Nanotechnol.*, **6**, 485–490 (2011).
- [45] Chen, G., Wang, Y., Tan, L. S. L. H., Yang, M., Chen, Y. and Chen, H. High-purity separation of gold nanoparticle dimers and trimers. *J. Am. Chem. Soc.*, **131**, 4218–4219 (2009).
- [46] Yang, M., Chen, G., Zhao, Y., Silber, G., Wang, Y., Xing, S., Han, Y. and Chen, H. Mechanistic investigation into the spontaneous linear assembly of gold nanospheres. *Phys. Chem. Chem. Phys.*, **12**, 11850–11860 (2010).
- [47] Xu, X., Stöttinger, S., Battagliarin, G., Hinze, G., Mugnaioli, E., Li, C., Müllen, K. and Basché, T. Assembly and separation of semiconductor quantum dot dimers and trimers. *J. Am. Chem. Soc.*, **133**, 18062–18065 (2011).
- [48] Järup, L. and Åkesson, A. Current status of cadmium as an environmental health problem. *Toxicol. Appl. Pharmacol.*, **238**, 201–208 (2009).
- [49] Peng, X. An essay on synthetic chemistry of colloidal nanocrystals. *Nano Res.*, **2**, 425–447 (2009).
- [50] Anc, M. J., Pickett, N. L., Gresty, N. C., Harris, J. a. and Mishra, K. C. Progress in non-Cd quantum dot development for lighting applications. *ECS J. Solid State Sci. Technol.*, **2**, R3071–R3082 (2013).
- [51] Xie, R., Battaglia, D. and Peng, X. Colloidal InP nanocrystals as efficient emitters covering blue to near-infrared. *J. Am. Chem. Soc.*, **129**, 15432–3 (2007).
- [52] Lim, J., Bae, W. K., Lee, D., Nam, M. K., Jung, J., Lee, C., Char, K. and Lee, S. InP@ZnSeS, core@composition gradient shell quantum dots with enhanced stability. *Chem. Mater.*, **23**, 4459–4463 (2011).
- [53] Cros-Gagneux, A., Delpech, F., Nayral, C., Cornejo, A., Coppel, Y. and Chaudret, B. Surface chemistry of InP quantum dots: a comprehensive study. *J. Am. Chem. Soc.*, **132**, 18147–18157 (2010).
- [54] Nirmal, M., Dabbousi, B. O., Bawendi, M. G., Macklin, J. J., Trautman, J. K., Harris, T. D. and Brus, L. E. Fluorescence intermittency in single cadmium selenide nanocrystals. *Nature*, **383**, 802–804 (1996).

- [55] Efros, A. and Rosen, M. Random telegraph signal in the photoluminescence intensity of a single quantum dot. *Phys. Rev. Lett.*, **78**, 1110–1113 (1997).
- [56] Neuhauser, R. G., Shimizu, K. T., Woo, W. K., Empedocles, S. A. and Bawendi, M. G. Correlation between fluorescence intermittency and spectral diffusion in single semiconductor quantum dots. *Phys. Rev. Lett.*, **85**, 3301–3304 (2000).
- [57] Shimizu, K. T., Neuhauser, R. G., Leatherdale, C. A., Empedocles, S. A., Woo, W. K. and Bawendi, M. G. Blinking statistics in single semiconductor nanocrystal quantum dots. *Phys. Rev. B*, **63**, 205316 (2001).
- [58] Tang, J. and Marcus, R. a. Diffusion-controlled electron transfer processes and power-law statistics of fluorescence intermittency of nanoparticles. *Phys. Rev. Lett.*, **95**, 107401 (2005).
- [59] Margolin, G., Protasenko, V., Kuno, M. and Barkai, E. Power-law blinking quantum dots: stochastic and physical models. In *Adv. Chem. Phys.*, volume 133, pages 327–356 (2005).
- [60] Verberk, R., van Oijen, A. and Orrit, M. Simple model for the power-law blinking of single semiconductor nanocrystals. *Phys. Rev. B*, **66**, 233202 (2002).
- [61] Kuno, M., Fromm, D. P., Hamann, H. F., Gallagher, A. and Nesbitt, D. J. “On”/“off” fluorescence intermittency of single semiconductor quantum dots. *J. Chem. Phys.*, **115**, 1028–1040 (2001).
- [62] Frantsuzov, P. a. and Marcus, R. a. Explanation of quantum dot blinking without the long-lived trap hypothesis. *Phys. Rev. B*, **72**, 155321 (2005).
- [63] Crouch, C. H., Sauter, O., Wu, X., Purcell, R., Querner, C., Drndic, M. and Pelton, M. Facts and artifacts in the blinking statistics of semiconductor nanocrystals. *Nano Lett.*, **10**, 1692–1698 (2010).
- [64] Lee, D.-H., Yuan, C.-T., Tachiya, M. and Tang, J. Influence of bin time and excitation intensity on fluorescence lifetime distribution and blinking statistics of single quantum dots. *Appl. Phys. Lett.*, **95**, 163101 (2009).
- [65] Crouch, C. H., Mohr, R., Emmons, T., Wang, S. and Drndic, M. Excitation energy dependence of fluorescence intermittency in CdSe/ZnS core–shell nanocrystals. *J. Phys. Chem. C*, **113**, 12059–12066 (2009).
- [66] Fu, Y., Zhang, J. and Lakowicz, J. R. Suppressed blinking in single quantum dots (QDs) immobilized near silver island films (SIFs). *Chem. Phys. Lett.*, **447**, 96–100 (2007).
- [67] Yuan, C. T., Yu, P. and Tang, J. Blinking suppression of colloidal CdSe/ZnS quantum dots by coupling to silver nanoprisms. *Appl. Phys. Lett.*, **94**, 243108 (2009).
- [68] Masuo, S., Naiki, H., Machida, S. and Itaya, A. Photon statistics in enhanced fluorescence from a single CdSe/ZnS quantum dot in the vicinity of silver nanoparticles. *Appl. Phys. Lett.*, **95**, 193106 (2009).

- [69] Hohng, S. and Ha, T. Near-complete suppression of quantum dot blinking in ambient conditions. *J. Am. Chem. Soc.*, **126**, 1324–1325 (2004).
- [70] Jeong, S., Achermann, M., Nanda, J., Ivanov, S., Klimov, V. I. and Hollingsworth, J. A. Effect of the thiol-thiolate equilibrium on the photophysical properties of aqueous CdSe/ZnS nanocrystal quantum dots. *J. Am. Chem. Soc.*, **127**, 10126–10127 (2005).
- [71] Zhang, A., Dong, C., Liu, H. and Ren, J. Blinking behavior of CdSe/CdS quantum dots controlled by alkylthiols as surface trap modifiers. *J. Phys. Chem. C*, **117**, 24592–24600 (2013).
- [72] Antelman, J., Ebenstein, Y., Dertinger, T., Michalet, X. and Weiss, S. Suppression of quantum dot blinking in DTT-doped polymer films. *J. Phys. Chem. C. Nanomater. Interfaces*, **113**, 11541–11545 (2009).
- [73] Biebricher, A., Sauer, M. and Tinnefeld, P. Radiative and nonradiative rate fluctuations of single colloidal semiconductor nanocrystals. *J. Phys. Chem. B*, **110**, 5174–5178 (2006).
- [74] Hammer, N. I., Early, K. T., Sill, K., Odoi, M. Y., Emrick, T. and Barnes, M. D. Coverage-mediated suppression of blinking in solid state quantum dot conjugated organic composite nanostructures. *J. Phys. Chem. B*, **110**, 14167–14171 (2006).
- [75] Ko, H. C., Yuan, C. T., Lin, S. H. and Tang, J. Blinking suppression of single quantum dots in agarose gel. *Appl. Phys. Lett.*, **96**, 012104 (2010).
- [76] Chen, Y., Vela, J., Htoon, H., Casson, J. L., Werder, D. J., Bussian, D. a., Klimov, V. I. and Hollingsworth, J. a. “Giant” multishell CdSe nanocrystal quantum dots with suppressed blinking. *J. Am. Chem. Soc.*, **130**, 5026–5027 (2008).
- [77] Mahler, B., Spinicelli, P., Buil, S., Quelin, X., Hermier, J.-P. and Dubertret, B. Towards non-blinking colloidal quantum dots. *Nat. Mater.*, **7**, 659–664 (2008).
- [78] García-Santamaría, F., Chen, Y., Vela, J., Schaller, R. D., Hollingsworth, J. A. and Klimov, V. I. Suppressed auger recombination in “giant” nanocrystals boosts optical gain performance. *Nano Lett.*, **9**, 3482–3488 (2009).
- [79] Efros, A. L. Nanocrystals: almost always bright. *Nat. Mater.*, **7**, 612–613 (2008).
- [80] Wang, X., Ren, X., Kahen, K., Hahn, M. a., Rajeswaran, M., Maccagnano-Zacher, S., Silcox, J., Cragg, G. E., Efros, A. L. and Krauss, T. D. Non-blinking semiconductor nanocrystals. *Nature*, **459**, 686–689 (2009).
- [81] Krauss, T. D. and Peterson, J. J. Bright future for fluorescence blinking in semiconductor nanocrystals. *J. Phys. Chem. Lett.*, **1**, 1377–1382 (2010).
- [82] Chen, O., Zhao, J., Chauhan, V. P., Cui, J., Wong, C., Harris, D. K., Wei, H., Han, H.-S., Fukumura, D., Jain, R. K. and Bawendi, M. G. Compact high-quality CdSe–CdS core–shell nanocrystals with narrow emission linewidths and suppressed blinking. *Nat. Mater.*, **12**, 445–451 (2013).

- [83] Qin, H., Niu, Y., Meng, R., Lin, X., Lai, R., Fang, W. and Peng, X. Single-dot spectroscopy of zinc-blende CdSe/CdS core/shell nanocrystals: nonblinking and correlation with ensemble measurements. *J. Am. Chem. Soc.*, **136**, 179–187 (2014).
- [84] Zhang, A., Dong, C., Li, L., Yin, J., Liu, H., Huang, X. and Ren, J. Non-blinking (Zn)CuInS/ZnS Quantum Dots Prepared by In Situ Interfacial Alloying Approach. *Sci. Rep.*, **5**, 15227 (2015).
- [85] Kuno, M., Fromm, D. P., Gallagher, A., Nesbitt, D. J., Micic, O. I. and Nozik, A. J. Fluorescence intermittency in single InP quantum dots. *Nano Lett.*, **1**, 557–564 (2001).
- [86] Zan, F., Dong, C., Liu, H. and Ren, J. Experimental studies on blinking behavior of single InP/ZnS quantum dots: effects of synthetic conditions and UV irradiation. *J. Phys. Chem. C*, **116**, 3944–3950 (2012).
- [87] Dennis, A. M., Mangum, B. D., Piryatinski, A., Park, Y.-S., Hannah, D. C., Casson, J. L., Williams, D. J., Schaller, R. D., Htoon, H. and Hollingsworth, J. a. Suppressed Blinking and Auger Recombination in Near-Infrared Type-II InP/CdS Nanocrystal Quantum Dots. *Nano Lett.*, **12**, 5545–5551 (2012).
- [88] Wei, S. H. and Zunger, A. Calculated natural band offsets of all II-VI and III-V semiconductors: chemical trends and the role of cation d orbitals. *Appl. Phys. Lett.*, **72**, 2011–2013 (1998).
- [89] Trindade, T., O'Brien, P. and Pickett, N. L. Nanocrystalline semiconductors: synthesis, properties, and perspectives. *Chem. Mater.*, **13**, 3843–3858 (2001).
- [90] Ekimov, a. I., Hache, F., Schanne-Klein, M. C., Ricard, D., Flytzanis, C., Kudryavtsev, I. A., Yazeva, T. V., Rodina, a. V. and Efros, A. L. Absorption and intensity-dependent photoluminescence measurements on CdSe quantum dots: assignment of the first electronic transitions. *J. Opt. Soc. Am. B*, **10**, 100–107 (1993).
- [91] Meulenbergh, R. W., Lee, J. R. I., Wolcott, A., Zhang, J. Z., Terminello, L. J. and van Buuren, T. Determination of the excitation binding energy in CdSe quantum dots. *ACS Nano*, **3**, 325–330 (2009).
- [92] Mic, O. I., Cheong, H. M., Fu, H., Zunger, A., Sprague, J. R., Mascarenhas, A. and Nozik, a. J. Size-dependent spectroscopy of InP quantum dots. *J. Phys. Chem. B*, **5647**, 4904–4912 (1997).
- [93] Bawendi, M. The quantum mechanics of larger semiconductor clusters. *Annu. Rev. Phys. Chem.*, **41**, 477–496 (1990).
- [94] Alivisatos, a. P., Harris, a. L., Levinos, N. J., Steigerwald, M. L. and Brus, L. E. Electronic states of semiconductor clusters: homogeneous and inhomogeneous broadening of the optical spectrum. *J. Chem. Phys.*, **89**, 4001–4011 (1988).
- [95] Brus, L. Quantum crystallites and nonlinear optics. *Appl. Phys. A Solids Surfaces*, **53**, 465–474 (1991).

- [96] Alivisatos, A. Perspectives on the physical chemistry of semiconductor nanocrystals. *J. Phys. Chem.*, **3654**, 13226–13239 (1996).
- [97] Sagar, D. M., Cooney, R. R., Sewall, S. L., Dias, E. a., Barsan, M. M., Butler, I. S. and Kambhampati, P. Size dependent, state-resolved studies of exciton-phonon couplings in strongly confined semiconductor quantum dots. *Phys. Rev. B*, **77**, 235321 (2008).
- [98] Bae, W. K., Park, Y.-S., Lim, J., Lee, D., Padilha, L. a., McDaniel, H., Robel, I., Lee, C., Pietryga, J. M. and Klimov, V. I. Controlling the influence of Auger recombination on the performance of quantum-dot light-emitting diodes. *Nat. Commun.*, **4**, 2661 (2013).
- [99] Klimov, V. I., Mikhailovsky, A. A., Xu, S., Malko, A., Hollingsworth, J. A., Leatherdale, C. A., Eisler, H. and Bawendi, M. G. Optical gain and stimulated emission in nanocrystal quantum dots. *Science*, **290**, 314–317 (2000).
- [100] Kazes, M., Lewis, D., Ebenstein, Y., Mokari, T. and Banin, U. Lasing from semiconductor quantum rods in a cylindrical microcavity. *Adv. Mater.*, **14**, 317–321 (2002).
- [101] Koberling, F. *Fluoreszenzmikroskopische Untersuchungen an einzelnen Halbleiter-Nanokristallen*. Ph.D. thesis, Johannes Gutenberg-Universität Mainz (2001).
- [102] Woggon, U. *Optical properties of semiconductor quantum dots*. Hamatologie Und Bluttransfusion. Springer, Berlin Heidelberg, Germany (1997).
- [103] Brus, L. E. A simple model for the ionization potential, electron affinity, and aqueous redox potentials of small semiconductor crystallites. *J. Chem. Phys.*, **79**, 5566–5571 (1983).
- [104] Brus, L. E. Electron–electron and electron-hole interactions in small semiconductor crystallites: the size dependence of the lowest excited electronic state. *J. Chem. Phys.*, **80**, 4403–4409 (1984).
- [105] Steigerwald, M. M. L. and Brus, L. E. L. Semiconductor crystallites: a class of large molecules. *Acc. Chem. Res.*, **23**, 183–188 (1990).
- [106] Efros, A., Rosen, M., Kuno, M., Nirmal, M., Norris, D. and Bawendi, M. Band-edge exciton in quantum dots of semiconductors with a degenerate valence band: dark and bright exciton states. *Phys. Rev. B. Condens. Matter*, **54**, 4843–4856 (1996).
- [107] Norris, D. and Bawendi, M. Measurement and assignment of the size-dependent optical spectrum in CdSe quantum dots. *Phys. Rev. B. Condens. Matter*, **53**, 16338–16346 (1996).
- [108] Grigoryan, G. B., Kazaryan, E. M., Efros, A. L. and Yezeva, T. V. Quantized holes and the absorption edge in spherical semiconductor microcrystals with a complex valence band structure. *Sov. Phys. Solid State*, **32**, 1031–1035 (1990).

- [109] Norris, D. J., Sacra, A., Murray, C. B. and Bawendi, M. G. Measurement of the size dependent hole spectrum in CdSe quantum dots. *Phys. Rev. Lett.*, **72**, 2612–2615 (1994).
- [110] Banin, U., Cerullo, G., Guzelian, a. a., Bardeen, C. J., Alivisatos, a. P. and Shank, C. V. Quantum confinement and ultrafast dephasing dynamics in InP nanocrystals. *Phys. Rev. B*, **55**, 7059–7067 (1997).
- [111] Yoffe, A. D. Semiconductor quantum dots and related systems: Electronic, optical, luminescence and related properties of low dimensional systems. *Adv. Phys.*, **50**, 1–208 (2001).
- [112] Ren, T. *Quantum Dot-Dye Hybrid Systems for Energy Transfer Applications*. Ph.D. thesis, Johannes Gutenberg-Universität Mainz (2010).
- [113] Houtepen, A. J. and Vanmaekelbergh, D. Orbital occupation in electron-charged CdSe quantum-dot solids. *J. Phys. Chem. B*, **109**, 19634–19642 (2005).
- [114] Yu, W. W., Qu, L., Guo, W. and Peng, X. Experimental determination of the extinction coefficient of CdTe, CdSe, and CdS nanocrystals. *Chem. Mater.*, **15**, 2854–2860 (2003).
- [115] Xie, R., Li, Z. and Peng, X. Nucleation kinetics vs chemical kinetics in the initial formation of semiconductor nanocrystals. *J. Am. Chem. Soc.*, **131**, 15457–66 (2009).
- [116] Brus, L. Electronic wave functions in semiconductor clusters: experiment and theory. *J. Phys. Chem.*, **90**, 2555–2560 (1986).
- [117] Weller, H., Schmidt, H., Koch, U., Fojtik, a., Baral, S., Henglein, a., Kunath, W., Weiss, K. and Dieman, E. Photochemistry of colloidal semiconductors. Onset of light absorption as a function of size of extremely small CdS particles. *Chem. Phys. Lett.*, **124**, 557–560 (1986).
- [118] Spanhel, L., Haase, M., Weller, H. and Henglein, A. Photochemistry of colloidal semiconductors. 20. Surface modification and stability of strong luminescing CdS particles. *J. Am. Chem. Soc.*, **109**, 5649–5655 (1987).
- [119] Henglein, A. Small-particle research: physicochemical properties of extremely small colloidal metal and semiconductor particles. *Chem. Rev.*, **89**, 1861–1873 (1989).
- [120] Yang, Y. A., Wu, H., Williams, K. R. and Cao, Y. C. Synthesis of CdSe and CdTe nanocrystals without precursor injection. *Angew. Chemie Int. Ed.*, **44**, 6712–6715 (2005).
- [121] Van Embden, J., Chesman, A. S. R. and Jasieniak, J. J. The heat-up synthesis of colloidal nanocrystals. *Chem. Mater.*, **27**, 2246–2285 (2015).
- [122] Zeng, R., Zhang, T., Liu, J., Hu, S., Wan, Q., Liu, X., Peng, Z. and Zou, B. Aqueous synthesis of type-II CdTe/CdSe core-shell quantum dots for fluorescent probe labeling tumor cells. *Nanotechnology*, **20**, 095102 (2009).

- [123] Li, Y., Jing, L., Qiao, R. and Gao, M. Aqueous synthesis of CdTe nanocrystals: progresses and perspectives. *Chem. Commun.*, **47**, 9293–9311 (2011).
- [124] Samanta, A., Deng, Z. and Liu, Y. Aqueous synthesis of glutathione-capped CdTe/CdS/ZnS and CdTe/CdSe/ZnS core/shell/shell nanocrystal heterostructures. *Langmuir*, **28**, 8205–8215 (2012).
- [125] Qu, L., Peng, Z. A. and Peng, X. Alternative routes toward high quality CdSe nanocrystals. *Nano Lett.*, **1**, 333–337 (2001).
- [126] Niu, J. Z., Shen, H., Wang, H., Xu, W., Lou, S., Du, Z. and Li, L. S. Investigation on the phosphine-free synthesis of CdSe nanocrystals by cadmium precursor injection. *New J. Chem.*, **33**, 2114–2119 (2009).
- [127] LaMer, V. K. and Dinegar, R. H. Theory, production and mechanism of formation of monodispersed hydrosols. *J. Am. Chem. Soc.*, **72**, 4847–4854 (1950).
- [128] Sugimoto, T. *Monodispersed Particles*. Elsevier, New York (2001).
- [129] Mullin, J. *Crystallization*. Butterworth-Heinemann, Oxford (2001).
- [130] Kwon, S. G. and Hyeon, T. Formation mechanisms of uniform nanocrystals via hot-injection and heat-up methods. *Small*, **7**, 2685–2702 (2011).
- [131] Murray, C. B., Kagan, C. R. and Bawendi, M. G. Synthesis and characterization of monodisperse nanocrystals and close-packed nanocrystal assemblies. *Annu. Rev. Mater. Sci.*, **30**, 545–610 (2000).
- [132] Sugimoto, T. Preparation of monodispersed colloidal particles. *Adv. Colloid Interface Sci.*, **28**, 65–108 (1987).
- [133] Peng, X., Wickham, J. and Alivisatos, A. P. Kinetics of II-VI and III-V colloidal semiconductor nanocrystal growth: “focusing” of size distributions. *J. Am. Chem. Soc.*, **120**, 5343–5344 (1998).
- [134] Rogach, A. L. *Semiconductor Nanocrystal Quantum Dots*, volume 2. Springer Vienna, Vienna (2008).
- [135] Peng, X., Manna, L., Yang, W., Wickham, J., Scher, E., Kadavanich, A. and Alivisatos, A. Shape control of CdSe nanocrystals. *Nature*, **404**, 59–61 (2000).
- [136] Peng, Z. A. and Peng, X. Mechanisms of the shape evolution of CdSe nanocrystals. *J. Am. Chem. Soc.*, **123**, 1389–1395 (2001).
- [137] Xie, R., Kolb, U. and Basché, T. Design and synthesis of colloidal nanocrystal heterostructures with tetrapod morphology. *Small*, **2**, 1454–7 (2006).
- [138] Yeh, C.-y., Lu, Z. W., Froyen, S. and Zunger, A. Zinc-blende-wurtzite polytypism in semiconductors. *Phys. Rev. B*, **46**, 10086–10097 (1992).
- [139] Shiang, J. J., Kadavanich, A. V., Grubbs, R. K. and Alivisatos, a. P. Symmetry of annealed wurtzite CdSe nanocrystals: assignment to the C_{3v} point group. *J. Phys. Chem.*, **99**, 17417–17422 (1995).

- [140] Tolbert, S. H. and Alivisatos, A. P. Size dependence of a first order solid-solid phase transition: the wurtzite to rock salt transformation in CdSe nanocrystals. *Science*, **265**, 373–376 (1994).
- [141] Xu, S., Kumar, S. and Nann, T. Rapid synthesis of high-quality InP nanocrystals. *J. Am. Chem. Soc.*, **128**, 1054–1055 (2006).
- [142] Huang, K., Demadrille, R., Silly, M. G., Sirotti, F., Reiss, P. and Renault, O. Internal structure of InP/ZnS nanocrystals unraveled by high-resolution soft X-ray photoelectron spectroscopy. *ACS Nano*, **4**, 4799–4805 (2010).
- [143] Mushonga, P., Onani, M. O., Madiehe, A. M. and Meyer, M. Indium phosphide-based semiconductor nanocrystals and their applications. *J. Nanomater.*, **2012**, 1–11 (2012).
- [144] Virieux, H., Le Troedec, M., Cros-Gagneux, A., Ojo, W.-S., Delpech, F., Nayral, C., Martinez, H. and Chaudret, B. InP/ZnS nanocrystals: coupling NMR and XPS for fine surface and interface description. *J. Am. Chem. Soc.*, **134**, 19701–19708 (2012).
- [145] Jacobs, K., Wickham, J. and Alivisatos, a. P. Threshold size for ambient metastability of rocksalt CdSe nanocrystals. *J. Phys. Chem. B*, **106**, 3759–3762 (2002).
- [146] Van Sark, W. G. J. H. M., Frederix, P. L. T. M., Bol, A. a., Gerritsen, H. C. and Meijerink, A. Blueing, bleaching, and blinking of single CdSe/ZnS quantum dots. *ChemPhysChem*, **3**, 871–879 (2002).
- [147] Ma, J., Chen, J.-Y., Guo, J., Wang, C. C., Yang, W. L., Xu, L. and Wang, P. N. Photostability of thiol-capped CdTe quantum dots in living cells: the effect of photo-oxidation. *Nanotechnology*, **17**, 2083–2089 (2006).
- [148] Reiss, P., Bleuse, J. and Pron, A. Highly luminescent CdSe/ZnSe core/shell nanocrystals of low size dispersion. *Nano Lett.*, **2**, 781–784 (2002).
- [149] He, R. and Gu, H. Synthesis and characterization of monodispersed CdSe nanocrystals at lower temperature. *Colloids Surfaces A Physicochem. Eng. Asp.*, **272**, 111–116 (2006).
- [150] Peng, X., Schlamp, M. C., Kadavanich, A. V. and Alivisatos, A. P. Epitaxial growth of highly luminescent CdSe/CdS core/shell nanocrystals with photostability and electronic accessibility. *J. Am. Chem. Soc.*, **119**, 7019–7029 (1997).
- [151] Dabbousi, B. O., Rodriguez-Viejo, J., Mikulec, F. V., Heine, J. R., Mattoussi, H., Ober, R., Jensen, K. F. and Bawendi, M. G. (CdSe)ZnS core–shell quantum dots: synthesis and characterization of a size series of highly luminescent nanocrystallites. *J. Phys. Chem. B*, **101**, 9463–9475 (1997).
- [152] Ivanov, S. a., Nanda, J., Piryatinski, A., Achermann, M., Balet, L. P., Bezel, I. V., Anikeeva, P. O., Tretiak, S. and Klimov, V. I. Light amplification using inverted core/shell nanocrystals: towards lasing in the single-exciton regime. *J. Phys. Chem. B*, **108**, 10625–10630 (2004).

- [153] Mekis, I., Talapin, D. V., Kornowski, A., Haase, M. and Weller, H. One-pot synthesis of highly luminescent CdSe/CdS core–shell nanocrystals via organometallic and “greener” chemical approaches. *J. Phys. Chem. B*, **107**, 7454–7462 (2003).
- [154] Baranov, A. V., Rakovich, Y. P., Donegan, J. F., Perova, T. S., Moore, R. A., Talapin, D. V., Rogach, A. L., Masumoto, Y. and Nabiev, I. Effect of ZnS shell thickness on the phonon spectra in CdSe quantum dots. *Phys. Rev. B*, **68**, 165306 (2003).
- [155] Talapin, D. V., Mekis, I., Götzinger, S., Kornowski, A., Benson, O. and Weller, H. CdSe/CdS/ZnS and CdSe/ZnSe/ZnS core–shell–shell nanocrystals. *J. Phys. Chem. B*, **108**, 18826–18831 (2004).
- [156] Deka, S., Quarta, A., Lupo, M. G., Falqui, A., Boninelli, S., Giannini, C., Morello, G., De Giorgi, M., Lanzani, G., Spinella, C., Cingolani, R., Pellegrino, T. and Manna, L. CdSe/CdS/ZnS double shell nanorods with high photoluminescence efficiency and their exploitation as biolabeling probes. *J. Am. Chem. Soc.*, **131**, 2948–2958 (2009).
- [157] Han, T.-T., Fu, Y., Wu, J., Yue, Y. and Dai, N. Optical properties of multicoated CdSe/CdS/ZnS quantum dots for multiphoton applications. *J. Phys. D. Appl. Phys.*, **41**, 115104 (2008).
- [158] Bang, J., Park, J., Lee, J. H., Won, N., Nam, J., Lim, J., Chang, B. Y., Lee, H. J., Chon, B., Shin, J., Park, J. B., Choi, J. H., Cho, K., Park, S. M., Joo, T. and Kim, S. ZnTe/ZnSe (core/shell) type-II quantum dots: their optical and photovoltaic properties. *Chem. Mater.*, **22**, 233–240 (2010).
- [159] Itzhakov, S., Shen, H., Buhbut, S., Lin, H. and Oron, D. Type-II quantum-dot-sensitized solar cell spanning the visible and near-infrared spectrum. *J. Phys. Chem. C*, **117**, 22203–22210 (2013).
- [160] Piryatinski, A., Ivanov, S. a., Tretiak, S. and Klimov, V. I. Effect of quantum and dielectric confinement on the exciton-exciton interaction energy in type II core/shell semiconductor nanocrystals. *Nano Lett.*, **7**, 108–115 (2007).
- [161] Lo, S. S., Mirkovic, T., Chuang, C. H., Burda, C. and Scholes, G. D. Emergent properties resulting from type-II band alignment in semiconductor nanoheterostructures. *Adv. Mater.*, **23**, 180–197 (2011).
- [162] Ghosh, Y., Mangum, B. D., Casson, J. L., Williams, D. J., Htoon, H. and Hollingsworth, J. a. New insights into the complexities of shell growth and the strong influence of particle volume in nonblinking “giant” core/shell nanocrystal quantum dots. *J. Am. Chem. Soc.*, **134**, 9634–9643 (2012).
- [163] Danek, M., Jensen, K. F., Murray, C. B. and Bawendi, M. G. Synthesis of luminescent thin-film CdSe/ZnSe quantum dot composites using CdSe quantum dots passivated with an overlayer of ZnSe. *Chem. Mater.*, **8**, 173–180 (1996).
- [164] Hoener, C. F., Allan, K. A., Bard, A. J., Champion, A., Fox, M. A., Mallouk, T. E., Webber, S. E. and White, J. M. Demonstration of a shell-core structure in layered CdSe-ZnSe small particles by X-ray photoelectron and Auger spectroscopies. *J. Phys. Chem.*, **96**, 3812–3817 (1992).

- [165] Kortan, a. R., Hull, R., Opila, R. L., Bawendi, M. G., Steigerwald, M. L., Carroll, P. J. and Brus, L. E. Nucleation and growth of cadmium selenide on zinc sulfide quantum crystallite seeds, and vice versa, in inverse micelle media. *J. Am. Chem. Soc.*, **112**, 1327–1332 (1990).
- [166] Tian, Y., Newton, T., Kotov, N. a., Guldi, D. M. and Fendler, J. H. Coupled composite CdS–CdSe and core–shell types of (CdS)CdSe and (CdSe)CdS nanoparticles. *J. Phys. Chem.*, **100**, 8927–8939 (1996).
- [167] Mews, A., Eychmüller, A., Giersig, M., Schooss, D. and Weller, H. Preparation, characterization, and photophysics of the quantum dot quantum well system cadmium sulfide/mercury sulfide/cadmium sulfide. *J. Phys. Chem.*, **98**, 934–941 (1994).
- [168] Mews, A., Kadavanich, A. V., Banin, U. and Alivisatos, A. P. Structural and spectroscopic investigations of CdS/HgS/CdS quantum-dot quantum wells. *Phys. Rev. B*, **53**, R13242–R13245 (1996).
- [169] Xu, J., Cui, D., Zhu, T., Paradee, G., Liang, Z., Wang, Q., Xu, S. and Wang, A. Y. Synthesis and surface modification of PbSe/PbS core-shell nanocrystals for potential device applications. *Nanotechnology*, **17**, 5428–5434 (2006).
- [170] Talapin, D. V., Yu, H., Shevchenko, E. V., Lobo, A. and Murray, C. B. Synthesis of colloidal PbSe/PbS core-shell nanowires and PbS/Au nanowire-nanocrystal heterostructures. *J. Phys. Chem. C*, **111**, 14049–14054 (2007).
- [171] Kim, S., Kim, T., Kang, M., Kwak, S. K., Yoo, T. W., Park, L. S., Yang, I., Hwang, S., Lee, J. E., Kim, S. K. and Kim, S.-W. Highly luminescent InP/GaP/ZnS nanocrystals and their application to white light-emitting diodes. *J. Am. Chem. Soc.*, **134**, 3804–3809 (2012).
- [172] Kim, T., Kim, S. W., Kang, M. and Kim, S.-W. Large-scale synthesis of InPZnS alloy quantum dots with dodecanethiol as a composition controller. *J. Phys. Chem. Lett.*, **3**, 214–218 (2012).
- [173] Micic, O. I., Curtis, C. J., Jones, K. M., Sprague, J. R. and Nozik, A. J. Synthesis and characterization of InP quantum dots. *J. Phys. Chem.*, **98**, 4966–4969 (1994).
- [174] Guzelian, a. a., Katari, J. E. B., Kadavanich, a. V., Banin, U., Hamad, K., Juban, E., Alivisatos, a. P., Wolters, R. H., Arnold, C. C. and Heath, J. R. Synthesis of size-selected, surface-passivated InP nanocrystals. *J. Phys. Chem.*, **100**, 7212–7219 (1996).
- [175] Battaglia, D. and Peng, X. Formation of high quality InP and InAs nanocrystals in a noncoordinating solvent. *Nano Lett.*, **2**, 1027–1030 (2002).
- [176] Xu, S., Ziegler, J. and Nann, T. Rapid synthesis of highly luminescent InP and InP/ZnS nanocrystals. *J. Mater. Chem.*, **18**, 2653 (2008).
- [177] Adam, S., Talapin, D. V., Borchert, H., Lobo, A., McGinley, C., de Castro, a. R. B., Haase, M., Weller, H. and Möller, T. The effect of nanocrystal surface structure on the luminescence properties: photoemission study of HF-etched InP nanocrystals. *J. Chem. Phys.*, **123**, 084706 (2005).

- [178] Alivisatos, A. P., Johnsson, K. P., Peng, X., Wilson, T. E., Loweth, C. J., Bruchez, M. P. and Schultz, P. G. Organization of nanocrystal molecules using DNA. *Nature*, **382**, 609–611 (1996).
- [179] Loweth, C. J., Caldwell, W. B., Peng, X., Alivisatos, a. P. and Schultz, P. G. DNA-based assembly of gold nanocrystals. *Angew. Chemie Int. Ed.*, **38**, 1808–1812 (1999).
- [180] Zanchet, D., Micheel, C. M., Parak, W. J., Gerion, D., Williams, S. C. and Alivisatos, a. P. Electrophoretic and structural studies of DNA-directed Au nanoparticle groupings. *J. Phys. Chem. B*, **106**, 11758–11763 (2002).
- [181] Israelachvili, J. N. Intermolecular and surface forces. Elsevier, London, 3rd edition (1997).
- [182] Zhang, H. and Wang, D. Controlling the growth of charged-nanoparticle chains through interparticle electrostatic repulsion. *Angew. Chemie Int. Ed.*, **47**, 3984–3987 (2008).
- [183] Shim, M. and Guyot-Sionnest, P. Permanent dipole moment and charges in colloidal semiconductor quantum dots. *J. Chem. Phys.*, **111**, 6955–6964 (1999).
- [184] Tang, Z. Spontaneous organization of single CdTe nanoparticles into luminescent nanowires. *Science*, **297**, 237–240 (2002).
- [185] Green, M. The nature of quantum dot capping ligands. *J. Mater. Chem.*, **20**, 5797–5809 (2010).
- [186] Kowalczyk, B., Lagzi, I. and Grzybowski, B. a. Nanoseparations: Strategies for size and/or shape-selective purification of nanoparticles. *Curr. Opin. Colloid Interface Sci.*, **16**, 135–148 (2011).
- [187] Hanauer, M., Pierrat, S., Zins, I., Lotz, A. and Sönnichsen, C. Separation of nanoparticles by gel electrophoresis according to size and shape. *Nano Lett.*, **7**, 2881–2885 (2007).
- [188] Carrillo-Carrion, C., Moliner-Martinez, Y., Simonet, B. M. and Valcarcel, M. Capillary electrophoresis method for the characterization and separation of CdSe quantum dots. *Anal. Chem.*, **83**, 2807–2813 (2011).
- [189] Latham, A. H., Latham, A. H., Freitas, R. S., Freitas, R. S., Schiffer, P., Schiffer, P., Williams, M. E. and Williams, M. E. Capillary magnetic field flow fractionation and analysis of magnetic nanoparticles. *Anal. Chem.*, **77**, 5055–5062 (2005).
- [190] Yavuz, C. T., Mayo, J. T., Yu, W. W., Prakash, A., Falkner, J. C., Yean, S., Cong, L., Shipley, H. J., Kan, A., Tomson, M., Natelson, D. and Colvin, V. L. Low-field magnetic separation of monodisperse Fe₃O₄ nanocrystals. *Science*, **314**, 964–967 (2006).
- [191] Lee, J. S., Stoeva, S. I. and Mirkin, C. a. DNA-induced size-selective separation of mixtures of gold nanoparticles. *J. Am. Chem. Soc.*, **128**, 8899–8903 (2006).
- [192] Anand, M., Odom, L. A. and Roberts, C. B. Finely controlled size-selective precipitation and separation of CdSe/ZnS semiconductor nanocrystals using CO₂-gas-expanded liquids. *Langmuir*, **23**, 7338–7343 (2007).

- [193] Saunders, S. R. and Roberts, C. B. Size-selective fractionation of nanoparticles at an application scale using CO₂ gas-expanded liquids. *Nanotechnology*, **20**, 475605 (2009).
- [194] Akthakul, A., Hochbaum, A. I., Stellacci, F. and Mayes, A. M. Size fractionation of metal nanoparticles by membrane filtration. *Adv. Mater.*, **17**, 532–535 (2005).
- [195] Sweeney, S. F., Woehrle, G. H. and Hutchison, J. E. Rapid purification and size separation of gold nanoparticles via diafiltration. *J. Am. Chem. Soc.*, **128**, 3190–3197 (2006).
- [196] Wilson, O. M., Scott, R. W. J., Garcia-Martinez, J. C. and Crooks, R. M. Separation of dendrimer-encapsulated Au and Ag nanoparticles by selective extraction. *Chem. Mater.*, **16**, 4202–4204 (2004).
- [197] Kim, Y.-G., Oh, S.-K. and Crooks, R. M. Preparation and characterization of 1–2 nm dendrimer-encapsulated gold nanoparticles having very narrow size distributions. *Chem. Mater.*, **16**, 167–172 (2004).
- [198] Arnold, M. S., Stupp, S. I. and Hersam, M. C. Enrichment of single-walled carbon nanotubes by diameter in density gradients. *Nano Lett.*, **5**, 713–718 (2005).
- [199] Arnold, M. S., Green, A. a., Hulvat, J. F., Stupp, S. I. and Hersam, M. C. Sorting carbon nanotubes by electronic structure using density differentiation. *Nat. Nanotechnol.*, **1**, 60–65 (2006).
- [200] Sun, X., Zaric, S., Daranciang, D., Welsher, K., Lu, Y., Li, X. and Dai, H. Optical properties of ultrashort semiconducting single-walled carbon nanotube capsules down to sub-10 nm. *J. Am. Chem. Soc.*, **130**, 6551–6555 (2008).
- [201] Sun, X., Tabakman, S. M., Seo, W.-S., Zhang, L., Zhang, G., Sherlock, S., Bai, L. and Dai, H. Separation of nanoparticles in a density gradient: FeCo@C and gold nanocrystals. *Angew. Chemie Int. Ed.*, **48**, 939–942 (2009).
- [202] Sharma, V., Park, K. and Srinivasarao, M. Shape separation of gold nanorods using centrifugation. *Proc. Natl. Acad. Sci.*, **106**, 4981–4985 (2009).
- [203] Ghosh, S., Bachilo, S. M. and Weisman, R. B. Advanced sorting of single-walled carbon nanotubes by nonlinear density-gradient ultracentrifugation. *Nat. Nanotechnol.*, **5**, 443–450 (2010).
- [204] Akbulut, O., MacE, C. R., Martinez, R. V., Kumar, A. a., Nie, Z., Patton, M. R. and Whitesides, G. M. Separation of nanoparticles in aqueous multiphase systems through centrifugation. *Nano Lett.*, **12**, 4060–4064 (2012).
- [205] Faraday, M. The Bakerian lecture: experimental relations of gold (and other metals) to light. *Philos. Trans. R. Soc. London*, **147**, 145–181 (1857).
- [206] Ramaswamy, S. Issues in the statistical mechanics of steady sedimentation. *Adv. Phys.*, **50**, 297–341 (2001).

- [207] Happel, J. and Brenner, H. *Low Reynolds number hydrodynamics*. Noordhoff International Publishing, leyden, 2nd edition (1973).
- [208] Wilczok, T. and Chorazy, K. Isolation of liver nuclei. *Nature*, **188**, 516–517 (1960).
- [209] Schröter, C. J., Braun, M., Englert, J., Beck, H., Schmid, H. and Kalbacher, H. A rapid method to separate endosomes from lysosomal contents using differential centrifugation and hypotonic lysis of lysosomes. *J. Immunol. Methods*, **227**, 161–168 (1999).
- [210] Dall'Osto, L., Lico, C., Alric, J., Giuliano, G., Havaux, M. and Bassi, R. Lutein is needed for efficient chlorophyll triplet quenching in the major LHCII antenna complex of higher plants and effective photoprotection in vivo under strong light. *BMC Plant Biol.*, **6**, 32 (2006).
- [211] Sorensen, S. B., Pedersen, T. G. and Ottesen, M. Fractionation of protein components from beer by density gradient centrifugation. *Carlsberg Res. Commun.*, **47**, 227–231 (1982).
- [212] Sun, X., Luo, D., Liu, J. and Evans, D. G. Monodisperse chemically modified graphene obtained by density gradient ultracentrifugal rate separation. *ACS Nano*, **4**, 3381–3389 (2010).
- [213] Steinigeweg, D., Schütz, M., Salehi, M. and Schlücker, S. Fast and cost-effective purification of gold nanoparticles in the 20–250 nm size range by continuous density gradient centrifugation. *Small*, **7**, 2443–2448 (2011).
- [214] Graham, J. *Biological Centrifugation*. Garland Science, 1st edition (2001).
- [215] Sandison, D. R. and Webb, W. W. Background rejection and signal-to-noise optimization in confocal and alternative fluorescence microscopes. *Appl. Opt.*, **33**, 603–615 (1994).
- [216] Born, Max; Wolf, E. *Principles of Optics*. Cambridge University Press, 6th edition (1993).
- [217] Sheppard, C. J. R. and Gu, M. Image formation in two-photon fluorescence microscopy. *Optik.*, **86**, 104–106 (1990).
- [218] Rayleigh. XXXI. Investigations in optics, with special reference to the spectroscope. *Philos. Mag. Ser. 5*, **8**, 261–274 (1879).
- [219] Boos, A. *Emissions- und Anregungsspektroskopie einzelner Halbleiternanokristalle bei kryogenen Temperaturen*. Ph.D. thesis, Johannes Gutenberg-Universität Mainz (2014).
- [220] Kulzer, F. *Untersuchungen zum nichtphotochemischen Lochbrennen auf Einzelmoleküle- bene am Modellsystem Terrylen in p-Terphenyl*. Ph.D. thesis, Johannes Gutenberg-Universität Mainz (2000).
- [221] Demtröder., W. *Laserspektroskopie*. Springer, Berlin (2000).

- [222] Schlegel, G. *Temperaturabhängige Fluoreszenzdynamik einzelner Halbleiternanokristalle*. Ph.D. thesis, Johannes Gutenberg-Universität Mainz (2005).
- [223] Moerner, W. E. and Basché, T. Optische Spektroskopie von einzelnen Dotierungsmolekülen in Festkörpern. *Angew. Chemie*, **105**, 537–557 (1993).
- [224] Tittel, J., Göhde, W., Koberling, F., Basché, T., Kornowski, A., Weller, H. and Eychmüller, A. Fluorescence spectroscopy on single CdS nanocrystals. *J. Phys. Chem. B*, **101**, 3013–3016 (1997).
- [225] Koberling, F., Mews, A. and Basché, T. Single-dot spectroscopy of CdS nanocrystals and CdS/HgS heterostructures. *Phys. Rev. B*, **60**, 1921–1927 (1999).
- [226] Cichos, F., Martin, J. and Von Borczyskowski, C. Emission intermittency in silicon nanocrystals. *Phys. Rev. B - Condens. Matter Mater. Phys.*, **70**, 1–9 (2004).
- [227] Peterson, J. J., Peterson, J. J., Krauss, T. D. and Krauss, T. D. Fluorescence spectroscopy of single lead sulfide quantum dots. *Nano Lett.*, **6**, 510–514 (2006).
- [228] Cichos, F., Vonborczyskowski, C. and Orrit, M. Power-law intermittency of single emitters. *Curr. Opin. Colloid Interface Sci.*, **12**, 272–284 (2007).
- [229] Lee, S. F. and Osborne, M. a. Brightening, blinking, bluing and bleaching in the life of a quantum dot: friend or foe? *ChemPhysChem*, **10**, 2174–2191 (2009).
- [230] Orrit, M. Chemical and physical aspects of charge transfer in the fluorescence intermittency of single molecules and quantum dots. *Photochem. Photobiol. Sci.*, **9**, 637–642 (2010).
- [231] Haase, M., Hübner, C. G., Reuther, E., Herrmann, A., Müllen, K. and Basché, T. Exponential and power-law kinetics in single-molecule fluorescence intermittency. *J. Phys. Chem. B*, **108**, 10445–10450 (2004).
- [232] Kuno, M., Fromm, D. P., Hamann, H. F., Gallagher, A. and Nesbitt, D. J. Nonexponential “blinking” kinetics of single CdSe quantum dots: a universal power law behavior. *J. Chem. Phys.*, **112**, 3117–3120 (2000).
- [233] Chepic, D., Efros, A., a.I. Ekimov, Ivanov, M., Kharchenko, V., Kudriavtsev, I. and Yazeva, T. Auger ionization of semiconductor quantum drops in a glass matrix. *J. Lumin.*, **47**, 113–127 (1990).
- [234] Krauss, T. D. and Peterson, J. J. Quantum dots: a charge for blinking. *Nat. Mater.*, **11**, 14–16 (2011).
- [235] Banin, U., Bruchez, M., Alivisatos, a. P., Ha, T., Weiss, S. and Chemla, D. S. Evidence for a thermal contribution to emission intermittency in single CdSe/CdS core/shell nanocrystals. *J. Chem. Phys.*, **110**, 1195–1201 (1999).
- [236] Spinicelli, P., Buil, S., Quélin, X., Mahler, B., Dubertret, B. and Hermier, J.-P. Bright and grey states in CdSe-CdS nanocrystals exhibiting strongly reduced blinking. *Phys. Rev. Lett.*, **102**, 136801 (2009).

- [237] Zhang, K., Chang, H., Fu, A., Alivisatos, a. P and Yang, H. Continuous distribution of emission states from single CdSe/ZnS quantum dots. *Nano Lett.*, **6**, 843–847 (2006).
- [238] Zhao, J., Nair, G., Fisher, B. R. and Bawendi, M. G. Challenge to the charging model of semiconductor-nanocrystal fluorescence intermittency from off-state quantum yields and multiexciton blinking. *Phys. Rev. Lett.*, **104**, 157403 (2010).
- [239] Rosen, S., Schwartz, O. and Oron, D. Transient fluorescence of the off state in blinking CdSe/CdS/ZnS semiconductor nanocrystals is not governed by Auger recombination. *Phys. Rev. Lett.*, **104**, 157404 (2010).
- [240] Cordones, A. A., Bixby, T. J. and Leone, S. R. Direct Measurement of Off-State Trapping Rate Fluctuations in Single Quantum Dot Fluorescence. *Nano Lett.*, **11**, 3366–3369 (2011).
- [241] Galland, C., Ghosh, Y., Steinbrück, A., Sykora, M., Hollingsworth, J. a., Klimov, V. I. and Htoon, H. Two types of luminescence blinking revealed by spectroelectrochemistry of single quantum dots. *Nature*, **479**, 203–207 (2011).
- [242] Goushi, K., Yamada, T. and Otomo, A. Excitation intensity dependence of power-law blinking statistics in nanocrystal quantum dots. *J. Phys. Chem. C*, **113**, 20161–20168 (2009).
- [243] He, H., Qian, H., Dong, C., Wang, K. and Ren, J. Single nonblinking CdTe quantum dots synthesized in aqueous thiopropionic acid. *Angew. Chemie Int. Ed.*, **45**, 7588–7591 (2006).
- [244] Dong, C., Liu, H., Zhang, A. and Ren, J. Controllable blinking-to-nonblinking behavior of aqueous CdTeS Alloyed quantum dots. *Chem. - A Eur. J.*, **20**, 1940–1946 (2014).
- [245] Malko, A. V., Park, Y.-S., Sampat, S., Galland, C., Vela, J., Chen, Y., Hollingsworth, J. a., Klimov, V. I. and Htoon, H. Pump-intensity- and shell-thickness-dependent evolution of photoluminescence blinking in individual core/shell CdSe/CdS nanocrystals. *Nano Lett.*, **11**, 5213–5218 (2011).
- [246] Cragg, G. E. and Efros, A. L. Suppression of Auger processes in confined structures. *Nano Lett.*, **10**, 313–317 (2010).
- [247] Borchert, H., Haubold, S., Haase, M., Weller, H., McGinley, C., Riedler, M. and Möller, T. Investigation of ZnS passivated InP nanocrystals by XPS. *Nano Lett.*, **2**, 151–154 (2002).
- [248] Coolen, L., Brokmann, X., Spinicelli, P. and Hermier, J. P. Emission characterization of a single CdSe-ZnS nanocrystal with high temporal and spectral resolution by photon-correlation fourier spectroscopy. *Phys. Rev. Lett.*, **100**, 18–21 (2008).
- [249] Fernée, M. J., Littleton, B., Plakhotnik, T., Rubinsztein-Dunlop, H., Gómez, D. E. and Mulvaney, P. Charge hopping revealed by jitter correlations in the photoluminescence spectra of single CdSe nanocrystals. *Phys. Rev. B*, **81**, 155307 (2010).

- [250] Empedocles, S. a., Neuhauser, R., Shimizu, K. and Bawendi, M. G. Photoluminescence from single semiconductor nanostructures. *Adv. Mater.*, **11**, 1243–1256 (1999).
- [251] Moerner, W. E. Examining nanoenvironments in solids on the scale of a single, isolated impurity molecule. *Science*, **265**, 46–53 (1994).
- [252] Kuno, M., Lee, J. K., Dabbousi, B. O., Mikulec, F. V. and Bawendi, M. G. The band edge luminescence of surface modified CdSe nanocrystallites: probing the luminescing state. *J. Chem. Phys.*, **106**, 9869–9882 (1997).
- [253] Empedocles, S. A., Norris, D. J. and Bawendi, M. G. Photoluminescence spectroscopy of single CdSe nanocrystallite quantum dots. *Phys. Rev. Lett.*, **77**, 3873–3876 (1996).
- [254] Empedocles, S. a. and Bawendi, M. G. Influence of spectral diffusion on the line shapes of single CdSe nanocrystallite quantum dots. *J. Phys. Chem. B*, **103**, 1826–1830 (1999).
- [255] Empedocles, S. a. Quantum-confined Stark effect in single CdSe nanocrystallite quantum dots. *Science*, **278**, 2114–2117 (1997).
- [256] Claus Klingshirn. *Semiconductor Optics*. Springer-Verlag, Berlin Heidelberg, Germany (2007).
- [257] Wang, Z. L. *Characterization of Nanophase Materials*. Wiley-VCH Verlag GmbH, Weinheim, Germany (2000).
- [258] Nomura, S. and Kobayashi, T. Exciton-LA and -TA phonon couplings in a spherical semiconductor microcrystallite. *Solid State Commun.*, **82**, 335–340 (1992).
- [259] Saviot, L., Champagnon, B., Duval, E., Kudriavtsev, I. and a.I. Ekimov. Size dependence of acoustic and optical vibrational modes of CdSe nanocrystals in glasses. *J. Non. Cryst. Solids*, **197**, 238–246 (1996).
- [260] Lamb, H. On the vibrations of an elastic sphere. *Proc. London Math. Soc.*, **1**, 189–212 (1882).
- [261] Talati, M. and Jha, P. K. Acoustic phonons in semiconductor nanocrystals. *Comput. Mater. Sci.*, **37**, 58–63 (2006).
- [262] Tamura, A., Higeta, K. and Ichinokawa, T. The size dependence of vibrational eigenfrequencies and the mean square vibrational displacement of a small particle. *J. Phys. C Solid State Phys.*, **16**, 1585–1592 (1983).
- [263] Tanaka, A., Onari, S. and Arai, T. Low-frequency Raman scattering from CdS microcrystals embedded in a germanium dioxide glass matrix. *Phys. Rev. B*, **47**, 1237–1243 (1993).
- [264] Saviot, L., Murray, D. B. and de Lucas, M. d. C. M. Vibrations of free and embedded anisotropic elastic spheres: application to low-frequency Raman scattering of silicon nanoparticles in silica. *Phys. Rev. B*, **69**, 113402 (2004).

- [265] Fujii, M., Nagareda, T., Hayashi, S. and Yamamoto, K. Low-frequency Raman scattering from small silver particles embedded in SiO₂ thin films. *Phys. Rev. B*, **44**, 6243–6248 (1991).
- [266] Fujii, M., Kanzawa, Y., Hayashi, S. and Yamamoto, K. Raman scattering from acoustic phonons confined in Si nanocrystals. *Phys. Rev. B*, **54**, R8373–R8376 (1996).
- [267] Ovsyuk, N. and Novikov, V. Influence of a glass matrix on acoustic phonons confined in microcrystals. *Phys. Rev. B*, **53**, 3113–3118 (1996).
- [268] Murray, D. B. and Saviot, L. Phonons in an inhomogeneous continuum: vibrations of an embedded nanoparticle. *Phys. Rev. B*, **69**, 094305 (2004).
- [269] Lautrup, B. *Physics of continuous matter: exotic and everyday phenomena in the macroscopic world*. Taylor & Francis (2004).
- [270] Tamura, a., Higeta, K. and Ichinokawa, T. Lattice vibrations and specific heat of a small particle. *J. Phys. C Solid State Phys.*, **15**, 4975–4991 (2000).
- [271] Kelley, A. M. Electron-phonon coupling in CdSe nanocrystals. *J. Phys. Chem. Lett.*, **1**, 1296–1300 (2010).
- [272] Fernee, M. J., Littleton, B. N., Cooper, S., Rubinsztein-Dunlop, H., Gómez, D. E. and Mulvaney, P. Acoustic phonon contributions to the emission spectrum of single CdSe nanocrystals. *J. Phys. Chem. C*, **112**, 1878–1884 (2008).
- [273] Biadala, L., Louyer, Y., Tamarat, P. and Lounis, B. Direct observation of the two lowest exciton zero-phonon lines in single CdSe/ZnS nanocrystals. *Phys. Rev. Lett.*, **103**, 037404 (2009).
- [274] Heisenberg, W. Über den anschaulichen Inhalt der quantentheoretischen Kinematik und Mechanik. *Zeitschrift für Phys.*, **43**, 172–198 (1927).
- [275] Hollas, J. M. *Modern spectroscopy*. John Wiley & Sons Ltd, Chichester, UK (2004).
- [276] Bransden, B. H. and Joachain, C. J. *Quantum mechanics*. Prentice Hall (2000).
- [277] Varshni, Y. Temperature dependence of the energy gap in semiconductors. *Physica*, **34**, 149–154 (1967).
- [278] Pässler, R. Semi-empirical descriptions of temperature dependences of band gaps in semiconductors. *Phys. status solidi*, **236**, 710–728 (2003).
- [279] O'Donnell, K. P. and Chen, X. Temperature dependence of semiconductor band gaps. *Appl. Phys. Lett.*, **58**, 2924–2926 (1991).
- [280] Narayanaswamy, A., Feiner, L. and VanderZaag, P. Temperature dependence of the photoluminescence of InP/ZnS quantum dots. *J. Phys. Chem. C*, **112**, 6775–6780 (2008).
- [281] Narayanaswamy, A., Feiner, L. F., Meijerink, A. and Van Der Zaag, P. J. The effect of temperature and dot size on the spectral properties of colloidal InP/ZnS core-shell quantum dots. *ACS Nano*, **3**, 2539–2546 (2009).

- [282] Nirmal, M., Norris, D. J., Kuno, M., Bawendi, M. G., Efros, A. L. and Rosen, M. Observation of the “dark exciton” in CdSe quantum dots. *Phys. Rev. Lett.*, **75**, 3728–3731 (1995).
- [283] Wu, S.-Y. and Casida, J. E. Stereospecific intramolecular cyclization for asymmetric synthesis of (Rp)- and (Sp)- enantiomers of 2-octyl- and 2-phenyl-4h-1,3,2-benzodioxaphosphorin 2-oxides. *Phosphorus. Sulfur. Silicon Relat. Elem.*, **102**, 177–184 (1995).
- [284] Schmelz, O., Mews, A., Basché, T., Herrmann, A. and Müllen, K. Supramolecular complexes from CdSe nanocrystals and organic fluorophors. *Langmuir*, **17**, 2861–2865 (2001).
- [285] Striolo, A., Ward, J., Prausnitz, J. M., Parak, W. J., Zanchet, D., Gerion, D., Milliron, D. and Alivisatos, A. P. Molecular weight, osmotic second virial coefficient, and extinction coefficient of colloidal CdSe nanocrystals. *J. Phys. Chem. B*, **106**, 5500–5505 (2002).
- [286] Leatherdale, C. a., Woo, W. K., Mikulec, F. V. and Bawendi, M. G. On the absorption cross section of CdSe nanocrystal quantum dots. *J. Phys. Chem. B*, **106**, 7619–7622 (2002).
- [287] Ding, T. X., Olshansky, J. H., Leone, S. R. and Alivisatos, a. P. Efficiency of hole transfer from photoexcited quantum dots to covalently linked molecular species. *J. Am. Chem. Soc.*, **137**, 2021–2029 (2015).
- [288] Kuçur, E., Boldt, F. M., Cavaliere-Jaricot, S., Ziegler, J. and Nann, T. Quantitative analysis of cadmium selenide nanocrystal concentration by comparative techniques. *Anal. Chem.*, **79**, 8987–8993 (2007).
- [289] De Mello Donegá, C. and Koole, R. Size dependence of the spontaneous emission rate and absorption cross section of CdSe and CdTe quantum dots. *J. Phys. Chem. C*, **113**, 6511–6520 (2009).
- [290] Crosby, G. a. and Demas, J. N. Measurement of photoluminescence quantum yields. A review. *J. Phys. Chem.*, **75**, 991–1024 (1971).
- [291] Williams, A. T. R., Winfield, S. a. and Miller, J. N. Relative fluorescence quantum yields using a computer-controlled luminescence spectrometer. *Analyst*, **108**, 1067–1071 (1983).
- [292] Lakowicz, J. R. *Principles of fluorescence spectroscopy*. Plenum Press, New York, 3rd edition (2006).
- [293] Hofkens, J., Latterini, L., De Belder, G., Gensch, T., Maus, M., Vosch, T., Karni, Y., Schweitzer, G., De Schryver, F., Hermann, a. and Müllen, K. Photophysical study of a multi-chromophoric dendrimer by time-resolved fluorescence and femtosecond transient absorption spectroscopy. *Chem. Phys. Lett.*, **304**, 1–9 (1999).
- [294] Haase, M. *Einzelmolekülspektroskopie an einer homologen Reihe von Rylendiimiden und an einem bichromophoren Modellsystem für elektronischen Energietransfer*. Ph.D. thesis, Johannes Gutenberg-Universität Mainz (2010).

- [295] Koch, F. J. *Optische Spektroskopie einzelner Halbleiter-Nanokristalle*. Diplomarbeit, Johannes Gutenberg-Universität Mainz (2012).
- [296] Shiang, J. J., Risbud, S. H. and Alivisatos, a. P. Resonance Raman studies of the ground and lowest electronic excited state in CdS nanocrystals. *J. Chem. Phys.*, **98**, 8432–8442 (1993).
- [297] Norris, D. J., Efros, A. L., Rosen, M. and Bawendi, M. G. Size dependence of exciton fine structure in CdSe quantum dots. *Phys. Rev. B*, **53**, 16347–16354 (1996).
- [298] Adachi, S. *Properties of group-IV, III-V and II-VI semiconductors*. John Wiley & Sons, Ltd, Chichester, UK (2005).
- [299] Chilla, G., Kipp, T., Menke, T., Heitmann, D., Nikolic, M., Frömsdorf, A., Kornowski, A., Förster, S. and Weller, H. Direct observation of confined acoustic phonons in the photoluminescence spectra of a single CdSe-CdS-ZnS core-shell-shell nanocrystal. *Phys. Rev. Lett.*, **100**, 057403 (2008).
- [300] Stöttinger, S., Hinze, G., Diezemann, G., Oesterling, I., Müllen, K. and Basché, T. Impact of local compressive stress on the optical transitions of single organic dye molecules. *Nat. Nanotechnol.*, **9**, 182–186 (2014).
- [301] Blanton, S. A., Leheny, R. L., Hines, M. A. and Guyot-Sionnest, P. Dielectric dispersion measurements of CdSe nanocrystal colloids: observation of a permanent dipole moment. *Phys. Rev. Lett.*, **79**, 865–868 (1997).
- [302] Clark, J. H. Green chemistry: challenges and opportunities. *Green Chem.*, **1**, 1–8 (1999).
- [303] Dahan, M. Diffusion dynamics of glycine receptors revealed by single-quantum dot tracking. *Science*, **302**, 442–445 (2003).
- [304] Kim, S., Lim, Y. T., Soltesz, E. G., De Grand, A. M., Lee, J., Nakayama, A., Parker, J. A., Mihaljevic, T., Laurence, R. G., Dor, D. M., Cohn, L. H., Bawendi, M. G. and Frangioni, J. V. Near-infrared fluorescent type II quantum dots for sentinel lymph node mapping. *Nat. Biotechnol.*, **22**, 93–97 (2004).
- [305] Vela, J., Htoon, H., Chen, Y., Park, Y. S., Ghosh, Y., Goodwin, P. M., Werner, J. H., Wells, N. P., Casson, J. L. and Hollingsworth, J. A. Effect of shell thickness and composition on blinking suppression and the blinking mechanism in “giant” CdSe/CdS nanocrystal quantum dots. *J. Biophotonics*, **3**, 706–717 (2010).
- [306] García-Santamaría, F., Brovelli, S., Viswanatha, R., Hollingsworth, J. a., Htoon, H., Crooker, S. a. and Klimov, V. I. Breakdown of volume scaling in Auger recombination in CdSe/CdS heteronanocrystals: the role of the core-shell interface. *Nano Lett.*, **11**, 687–693 (2011).
- [307] Zhong, X., Han, M., Dong, Z., White, T. J. and Knoll, W. Composition-tunable $Zn_xCd_{1-x}Se$ nanocrystals with high luminescence and stability. *J. Am. Chem. Soc.*, **125**, 8589–8594 (2003).

- [308] Bertram, D., Mičić, O. I. and Nozik, A. J. Excited-state spectroscopy of InP quantum dots. *Phys. Rev. B*, **57**, R4265–R4268 (1998).
- [309] Devreese, J. T. *Polarons in ionic crystals and polar semiconductors: Antwerp Advanced Study Institute 1971 on Fröhlich polarons and electron-phonon interaction in polar semiconductors*. NATO Advanced Study Institutes Series. North-Holland Pub. Co. (1972).
- [310] Mittleman, D. M., Schoenlein, R. W., Shiang, J. J., Colvin, V. L., Alivisatos, a. P. and Shank, C. V. Quantum size dependence of femtosecond electronic dephasing and vibrational dynamics in CdSe nanocrystals. *Phys. Rev. B*, **49**, 14435–14447 (1994).
- [311] Seong, M. J., Micic, O. I., Nozik, a. J., Mascarenhas, A. and Cheong, H. M. Size-dependent Raman study of InP quantum dots. *Appl. Phys. Lett.*, **82**, 185–187 (2003).
- [312] Yin, Y. and Alivisatos, a. P. Colloidal nanocrystal synthesis and the organic–inorganic interface. *Nature*, **437**, 664–670 (2005).
- [313] Heyes, C., Kobitski, A., Breus, V. and Nienhaus, G. Effect of the shell on the blinking statistics of core-shell quantum dots: a single-particle fluorescence study. *Phys. Rev. B*, **75**, 125431 (2007).
- [314] Fu, H. and Zunger, A. InP quantum dots: Electronic structure, surface effects, and the redshifted emission. *Phys. Rev. B*, **56**, 1496–1508 (1997).
- [315] Kundu, J., Ghosh, Y., Dennis, A. M., Htoon, H. and Hollingsworth, J. a. Giant nanocrystal quantum dots: stable down-conversion phosphors that exploit a large Stokes shift and efficient shell-to-core energy relaxation. *Nano Lett.*, **12**, 3031–3037 (2012).
- [316] Nanda, J., Ivanov, S. A., Achermann, M., Bezel, I., Piryatinski, A. and Klimov, V. I. Light amplification in the single-exciton regime using exciton–exciton repulsion in type-II nanocrystal quantum dots. *J. Phys. Chem. C*, **111**, 15382–15390 (2007).
- [317] Oron, D., Kazes, M. and Banin, U. Multiexcitons in type-II colloidal semiconductor quantum dots. *Phys. Rev. B*, **75**, 035330 (2007).
- [318] Hollingsworth, J. A. Heterostructuring nanocrystal quantum dots toward intentional suppression of blinking and Auger recombination. *Chem. Mater.*, **25**, 1318–1331 (2013).
- [319] Zhang, A., Dong, C., Liu, H. and Ren, J. Blinking behavior of CdSe/CdS quantum dots controlled by alkylthiols as surface trap modifiers. *J. Phys. Chem. C*, **117**, 24592–24600 (2013).